VB

3rd Numerical Towing Tank Symposium

9.-13. September 2000

Tjärnö/Sweden

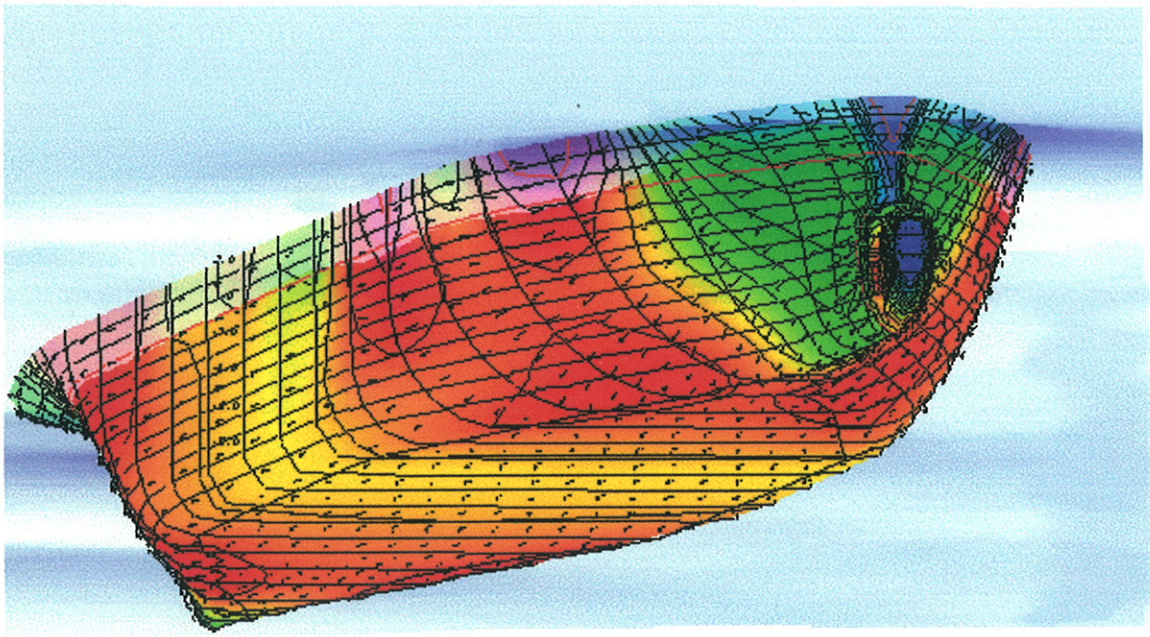

Volker Bertram (Ed.)

WEGEMT

Sponsored by

TMR Training and Mobility of Researchers

FLUENT SWEDEN AB

NUTTS'2000, 9.-13. September 2000, Tjärnö/Sweden

A WEGEMT Event Sponsored by the European Commission and Fluent AB Sweden

Papers are ordered in alphabetical order of author(s):

Haavard Holm, Aslaug Stakkestad, Bjornar Pettersen
Flow around a Ship Section, Heave and Sway Motion - Numerical and Experimental Results

Sung-Eun Kim, Robert Nyiredy
Assessment of Turbulence Models for Sternand Wake Flow Past a Modern VLCC Hull Form

Claudio Lugni, Maurizio Landrini, Andrea Colagrossi
Further Developments in Time Domain Computations for Seakeeping of Ships

Roberto Muscari, Andrea Di Mascio, R. Broglia
Application of a Body Force Method to the Study of the Wake past a Ship Hull

Kristian Bendix Nielsen, Stefan Mayer
Numerical Simulation of a Simplified Water Entry Problem

Sergio Parisi, Maurizio Landrini, Georgio Graziani
A Study on Roll-Motion by Viscous Vortex Method

Tanmay Sarkar, K.Bappa Salui, Dracos Vassalos
A RANS-Based Technique and its Application to Free Surface Flow Phenomena of Relevance in Marine Technology

Vladimir Shigunov, Lars Muck
Two Eulerian Approaches for Free-Surface Problems

Urban Svennberg
A Test of Turbulence Models for Steady Flow around Ships

Noritaka Takada, Ould M. El Moctar
Simulation of Viscous Flow about "Esso Osaka" in Manoeuvring Motion

Stephen Turnock, A.M. Wright, Richard Pattenden, Richard Pemberton
Adaptive Grid Flow Solutions around a Mariner Hull at Drift

George Tzabiras, Vagelis Papakonstantinou, T. Loukakis
Self-Propulsion Calculations Past a Fast Ferry

Mathias Vogt
Oblique Viscous Flow around a Twin Skeg Tanker Model

Stephen Watson, Peter Bull
Viscous Flow Prediction around a VLCC using Adaptive Grid Techniques

Jaap Windt, Hoyte Raven
A Composite Procedure for Ship Viscous Flow with Free Surface

Hironori Yasukawa
Nonlinear Time Domain Analysis of Ship Motions in Head Waves

NUMERICAL ANALYSIS OF SCREW PROPELLER HYDRODYNAMICS DURING MANOEUVRING

Tomasz Abramowski
Technical University of Szczecin, Faculty of Maritime Technology
Al. Piastów 41 , 71 – 065 Szczecin, Poland
e-mail : abramax@shiptech.tuniv.szczecin.pl

Extended abstract:

In order to provide the exact modelling of manoeuvring dynamics it is essential to calculate the hydrodynamic interactions in the stern region of a ship moving with drift. These interactions take place because of the oblique flow around the ship's hull. Velocity field in the plane of rotating screw is thus considerably modified.

The result of the ship's manoeuvres is a component of the ship's speed vector perpendicular to the plane of symmetry. This phenomenon deflects the hull's flow out of the course straight ahead. The hydrodynamic characteristics of the propeller are modified in such a condition. The discussed case occurs frequently in ship's service – for example only a weak wind may cause a certain significant drift angle - it is purposeful to determine hydrodynamic characteristics of the propeller at discussed service conditions.

The presented abstract provides a short information on the research currently performed at the Technical University of Szczecin concerning the problem mentioned above. The project is financially supported by the Komitet Badan Naukowych – no. 4-22-0553/17-00-00 (State Committee for Scientific Research, Poland). The aim of this research is to develop a computational method for determining the changes of velocity field at the working propeller and for calculating its thrust, torque and efficiency at the time of manoeuvring. The project will be executed in the following two steps:

1. Calculation of the nominal and effective velocity field in the wake of ship moving with a drift
2. Calculation of propeller hydrodynamic characteristics for operation in non-zero drift.

Despite the first step is a very complicated problem, which demands more time for analysis and its proper validation, the second aim has already been achieved, and the calculation method for screw hydrodynamic characteristics is presently validated. The unsteady lifting surface algorithm for the propeller working in the non-uniform inflow velocity field was employed in the research. It

lets us calculate the velocities and pressures around the arbitrarily given geometry of a screw. Velocity field is given in form of three-dimensional vectors for chosen points. The following assumptions were adopted:

- Propeller is moving in ideal fluid,
- Potential flow is assumed excluding vortex lines replacing screw blades and its wake
- Inflow velocity field is arbitrarily given

The vortex lattice replaces the screw, and the source lines, placed in the same locations as the vortex lines, represent its thickness. Standard data describing the screw shape was transformed into a grid of points with Cartesian co-ordinates x,y,z, being the endpoints of vortex lines. Bound and free vortices were placed on that basis. Each couple of two bound and two free vortices form a quadrangle having the centre C point, where normal to the surface vector has its starting point.

The determination of the blade forces requires the application of the proper wake vortex sheet. Wake vortex geometry used in the method is not constant in time, because the propeller is moving. It is necessary to modify the geometry of wake vortex according to propeller's velocities. The boundary condition on the blade surface is assumed, as the total normal velocity of the flow must be equal to zero on the surface.

The total velocity at the chosen point consists of the following:

- inflow velocity,
- velocity induced by the bound vortex system,
- velocity induced by the wake vortex sheet,
- velocity induced by the line sources system, modelling the blade thickness.

Moreover, the Kutta condition is assumed to close the system of equations, because the number of control points C is lower than the number of bound vortices. The Kutta condition says that on the trailing edge the circulation is equal to zero. By applying the Biot-Savart's law the velocities induced by the described system of vortex lines are obtained:

$$V = \frac{\gamma}{4\pi} \frac{B \times L}{L^3},$$

B – vector of the vortex line section,
L – vector connecting the vortex line with the control points.

The sources modelling the thickness of screw blade induce the velocities and are calculated according to the formula as below:

$$V_Q = \frac{Q}{4\pi L^2}$$

Intensity of source Q was determined by the assumption that it should balance the inflow of water to the appropriate volume of the blade. This can have two reasons: the change of volume of the blade on the same streamline, and the difference between the inflow velocities for each element of the blade.

Having calculated the velocity field around the screw, the pressure coefficients C_p for suction and pressure sides of the blade are determined using the Bernoulli equation for unsteady flows, followed by the forces and moments acting on the element of the screw blades. Total forces and moments were obtained by integration of partial forces along the whole propeller's surface.

For the assessment of presented mathematical model the computer program was compiled and the calculations of propeller's forces for ship performing standard Williamson's test were carried out. The three-dimensional velocity field was modified by the velocities on y-direction. These were sinusoidal changed according to the present drift angle. Of course, taking such assumption, the wake of the ship is only roughly approximated because the real interactions are much more complicated. Nevertheless for the validation purposes of calculations in variable non-uniform velocity field it is the sufficient assumption. Analysed values of the drift angles was relatively wide (up to 40^0) – which was the result of test condition (ballast). Results of the Williamson's test were gathered from full scale tests, except the drift angle which was calculated as the angle between the actual true course of the ship, and the line tangent to its path at the considered point. Drift angle $\bullet_D$ at the gravity centre of the ship must be corrected to the drift angle $\bullet\ a$ at the propeller plane. Drift angle undergoes a change along the ship length according to the function presented below:

$$\beta_X = \beta_D - \frac{\bar{x} \cdot \varpi}{V_S}$$

where:

- $\bullet_x$ - drift angle along the ship length,
- x - the distance from the considered point to the gravity centre
- $\bullet$ - angular speed
- V_s - ship's speed

The calculated average values of the thrust and torque in time domain, for the ship performing Williamson's test, are presented below.

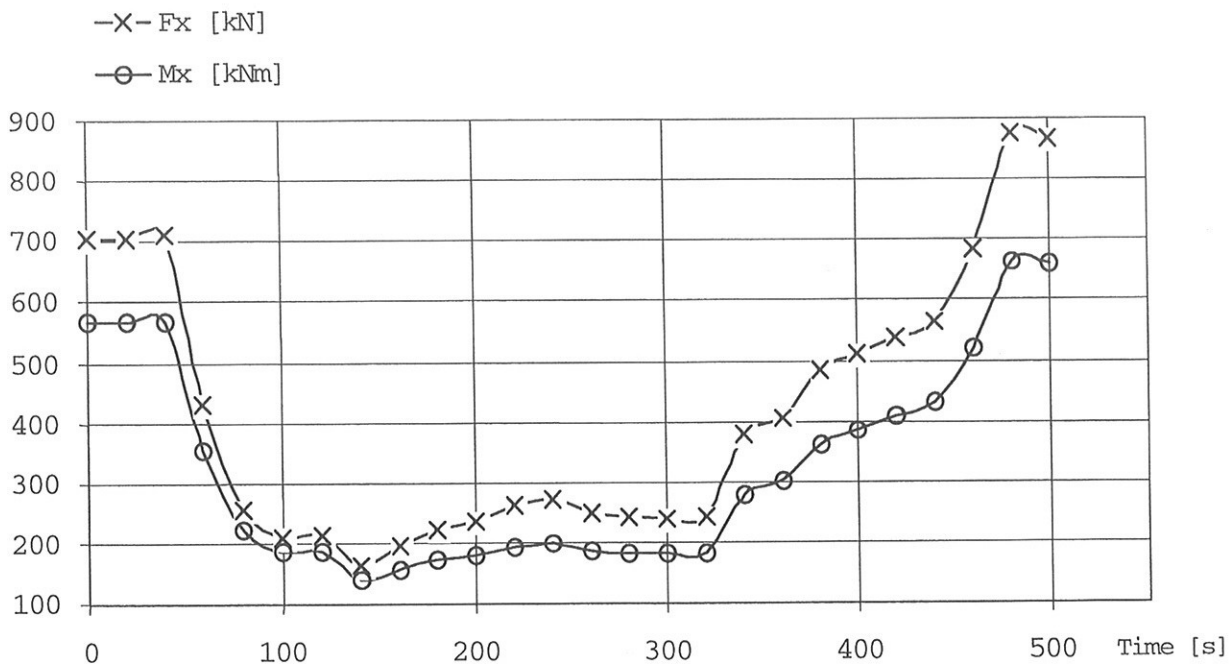

The more accurate assessment of the ship's wake during manoeuvring requires the numerical solution for RANSE being presently the subject of investigations of presented research:

$$\frac{d\,\bar{q}}{dt} = \bar{F} - \frac{1}{\rho}\,grad\;\;\bar{p} + \nu\Delta\,\bar{q} - div\,[R]$$

To obtain a closed system of these equations it is necessary to use a suitable turbulence model. Turbulent stress tensor puts 6 additional unknowns in the Reynolds equations and as a result of this the RANSEs are an open system. Because there are no physical premises concerning the connection of turbulent stresses with the other parameters of fluid then it is recognised as one of the most important problems in turbulent flows theory. Up so far, the Baldwin-Lomax and k-• models are the most popular. The k-• model is based on additional, semi-empirical equations for the kinetic turbulence energy and dissipation – unfortunately no effective turbulence models used presently make it possible to avoid empirical factors.

The Finite-Volume method will be applied to solving the RANS equations. It is based on direct discretization in the physical space - construction of three-dimensional, curvilinear, discrete grid.

Convergence Study of Viscous Flow Computations Around a High Loaded Nozzle Propeller

Moustafa Abdel-Maksoud[1], Potsdam Model Basin

Nozzle propellers are an ideal propulsion system for many marine applications such as fishing and tug boats, dynamic positioning of platforms, etc. The operation conditions for these applications are high thrust loading coefficients (C_{Th}) and low propeller inflow velocities (V_a). In this case, high loaded nozzle propellers are is much more efficient than conventional ones. Nozzle propellers have many advantages. The contraction of the flow through the nozzle reduce the inhomogenity of the propeller inflow. High thrust loading can be achieved along the propeller blade also near the tip. The pressure reduction of the flow around the nozzle produces an additional thrust. The ratio of the nozzle thrust to the propeller one increases with increasing the thrust loading coefficient. The thrust of the nozzle may be exceed the propeller thrust at bollard pull conditions.

The accuracy of the results of the numerical calculation is effected by the accuracy of the simulation of the flow in the gap between the propeller tip and the inside wall of the nozzle. With increasing the thrust loading, the influence of this gap will be strongly increased. In model scale this gap could be less than one millimetre. The application of RANS method for the prediction of the flow around nozzle propellers has many advantages. More detail information on the flow can be captured than in the experiment, e.g. the velocity and pressure distribution on the propeller blades and on the nozzle. Unfortunately, the required computational effort increases rapidly when the thrust loading coefficient increases. The combination of the experimental and numerical investigations can overcome the short-coming of each method. The experimental data can give a good overview on the forces and moments for the whole range of operational conditions. The numerical computations can be applied to focus the detail of the flow for selected loading conditions.

The increasing of the thrust loading means also the increase of the ratio between the circumferential and axial velocity components of the propeller flow. Close to the bollard pull condition, where the propeller inflow velocity is nearly zero, this ratio and the thrust loading coefficient go to infinity. For $C_{Th}>1000$, the increase of the axial velocity component behind the propeller may be more than 30 times of the inflow velocity. At the begin of the experiment, when the propeller starts to rotate, the axial velocity component is still very low, the thrust loading of the propeller is extremely high and the produced nozzle thrust is very low. With acceleration of the flow due to the propeller action the thrust loading of nozzle is increased and the propeller loading is decreased.

The computation of the viscous flow for a nozzle propeller is more complicated than for a conventional one. Convergence problems should be expected due to unsteady behaviour of the problem and the large difference between the inflow velocity of the computational domain and the inflow velocity of the propeller. The first is independent of the simulation time t_s, the second one is strongly depending on it. In addition, the total thrust and the ratio between the propeller and the nozzle thrust are effected also by the simulation time. Many other factors influence the convergence behaviour negatively, e.g. the high number of revolutions of the propeller and the small gap between the propeller and nozzle.

The numerical computations of the viscous flow were carried out for a four blade nozzle propeller. One propeller blade is considered in the computations. The calculation domain is a quarter of a cylinder. On the sides of the computational domain a periodic boundary condition is applied to consider the influence of the other blades. The calculation domain is divided into a stationary part and a rotating one. The stationary part includes the inflow and outflow regions and the nozzle. The propeller blade and a part of the propeller shaft are included in the rotating part of the computational domain. In the stationary part a Cartesian co-ordinate system is employed. The flow around the propeller is computed in a rotating co-ordinate system attached to the propeller. The number of revolutions and the inflow velocity are kept constant during the computations. The RANS equations in a rotating co-ordinate system involve additional terms compared to those in an inertial system. The computations were carried out with the commercial CFD software package CFX-TASCflow of AEA Technology. CFX-TASCflow uses a Finite Element based Finite Volume method. It uses block-structured non-orthogonal grids with grid attachment to discretise the domain. CFX-TASCflow models the equation for the conservation of mass, momentum and energy in terms of the dependent variables velocity and pressure in their Reynolds averaged form. The variables are discretised on a co-located grid with a second order fully conservative vertex based scheme. In the computations the "Linear Profile"

[1] Potsdam Model Basin, Marquardter Chaussee 100, D-14669 Potsdam, Maksoud@sva-potsdam.de

scheme with "Physical Advection Correction" of Schneider and Raw [1] was applied. The resulting linear equation system is solved with an Algebraic Multi-Grid (AMG) solver, which shows a linear scalability of the code with the number of grid cells. The equations are solved fully coupled.

Two turbulence models were applied in the present investigation, the standard k-ε model with a scalable wall function and advanced k-ω based model for improved separation prediction (SST model [2]). All formulations used in this study use a scalable near wall treatment, which allows a consistent grid refinement near the wall [3]. Special attention was paid to the stagnation point problems of two-equation models, using the Kato-Launder [4] modification or a production term limiter [2] for the k-ω based models.

The code was optimised and intensively tested for propellers in uniform flow and for behind ship condition. The investigations were carried out within a joint research project between the Potsdam Model Basin GmbH and AEA Technology GmbH, supported by the German Ministry for Education, Research and Technology [5]. The numerical method includes fully conservative stage capabilities to simulate the interaction of the nozzle and the propeller. Non-matching sliding grid interface is applied at the interfaces between the numerical grids in the rotating and the stationary frame.

The computations were carried out for model scale. A 3D solid CAD model was used for the grid generation. The geometry of the propeller blade and of the nozzle were considered without simplification. The gap between them was also included in the computation. Two different numerical grid configurations were applied. The first one consisted of 15 blocks and 320,000 control volumes. In the second grid approximately twice number of blocks and control volumes were used, Fig.1.

The investigation was carried out for many thrust loading coefficients. The results of 5 computations for the thrust loading coefficient 1000 will be discussed and compared with the measured results. Table 1 summarizes the results for the thrust and torque coefficients. The computations were carried out for different dimensions of the computation domain and turbulence models. The topology of the numerical grid and grid resolution were also varied, Table 1. Dp is the propeller diameter. The simulation time (t_s)was at least 30 seconds for each test case.

In the first test case, the calculated thrust of the propeller and the nozzle were lower than the measured values, specially the nozzle thrust is too low. In test case 2, the effect of the dimensions of the computational domain on the numerical results was investigated. The location of the outlet was moved from 6.5 to 20 Dp behind the propeller. The diameter of the computation domain D_{comp} was also increased from 4 to 9 Dp. The results show that the calculated thrust of the propeller and the nozzle are much higher than the corresponding values for case 1, specially the nozzle thrust, Table 1. At C_{Th}=1000 the axial velocity component in the propeller slip stream is much higher than the axial velocity component of the flow surrounding it. The high velocity gradient causes a re-circulation region and back flow may occur near the outlet region. That was the case for the second test case.

The dimensions of the calculation domain were increased again to avoid the back flow problem at the outlet, see test case 3. The distance between the propeller plane and of the inflow and outflow planes were increased to 87, 130.5 Dp respectively. The diameter of the calculation domain was also increased to 90 Dp. The numerical results of this test case show that the calculated propeller and nozzle thrust were increased. The calculated propeller thrust and the calculated ratio of propeller thrust to propeller torque are much higher than measured.

In test case 4, the effect of the turbulence model on the results of case 3 was investigated. The SST turbulence model can predict flow separation better than the standard k-ε model with wall function. Therefore, the SST turbulence model was applied in case 4 reducing the differences between the measured and calculated propeller thrust were reduced. This confirms that a good predication of the flow separation is important to calculate the flow on the propeller blade at high loading coefficient.

The y^+ values used in the first grid, used in cases 1 to 4, were not optimum for application of the SST model. Therefore a new grid was generated using the double grid resolution near the walls. The results with the test case 5 show that the thrust of the nozzle and the propeller are well predicted. The calculated propeller torque coefficient and the ratio of total thrust to the propeller torque agree well with the measured values. In addition, good convergence behaviour was achieved.

In the following some aspects of the nozzle propeller flow will be focused. The presented results are for test case 5. Figs.1 and 2 show the streamlines of the propeller inflow. The contraction of the flow in the front of the propeller is very high and there is back flow near the leading edge of the nozzle.

The unsteady behaviour of the nozzle propeller can be divided into two stages. The duration of first stage is about one second. In this stage the propeller trust is increased rapidly in the first 0.15 seconds. With increasing the nozzle thrust, the propeller thrust is decreased, Fig.3. The duration of the second stage is about 25 seconds, Fig.4. In this stage the propeller thrust is nearly constant and the nozzle thrust is increased very slowly. Concerning the convergence behaviour, the first 0.1 second is the most critical phase of the simulation.

Figs.5–8 show the velocity vectors in the most important regions of the computation. Fig.5 shows the flow outside the nozzle. Due to the lack of the axial flow, the propeller gets its inflow from its surrounding. The stagnation point is located at the middle of the nozzle where the flow is divided into two regions. The first one flows toward the leading edge and the other one toward the trailing edge. Fig.6 shows the velocity vectors at the leading edge. Due to the suction effect of the propeller, the velocity of the propeller inflow increased rapidly in this region. Fig.7 shows the flow at the trailing edge of the nozzle. The velocity vectors of the flow inside the nozzle are much higher than the flow outside it resulting in a very high velocity gradient in this region. Fig.8 shows the flow in gap between propeller blade and nozzle with a tip vortex on the propeller blade and back flow on the inside wall of the nozzle.

References

[1] Schneider G. E. and Raw, M. J., *Control Volume Finite Element Method for Heat Transfer and Fluid Flow using Co-located Variables*, Numerical Heat Transfer, Vol. 11, pp. 363-390, 1987.

[2] Menter F. R., *Two-Equation Eddy-Viscosity Turbulence Models for Engineering Applications*, AIAA- Journal, Vol. 32 (8), pp. 269-289, 1994.

[3] Grotjans, H. and Menter F. R. *Wall Functions for Industrial Applications*, In Papailiou, K. D. Editor, Computational Fluid Dynamics 98, Volume 1, Part 2, pp.1112-1117, Chichester, 1998, ECCOMAS, John Wiley & Sons.

[4] Kato, M. and Launder B. E., *The Modelling of Turbulent Flow around Stationary and Vibrating Cylinders*, In Ninth Symposium on Turbulent Shear Flows, Kyoto, Japan, 1993

[5] Abdel-Maksoud, M., Menter, F. R., Wuttke, H.: *Numerical Computation of the Viscous Flow around the Series 60 C_B = 0.6 Ship with Rotating Propeller*, 3rd Osaka Coll.. on Advanced CFD Appl. to Ship and Hull Form Design, Osaka, May 1998

Table 1: Summary of the numerical results and boundary conditions.

Test case	1	2	3	4	5	Experiment
Propeller thrust coeff. K_{TP}	0.186	0.229	0.243	0.238	0.225	0.222
Propeller torque coeff. $10K_Q$	0.363	0.387	0.372	0.365	0.381	0.373
Nozzle thrust coeff. K_{TD}	0.084	0.208	0.214	0.211	0.216	0.215
Total thrust coef. K_{TT}	0.271	0.437	0.457	0.449	0.441	0.437
K_{TP}/K_Q	5.127	5.925	6.539	6.537	5.896	5.960
K_{TT}/KQ	7.450	11.289	12.304	12.323	11.545	11.718
K_{TD}/K_{TP}	0.453	0.905	0.882	0.885	0.958	0.966
Thrust loading coefficient C_{TH}	621	1004	1050	1032	1012	1002
D_{comp}/D_p	4	9	90	90	70	
Location of inflow plane X/D_P	3.5	3.5	87	87	87	
Location of outflow plane X/D_P	6.5	22	130.5	130.5	130.5	
Turbulence model	K-ε	K-ε	K-ε	SST	SST	
Convergence	fast.	back flow	slow.	slow	Fast	

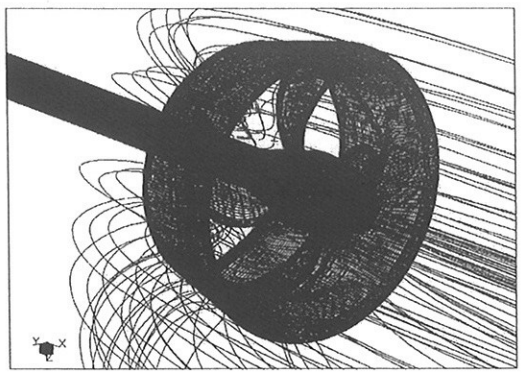

Fig.1: Grid on the surface of the propeller and the nozzle.

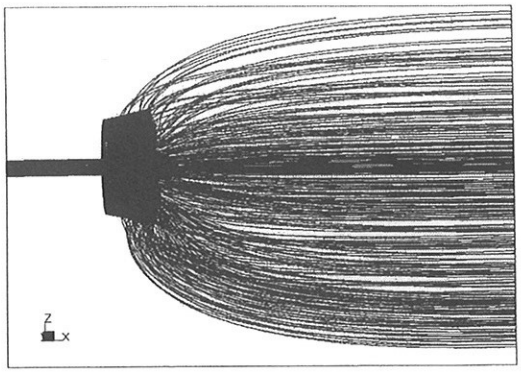

Fig.2: streamlines of the propeller inflow.

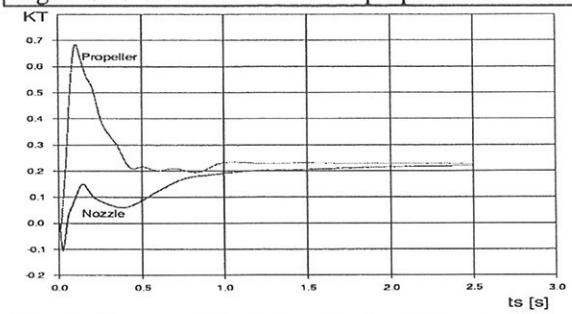

Fig. 3: Change of K_T during the first 2.5 seconds

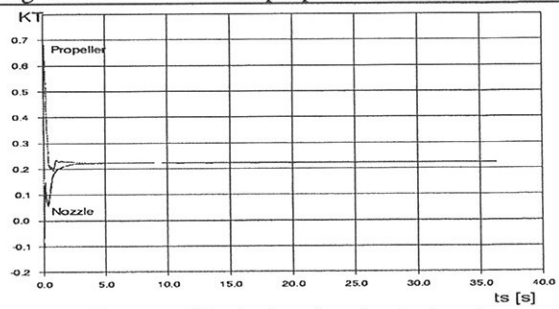

Fig. 4: Change of K_T during the simulation time t_s

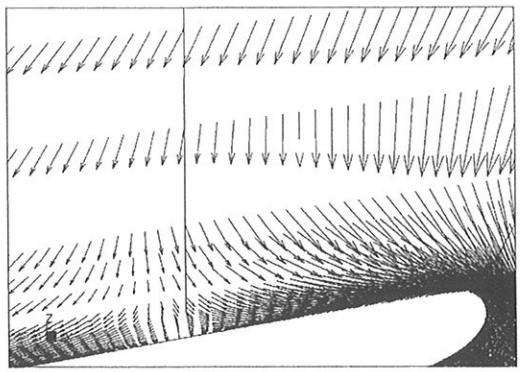

Fig. 5: Velocity vectors outside the nozzle

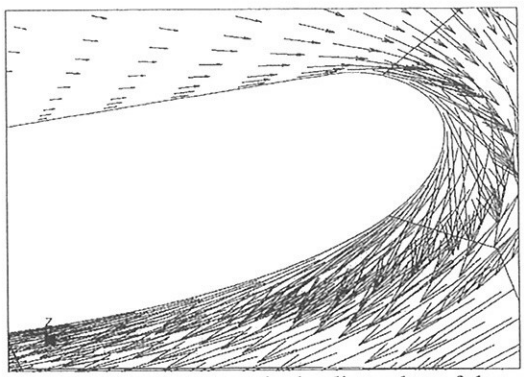

Fig.6: Velocity vectors on the leading edge of the nozzle

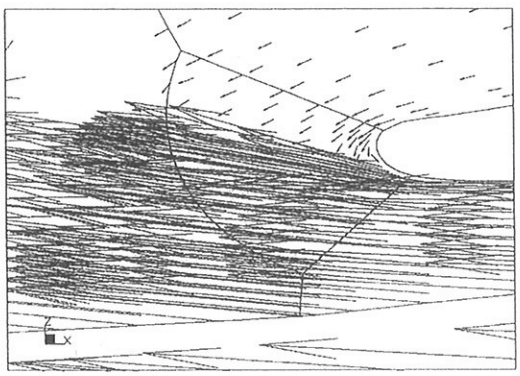

Fig.7: Velocity vectors on the trailing edge of the nozzle

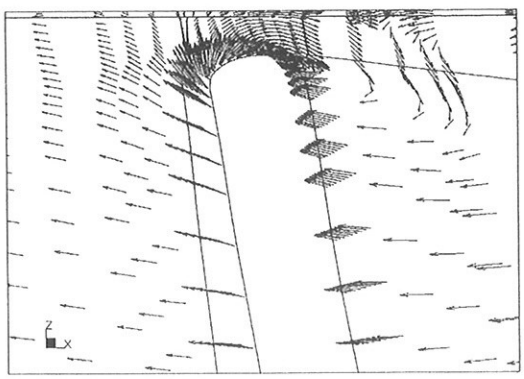

Fig.8: Velocity vectors on the tip of the propeller blade

The Effect of Non-Linear Froude-Krylov Forces on the Seakeeping of Monohull Vessels Using a Novel Calculation Method

by P.A. Bailey[1], E.J. Ballard[1], D.A. Hudson[1] and P. Temarel[1].

Introduction

A time domain mathematical model of ship motions allows for the incorporation of arbitrary and/or transient excitation, such as the influence of control surfaces and random waves. When compared to more conventional frequency domain analyses of ship motions [1–3], the possible arbitrary nature of motion/excitation in a time simulation leads to additional complications in the formulation and calculation of the forces and moments. In essence the fluid memory effect, exemplified by the generation of motion induced surface waves, introduces a dependence of the forces and moments on the past motions/excitations [4].

Recent studies [5–8] have investigated the use of convolution type expressions to represent fluid forces and moments on the ship. These expressions, applicable to arbitrary forms of linear motion/excitation, require the calculation of impulse response functions. This has been achieved using transforms of frequency domain data from three dimensional Green's function seakeeping methods [9–12].

It is believed by some that observed differences between theoretical linear motion predictions and experimental results can be attributed, to some extent, to the nature of the excitation, particularly for ships with large flare. To this end, it is possible to introduce a non-linear component of excitation into an otherwise linear system [13]. Integration of the Froude-Krylov wave excitation pressure over the instantaneous wetted surface yields such a contribution, but the integration method is complicated by the changing nature of the underwater form.

Mathematical Model

Seakeeping theory has traditionally referenced rigid body motions of a vessel to equilibrium axes. However, the behaviour of frequency domain added mass and hydrodynamic damping calculated with reference to these axes results in problematic evaluation of the corresponding impulse response functions [5]. Recently it has been shown by Bailey [14] that frequency domain data transformed to a set of body fixed axes is more amenable to accurate calculation of impulse response functions. The required transformation of data is discussed in detail by Bailey et. al. [6].

The heave and pitch (z^* and θ) equations of motion referenced to a right handed body fixed axis $Cxyz$ are written as

$$\begin{bmatrix} \dot{w}(t) \\ \dot{q}(t) \end{bmatrix} = \mathbf{M}^{-1} \begin{bmatrix} f_3(w,q,z^*,\theta,t) \\ f_5(w,q,z^*,\theta,t) \end{bmatrix}, \tag{1}$$

where w is the heave velocity, q is the pitch angular velocity and where

$$\begin{aligned} f_3 &= Z_\tau + Z_\alpha + \tilde{Z}_w(\infty)w + \tilde{Z}_q(\infty)q + mq\bar{U} \\ f_5 &= M_\tau + M_\alpha + \tilde{M}_w(\infty)w + \tilde{M}_q(\infty)q. \end{aligned}$$

The combination of weight, buoyancy and wave excitation actions are, for the present, denoted using terms with a subscript α. In due course, the detail of these terms will be discussed with reference to particular methods. The mass matrix is given by

$$\mathbf{M} = \begin{bmatrix} m - \tilde{Z}_{\dot{w}}(\infty) & -\tilde{Z}_{\dot{q}}(\infty) \\ -\tilde{M}_{\dot{w}}(\infty) & I_{yy} - \tilde{M}_{\dot{q}}(\infty) \end{bmatrix}.$$

Terms such as $\tilde{M}_w(\omega_e)$ and $\tilde{M}_{\dot{w}}(\omega_e)$ are the frequency dependent velocity and acceleration derivatives respectively, calculated by transforming seakeeping coefficients of added mass and damping to the body fixed axis system [6]. The terms with the subscript τ are the motion dependent hydrodynamic forces and moments (radiation actions) and are expressed using the impulse response functions as follows

$$Z_\tau = \int_0^t z_w(\tau)w(t-\tau)d\tau + \int_0^t z_q(\tau)q(t-\tau)d\tau$$

[1]School of Engineering Sciences, Ship Science, University of Southampton, United Kingdom.

$$M_\tau = \int_0^t m_w(\tau)w(t-\tau)d\tau + \int_0^t m_q(\tau)q(t-\tau)d\tau.$$

For $\tau > 0$, the impulse response functions can be calculated using either the velocity or acceleration frequency domain data [5–8], for example

$$z_w = \frac{2}{\pi}\int_0^\infty \tilde{Z}_w(\omega_e)\cos(\omega_e\tau)\,d\omega_e \quad = \quad \frac{-2}{\pi}\int_0^\infty \omega_e\tilde{Z}_{\dot{w}}(\omega_e)\sin(\omega_e\tau)\,d\omega_e.$$

The three dimensional theoretical methods used to calculate the frequency domain data in these these expressions are discussed in detail by Du et. al. [9,11] and Bailey et. al. [10,12].

Two time simulation methods have been developed, both of which use this formulation for the radiation actions but which use differing formulations for the wave excitations. These two methods will be referred to as methods A and B.

Method A: Linear Wave Excitation

It has been shown by Bailey et. al. [5] that linear wave excitation actions can be represented using a convolution type formulation such that terms with a subscript α in equation (1) can be represented as

$$Z_\alpha = \int_{-\infty}^\infty z^F(\tau)\alpha(t-\tau)d\tau + \int_{-\infty}^\infty z^D(\tau)\alpha(t-\tau)d\tau + Z_{z^*}z^* + Z_\theta\theta$$

$$M_\alpha = \int_{-\infty}^\infty m^F(\tau)\alpha(t-\tau)d\tau + \int_{-\infty}^\infty m^D(\tau)\alpha(t-\tau)d\tau + M_{z^*}z^* + M_\theta\theta.$$

Here the superscripts F and D refer to the Froude-Krylov and diffraction components respectively. Calculation of these wave excitation impulse response functions is more difficult than calculation of the radiation impulse response functions, since the influence a wave has before it reaches the reference must be accounted for. Effectively, the wave excitation impulse response functions are non-zero for $\tau < 0$ [5,15], and unlike the radiation impulse response functions their calculation requires both the real and imaginary parts. For example,

$$z^D = \frac{1}{\pi}\int_0^\infty \{\Xi_z^R(\omega_e)\cos(\omega_e\tau) - \Xi_z^I(\omega_e)\sin(\omega_e\tau)\}d\omega_e \qquad \text{for } \mathbf{all}\ \tau.$$

Method B: Non-Linear Froude-Krylov

In this method, the terms in equation (1) denoted with a subscript α represent non-linear restoring and Froude-Krylov forces and moments. In order to calculate these terms, a method of determining the buoyancy and Froude-Krylov wave excitations up to the incident waterline with the ship in its perturbed state has been developed. The non-linear Froude Krylov and restoring forces and moments are then calculated by subtracting the relevant components of weight.

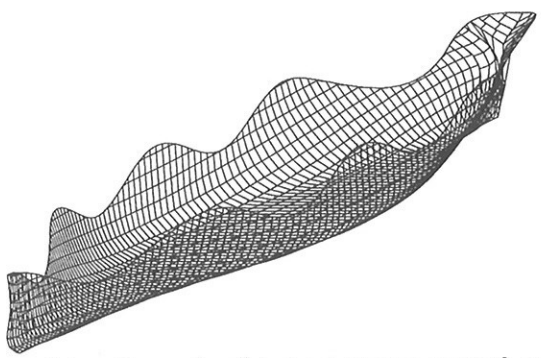

Figure 1: Example of instantaneous wetted portion of *Mariner* ship. $L = 160.93$m, $\chi_0 = 0$, $\alpha_0 = 2.0$m, $\lambda = 40.2$m.

Starting with a mesh of quadrilateral panels representing the entire surface of the ship hull, the method for calculating non-linear Froude-Krylov wave excitation and buoyancy first extracts the instantaneous underwater portion of the hull. At any instant, panels which are entirely above the surface are ignored and panels which cross the water surface are either split or replaced with two smaller panels. This is illustrated in figure 1. The static and Froude-Krylov fluid pressures are evaluated at the geometric centre of each panel, and contributions to each of the forces and moments are determined using this with the panel area and normals. The total Froude-Krylov and buoyancy components are calculated by simply summing contributions

from all the panels.

In the development of this scheme, great care has been taken to ensure that splitting, adding or destroying panels as the motion progresses does not introduce step changes in the resulting forces and moments [14].

At present, this method excludes any contribution from the diffraction wave excitation.

Results and Discussion

Both time simulation methods A and B were implemented using a Runge-Kutta time stepping scheme [16]. Validation of these methods has involved performing time domain simulations in sinusoidal head seas to determine transfer functions for the ships motions. Both time simulation methods have been compared against corresponding predictions made using a pulsating source three dimensional seakeeping method [17].

Figure 2 illustrates heave and pitch response amplitude operators for a Series 60 hull form calculated using method A. It can be seen that the time simulation and frequency domain predictions are in good agreement, providing validation of the calculated radiation and wave excitation impulse response functions as well validation of the time simulation implementation.

Figures 3 and 4 illustrate heave and pitch transfer functions for the *Mariner* ship calculated using the non-linear method B. It can be seen that for the mainly wall sided *Mariner* ship the responses retain linear characteristics, even in wave heights of comparable size to the draught of the vessel ($T = 7.467m$). Larger wave heights greater than the draught of the vessel do produce more of a non-linear response.

Future investigations will combine the diffraction excitation impulse response function components of method A with the non-linear Froude-Krylov of components of method B. The study will then be extended to more flared vessels, such as yacht forms, for which greater non-linearity in response is expected.

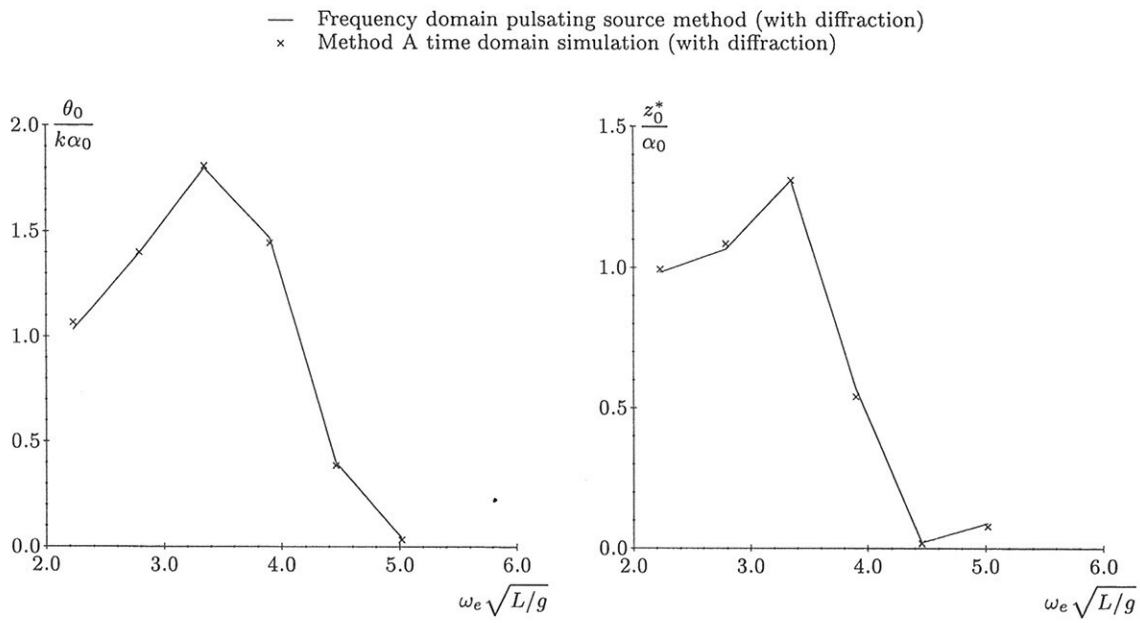

Figure 2: Heave and pitch response amplitude operators of a Series 60 ship type in head waves calculated using a frequency domain pulsating source seakeeping method and the time simulation method A. $F_n = 0.2$, $L = 3.048$m.

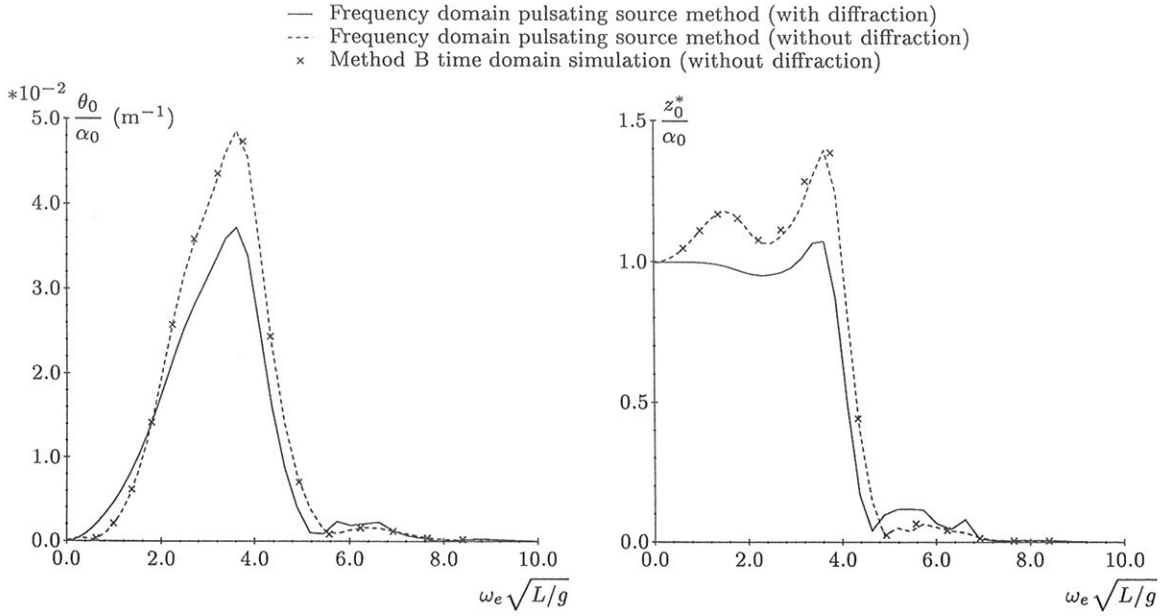

Figure 3: Heave and pitch transfer functions of *Mariner* ship type in head waves calculated using a frequency domain pulsating source seakeeping method and the time simulation method B. $F_n = 0.19$, $L = 160.93$m, wave amplitude $\alpha_0 = 0.01$m.

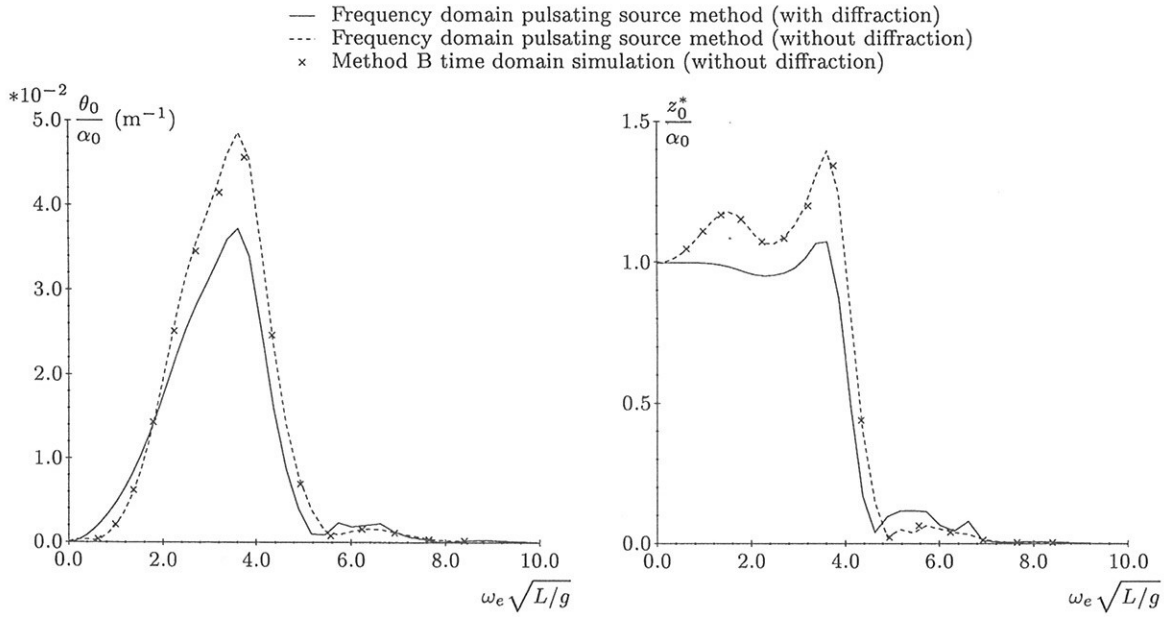

Figure 4: Heave and pitch transfer functions of *Mariner* ship type in head waves calculated using a frequency domain pulsating source seakeeping method and the time simulation method B. $F_n = 0.19$, $L = 160.93$m, wave amplitude $\alpha_0 = 2.0$m

References

[1] R. F. Beck, W. E. Cummins, J. F. Dalzell, P. Mandel, and W. C. Webster. *Principles of Naval Architecture*, volume 3, chapter 8. Trans. SNAME, 1989.

[2] J. N. Newman. *Marine Hydrodynamics.* MIT Press, 1977.

[3] O. M. Faltinsen. *Sea Loads on Ships and Offshore Structures.* Cambridge Ocean Technology Series. Cambridge University Press, 1990.

[4] R. E. D. Bishop, R. K. Burcher, and W. G. Price. The fifth annual Fairey Lecture: on the linear representation of fluid forces and moments in unsteady flow. *Journal of Sound and Vibration*, 29(1):113–128, 1973.

[5] P. A. Bailey, E. J. Ballard, D. A. Hudson, and P. Temarel. Time domain analysis of vessels in waves accounting for fluid memory effects. In *To be published in Proc. NAV'2000*, Viena, 2000.

[6] P. A. Bailey, W. G. Price, and P. Temarel. A unified mathematical model describing the manoeuvring of a ship travelling in a seaway. *Trans. RINA*, 140:131–149, 1998.

[7] P. A. Bailey, D. A. Hudson, W. G. Price, and P. Temarel. Theoretical and experimental techniques for predicting seakeeping and manoeuvring ship characteristics. In *RINA Intl. Conf. on Ship Motions and Manoeuvrability, Paper No. 5*, London, 1998.

[8] P. A. Bailey, D. A. Hudson, W. G. Price, and P. Temarel. The measurement and prediction of fluid actions experienced by a manoeuvring vessel. In *Proc. Intl. Symposium and Workshop on Forces acting on a Manoeuvring Vessel, MAN '98*, pages 117–123, Val de Reuil, France, 1998.

[9] S. X. Du, D. A. Hudson, W. G. Price, and P. Temarel. Comparison of numerical evaluation techniques for the hydrodynamic analysis of a ship travelling in waves. *Trans. RINA*, 141, 1999.

[10] P. A. Bailey, D. A. Hudson, W. G. Price, and P. Temarel. Theoretical validation of the hydrodynamics of high speed mono- and multi- hull vessels travelling in a seaway. In *PRADS '98: The Seventh International Symposium on Practical Design of Ships and Mobile Units*, pages 567–576, The Hague, September 1998. Elsevier Science, B.V.

[11] S. X. Du, D. A. Hudson, W.G. Price, and P. Temarel. A validation study on mathematical models of speed and frequency dependence in seakeeping. *Proceedings of the Institution of Mechanical Engineers, Part C*, 214:181–202, 2000.

[12] P. A. Bailey, D. A. Hudson, W. G. Price, and P. Temarel. Comparison between theory and experiment in a seakeeping validation study. (accepted for publication). *Trans. RINA*, 2000.

[13] N. Fonseca and C. Guedes Soares, editors. *Marine, Offshore and Ice Technology*, chapter Time domain analysis of vertical ship motions, pages 225–242. Computational Mechanics Publication, 1994.

[14] P. A. Bailey. *Manoeuvring of a ship in a seaway.* PhD Thesis, University of Southampton, 1999.

[15] B. K. King, R. F. Beck, and A. R. Magee. Seakeeping calculations with forward speed using time-domain analysis. In *17th Symposium on Naval Hydrodynamics*, pages 577–596, The Hague, The Netherlands, 1988.

[16] S. Nakamura. *Applied Numerical Methods in C.* Prentice Hall, 1993.

[17] R. B. Inglis. *A Three Dimensional Analysis of the Motion of a Rigid Ship in Waves.* PhD thesis, University of London, 1980.

Post-Processing of Time-Dependent CFD Analyses using Virtual Reality Modelling Language

Marco Barcellona, INSEAN, Via di Vallerano 139, I-00128 Rome, marco@rios3.insean.it
Volker Bertram, HSVA, Bramfelder Str 164, D-22305 Hamburg, bertram@hsva.de

The predominant CFD application today is the simulation of resistance and propulsion tests, i.e. the computation of the flow about a ship moving steadily ahead with constant speed. However, research is active on unsteady flow simulations, namely seakeeping and maneuvering simulations. A natural extension of current 'snap-shot' plots are animations or - one step further - Virtual Reality animations allowing customers to browse arbitrarily through flow fields in time and space. We use here the term "Virtual Reality" for the "poor man's" version of Virtual Reality, i.e. a usually mouse-controlled navigation through a three-dimensional environment on a graphics monitor. This is far from what fully immersive Virtual Reality envisions, but can be realized on computer hardware widely available in industry and is sufficient for the applications we have in mind.

Most CFD applications in naval architecture involve dedicated hydrodynamic experts consulting shipyard designers. The consultants are usually at some other location than the customers. Ideally, we would like to have a commercial-of-the-shelf (COTS) visualization tool capable of producing 'unlimited' or 'continuous' views in space and time, with the ability to 'zoom' in space or time (slow-motion). The models should be easily communicated via the web and should be readable for customers without requiring significant investment in hardware and software, preferably running on 'plain-vanilla' PCs. Ideally, software should be public domain and be available in both Windows and Linux versions. The Virtual Reality Modeling Language VRML supports these requirements to a large extent. The language is worldwide ISO/IEC standard in the version of VRML 2.0 and standard browser to view the models can be downloaded from the internet. Inclusion in websites is straightforward and customers could e.g. access models via internet. Confidentiality can be protected by passwords. VRML like any other programming language has a relatively simple set of commands and structures. However, the creation of 'Virtual Reality' models is cumbersome for practical applications. In addition, tailor-made interfaces have to be written for CFD programs used. The effort and expense in writing these should not be underestimated, but this is largely a once-time, initial investment. A simple interface may be written in half a day. Such interfaces are readily converted to other CFD program formats and sharing the burden with other users may lower the threshold of using 'Virtual Reality' in practice.

After an initial phase of getting acquainted with VRML in studying similar applications available on the internet in simple tutorials and the website of the VRL of the University of Michigan (www-URL.umich.edu), we applied 'Virtual Reality' to projects of our own, Barcellona and Bertram (2000):

Our first application concerns a multi-body structure in current and waves. The particular study was for a mobile offshore base (MOB) structure and submarines configuration of the Italian navy. This stationary platform moving in a seaway can be regarded as a representative of typical applications in offshore engineering. The application is relatively complex involving the following 'advanced' features:
complex body shapes (the actual confidential shape is complex, we show simplified generic structures)

- time as 4th dimension
- free surface
- multiple degrees of freedom in the time simulation, to be correctly routed with timer and event-generation mechanism

Moreover, a small tool had to be developed to correctly combine Eulerian rotations in single axis rotation, and then rewritten in the VRML-understandable format, i.e. a vector and an angle (positive in clockwise direction). Such tools are freely available on the web, but they are not intended to deal with huge amounts of data, necessary for a time simulation.

The second application concerned a trimaran in irregular waves. The region between outrigger and main hull is usually hidden from a side view and the ability to fly at will through the model and turn the perspective quickly is useful even for steady flow applications. The 'advanced' features of this model are:

- body of complex shape
- time evolution of pressure on hull
- free surface

People who want to create advanced VRML models will have to learn the language despite contrary claims by vendors of VRML editors. You can indeed create simple Virtual Reality models using these tools without any knowledge of the VRML syntax. However, reality is seldom that simple. Our applications involved aspects that were practically impossible to include by using such editors:

1. CFD simulations in time require also VRML time simulations. Editing and authoring tools as the 'animation wizard' of Spazz3d are so far too limited in their 'wizardry'. They do not allow to prescribe an arbitrary motion for an object by giving a set of non-uniform points in time with related sets of rotations and translations to generate automatically an interpolated animation. Even if this were possible the user must have at least a profound knowledge about the format in which data have to be stored. The routing process, i.e. the mechanism by which the browser connect timers processes, is not trivial, especially if you need to add time-evolving processes to be interactively started and stopped during the 'navigation' across the virtual world.
2. The VRML model exported by a VRML editor like Spazz3d contains many complex, deeply nested, repeated structures. It may be seen as roughly comparable to a Fortran or C code generated by a mathematical manipulation shell like Maple. It works, but it is very difficult to understand and thus to modify or extend. For our CFD visualization problems, we were confronted with megabytes of CFD data at each time instant. The velocity of the parser and the browser during the analysis of these structures strongly affect the reliability and the level of 'reality' of the simulation. Thus, the automatically generated models by a VRML authoring tool need often to be 'optimized' to run fast enough on a PC. Data reduction is also desirable for sending VRML files across the web. Again, the minimum-size format (browsers are also capable to read gzipped worlds) is in conflict with the requirements of cleaniness and readability, to modify and debug the world. A common situation is that one wants to create in principle identical worlds with different data sets. This implies reopening the code by the graphic VRML editor losing time to reload the new sets. A simple C, FORTRAN, or PERL program or script could do the work simpler and much faster, even in a non-graphic environment.
3. A very complex, storage-demanding grid can be imported automatically in the Virtual Reality model only if it has the right format. Many commercial grid generators include in their newest releases VRML import/export facilities for this purpose. However, individual grid generators still popular in the marine CFD community require custom-made programming to interface to VRML.
4. Typically, CFD simulations involve huge amounts of data in the output. Time simulations require a sometimes very small time steps to prevent the numerical scheme from instabilities. The human eye does often not require such a high resolution in time in an animation. Timers in VRML are object that can be activated by signals and retrieves a value (boolean, real and so on) for each call. One of the basic features in VMRL is that at each timer signal (*event*) the routed processes (=connected with the timer) perform an interpolation (PositionInterpolator, OrientationInterpolator, CoordinateInterpolator etc.) between the last and the actual status, thus allowing the user to clean up the data set by purging several unnecessary (for the animation) configurations. This results in a considerable reduction of the data size. This we call 'data optimization in time'. Similarly, the spatial resolution in CFD grids is often much finer than required for the animation. Simple objects like boxes, cylinders and spheres are built-in in the browser and, even if it must perform triangularization and 3D-rendering process to represent them, it does the work in a simpler and faster way, saving considerable time and memory.

There is a clear learning curve as with any software. The first application of the multi-body system took approximately 10 days to develop, the second application of the trimaran only approximately 5

days, mostly spent in building suitable FORTRAN and PERL tools to convert and recast data in VRML-accessible format. An experienced user may be able to create such models in a fraction of the time we needed. Generally, the time needed depends upon the desired degree of 'reality'. Based on our experience, we can recommend to newcomers to 'Virtual Reality' for CFD:

- get the complete VRML ISO/IEC specification
- get some VRML tutorials to have an overview of the topic, of the results you can obtain, and the effort it takes.
- get a complete VRML 2.0 handbook for reference
- learn by modifying examples; many commands and structures are unnecessary for your application
- establish a network to colleagues working on similar applications and share experience and macros
- count on several days before you have a model that satisfies you in the initial stage
- a background in object-oriented languages like C++ helps
- get a dedicated PC and use Windows
- add complexity gradually in creating large 'Virtual Reality' models
- make the model only as complex as it needs to be; 'cosmetics' can be expensive

'Virtual Reality' models are in many ways like traditional CAD models. Initial model creation is cumbersome, but model modification is relatively fast. Thus 'Virtual Reality' model designers will typically start collecting a 'database' of models and, after a while, especially if there are essentially always the same applications, be quite fast in creating such adjusted models. Sharing models with colleagues should accelerate the process of setting up a set of 'parent' applications which only need to be modified to particular projects.

BARCELLONA, M.; BERTRAM, V. (2000), *Virtual Reality for CFD Post-Processing,* COMPIT, Potsdam

VRML models: www.schiffbau.uni-hamburg.de/IFS/AB/AB-3-14/VR/

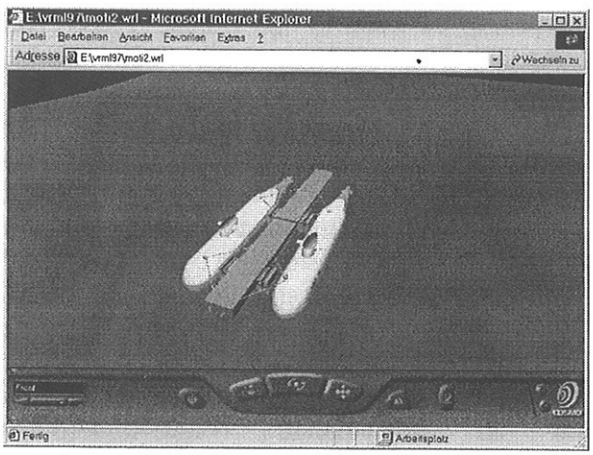

VRML model of Mobile Offshore Base

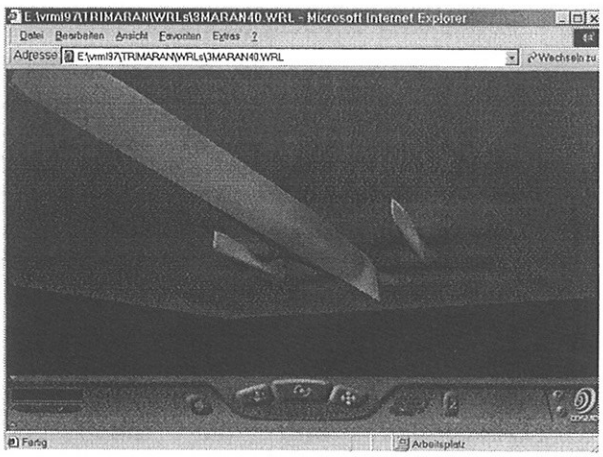

VRML model of trimaran

STEADY AND UNSTEADY COMPUTATIONS OF SHIP FLOWS IN A STRAIGHT CHANNEL

Marco Barcellona[*], *Giorgio Graziani*[‡], *Maurizio Landrini*[*]

[*] *INSEAN, The Italian Ship Model Basin*

[‡] *Dipartimento di Meccanica e Aeronautica, Università di Roma "La Sapienza"*

The growing interest for fast transportation in natural and artificial inland channels calls for the analysis of the related problems, like possible damages to shores and moored floating structures, drop of the efficiency of vessels and safety aspects (Bertram et. al. 1999, Yasukawa 1999). In this paper we present our first attempts to predict numerically forces and wave pattern associated with the motion of a vessel in a channel. A well established potential flow model is considered and the problem is solved numerically by a boundary integral method. For straight channels, a suitable Green function is used and only the free surface and the hull boundary have been discretized. Preliminary results for steady, symmetric flows are reported. An extended set of results will be discussed at the workshop.

1 MATHEMATICAL MODEL

In the following, the flow around a hull advancing with speed $\mathbf{V(t)}$ is studied by a potential flow model. A frame of reference moving with the ship is considered, with x-axis aligned with the ship motion and the vertical axis opposite to the gravity direction. The y-coordinate spans across the channel. The considered fluid domain includes a portion of the channel $\partial\Omega_{\text{bottom}} \cup \partial\Omega_{\text{lat wal}}$, the hull surface $\partial\Omega_{\mathcal{B}}$ and the free surface $\partial\Omega_{\mathcal{F}}$. The total velocity of the fluid is written as

$$\mathbf{U}(\mathbf{P},t) = -\mathbf{V}(t) + \mathbf{u}'(\mathbf{P},t) = -\mathbf{V} + \nabla\varphi(\mathbf{P},t)$$

where the perturbation velocity $\mathbf{u}'$ is described in terms of the velocity potential φ. The latter satisfies the Laplace equation $\nabla^2\varphi = 0$, the no penetration boundary condition

$$(\mathbf{V} + \nabla\varphi)\cdot\mathbf{n}_{\mathcal{B}} = 0 \quad \text{on} \quad \Omega_{\mathcal{B}}$$

on the surface of the moving vessel, and the kinematic

$$\frac{\partial\eta(x,y,t)}{\partial t} + (-\mathbf{V} + \nabla\varphi)\cdot\nabla\eta = \frac{\partial\varphi}{\partial \mathbf{z}} \qquad (1)$$

and dynamic

$$\frac{D\varphi}{Dt} - \frac{1}{2}|\nabla\varphi|^2 + g\eta = const$$

boundary conditions on the free surface.

In principle, the above formulation is generally valid for the unsteady, nonlinear, nonbreaking case. In this preliminary study, the problem is linearized with respect to the unperturbed free surface configuration ($z = 0, \forall x, y$) and the hull in even keel conditions.

For numerical purposes, the potential is represented by a distribution of sources and dipoles, the latter being introduced to enforce a Kutta condition along the stern line in case of non-symmetric flows. In short, the velocity potential in the point $\mathbf{P}$ can be written as

$$\varphi(\mathbf{P}) = \mathcal{I}_{\mathcal{F}} + \mathcal{I}_{\mathcal{B}} + \mathcal{I}_{\text{bottom}} + \mathcal{I}_{\text{lat wal}}$$

where

$$\mathcal{I}_{\mathcal{F}} = \iint_{\mathcal{F}} \sigma_{\mathcal{F}} G(x,\mathbf{P}) dS \qquad (2)$$

is the influence of the free surface and

$$\mathcal{I}_{\mathcal{B}} = \iint_{\mathcal{B}} \sigma_{\mathcal{B}} G(x,\mathbf{P}) dS + \iint_{\mathcal{B}_I} \mu_{\mathcal{B}_I} \frac{\partial G}{\partial n}(x,\mathbf{P}) dS \qquad (3)$$

is the influence of the body. The dipoles are distributed over a fictitious surface $\mathcal{B}_I$ inside the hull and along a trailing wake of zero thickness.

The influence of the channel (bottom and lateral walls) is computed by mirror images. It is worth noticing that for the lateral walls, an infinite series of images should be used. To reduce the computational effort, a fast summation algorithm due to Breit (1991) is here adopted. This imply the use of a modified Green function in integrals (2)-(3).

The relevant integral equations are obtained by collocating on the hull and on the free surface and are discretized by a collection of flat panels. Influence coefficients are evaluated by a combination of analytical formulas (Hess & Smith, 1965) for the singular part of the Green function, and of numerical quadratures (Lyness & Jespersen ,1975), for the non singular contribution. An alternative desingularized algorithm on the free surface (Bertram, 1990, Cao et al., 1991) has also been

tested, with a significant reduction of the cpu-time requirements.

The time stepping procedure, based on a fourth-order Runge-Kutta scheme, can be summarised as follows:

1. for a given time t_0, a b.v.p. of the form

$$\begin{cases} \nabla^2\varphi = 0 \\ \varphi|_{\mathcal{F}} = \varphi_{\mathcal{F}} \\ (\mathbf{V} + \nabla\varphi|_{\mathcal{B}}) \cdot \mathbf{n}_{\mathcal{B}} = 0 \\ (\mathbf{V} + \nabla\varphi|_{\mathcal{B}_I}) \cdot \mathbf{n}_{\mathcal{B}_I} = 0 \\ \text{Kutta condition} \end{cases}$$

   is solved by the panel method above.

2. a new set of boundary data is determined by stepping forward in time the evolution equations

$$\dot{\varphi}|_{\mathcal{F}} = -g\eta - V_x \left.\frac{\partial\varphi}{\partial x}\right|_{\mathcal{F}} \qquad (4)$$

$$\dot{\eta} = \frac{\partial\varphi}{\partial z} - \frac{V_x}{g}\dot{\varphi}_x - \frac{V_x^2}{g}\frac{\partial^2\varphi}{\partial x^2}$$

Alternatively, the kinematic equation (1) can be rewritten as

$$\dot{\eta} = \frac{\partial\varphi}{\partial z} - \frac{V_x}{g}\dot{\varphi}_x - \frac{V_x^2}{g}\frac{\partial^2\varphi}{\partial x^2}$$

which avoids the need to compute $\partial\eta/\partial x$ but implies the solution of an extra integral equation for $\dot{\varphi}$. This second approach does not increase the computational effort and allows to handle easily unstructured free surface grids. On the other hand, this scheme suffers more stringent stability requirements than the previous one and a systematic use of free surface filtering and smaller time steps are needed. Results and performances from both algorithms will be discussed.

In any case, a numerical beach (Israeli and Orszag, 1981) is used to prevent unphysical reflection from the truncated boundaries.

2 Preliminary results

To gain some confidence with the problem in confined water, we first considered the motion of a Wigley hull under the assumption of steady state conditions and symmetric flow.

In this case, the radiation condition is enforced shifting upstream the collocation points. The influence of the rear extent of computational domain seems to be quite negligible, as shown in figure 1, where two different discretizations of the computational domain are considered. The length is taken $7.0L_{pp}$ in the first case and $3.5L_{pp}$ in the second, L_{pp} being the hull length between the perpendiculars. The channel is $1.5L_{pp}$ broad, the speed is $F_n = 0.22$.

For the same channel width, figure 2 shows the effect of the Froude number F_n. Here, the maximum number of elements on the free surface (for the lowest F_n) is 150×32, that gives approximately 8 panels per wavelength at $F_n = 0.2$. In the upper plot a comparison between the wave cuts in proximity of the channel boundary is shown.

Finally, a preliminary example of unsteady computations is given by considering a source/sink pair, aligned with $x-$axis, moving below the free surface. The choice for the relevant parameters is made with the aim to mimic the disturbance due to a slender hull. Upon assuming $L_{pp} = 1$ and the draught $d = 0.0625L_{pp}$, the distance between source and sink is $0.877L_{pp}$, and they are placed symmetrically around $(0.0, 0.0, -d/2)$.

To reduce transient effects, the strength σ_0 starts from zero and reaches the steady state value $V_x A_w$, A_w being the cross sectional area near midship. In particular, the law $\sigma(t) = \sigma_0(1 - e^{-4t})$ is used. The same law is assumed for the dimensionless speed $F_n(t)$ of the pair.

Plots in figure 3 show the time evolution of the free surface. The domain considered here is $6.0L_{pp}$ broad. The upstream extent of the computational domain depends on the need to minimize possible reflections of long starting waves. The downstream extent is related both the length of the adsorbing beach and to far field nedeed, for example for wave wash prediction. In particular, for the selected F_n, 90×20 panels are distributed over a computational free surface with length of $15L_{pp}$.

3 Further developments

At the workshop some results concerning the unsteady, linearized and non-symmetric case of a hull moving in a straight channel will be presented.
The numerical algorithm has been already developed and validated using some simple test cases (i.e. moving singularities). Results from the linearized code have been compared with those from a nonlinear algorithm, giving a reasonable agreement.

Our final goal is to build an efficient tool to handle unsteady interactions between moving bodies in restricted water.

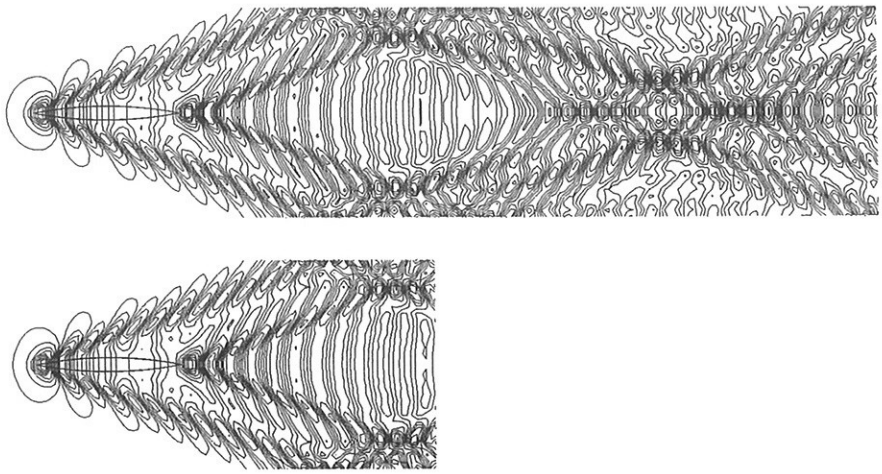

Figure 1: Wigley hull (steady case): comparison between wave contours for two lengths of the computational domain. Upper plot: domain length=$7.0L_{pp}$. Lower plot: domain length=$3.5L_{pp}$. ($F_n = 0.22$, channel depth=$2.0L_{pp}$; channel width $1.5L_{pp}$; 225×32 panels on the free surface).

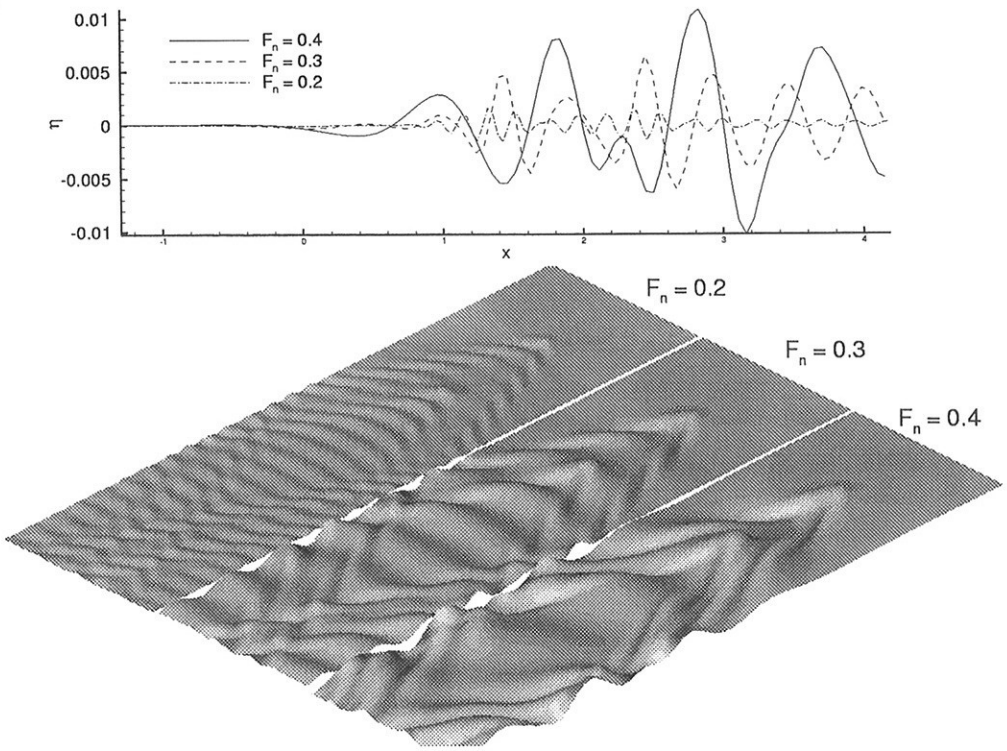

Figure 2: Wigley hull (steady case): comparison between different Froude numbers. Upper plot: wave cuts at the wall. Lower plots: perspective views of the free surface (channel depth=$2.0L_{pp}$; channel width $1.5L_{pp}$; 150×32 panels on the free surface).

BIBLIOGRAPHY

BERTRAM, V., BULGARELLI U. (1999) *Numerical wash prediction*, First Int. Conf. on High-Performance Marine Vehicles (HIPER '99), Zevenwacht, South Africa.

BERTRAM, V. (1990) *A Rankine source method for forward-speed diffraction problem*, Report No. 508, IFS, university of Hamburg, June.

BREIT, S.R., (1991) *The potential of a Rankine Source between parallel planes and in a rectangular cylinder*, Journal of Eng. Math., 25, 151-163.

CAO, Y., SCHULTZ, W. W., BECK, R. (1991), *Three-dimensional desingularized boundary integral methods for potential problems*, Int. J. Num. Meth. Fluids, Vol. 12, 785-803.

ISRAELI, M., ORSZAG, S. A. (1981), *Approximation of radiation boundary conditions*, J. Comp. Phys., Vol. 41, pp. 115-135.

LONGUET-HIGGING, M. S., COKELET, E. D. (1976), *The deformation of steep surface waves on water. I. A numerical method of computation*, Proc. Roy. Soc. Lond., Vol. 350, pp. 1-26.

LYNESS, J.N., JESPERSEN, D. (1975), *Moderate Degree Symmetric Quadrature Rules for the Triangle*, Inst. Math. Appl. 15, 19-32.

SMITH J., HESS A.M.O. (1965), *Calculation of non–lifting potential flow about arbitrary bodies*, Prog. Aero. Sci. 8,1–138.

YASUKAWA, H. (1999) *Unsteady wash computation for a high speed vessel*, 2^{nd} Num. Towing Tank Symp. (NuTTS 1999), Rome.

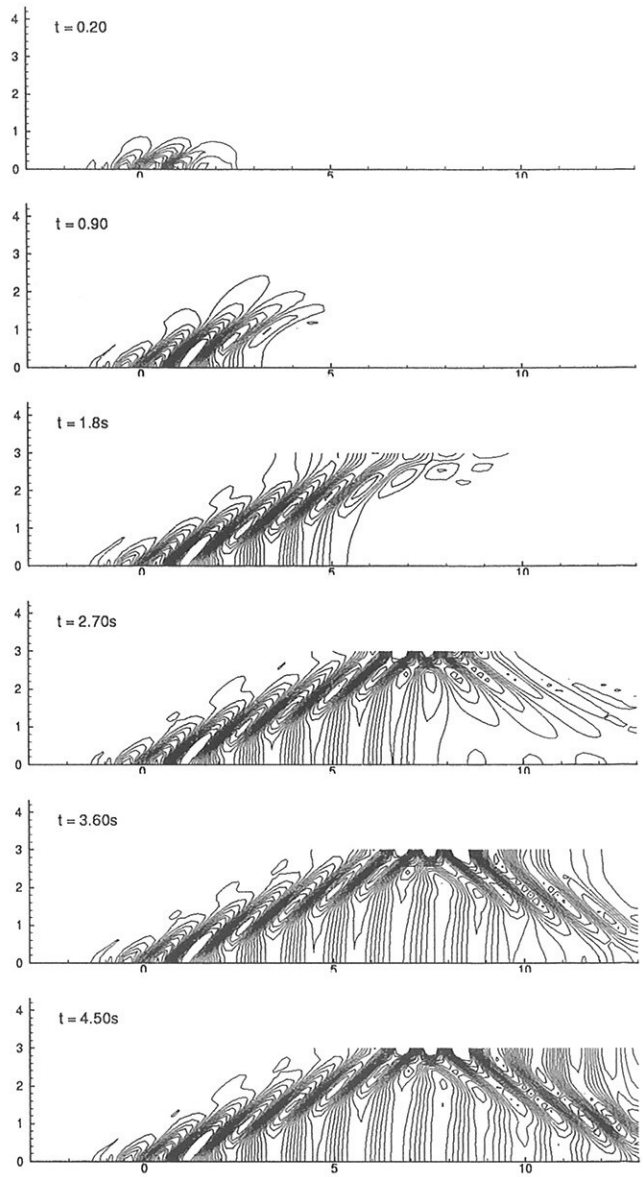

Figure 3: Evolution of the wave pattern generated by a source/sink pair accelerating from rest up to the final speed $F_n = 0.6$.

CFD in Ship Design - Some Recent Advances

Volker Bertram, HSVA, bertram@hsva.de

The applications given here will be explained in more detail in Bertram et al. (2000). Here I selected subjectively some applications from previous experience that seemed to highlight particularly well how we use now CFD to support ship design - or how we may use it in the very near future. The applications are taken from HSVA's practice, but I believe they reflect in many cases the general state of the art of other first-class CFD providers in the marine industry.

For steady free-surface flows ('wave resistance problem'), inviscid BEM codes are still the workhorse in industry, being quite capable to analyze also complex geometries. Although the pressure distribution over a large part of the ship with the exception of the aftbody is believed to be quite accurate and wave cuts computed by state-of-the-art codes agree usually well with experiments, the computed wave resistance for real ships may still differ considerably from measured residual resistance or even estimated wave resistance using form factor methods. Ships with large transom sterns are particularly problematic. Third-generation codes should overcome these short-comings by providing better resistance prognoses. These codes employ new techniques to increase the accuracy. Examples pointing that way are the KELVIN code, Söding (1999), and the ν-SHALLO code of HSVA. Here the boundary condition on the hull is integrated over each element and better force integration approximations are used. As a result, the error in predicting the resistance is typically reduced by one order of magnitude. Improvements in transom stern treatment allow to capture also typical rooster tails behind fast ships, Fig.1.

Most seakeeping properties of practical relevance are calculated accurately enough for most cargo vessels by strip methods, although the underlying physical models are generally considered as crude. Nevertheless, research is active on more advanced computational methods for ship seakeeping. A natural extension of the experience gained in wave-resistance codes are 3-d Rankine singularity methods (RSM) seakeeping codes, as reviewed by Bertram and Landrini (1999). Research on RSM seakeeping methods is active, but recent experiments by Iwashita (1999) suggest that only viscous flow codes may have a chance to represent pressures in the bow region of blunt ships properly. In practice then strip methods for most problems and field methods for few selected highly nonlinear problems may ultimately be used. One recent extension of classical strip method approaches are non-linear strip methods accounting alšo for partially damaged ships. We validated successfully such a simulation tool calculating roll and surge motions nonlinearly, and all other degrees of freedom linearly in the time domain, Chang and Blume (1998).

A typical application of RANSE codes is the prediction of the velocity inflow field in the propeller plane. Usually be believe experiments and try to explain discrepancies with shortcomings in the CFD model, e.g. insufficient grid resolution, employed differencing schemes and turbulence models. Fig.2 shows one case, where for a dredger the induced in-plane velocities exceeded in the 'south-west' region by far the margin of calibration specified by the supplier of the experimental instruments. Thus the experiments may be considered as less reliable than CFD. Other typical applications of RANSE concern appendages (like rudders and brackets) and 'negative' appendages as waterjet inlets, sea chests, Fig.3, side thruster tunnels etc.

RANSE computations including the propeller action ('propulsion problem') use generally equivalent body force in the r.h.s. of the RANSE. The body forces are often prescribed based on experience or experimental results. More recently, hybrid computations coupling RANSE for the effective wake and boundary element methods (or vortex-lattice methods) for the propeller loading have been developed. The distributions obtained by this approach depend on the propeller inflow and are determined iteratively using the RANSE data as input for the propeller computation and vice versa. This procedure allows a complete simulation of a propulsion test, i.e. no results from the tank test are

required. Integral values like thrust deduction fraction $t = (T-R_T)/T$, mean wake fraction w, propulsive efficiency η_D, hull efficiency η_H, and relative rotational efficiency η_R agree well with measurements.

The simultaneous consideration of viscosity and wave-making has progressed considerably over the past decade. A number of methods try to capture wave making with various degrees of success. Most real ship flow problems require interface-capturing methods. Most schemes reproduce the wave profile on the hull accurately, but problems persist with numerical damping of the ship wave propagation, Fig.4. It is debatable if an accurate prediction of the wave pattern is necessary for practical applications, but certainly everyone would prefer to see this problem overcome.

Predicting the flow around the hull and appendages (including propellers and rudders) in maneuvering is much more complicated than predicting the steady flow in resistance and propulsion problems. Often, both viscosity and free-surface effects play an important role. The rudder is most likely in the hull boundary layer, often operating at high angles of attack and in the propeller wake. The hull forces themselves are also difficult to predict computationally, because sway and yaw motions induce considerable cross flows with shedding of strong vortices. Most computations are also limited to small yaw angles, with recent computations at HSVA for a ship at yaw angles up to 50° being a notable exception, Fig.5 and 6. The progress is promising, even though the time needed for such analyses is still excessive for most practical applications.

Post-processing progresses as the core hydrodynamic analyses progress. State of the art are still static views. Series of snapshots are used for unsteady problems or complex geometries. Rarely and only for simple geometries, we see animations for research applications. A natural extension to current post-processing may be Virtual Reality models, Barcellona and Bertram (2000). These allow a user to fly through the model in space and time, with storage requirements one or two orders lower than for electronic videos.

Acknowledgement

Many colleagues have supported this paper by supplying material from their respective experience. Foremost these are in alphabetical order Peter Blume, Andres Cura, Dieke Hafermann, Jochen Laudan, Jochen Marzi, and Mathias Vogt.

References

BARCELLONA, M.; BERTRAM, V. (2000), *Post-processing of time-dependent CFD analyses using Virtual Reality Modelling Language,* NuTTS'2000, Tjarno

BERTRAM, V.; CURA, A.; LAUDAN, J.; MARZI, J.; STRECKWALL; H. (2000), *CFD simulations in ship design,* SIMOUEST, Nantes

BERTRAM, V.; LANDRINI, M. (1999), *Panel methods for ship seakeeping computations*, 31. WEGEMT School 'CFD for Ship and Offshore Design', Hamburg

CHANG, B.C.; BLUME, P (1998), *Survivability of damaged ro-ro passenger vessels,* Ship Technology Research 45/3, pp.105-117

IWASHITA, H. (1999), *Prediction of diffraction waves of a blunt ship with forward speed taking account of the steady nonlinear wave field,* NuTTS'99, Rome

SÖDING, H. (1999*), Strömungsberechnungen in der Schiffstechnik*, Jahrbuch Schiffbautechnische Gesellscahft, Springer

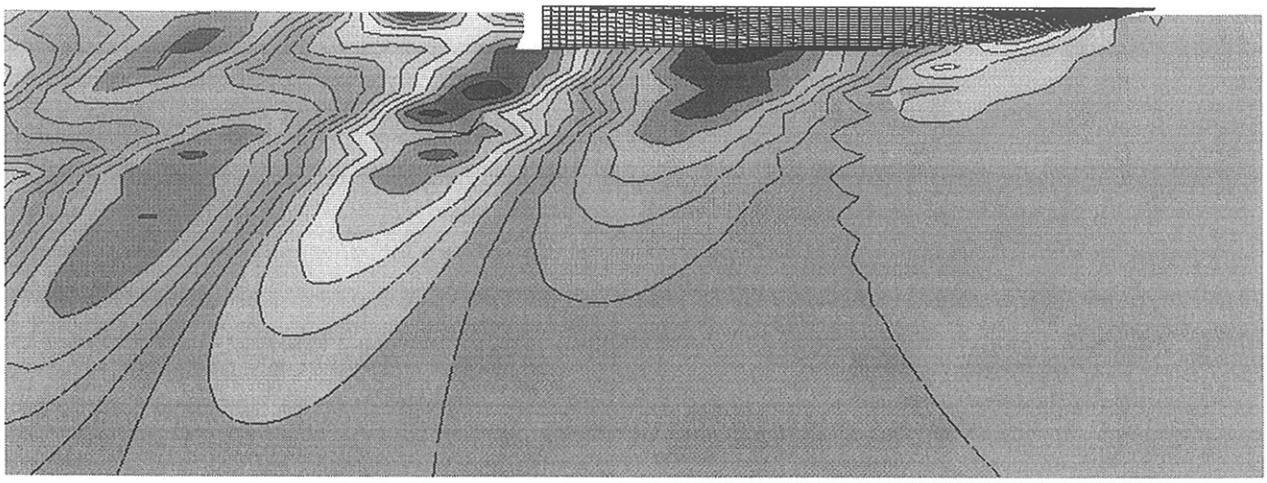

Fig.1: Rooster tail behind fast ship with large transom, panel code ν-SHALLO

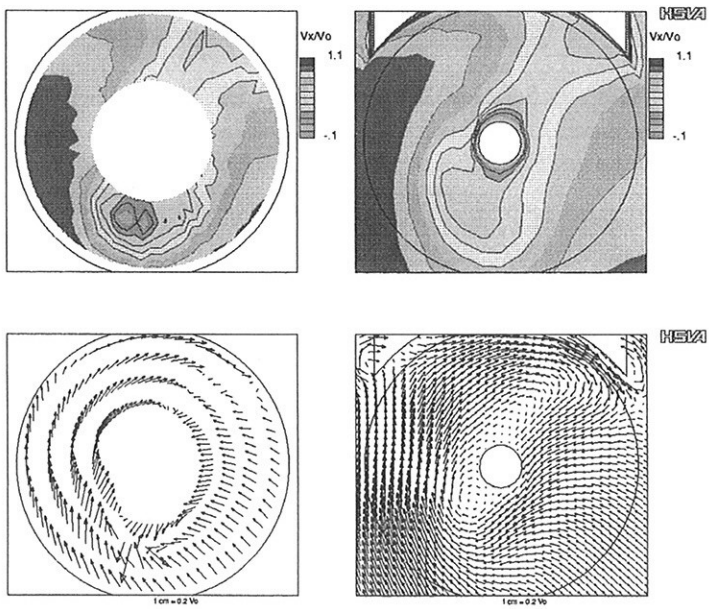

Fig.2: Wake distribution for podded aftbody; left experiment, right CFD (RANSE)

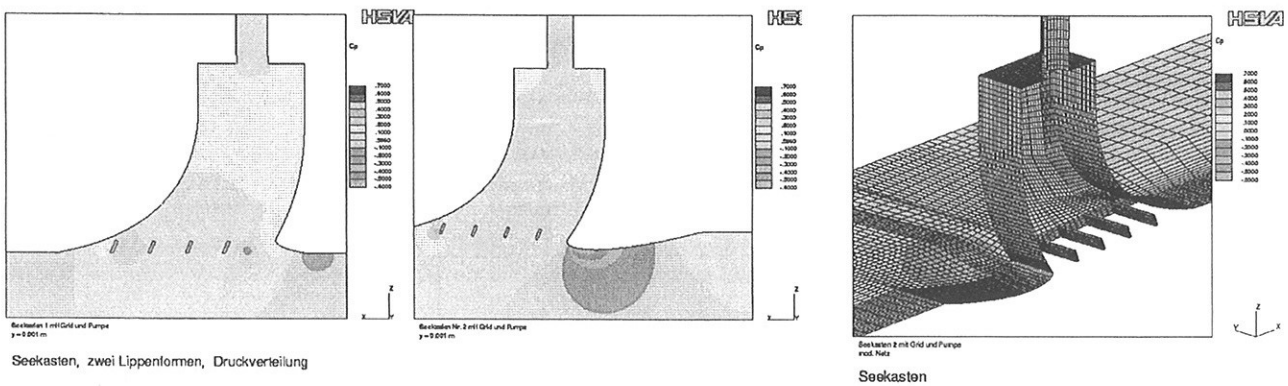

Fig.3: Sea chest; version on right expected to have severe cavitation problems

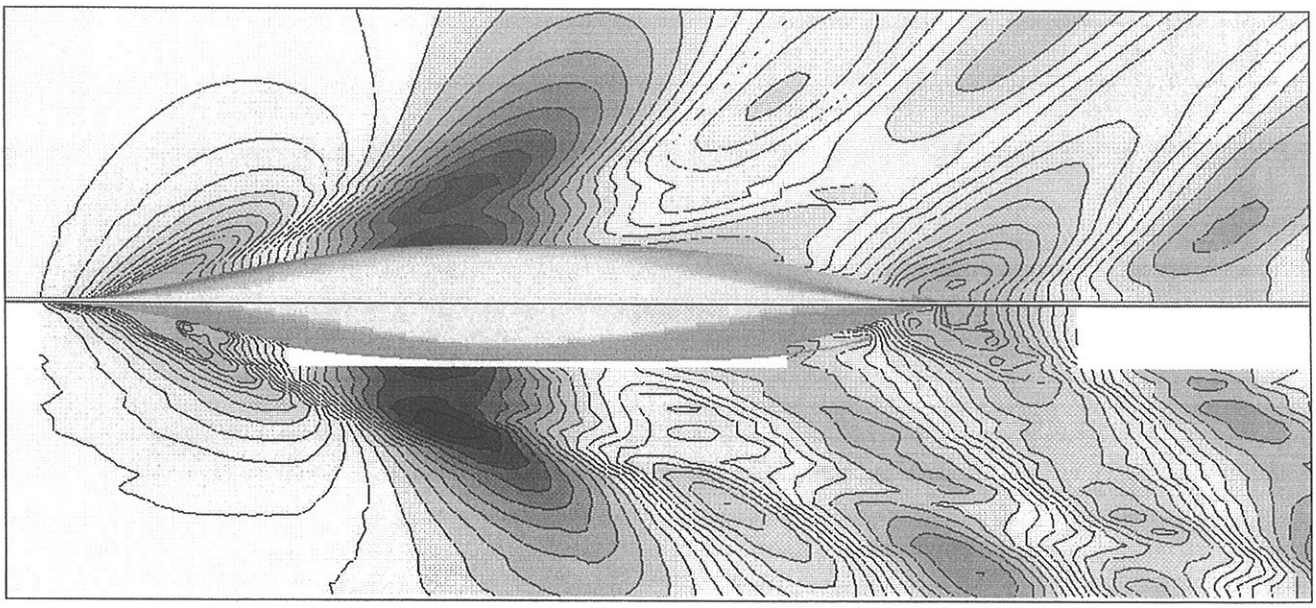

Fig.4: Wave pattern for Series-60, Neptun code (RANSE), top CFD, bottom experiment

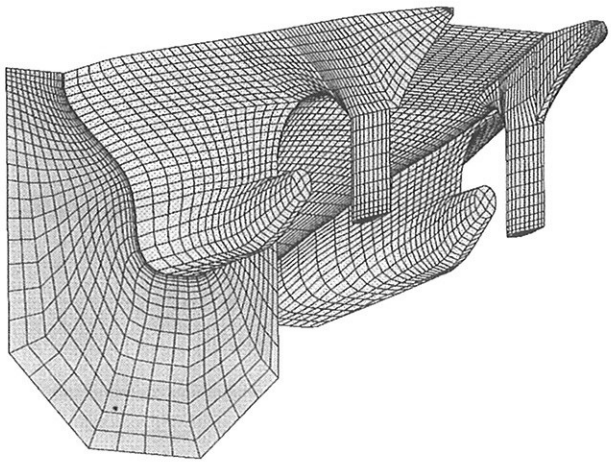

Fig.5: Grid around aftbody of tanker for maneuvering computations with RANSE code

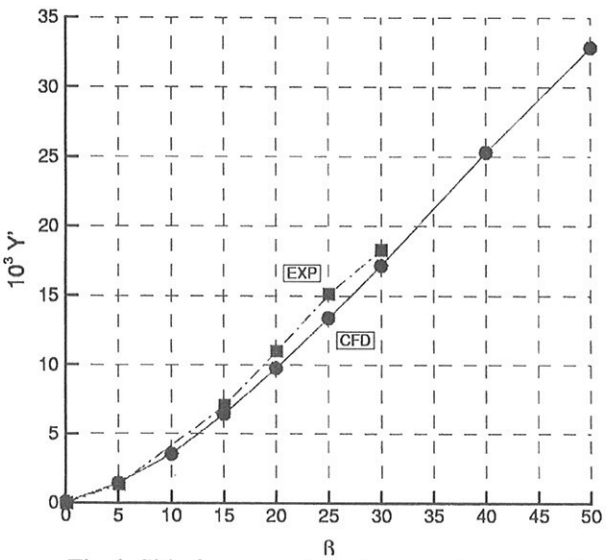

Fig.6: Side force coefficients for tanker in Fig.5

Added Resistance in Fully 3-d Ship Seakeeping - Revised

Volker Bertram, HSVA, bertram@hsva.de
Hironori Yasukawa, MHI, yasukawa@ngsrdc.mhi.co.jp
Maxime Berthome, Ecole Centrale Nantes, maxime@berthome.net
Thomas Tvergaard, Danish Technical Univ., i929617@student.ish.dtu.dk

Bertram (1998) described a fully three-dimensional ship seakeeping method that considers the steady flow contribution completely (within the framework of potential flow) and linearizes the unsteady flow contribution with respect to wave height around the steady flow (including steady wave system, steady trim and sinkage of ship). Bertram and Yasukawa (1999) described the problems with extending the theory to include also added resistance as representative for second order forces. The problem was that while the motions were predicted well, the added resistance was increasingly wrong for higher Froude numbers. The error was obviously in the added resistance formula. Discussion following the last NuTTS meeting helped in tracing the error in the mathematical formulation which was essentially the omission of one term and a sign error in another term. The errors were corrected and tested. The theory for the determination of the linear RAOs for motions in only summarized here to the extent necessary for understanding the added resistance formula. The extensive updated theory is presented in Bertram and Yasukawa (2000).

We consider a ship moving with mean speed U in a harmonic wave of small amplitude h. For numerical practicality, we limit our considerations here to $\tau = U\omega_e/g > 0.4$, but the formula for added resistance is universally applicable regardless of the τ-value. As usual, ω_e is the encounter frequency and $g = 9.81\text{m/s}^2$. All coordinate systems here are right-handed Cartesian systems. The inertial $Oxyz$ system moves uniformly with velocity U. x points in the direction of the body's mean velocity U, z points vertically downward. The $\underline{Oxyz}$ system is fixed at the body and follows its motions. When the body is at rest position, $\underline{x}$, $\underline{y}$, $\underline{z}$ coincide with x, y, z. The angle of encounter μ between body and incident wave is defined such that $\mu = 180°$ denotes head sea and $\mu = 90°$ beam sea. $u_i (i = 1...6)$ denotes the body motions. $\alpha_i = u_{i+3} (i = 1...3)$ denotes just the rotational motions.

We use a standard perturbation approach linearizing with respect to wave amplitude h of the incident wave. We formulate the problem within the frequency domain:

$$\phi^{total}(x,y,z;t) = \phi^{(0)}(x,y,z) + \phi^{(1)}(x,y,z;t) = \phi^{(0)} + Re(\hat{\phi}^{(1)}(x,y,z)e^{i\omega_e t}) \quad (1)$$

$$\zeta^{total}(x,y;t) = \zeta^{(0)}(x,y) + \zeta^{(1)}(x,y;t) = \zeta^{(0)} + Re(\hat{\zeta}^{(1)}(x,y)e^{i\omega_e t}) \quad (2)$$

The index (0) denotes solutions of the steady 'fully nonlinear' wave resistance problem. (1) is the time-harmonic unknown part. ϕ is the potential, ζ the coordinate of the free surface (negative wave elevation).

We decompose the unknown potential into the symmetric and anti-symmetric part of the incident wave potential ϕ^w, radiation potentials ($i = 1...6$) and symmetric and anti-symmetric part of the diffraction potential ϕ^7 and ϕ^8:

$$\phi^{(1)} = \phi^{w,s} + \phi^{w,a} + \sum_{i=1}^{6} \phi^i u_i + \phi^7 + \phi^8 \quad (3)$$

The following abbreviations are useful: $\vec{a}^{(0)} = (\nabla\phi^{(0)}\nabla)\nabla\phi^{(0)}$, $\vec{a}^g = \vec{a}^{(0)} - \{0,0,g\}^T$, $B = -\frac{1}{a_3^g}\frac{\partial}{\partial z}(\nabla\phi^{(0)}\vec{a}^g)$, $\vec{m} = (\underline{\vec{n}}\nabla)\nabla\phi^{(0)}$. $\underline{\vec{n}}$ is the inward normal vector.

The 2 unknown diffraction potentials and the 6 unknown radiation potentials are determined by approximating the unknown potentials by a superposition of a finite number of Rankine higher-order panels on the ship and above the free surface solving for the element strength as unknown. For the antisymmetric cases, in addition Thiart elements (semi-infinite dipole strips on the plane

$y = 0$), e.g. Bertram (1998), are arranged and a Kutta condition is imposed on collocation points at the last column of collocation points on the stern. Elements use mirror images at $y = 0$. For the symmetrical cases, all mirror images have same strength. For the anti-symmetrical case, the mirror images on the negative y-sector have negative element strength of same absolute magnitude. The problem is formulated in a collocation scheme. The same grid on the hull is used as for the steady problem, but in the steady wave resistance problem the panels are interpreted as higher-order panels, while for the seakeeping problem they are interpreted as first-order panels. The grid on the free surface is created new. The quantities on the new grid are linearly interpolated within the new grid from the values on the old grid. Outside the old grid in the far field, all quantities are set to uniform flow on the new grid. The interpolation of results introduces only small differences as observed in various test cases. Radiation and open-boundary conditions are fulfilled by the 'shifting' technique' which works well for the considered larger τ-values. The l.h.s. of the four systems of equations for the symmetrical cases and the l.h.s. for the four systems of equations for the anti-symmetrical cases share the same coefficients each. Thus four systems of equations can be solved simultaneously using Gauss elimination. After the potentials $\hat{\phi}^i (i = 1...8)$ have been thus determined, only the 6 motions u_i remain as unknowns. These are determined in principle from the 'ansatz' $F = m \cdot a$ (as vector equations in 6 degrees of freedom). This yields a linear system of equations in $\hat{u}_i$ which is quickly solved using Gauss elimination.

Following a similar approach as for the first-order forces, a formula for the added resistance can be derived that uses only first-order quantities. The added resistance is the negative time-averaged value of the x-component of the second-order force. If t_1 and t_2 are time-harmonic quantities, the time-average of $t_1 t_2$ is $\frac{1}{2} Re(\hat{t}_1 \hat{t}_2^*)$, where $\hat{t}_2^*$ is the conjugate complex of $\hat{t}_2$.

This yields eventually:

$$
\begin{aligned}
R_{aw} &= \frac{1}{2} Re \frac{\underline{n}_1}{\sqrt{1-\underline{n}_3^2}} \cdot \left\{ \int_C \left(\frac{1}{2} (\hat{Z}^s \hat{Z}^{s,*} + \hat{Z}^a \hat{Z}^{a,*}) [p_{z'}^{(0)}(0) + (n_1' p_x^{(0)} + n_2' p_y^{(0)}) n_3'] \right. \right. \\
&\quad \left. \left. + (\hat{p}^{(1),s} + p_x^{(0)} \hat{h}_1^s + p_y^{(0)} \hat{h}_2^a + p_z^{(0)} \hat{h}_3^s) \hat{Z}^{s,*} + (\hat{p}^{(1),a} + p_x^{(0)} \hat{h}_1^a + p_y^{(0)} \hat{h}_2^s + p_z^{(0)} \hat{h}_3^a) \hat{Z}^{a,*} \right) \, dc \right\} \\
&- \frac{1}{2} Re \left\{ \int_{\underline{S}^{(0)}} -[\frac{\rho}{2} (\nabla \hat{\phi}^{(1),s} \nabla \hat{\phi}^{(1),s*} + \nabla \hat{\phi}^{(1),a} \nabla \hat{\phi}^{(1),a*}) + (\nabla \hat{p}^{(1)})^s \hat{\vec{h}}^{s*} + (\nabla \hat{p}^{(1)})^a \hat{\vec{h}}^{a*}] \underline{n}_1 \, d\underline{S} \right\} \\
&- \frac{1}{2} Re \{ mg \hat{\alpha_1} \hat{\alpha}_3^* - m\omega_e^2 (\hat{\alpha}_2^* (\hat{u}_3 - \hat{\alpha}_2 \underline{x}_g) - \hat{\alpha}_3^* (\hat{u}_2 + \hat{\alpha}_3 \underline{x}_g - \hat{\alpha}_1 \underline{z}_g)) \}
\end{aligned}
$$

Due to symmetry, the above integrals are twice the value of the integrals over the starboard half only. The new terms mean m ship's mass, $\underline{x}_g$ ship's center of gravity, $\nabla p^{(0)} = -\rho \vec{a}^g$, and:

$$
\hat{\phi}^{(1),s} = \hat{\phi}^1 \hat{u}_1 + \hat{\phi}^3 \hat{u}_3 + \hat{\phi}^5 \hat{u}_5 + \hat{\phi}^7 + \hat{\phi}^{w,s} \tag{4}
$$

$$
\hat{\phi}^{(1),a} = \hat{\phi}^2 \hat{u}_2 + \hat{\phi}^4 \hat{u}_4 + \hat{\phi}^6 \hat{u}_6 + \hat{\phi}^8 + \hat{\phi}^{w,a} \tag{5}
$$

$$
\hat{p}^{(1),s} = -\rho (i\omega_e \hat{\phi}^{(1),s} + \nabla \phi^{(0)} \nabla \phi^{(1),s}) \tag{6}
$$

$$
\hat{p}^{(1),a} = -\rho (i\omega_e \hat{\phi}^{(1),a} + \nabla \phi^{(0)} \nabla \phi^{(1),a}) \tag{7}
$$

$$
(\nabla \hat{p}^{(1)})^s = -\rho \begin{Bmatrix} i\omega_e \hat{\phi}_x^{(1),s} + \phi_{xx}^{(0)} \hat{\phi}_x^{(1),s} + \phi_{xy}^{(0)} \hat{\phi}_y^{(1),s} + \phi_{xz}^{(0)} \hat{\phi}_z^{(1),s} \\ i\omega_e \hat{\phi}_y^{(1),a} + \phi_{xy}^{(0)} \hat{\phi}_x^{(1),a} + \phi_{yy}^{(0)} \hat{\phi}_y^{(1),a} + \phi_{yz}^{(0)} \hat{\phi}_z^{(1),a} \\ i\omega_e \hat{\phi}_z^{(1),s} + \phi_{xz}^{(0)} \hat{\phi}_x^{(1),s} + \phi_{yz}^{(0)} \hat{\phi}_y^{(1),s} + \phi_{zz}^{(0)} \hat{\phi}_z^{(1),s} \end{Bmatrix} \tag{8}
$$

$$
(\nabla \hat{p}^{(1)})^a = -\rho \begin{Bmatrix} i\omega_e \hat{\phi}_x^{(1),a} + \phi_{xx}^{(0)} \hat{\phi}_x^{(1),a} + \phi_{xy}^{(0)} \hat{\phi}_y^{(1),a} + \phi_{xz}^{(0)} \hat{\phi}_z^{(1),a} \\ i\omega_e \hat{\phi}_y^{(1),s} + \phi_{xy}^{(0)} \hat{\phi}_x^{(1),s} + \phi_{yy}^{(0)} \hat{\phi}_y^{(1),s} + \phi_{yz}^{(0)} \hat{\phi}_z^{(1),s} \\ i\omega_e \hat{\phi}_z^{(1),a} + \phi_{xz}^{(0)} \hat{\phi}_x^{(1),a} + \phi_{yz}^{(0)} \hat{\phi}_y^{(1),a} + \phi_{zz}^{(0)} \hat{\phi}_z^{(1),a} \end{Bmatrix} \tag{9}
$$

$$\hat{\vec{h}} = \hat{\vec{\alpha}} \times \underline{\vec{x}} + \hat{\vec{u}} = \hat{\vec{h}}^s + \hat{\vec{h}}^a = \left\{ \begin{array}{c} \hat{u}_5 \underline{z} + \hat{u}_1 \\ \hat{u}_6 \underline{x} - \hat{u}_4 \underline{z} + \hat{u}_2 \\ -\hat{u}_5 \underline{x} + \hat{u}_3 \end{array} \right\} + \left\{ \begin{array}{c} -\hat{u}_6 \underline{y} \\ 0 \\ \hat{u}_4 \underline{y} \end{array} \right\} \tag{10}$$

$$\begin{aligned} \hat{Z}^s &= -\frac{i\omega_e \hat{\phi}^{(1),s} + \nabla\phi^{(0)} \nabla\hat{\phi}^{(1),s}}{a_3^g} - \hat{u}_3 + \hat{u}_5 \underline{x} = \frac{\hat{p}^{(1),s}}{\rho a_3^g} - \hat{h}_3^s \\ \hat{Z}^a &= -\frac{i\omega_e \hat{\phi}^{(1),a} + \nabla\phi^{(0)} \nabla\hat{\phi}^{(1),a}}{a_3^g} + \hat{u}_4 \underline{y} = \frac{\hat{p}^{(1),a}}{\rho a_3^g} - \hat{h}_3^a \end{aligned}$$

We show here applications to the ITTC standard test case S-175 containership in head seas. Computations are compared to experiments of Mitsubishi Heavy Industries. Fig.1 shows results for $F_n = 0.25$ and Fig.2 for $F_n = 0.3$. For all motions the agreement is good. In fact, the computational results for heave for long waves appear to be more plausible, as they tend as expected monotonously to 1. The discrepancies between experiments and computations for the higher Froude number $F_n = 0.3$ are most likely due to nonlinear damping effects in the experiments. For $F_n = 0.275$, Bertram (1998) showed that the phase information is also correctly captured, at least for wave lengths where the RAOs are not approximately zero.

The added resistance is reasonably well captured. One should keep in mind that the margin of accuracy for experiments is also less accurate for added resistance than for motions. The differences in measured added resistance and computed added resistance for the higher Froude number occur where also the pitch motions differ most. Generally, good agreement between added resistance can only be expected if also motions are predicted well. Especially for low frequencies of encounters in oblique waves, larger differences are expected unless empirical corrections or a model for an autopilot are included, but this has not yet been investigated.

In summary, the RSM predicted added resistance well, as long as it predicted also motions well. The formula for the added resistance appears now to be debugged and ready for use for other fully three-dimensional methods.

References

BERTRAM, V. (1990), *Fulfilling open-boundary and radiation condition in free-surface problems using Rankine sources*, Ship Technology Research 37, pp.47-52

BERTRAM, V. (1998), *Numerical investigation of steady flow effects in 3-d seakeeping computations*, 22. Symp. Naval Hydrodyn., Washington

BERTRAM, V.; YASUKAWA, H. (1999), *Added resistance for a fully three-dimensional ship seakeeping method*, NuTTS'99, Rome

BERTRAM, V.; YASUKAWA, H. (2000), *Investigation of global and local flow details by a fully three-dimensional seakeeping method*, 23. Symp. Naval Hydrodyn., Val de Reuil

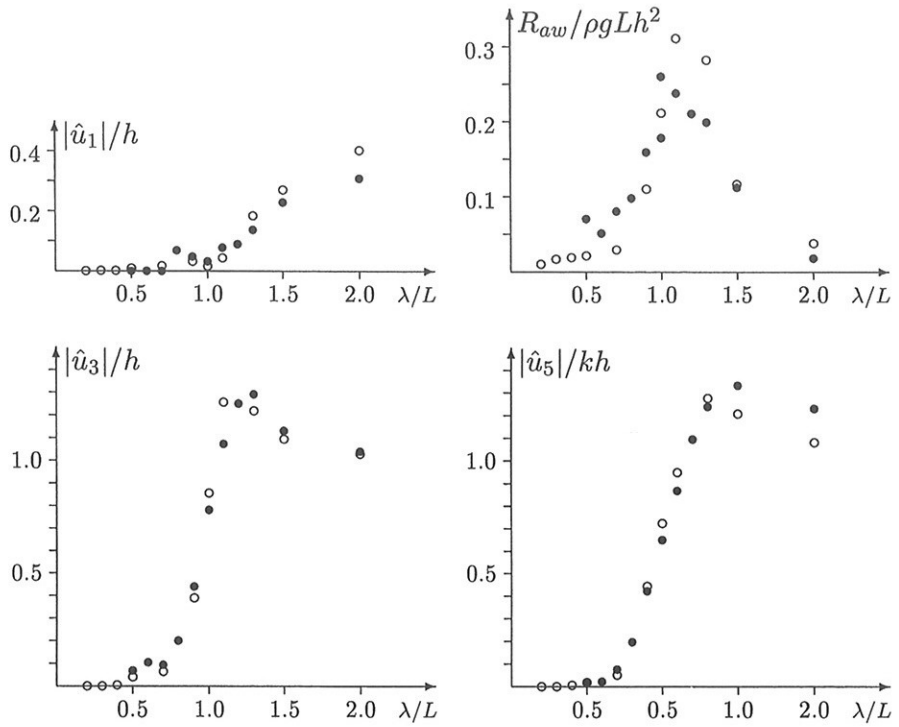

Fig.1: RAOs for motions and added resistance for S175, $F_n = 0.25$, $\mu = 180°$, • exp., ∘ RSM

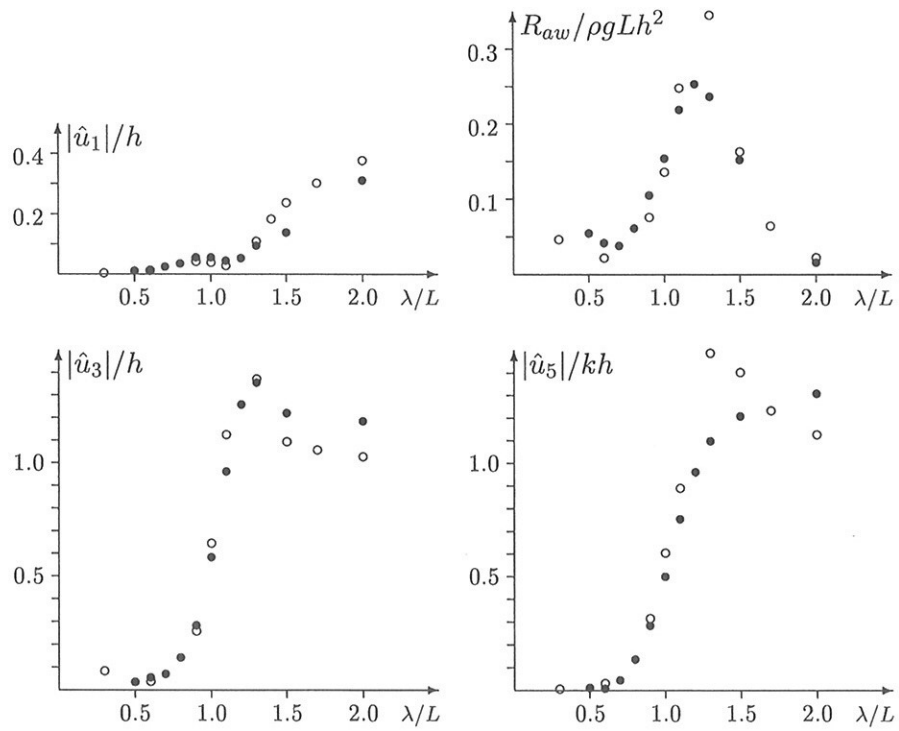

Fig.2: As Fig.1, but for $F_n = 0.3$

Numerical Simulation of Planing Hulls

Mario Caponnetto, Rolla SP Propellers SA, Switzerland, mario.caponetto@rolla-propellers.ch

The present paper deals with the numerical simulation of the flow on hard chine planing vessels. In the past it has been difficult to study this kind of vessel by means of the available methods, such as panel methods, usually applied to conventional ships. The reason is due to the particularly complicated flow field generated by planing hulls.
A thin layer of water (spray) is generated at the stagnation line, and in this zone the pressure gradient is very high. Depending on the hull shape and speed the flow may separate sharply at the chine, and eventually reattach along the hull sides, or generate vortices. The transom can be dry at high speed, while partly wetted, with recirculating water, at lower speed. The generated bow and stern waves are normally steep and may break, dissipating their content of energy. Due to these particular features, potential flow methods are not suitable for planing hull computation, nor are any methods that are unable to compute highly geometrically nonlinear free surfaces.
The method presented in this paper approaches the problem using a RANS code based on Finite Volumes, where the free surface is computed using a Front-capturing Method (Volume of Fluids).
The results obtained using this method for real hull shapes and monoedric hulls are very satisfactory; some examples are presented in the paper.

Introduction

Hard chine planing hulls represent nearly the totality of the vessels employed in the nautical field for pleasure crafts, and are also largely used for small and medium size civil and military applications.
Despite this fact there is a lack of tools at disposal of the naval architect to design, analise and optimize this kind of vessel. The analytical method normally used to predict the resistance and the trim of the boat is the well known Savitsky method, with its variations. The main drawback is that the Savitsky method is strictly applicable only for monoedric hull shapes, namely any variation of the beam and deadrise angle cannot be properly taken into account. The formula are a mixture of experimental and theoretical data and some of the approximations adopted may become important. For example the effect of the hydrostatic pressure and the position of the center of pressure are a too simple approximation of the real phenomenon. In general large errors may occur for warped hulls and when computing performances at low speed.
There are also a number of systematic series, but again the shape of the real planing hulls used nowadays normally differs from that of the series.
Moreover it is not a common practice of the majority of the shipyards to perform model testing in the towing tank, and this is mainly due to the obvious time and cost constraints typical of small boats.
All these factors make the prediction of planing boat performance more an art then a science, and the result is a large margin of uncertainty.
The need for a reliable direct method able to compute the flow field around planing hulls is then highly requested by designers, but the mathematical complications due to the complexity of the flow are obvious. This is due to the presence of the spray, detachment of the flow at the chine and reattachment along the side, complicated flow at the transom and presence of breaking waves.
A number of recently developed CFD codes are now able to compute flows with large deformations of the free surface. Particularly successful are those adopting the Volume of Fluid technique. In this case both air and water are computed simultaneously; the two fluids are not considered separately, but as a continuum fluid with different physical properties. The physical property of the actual fluid depends on the properties of the two constituent fluids and a scalar quantity (C) that represents the volume fraction of the two phases (i.e. C=1 for water and C=0 for air). A value of C between 0 and 1 indicates the presence of the interface, that is not discontinuous but mainly depending on the mesh size.
A similar approach is used in the commercial code Comet, developed at the ICCM of Hamburg. The code is a Finite Volume method able to solve RANS equations with the additional above mentioned capability to include free surface calculation.
The code has been used to compute a large number of planing hulls and the comparison with the available experimental data has been very satisfactory. Accurate resistance curves for different displacements and center of gravity positions can now be computed in a couple of days, with obvious advantages for the boat (and propeller) designers.

Mesh and test procedure

An accurate and efficient mesh is needed to compute the flow field with the requested precision and within practical time constraints. While Comet allows both structured and unstructured mesh, for our problem we use multi-block mesh with structured hexahedral cells. Nine blocks are normally used to define the computational domain, distributing the cells between the blocks in order to refine the mesh where the gradients are expected to be higher. Cells are refined along the hull surface to capture the spray and the boundary layer, as well as above and below the undisturbed water surface to compute waves. Cells do not have to match at block interfaces. A typical mesh is represented in figure 1.

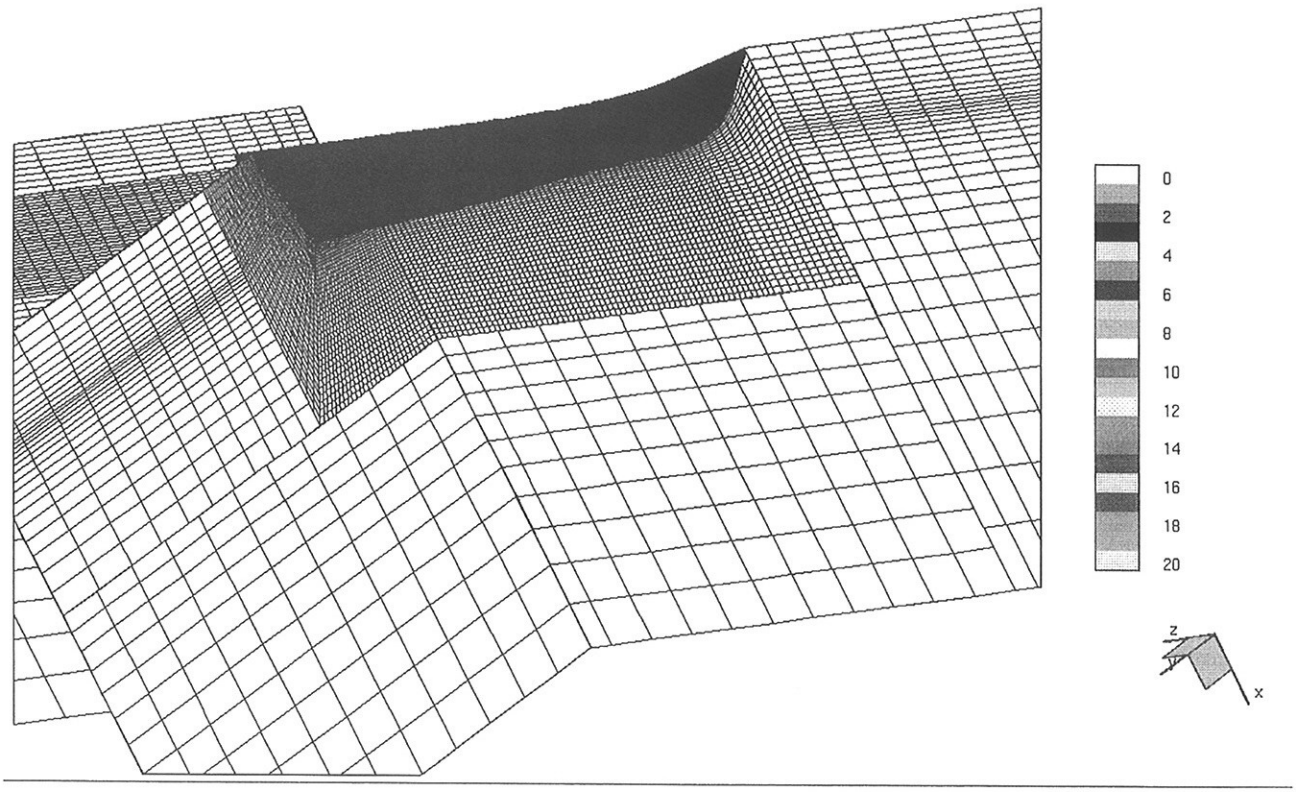

Figure 1

After a number of convergence tests we have noticed that, while the flow detail increases with the cell number, a mesh having about 400.000 cells (for one half of the boat) is sufficient to have converged values of the forces acting on the hull (lift and drag) and of the center of pressure.

Given the hull shape, displacement, center of gravity and speed, the trim of the boat remains unknown. In theory we should test different trim (and submergence) until we obtain, with a trial and error procedure, the trim that satisfies the equilibrium of the forces and moments. Since the displacement of the boat may vary and moreover we could be interested to know how the resistance changes moving the center of gravity, we prefer to test the boat at a number of predefined trim and submergence, to compute the lift, resistance and the center of pressure, and then to interpolate these values at the desired displacement (lift) and center of gravity (center of pressure).

In general for each speed the boat is tested at a combination of 3 trim angles and 3 immersions of the transom. The results of the 9 tests allow later a bi-quadratic interpolation of the values. While Comet can perform parallel computation, in our case it is has been found convenient to run the cases serially, each one on a different processor that we have at disposal (2 processors of SGI Octane, 4 processors of SGI Origin 2000).

Figures 2 and 3 show some typical result; in this case the data are for a 80 foot boat at 34 knots. Figure 2 shows how the position of the center of pressure (from transom) and the lift change with trim and submergence. Each curve is for a different trim angle (2, 3 and 4 degrees), while each point over the curve is a different submergence at the transom. Figure 3 shows similar results for the total resistance.

In many cases not only the value of the forces are of interest, but also the pressure distribution and the wave pattern visualization can be useful to understand the behavior of the boat. Figure 4 shows the free surface elevation calculated for a boat with unusual hull shape running at 40 knots. It can be observed the rise of the spray at the stagnation line; the spray is then deflected at the chine and moves sideway generating a thin breaking wave. The level of the free surface is taken conventionally where the volume fraction is C=0.5.

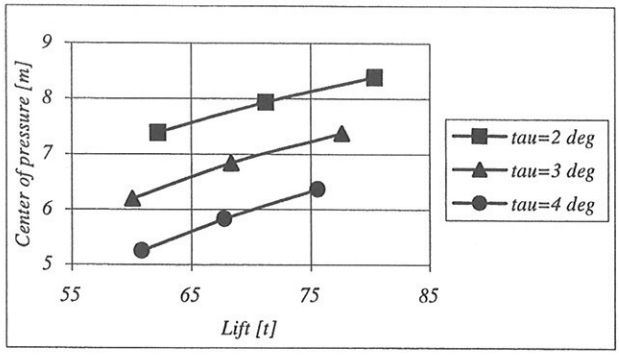

Figure 2

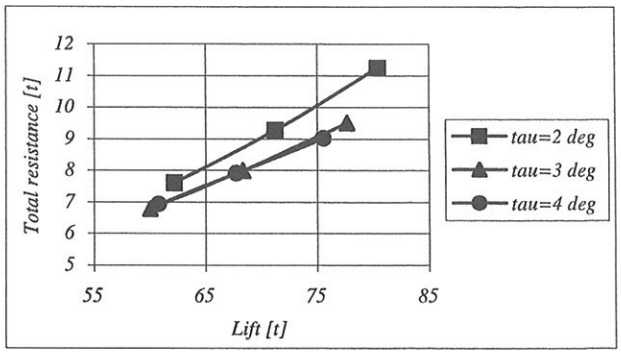

Figure 3

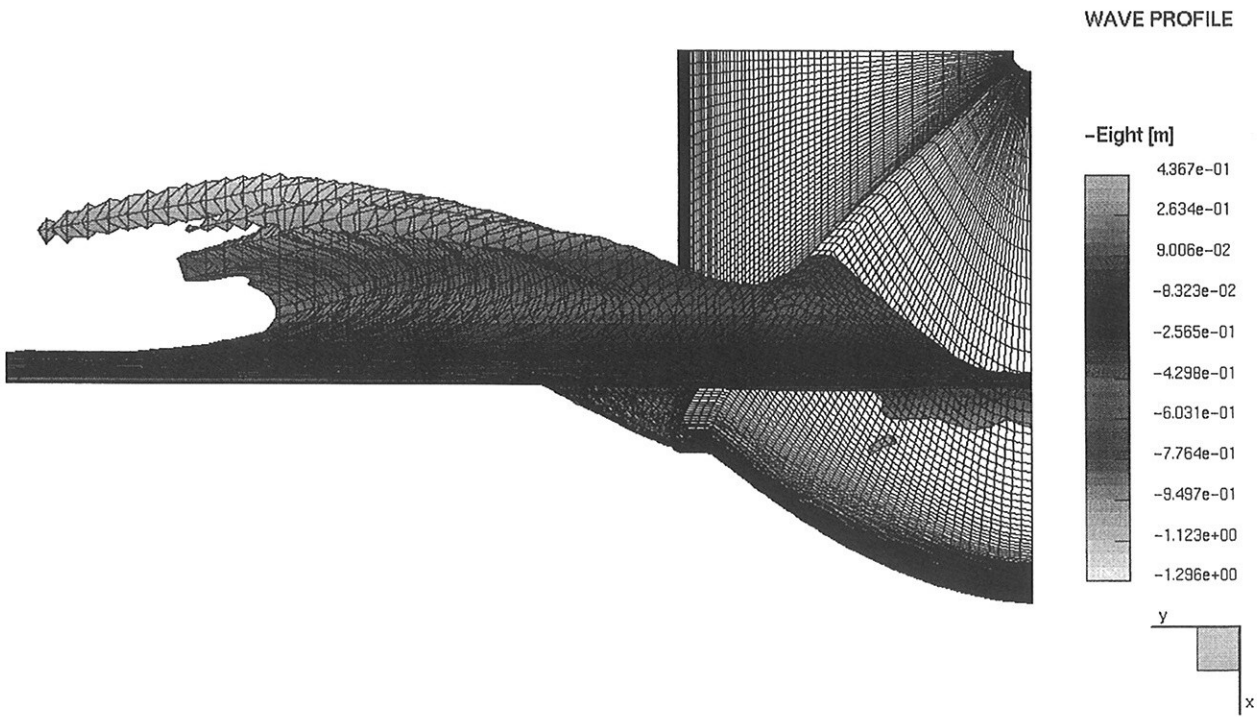

Figure 4

Validation of the method

A number of computations have been performed for comparison with the available experimental data. In particular the code has been extensively compared with the Savitsky method in a wide range of speeds and for different geometries. Figure 5 and 6 show one of these comparisons for a monoedric hull having 12 degrees of deadrise angle. The hull is fixed at a given trim and submergence and the speed is increased from 25 to 80 knots. As expected the lift increases with speed more or less quadratically, while the center of pressure moves forward reaching asymptotically the limiting value of 0.75Lm predicted by Savitsky method. The lift is overpredicted, but the difference between the two methods decreases with increasing speed.

As already mentioned 400.000 cells are normally used for hull computation; this figure has been chosen as a compromise between precision and computational time constraints. In order to see the effect of the mesh size, figure 7 shows the longitudinal lift distribution calculated for the same (warped) hull but using different meshes (200.000 and 700.000 cells). The two results are very close, but the finer mesh supplies a higher lift (+4% in this case). In general this difference goes to about 1% when using the mesh with 400.000 cells.

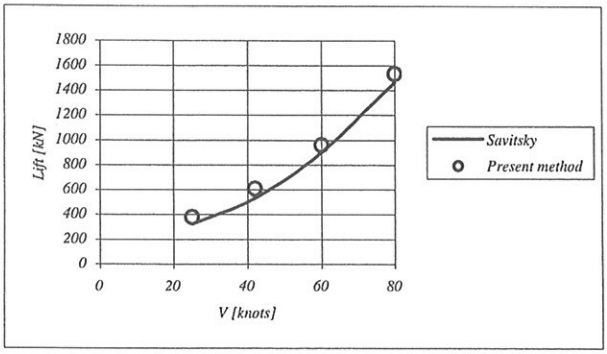

Figure 5

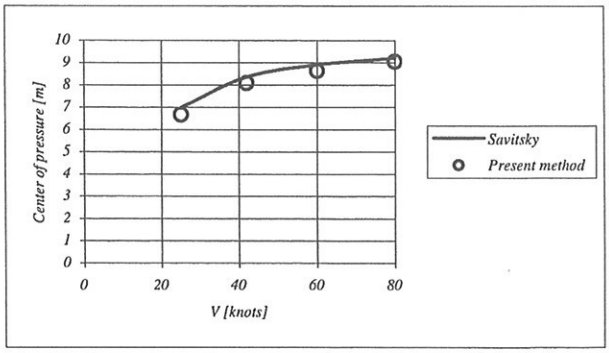

Figure 6

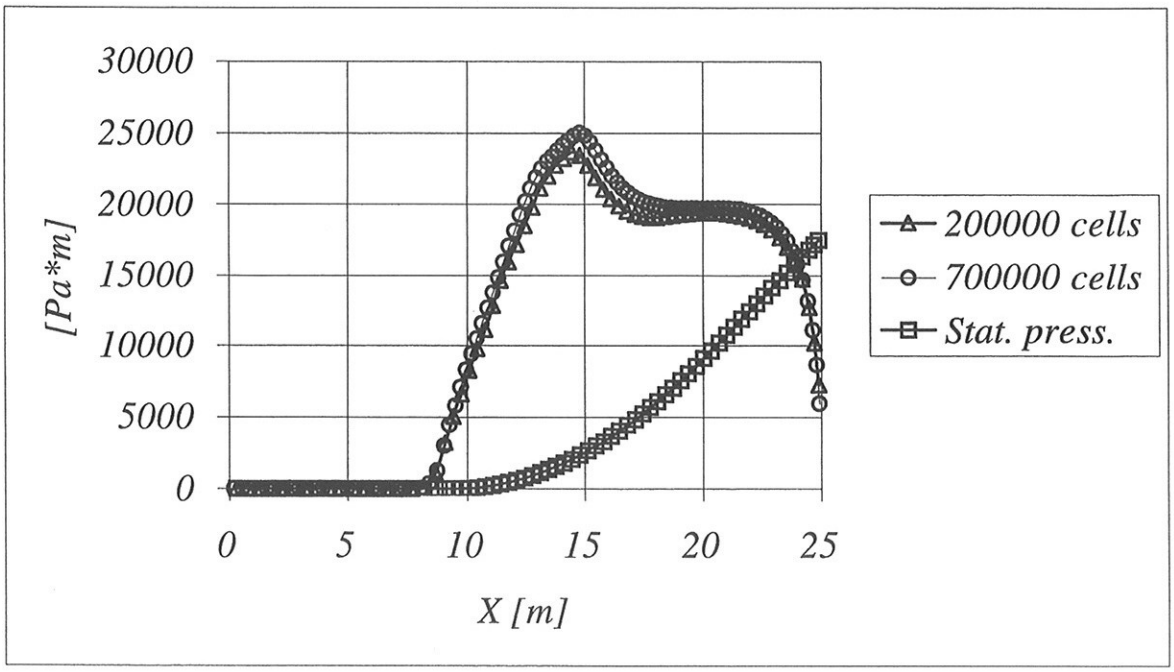

Figure 7

Figure 7 shows that the lift increases steeply from the point of attachment of flow at the keel (X=8 m) to the point of detachment at the chine (X=15 m). Then the lift decreases, going rapidly to zero close to the stern, since in this case the transom was completely dry.

Conclusion

In this paper has shown the possibility to compute planing hull flow using a numerical method. The method used is based on the Finite Volume formulation and the free surface deformation is computed using a Volume of Fluid approach. With this technique it is possible to predict the complex behavior of the flow typical of planing hulls (spray generation, detachment and reattachment of the water at the chine, breaking waves). The computed forces are in general in good agreement with the experimental data available, and some comparison is presented in the paper. Any realistic hull shape can be computed, and this is a great improvement for planing hull designers, compared with the methods commonly used in the past.

An Investigation of the Time-Step for a Line-Implicit Time-Stepping Scheme for the $k-\omega$ and Reynolds-Averaged Incompressible Navier-Stokes Equations

Lars Carlsson
Hydromechanics division
Department of Naval Architecture and Ocean Engineering
Chalmers University of Technology
SE-412 96 Göteborg
lc@na.chalmers.se

Extended Abstract

This is work in progress. Eventually we want to compute turbulence modeled unsteady flow in boundary layers. More specifically, the flow around sails and hulls. We will advance the solution in time using a second-order accurate method and we want to avoid the severe time-step restrictions that occur in boundary layers for explicit methods. If our investigation turns out well and time permits, we will add the time-stepping algorithm to an existing flow solver and present some computations.

We will investigate the impact of a line-implicit time-stepping technique on the size of the time-step in a turbulence modeled channel flow. The turbulence model that we are going to investigate is a $k-\omega$-model along with a velocity-pressure formulation of the Reynolds-averaged incompressible Navier-Stokes equations. Previous results, for the incompressible Navier-Stokes equations, show that it is possible to split the spatial operators in the momentum equations and treat components belonging to a specific grid direction implicitly and the rest of the terms explicitly.

The flow solver is based on a discretization in space on what is known as Chimera or composite overlapping grids. This discretization technique gives us the possibility to choose the type of time-stepping scheme to be used in each component grid individually. Another benefit is that the Chimera technique also lets us construct body-fitted grids that resolve boundary layers. At each time step we want our flow solver to accurately predict the length of the largest possible time step. The algorithm for the time-step prediction rely on von Neumann analysis of the amplification factors. The von Neumann analysis in turn is only valid for periodic solutions. Instead a more computationally costly technique could be used; computing the amplification factors for a semi-discrete case. In practice this is not an option, because in addition to solving the governing equations, we would have to solve a corresponding generalized eigenvalue problem.

Our analysis will be conducted for a two-dimensional channel with periodic boundary conditions in the x-direction and no-slip boundary conditions in the y-direction. Within this investigation, we hope to find answers to two questions; Can the operators in the $k-\omega$-model equations be divided to accomplish a stable time-stepping algorithm using a large time step? How does the amplification factors estimated by the von Neumann analysis correspond to those in the channel case?

Study on the Hydrodynamic Characteristics of Foil-Assistance Arrangement for a Catamaran

S.W. CHAU C.C. JAN

United Ship Design and Development Center
TAIWAN, R.O.C

C.L. HWANG

Institute of Naval Architecture and Ocean Engineering, National Taiwan University
TAIWAN, R.O.C.

1. INTORDUCTION

Recently the United Ship Design and Development center (USDDC) has devoted efforts to develop high-speed catamarans for passenger transport. Foil-assistance arrangement is employed to increase the service speed and improve the ride performance. Two demi-hulls of catamaran can provide good support and protection for hydrofoils, and hence they generally extend between the demi-hulls. The main advantage of hydrofoil is the low cost of installment, and high effectiveness in speed increase. Hydrofoils are often installed with fixed orientation on ship. This leads to that the cost for building and maintaining is relatively low. The speed increase mainly depends on the section shape of hydrofoil, the longitudinal position, the vertical position, and the angle between foil and hull. From the resistance point of view, the lift-drag ratio of hydrofoil is especially important. The hydrodynamic lift generated by hydrofoils can reduce the displacement of ship, and hence also the total resistance. However, the hydrodynamic drag compensates the resistance decrease effect. Generally speaking, the required propulsion power can be obviously reduced at high Froude number, but could be little influenced for low Froude number. Due to the small draft of catamaran the hydrofoil should have its submergence as deep as possible to reduce the free surface effect, because it causes considerably loss of hydrodynamic lift. The longitudinal position of hydrofoil can help catamaran to keep a favorable trim and minimum resistance. Because the trim angle of catamaran is small, a sufficient large angle of attack for hydrofoil is necessary to provide required lift. Too large angel of attack is not preferred due to its rapid drag increase.

The flow around hydrofoil is basically three-dimensional, although it is bounded by two demi-hulls. Besides, the wave system generated by the interaction of two demi-hulls make the hydrofoil flow more complicated. The foil-assistance system has been investigated using experimental approach discussed in the next section. This paper tries to isolate the hydrodynamic behavior of hydrofoil from the complete system by using measured results and a simplified numerical computation in order to understand the hydrodynamic characteristics for designing the foil-assistance system of catamarans.

2. EXPERIMENTAL STUDY

A 25m long passenger catamaran with foil-assistance arrangement, Fig. 1, has been tested in the large towing tank at the Institute of Naval Architecture and Ocean Engineering of National Taiwan University [1]. The foil system is comprised of two hydrofoils. The main foil located near LCB provides lift to reduce total resistance, and the sub-foil near stern gives pitching moment to improve riding performance. Both foils are tested at 0°, 2° and 5°, respectively. Two different longitudinal positions for aft foil are used to study the influence on total resistance due to the sub-foil. The ship with both foils installed are tested from Fn=0.1 to 1.2. Additionally, the catamaran only with main foil installed is also tested. This can help to simplify the hydrofoil flow field and analyze the catamaran-foil system more easily, because there is strong interaction between two hydrofoils. Our numerical computation only focuses on the last case. The force measurement device is specially designed that the hydrodynamic lift and drag of the hydrofoil can be precisely and separately measured [1].

3. SIMPLIFIED NUMERICAL COMPUTATION

The numerical model of the interested case is simplified due to the following two main reasons: First, the complete three-dimensional computation of the catamaran with hydrofoil is too time-consuming and complicated, which is not very practical in the design stage. Second, an engineering approach based on simplified theories and experimental correlations is more preferable for design purpose. Although the flow around foil is three-dimensional, it seems to approach two-dimensional at high Froude. The wave system induced by two demi-hulls is also neglected for the sake of simplicity. Ship performance is interested at the design speed (high Froude number) in the design stage, which seems to justify the two-dimensional and no hull assumption. But the angle of attack of hydrofoil with respect to the still water line and the submergence of foil are directly taken form the experimental data.

Extensive study of two-dimensional hydrofoils without considering the free surface effect is performed by *Chau*

and Kouh [2]. Because the hydrofoil has quite limited submergence, the free surface effect should be taken into account. *Chau* [3] has investigated the hydrodynamic characteristics of NACA 4412 with depth-chord ratio 0.5. He has further studied the influence of depth-chord ratio and Froude number on the lift and drag coefficient for the same foil [4]. Here the numerical method used in [3][4] is employed. The interface-capturing method, combining finite volume method and volume-of-fluid method, is used to compute the flow around a two-dimensional hydrofoil near free surface, Fig.2. The hydrofoil travels with a horizontal speed (ship speed) V, and the chord length of this hydrofoil is c, while its still water submergence is h. The still water level is defined at z=0. More details about the applied numerical scheme are discussed in *Chau et al.* [5].

4. COMPARISON BETWEEN EXPERIMENTAL RESULT AND NUMERICAL COMPUTATION

Fig.3 shows the measured submergence of QC (quarter chord from the leading edge) h of the hydrofoil under free surface. The non-dimensional value h/c varies between 0.4 and 1.6 for different Froude number Fn, which is defined as:

$$Fn = V / \sqrt{gc},$$

where g denotes the gravtational acceralation. The submergence is little influenced by small Froude number, while it steadily decreases at high Froude number. This is explained by the obvious hydrodynamic effect at high Froude number. The deepest submergence at about Fn=0.3 is corresponding to the speed hump of catamaran at model speed between 2.0 to 2.5 m/s. Fig.4 shows the measured angle of attack (AOA, in degree) for hydrofoil with respect to the still water line (SWL). The hydrofoil has a fixed angle of attack 5° with respect to the keel line, and the trim angle of this ship ranges between 0° and 2.6°. For small Froude number the catamaran has almost no trim, while the trim angle is approximate to 2° for Froude number larger than 4.5. It seems to indicate that the hydrodynamic effect is not obvious for Fn<0.2, and becomes effective for Fn>0.2.

The hydrodynamic coefficients, i.e. the drag coefficient C_D and lift coefficient C_L are defined as follows:

$$C_D = \frac{F_x}{0.5\rho V^2 c}$$

$$C_L = \frac{F_z}{0.5\rho V^2 c}$$

where F_x denotes the force component in the x-direction, F_z the force component in the z-direction, and ρ the fluid density. The measured drag and lift coefficients are shown in Fig.5 and Fig.6, respectively. The wave system due to the interaction between two demi-hulls influences the flow around hydrofoil near free surface significantly, which show strongly three-dimensional nature. When the Froude number increases, the starting point of wave interaction shifts in the downstream direction. Therefore, the foil is less influenced by the wave system generated by ship hulls, and is more close to a two-dimensional situation. Another factors influencing the drag are the submergence of foil and the Froude number. According to the previous study [4], the increase of Froude number and the small submergence both result in drag coefficient decrease. The experimental result seems to support the above statement. The strong wave interaction could be the most important reason for the large variation of drag coefficient for Fn<4.0. The study of *Chau* [6] indicates that the drag coefficient for a three-dimensional finite wing is generally much larger than its two-dimensional foil section. This agrees well with the measurement: For Fn>4.0 the drag coefficient decreases, when the Froude number increases. The higher Froude number shows less three-dimensionality, and hence smaller drag coefficient. The drag coefficient finally approaches to the value 0.15.

The measured lift coefficient increases with the Froude number, except for Fn<0.2, and approaches to the value about 0.8. This is also in good agreement with the well-known fact [6]: two-dimensional lift coefficient is larger than three–dimensional one. The increase of Froude number results in larger lift coefficient, while the small submergence decreases the lift coefficient. The effect of these three factors seems to balance for Fn>6.0, and the lift coefficient varied little from 0.8.

Fig.7 and Fig.8 show the computed drag and lift coefficient, respectively. Because the numerical computation is under the two-dimensional assumption, the drag coefficient decreases, except the speed hump region at Fn=3.0, with increased Froude number. The lift coefficient shows the same tendency, but a large fluctuation appears in the hump region. Although the measured and computed hydrodynamic coefficients show somehow different behavior, the tendency of lift-drag-ratio (C_L/C_D) is quite similar (increase with the Froude number), Fig.9 and Fig.10. But they are different in scale of y-axis. This points out that the hydrofoil become more effective at high Froude number.

Fig.11, Fig.12 and Fig.13 are the ratio between calculated and measured hydrodynamic coefficients. The value R_{CD}, R_{CL} and $R_{L/D}$ are defined as follows:

$$R_{CD} = \frac{C_{D\_measured}}{C_{D\_calculated}}$$

$$R_{CL} = \frac{C_{L\_measured}}{C_{L\_calculated}}$$

$$R_{L/D} = \frac{(C_L / C_D)_{measured}}{(C_L / C_D)_{calculated}}$$

The R_{CD} value is about 4.2 for Froude number larger than 4.0. This means that the calculated value from the simplified assumption is too small. But it is a good way to estimate the three-dimensional drag coefficient in the primary design stage. The R_{CL} value deviates from 1.0 for small Froude number, but it is quite close to 1.0 at design speed. This indicates that the two-dimensional assumption is acceptable for very high Froude number (>8.0). To estimate the $R_{L/D}$ value from the numerical computation, the measured one is only about 25% of the calculated one due to too small drag prediction in numerical computation.

5. CONCLUSION

The prediction of the hydrodynamic coefficients for a single hydrofoil installed on a 25m long passenger catamaran has been performed both numerically and experimentally. The numerical computation is performed under the two-dimensional flow assumption and neglecting the interaction between hull and foil. At high Froude number the measured lift coefficient of hydrofoil approximates the value for two-dimensional case, and the drag coefficient for two-dimensional one is about 25% of the experimental result.

REFERENCES

1. *Model Test for a High-Speed Catamaran*, United Ship Development Center (1999).
2. Chau, S.W., Kouh, J.S., "Analysis of Incompressible Flow around Profiles Used for Marine Applications", *Bulletin of the College of Engineering, N.T.U.*, No.76, pp85-102 (1999).
3. Chau, S.W., "On the Hydrodynamic Performance of a 2D-Foil near Free Surface", *Proceeding of the Seventh National Conference on Naval Ship Engineering*, pp.21-28 (1999).
4. Chau, S.W., "Numerical Study of Small Submerged Depth on Hydrodynamic Coefficients of a Two-Dimensional Hydrofoil at High Froude Number", *Proceedings of the Sixth National Conference on Computational Fluid Dynamics*, pp.656-661 (1999).
5. Chau, S.W., Peric, M., Muzaferija, S., "An Interface-Capturing Method for Prediction of Sloshing Problems", *Proceedings of the 22nd National Conference on Theoretical and Applied Mechanics*, Vol.2, pp.363-370 (1998).
6. Chau, S.W., "Numerical Investigation of Free-Stream Rudder Characteristics Using a Multi-Block Finite Volume Method", Bericht Nr. 580, IfS der Uni. Hamburg (1997).

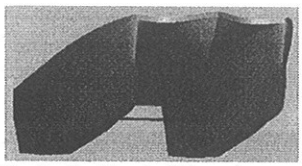

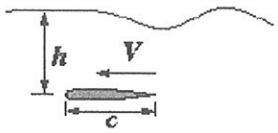

Fig.1 (left) A 25m long passenger catamaran with hydrofoil arrangement

Fig.2 (right) Schematic sketch of hydrofoil near free surface

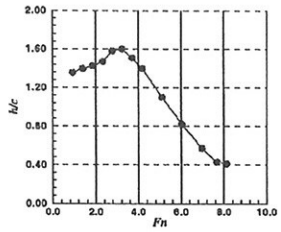

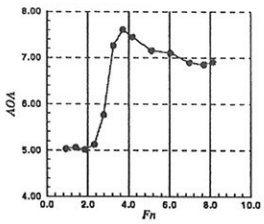

Fig.3 (left) Submerged depth of hydrofoil under free surface

Fig.4 (right) Angle of attack for hydrofoil with respect to *SWL*

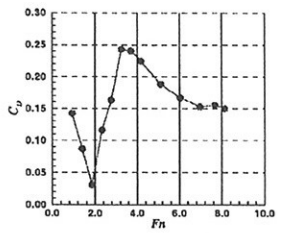

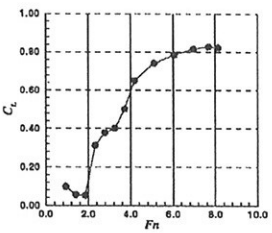

Fig.5 (left) Measured C_D of hydrofoil at different ***Fn***

Fig.6 (right) Measured C_L of hydrofoil at different ***Fn***

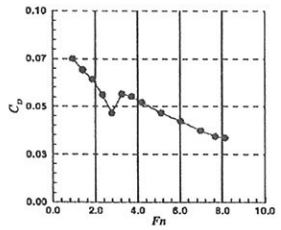

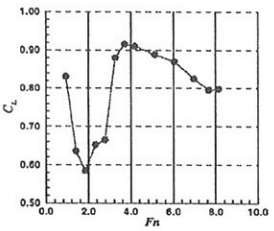

Fig.7 (left) Computed C_D of hydrofoil at different ***Fn***

Fig.8 (right) Computed C_L of hydrofoil at different ***Fn***

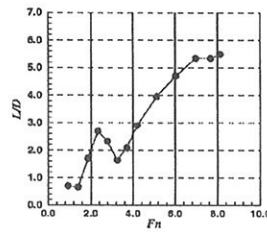

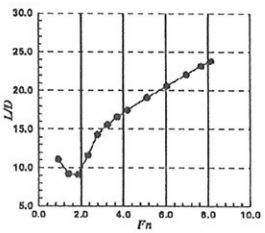

Fig.9 (left) Measured ***L/D*** value of hydrofoil at different ***Fn***

Fig.10 (right) Computed ***L/D*** value of hydrofoil at different ***Fn***

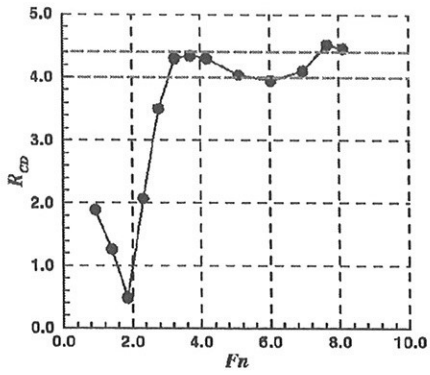

Fig.11 R_{CD} value of hydrofoil at different ***Fn***

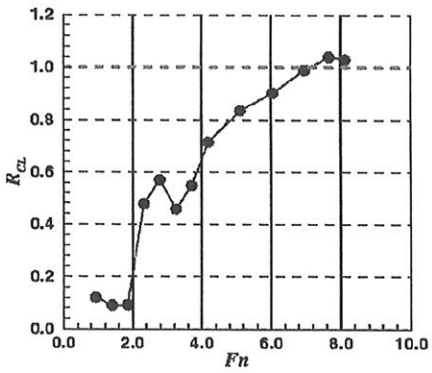

Fig.12 R_{CL} value of hydrofoil at different ***Fn***

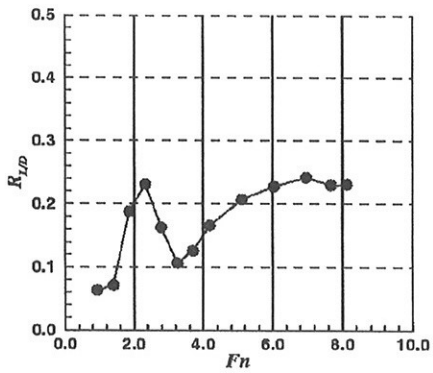

Fig.13 $R_{L/D}$ value of hydrofoil at different ***Fn***

Comparison of Explicit Algebraic Stress Models and Second-Order Turbulence Closures for Steady Flows around the KVLCC2 ship at model and full scales

G.B. Deng & M. Visonneau
Laboratoire de Mécanique des Fluides, Ecole Centrale de Nantes
1 Rue de la Noë, B.P. 92101, 44321 Nantes Cedex 3, France
Fax: (33) 2 40 37 25 23
E-Mail: Ganbo.Deng@ec-nantes.fr, Michel.Visonneau@ec-nantes.fr

June 30, 2000

1 Introduction

This paper is devoted to the assessment of the most recent turbulence models for steady flows around a modern ship, the so-called KVLCC2 ship which has been studied experimentally by Dr. Kim & al. at KRISO [8]. The flow is characterized by a strong thickening of the boundary layer, the generation of an intense longitudinal vortex motion creating complex "hook-shaped" velocity contours in the central part of the wake near the location of propeller.

The aim of this study is therefore, (i) to compare, at model scale, the relative merits of different statistical closures ranging from eddy-viscosity models to second-order formulations based on the Reynolds Stress transport equations, (ii) to evaluate, at full scale, the differences between the solutions provided by the various models in order to check if the dependancy of the solution on the turbulence modelisation is also critical for flows around real ships.

2 Numerical Method

The simulation has been performed with the HORUS code developed in our CFD group (Division Modélisation Numérique). The solution of the Reynolds Averaged Navier-Stokes Equations is obtained by using finite difference method with a body-fitted structured grid. A cell-centered layout is employed in which the pressure, turbulence and velocity unknowns share the same location. The momentum and continuity equations are coupled through the PISO procedure and several implicit first and second order accurate schemes are implemented for the space and time discretizations. In the present computation, convection terms written in convective form are discretized with a third order upwind-biased scheme which is similar to the well known Quick scheme for the conservative formulation. Finally, preconditioned conjugate gradient solvers (CGS, CGSTAB) are used to solve the linear systems.

Implementation of Reynolds stress transport model in a non-staggered layout is not straightforward. Due to the absence of numerically stabilizing eddy viscosity and the predominant influence in the momentum transport equations of the equilibrium between several strong and opposite source terms, namely the pressure and Reynolds stress gradients, a special numerical stabilizing technique has to be implemented. The main characteristics of these numerical amendments are recalled in previous contributions of Deng & Visonneau ([3], [2]).

2.1 Reynolds Stress Models

The Rij-ω closure which has been used in this study is a more robust variant of the original Shima model [9] which shares the same overall formulation but differs only in the model coefficients. The Reynolds stress transport equations are not recalled here for the sake of brevity here but can be found in [3].

2.2 Explicit Algebraic Stress Model

By using a local equilibrium assumption, Rodi [7] has deduced an algebraic stress model (ASM) from the Reynolds stress transport model. Actually, the ASM model can be explicitly solved and such an explicit algebraic stress model (EASM) has been first proposed by Pope [6] for two-dimensional flows. EASM models for three-dimensional flows have been developed by Gatski & Speziale [4] and are widely used. In this study, we use the EASM model proposed by Gatski & Speziale [4] based on a three-term basis which is the exact solution of the ASM model only for 2D flows. For three-dimensional flows, this formulation can be only considered as an approximation. However, it is expected that this model can improve the prediction compared with a linear eddy-viscosity model. Here again, the details of the closure modified by the authors in the near-wall region are not recalled here but can be found in [3].

3 Numerical Results

Computations have been performed on a domain covering the whole ship with $121 \times 81 \times 41$ nodes in the streamwise, radial and girthwise directions respectively. A third order upwind-biased scheme is used to discretize the convection term. The convergence is ensured by checking the evolution of the wall friction velocity. Several thousand iterations are necessary to achieve convergence. Computational time with the Reynolds stress model is about twice more important than with the EASM or two-equation models.

X/L=0.485 is the station where the propeller should be present. The successful prediction of the hook-shaped mean streamwise velocity contours observed in the measurements has always been considered as a key criterion for assessing the performance of a turbulence model designed for ship flows.

By comparing the predicted mean streamwise velocity contours with the experimental measurements at this station (figures 1(a) to 1(c)), it can be observed that the hook-shaped velocity contours are remarkably well captured with this new Reynolds stress model (figure 1(c)). However, an additional secondary vortex near the vertical plane of symmetry is found by the second order model, which is not present in the experiments. With the EASM model and the SST model, the streamwise velocity at the center of the longitudinal vortex is clearly under-predicted. The EASM-SSG model provides a simulated flow in slightly better agreement with the experiments (figure 1(b)) but the improvement is not spectacular.

Figures 2(a) to 2(b) show the predicted turbulent kinetic energy scales obtained with a $K-\omega$ and the $Rij-\omega$ models. All the models implemented tend to overpredict the maximum value of the turbulent kinetic energy near the plane of symmetry. However, the prediction provided by the $Rij-\omega$ model is the closest from the experiments.

In a previous study on the HSVA tanker, Deng & Visonneau [3] found that the sum of the convection and the turbulent diffusion terms in the turbulent kinetic energy budget was almost as important as the turbulent dissipation term in this region. Consequently, the convection and the turbulent diffusion terms, intrinsically present in the Reynolds stress transport equations, should not be neglected. This analysis has not yet been done for this testcase but all the results available here suggest that this explanation is also valid for this ship.

Finally, the computations are performed at the full scale Reynolds number. It is very encouraging to see that no particular numerical problems appear during these validations. Figures 3(a) to 3(b) show the isowakes and turbulent kinetic energy contours simulated by the $K-\omega$ and the $Rij-\omega$ closures. First, compared with the model scale, the overall intensity of the longitudinal vorticity is drastically reduced since the convection effect is more important. However, the importance of the turbulence modelisation is still clearly illustrated by these results since the second-order closure provides again a significantly more intense longitudinal vorticity.

4 Concluding Remarks

The flow around the KVLCC2 ship has been calculated by using different turbulent models ranging from linear eddy-viscosity model, explicit algebraic stress model, to full Reynolds stress transport model. A stable solution of the Reynolds stress transport equations has been obtained by implementing the same near-wall model and defect correction approach already validated on the HSVA tanker (Deng & Visonneau, [3]).

On one hand, non-linear models obtained from an approximate explicit solution of the algebraic stress models slightly improve the prediction in all aspects compared with simple linear eddy-viscosity models. However, the solution of the Reynolds stress transport equations shows that the local equilibrium assumption on which the algebraic stress model is based is not valid in the region where the longitudinal vortex is intense. Physically accurate computations of this flow can only be obtained by solving the Reynolds stress transport equations. Finally, the computational results on the full scale problem suggest that the accurate representation of the turbulence effects is still mandatory if an accurate prediction of the near wake flow is looked for.

5 Acknowledgments

Thanks are due to the Scientific Committee of IDRIS and the DS/SPI for attributions of CPU on the Cray C98, the Cray T3E and the VPP machines.

References

[1] G.B. Deng, P. Queutey, and M. Visonneau. Navier-stokes computations of ship stern flows: A detailed comparative study of turbulence models and discretisation schemes. In V.C. Patel and F. Stern, editors, *Proc. 6th Int. Conf. on Numerical Ship Hydrodynamics*, pages 367–386. National Academy Press, 1993.

[2] G.B. Deng and M. Visonneau. Evaluation of eddy-viscosity and second-moment turbulence closures for steady flows around ships. In *21st Symposium on Naval Hydrodynamics*, 1996.

[3] G.B. Deng and M. Visonneau. Comparison of explicit algebraic stress models and second-order turbulence closures for steady flows around ships. In *Seventh International Conference on Numerical Ship Hydrodynamics*, 1999.

[4] T.B. Gatski and C.G. Speziale. On explicit algebraic stress models for complex turbulent flow. *J. Fluid Mech.*, 254:59–78, 1993.

[5] F.R. Menter. Zonal two-equations $k-\omega$ turbulence models for aerodynamic flows. In *AIAA 24th Fluid Dynamics Conf.*, AIAA Paper 93-2906, 1993.

[6] S.B. Pope. A more general effective viscosity hypothesis. *J. Fluid Mech.*, 72:331–340, 1975.

[7] W. Rodi. A new algebraic relation for calculating the Reynolds stresses. *ZAMM*, 56:219–221, 1976.

[8] Van S.H., Kim W.J., Yim D.H., Kim G.T., Lee C.J., and Eom J.Y. Flow measurement around a 300K VLCC model. In *Proceedings of the Annual Spring Meeting, SNAK, Ulsan*, pages 185–188, 1998.

[9] N. Shima. Prediction of turbulent boundary layers with a second moment closure. *Journal of Fluids Engineering*, 115:1–27, 1993.

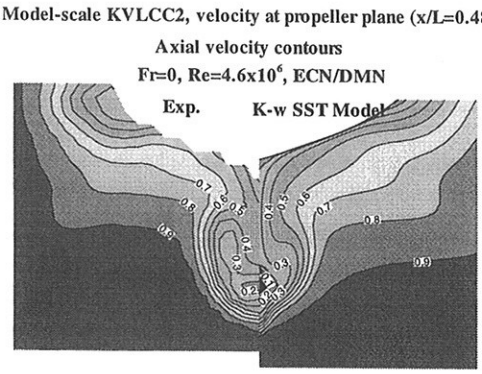

(a) K-ω SST model

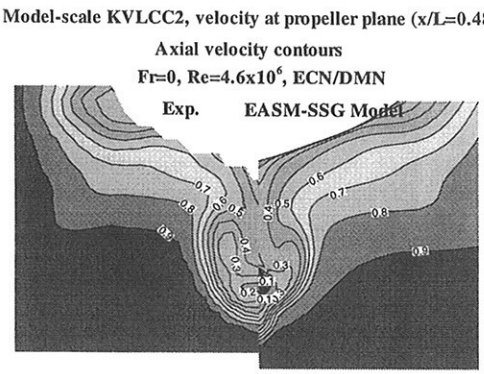

(b) EASM-SSG model

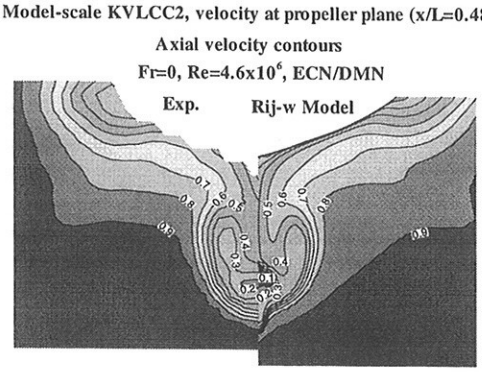

(c) Rij-w model

Figure 1: Comparison between experimental and computed isowakes at x/L=0.485 - Model Scale

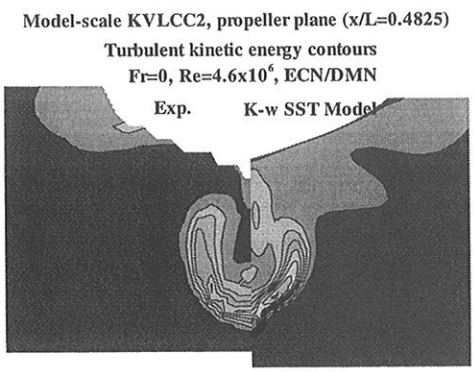

(a) K-ω SST model

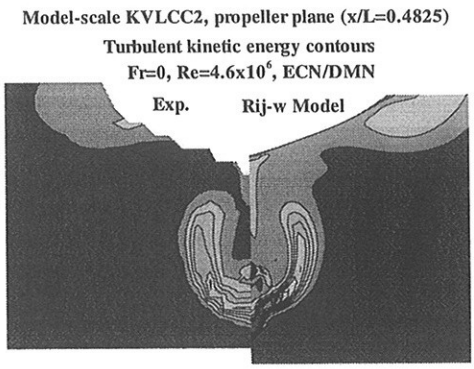

(b) Rij-w model

Figure 2: Comparison between experimental and computed turbulent kinetic energy contours at x/L=0.485 - Model Scale

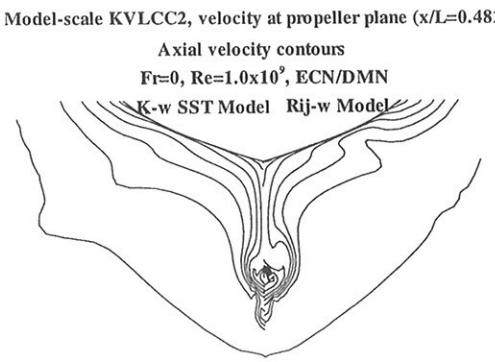

(a) Isowake contours

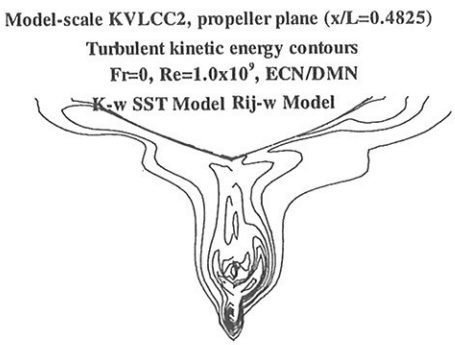

(b) Turbulent kinetic energy contours

Figure 3: Comparison between the $K-\omega$ SST model and the $Rij-\omega$ model at x/L=0.485 - Full Scale

RANS Simulation of Propeller in Oblique Flow

Ould M. El Moctar, Volker Bertram
Hamburg Ship Model Basin, elmoctar@hsva.de

Propellers operate most of the time in oblique flow, not only in fast ships where the propeller shaft is often inclined due to geometrical restrictions. The deviation from the axial direction in all ships is caused by ship motions in manoeuvring and seakeeping. In addition, the ship's wake always introduces locally oblique flow direction for propeller blades. The oblique inflow changes the flow conditions at the propeller blades: The angle of attack and relative velocities depend now on the blade position, s. Eq.(1). The oblique inflow causes transverse forces on the propeller shaft which affect the manoeuvring and stability characteristics of the ship. The local flow conditions are important for the propeller blade design as the cyclic loading of the blades affects fatigue strength.

In the following we consider a four-bladed modern propeller in homogeneous wake at oblique angles up to 12°. We compute propeller forces for various advance numbers to investigate the effect on the propeller load for oblique inflow. In addition we will discuss the forces on the individual blades as well as the asymmetry in thrust due to oblique flow. The possible effects of cavitation will not be considered. There are no experimental data available to validate our computational investigations.

We used the commercial RANS solver COMET, ICCM (1999). The conservation equations for mass and momentum in their integral form serve as the starting point. The solution domain is subdivided in a finite number of CV's which may be of arbitrary shape. The integrals are numerically approximated using the midpoint rule approximation. The discretization in time used an implicit Euler method. The gradient is calculated using a conservative approximation of second order. The discretized continuity equation is transformed in to a pressure-correction equation following the SIMPLE algorithm, adapted to colocated grids. The momentum component equations are linearized using the Picard Iteration scheme. The RNG k-ε-Model with wall functions models the Reynolds stresses. The discretization and linearization lead to a system of coupled algebraic equations, solved by a segregated iterative approach. The inter-equations coupling and non-linearities are resolved in a predictor corrector scheme within outer iterations, which represent the update of the coefficient matrix and source vector. The solution method is designed to use unstructured grids with cell-wise refinement. For more details see Demirdzic and Muzaferija (1995), ICCM (1999)

We used here unstructured hexahedral grids with 600,000 cells, El Moctar (1999) Grids were locally refined at the propeller. The innermost cell thickness was chosen such that on average $y^+ = 60$. The flow was assumed to be fully turbulent..

The turning of the propeller introduces instationary changes in angle of attack and relative velocity at each blade making a solution in time domain mandatory. In each time step, the complete grid is turned corresponding to the advance of the propeller. The time step corresponds to a turn of the propeller of 1°. Finer time steps had virtually no influence on average forces on the propeller. Two full propeller revolutions are required to obtain a stable period solution, Fig.2. CPU times were 30h per propeller speed and angle of attack on one Pentium II processor with 500MHz.

In a global fixed coordinate system each blade segment experiences (neglecting the effect of induced flows) a velocity V_δ under an angle of attack β_δ, Fig.1.

$$v_\phi(r,\delta) = \sqrt{(v\cos\delta)^2 + (\pi nr + v\sin\delta\cos\theta)^2 + (v\sin\delta\sin\theta)^2} \tag{1}$$

$$\beta_\delta = \tan^- 1\left[\frac{v\cos\delta}{\pi nr + v\sin\delta\cos\theta}\right] \tag{2}$$

v is inflow speed to the propeller, n its rpm, r the radial coordinate, δ the angle of attack and θ the blade position. β_δ changes with speed.

The nondimensional force coefficients for individual blades defined as follows:

$$K_{tb} = \frac{\int f_z(r,\theta)dA}{\rho \cdot n^2 \cdot D^4}, \quad K_{Qb} = \frac{\int (f_x(r,\theta) \cdot y - f_y(r,\theta) \cdot x)dA}{\rho \cdot n^2 \cdot D^5} \tag{3}$$

$$K_{fxb} = \frac{\int f_x(r,\theta)dA}{\rho \cdot n^2 \cdot D^4}, \quad K_{fyb} = \frac{\int f_y(r,\theta)dA}{\rho \cdot n^2 \cdot D^4} \tag{4}$$

The integral mean values of the nondimensional forces coefficients for the whole propeller (K_t, K_Q, K_{fx}) were obtained by summing over all N_b blades. The deviation of the thrust direction from the propeller axis in x made nondimensional with propeller radius R is computed as:

$$e_x = \frac{\sum\limits_{N_b} f_z(r,\theta) \cdot r \cdot \cos\theta}{\sum\limits_{N_b} f_z(r,\theta)} \tag{5}$$

The propeller position at y axis was chosen as $\theta = 0°$. The forces acting on the propeller shaft were not considered.

When the blade runs against the direction of the oblique flow, the angle of attack and the velocity increase and thus the forces on the blade. Correspondingly, the forces on the blade decrease in the other half period. The increase above the time mean value of the forces is larger than the decrease, Fig.4 and 5. As a result the mean thrust and torque coefficients are larger than in homogeneous axial inflow of same advance number $J = v/\pi nD$. These differences increase with the obliqueness of the inflow and the advance number, Fig.6. The forces at the propeller oscillate with a frequency of n/N_b, Fig.2 and 3. The amplitude of the oscillations increases with angle of attack, Fig.4 and 5.

The unsymmetry of the force distribution results in a transverse force f_x perpendicular to the propeller shaft. This transverse force superimposes to the rudder transverse force and has an important effect on the manoeuvring behavior of the ship due to the large leverage. The vertical force f_y is for horizontal oblique flow smaller than f_x by one order of magnitude. The point where the resulting axial force acts depends on the geometry of the blades. It lies behind always the reference line of the blade position. Therefore the force maximum has a phase shift with respect to the blade position, Fig.4 and 5. The unsymmetry of the force distribution shifts the mean thrust by a distance e to the side where the propeller blades run against the oblique inflow. e increases also with advance number and angle of attack, Fig.7. The shift of the axial force causes moments about the x and y axes. These moments affect trim and stability, particularly for fast ships with high ratios of propeller thrust to ship weight.
Full details will appear in my Ph.D. thesis which will appear in late 2000.

DEMIRDZIC, I.; MUZAFERIJA, S. (1995), *Numerical method for coupled fluid flow, heat transfer and stress analysis using unstructured moving meshes with cells of arbitrary topology*, Comput. Methods Appl. Mech. Engrg. 125, pp.235-255

EL MOCTAR, O.M. (1999), *Numerical investigation of propeller rudder interaction*, NuTTS'99, Rome

ICCM (1999), *Comet Version 1.04 User Manual*, ICCM GmbH, Hamburg

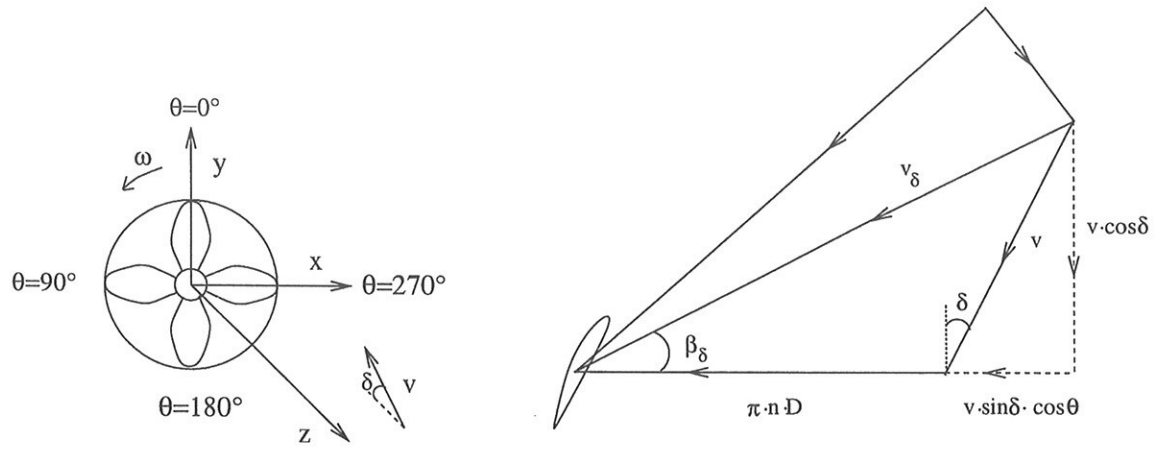

Fig.1: Velocity vectors at blade segment on right-turning propeller

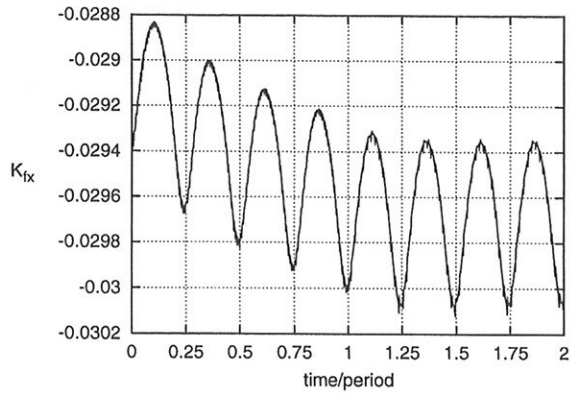

Fig.2: Convergence history of K_{fx}

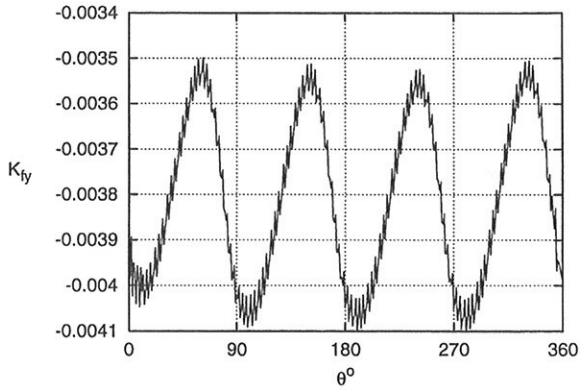

Fig.3: K_{fy} during one period

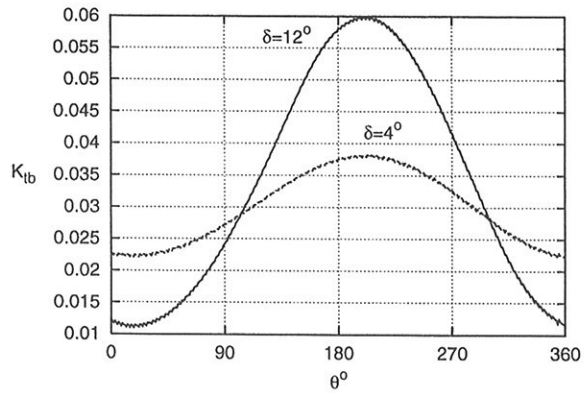

Fig.4: Thrust coefficient at one blade

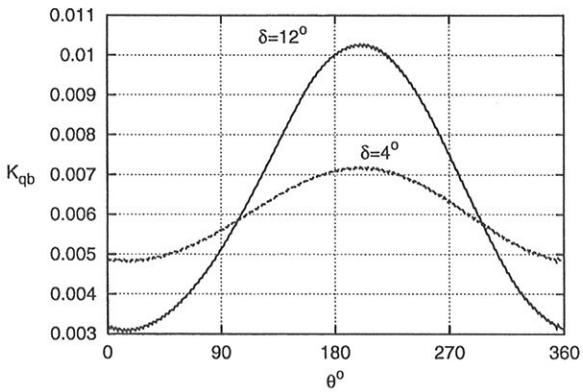

Fig.5: Torque coefficient at one blade

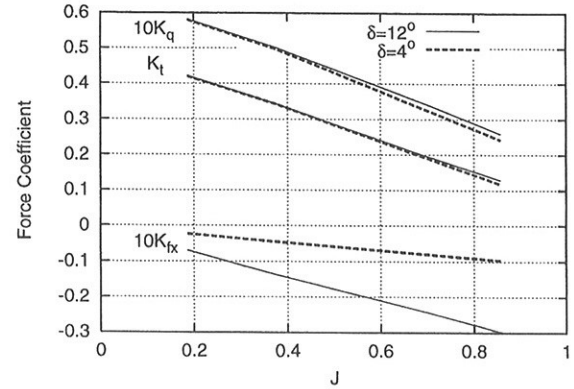

Fig.6: Propeller force coefficients

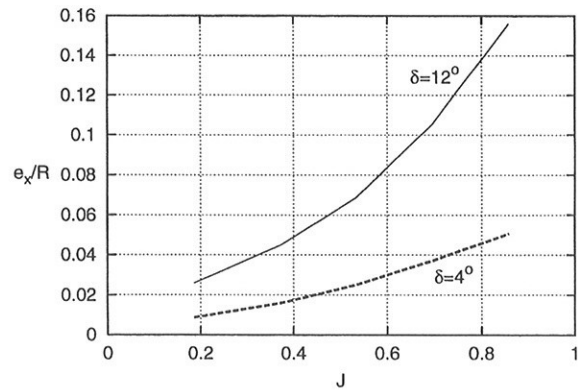

Fig.7: Shift of point of action for thrust

Extended Abstract

Predictions of flow-induced motions of floating rigid-bodies

I. Hadžić, S. Muzaferija[a], Y. Xing and P. Kaeding[b]

TU Hamburg-Harburg, AB Fluiddynamik und Schiffstheorie
Lämmersieth 90, 22305 Hamburg, Germany
[a] ICCM, Bramfelder Strasse 164, D-22 305 Hamburg, Germany
[b] Mittelstr. 16b, 22851 Norderstedt, Germany

Computational fluid dynamics in shipbuilding has been mainly used to predict flows around bodies moving with a prescribed velocity and vertical position, and the forces acting on the body do not have an influence on its motion. However, the motion of floating bodies is a direct consequence of the forces acting on it, while at the same time these forces are a function of the body movement itself. Therefore, the prediction of flow-induced body motion is a challenging task. It is relevant for many applications in ship and ocean engineering (sea-keeping, slamming, etc). In this paper a computational procedure for the prediction of motion of floating rigid bodies influenced by a viscous-flow is presented.

Mathematical Model The fluid flow is described by the Navier-Stokes equations. For the movement of control volumes, the so-called space conservation low is obeyed. In order to determine the distribution of air and water, an additional equation for the void fraction of one phase is solved. Both fluids are treated as a single effective fluid whose properties vary in space according to the volume fraction of each fluid. Motion of a rigid body is entirely described by two vector equations, namely the linear momentum equation for the mass center of the rigid body and the angular momentum equation for the rigid body. In order to solve these equations one needs to know the distribution of the pressure and the shear stress at the body surface. These are obtained as the solution of the Navier-Stokes equations.

Numerical Method Discretization of the Navier-Stokes equations is done using a finite volume method with control volumes of arbitrary shape. The pressure is predicted using the SIMPLE algorithm [3]. The interface-capturing method is used to compute flows with free-surfaces. The solution domain extends over both air and water. The influence of the surface tension is introduced into momentum equations through equivalent volume forces. In order to achieve the sharpness of the interface between water and air, the HRIC [2] (high-resolution interface capturing) scheme is used. The implicit second-order three-time-level scheme is performed for integration in time.The accuracy of the numerical procedure is of second order. Due to nonlinearity of the underlaying equations the procedure for prediction of fluid flow in one time step is iterative. For the prediction of body movements a fully-implicit predictor-corrector procedure is applied, using the iterative nature of the fluid-flow solver. Prediction of the fluid flow is done by the program **Comet** of ICCM (`www.iccm.de`) and the body movement is simulated via user-defined modifications of flow equations, grids and boundary conditions.

Simulation of Body-Movement We have employed different strategies to simulate the body movement. These possibilities come mainly from the features which are offered by the **Comet** code. The influence of the rigid-body on the fluid flow can be taken into account by either:

a) Adding the body-acceleration vector to the gravity acceleration in the Navier-Stokes equations. The acceleration is predicted according to the linear momentum equations for the center of mass of the rigid body or the angular momentum equations for the rigid body.

b) Shifting the computational-domain boundary which is common with the body surface. The surrounding grid cells are rearranged so that the grid quality is retained.

c) Moving the entire numerical grid or some parts of it. For large angles of rotation, the sliding interface between a block attached to the body and the rest of computational domain is used. If the grid is moved, spacial care needs to be taken about the computational-domain boundaries.

For complex cases it is necessary to combine some of these methods.

Results In this paper we will present results and report on experience while simulating flow-induced rigid-body motions. A number of simple test cases, with translation or rotation only, was analyzed first in order to verify the procedure and estimate the numerical accuracy. Applications of the method to more complex problems will be presented and the results obtained will be discussed. Some results with animations can be found at: `http://www.schiffbau.uni-hamburg.de/~ibro/rolls.html`.

The impact of a cylindrical shell on water was subject of an experimental investigation conducted by [1]. The cylinder, with an outer diameter of 306 mm and wall thickness 3 mm, was dropped onto the water surface from a height of 75 cm. Figure 1a shows comparison of measured and computed positions of the cylinder center as a function of time. The shape of the free surface at time $t = 0.4871$ s together with the pressure distribution is shown in Fig. 1b.

Fig. 2a shows free-surface and body position at time $t = 0.6s$ in another test case. The center of square cylinder is initially located at $y_c = 1.25D$ (D is cylinder width) below the free surface and is at rest as well as the fluid itself. The cylinder can move only in the vertical direction. After being released, due to the buoyancy force (density of the body is half of the water density), the body first moves upwards and oscillates towards the equilibrium state. Fig. 2b shows the integral vertical force F_y, velocity v_c and position y_c of the body center as a function of time. The horizontal lines indicate the equilibrium values. Until $t \approx 2$ s the strong dumping of body movement due to viscous forces and generation of waves is present and then large oscillations of body are caused by the reflection of waves from side walls of the channel. A very complex situation is generated while the body brakes the free surface moving upwards and downwards, as indicated in Fig. 2a, and in Fig. 2b by rapid change of force F_y representing the impingement of water at the body.

Fig. 3a and b show position and velocity of the center and the angle of rotation and the angular velocity of an open cylinder falling into still water. The cylinder is partially filled by water and falls at an inclination of 15 degrees to the water surface. The body has one linear and one rotational degree of freedom. Both the slamming and the sloshing occur in such a situation. An amount of water flows into cylinder, as shown in Fig. 3c, which influences floating characteristics of the body.

Fig. 4a shows trajectory of the center of a rectangular cylinder falling in water and Fig. 4b shows angular velocity of the body. The angular movement is initiated by the inclined start position (15 degrees) and the later development is mainly dominated by waves as shown in Fig. 4c. The body had all three degrees of freedom which are possible in a two-dimensional simulation.

Fig. 5a and b show comparison of free-surface waves predicted using the Euler scheme and the three-time-level scheme. Waves are generated by moving sinusoidally a flapping wall at $x = 0$. Due to large numerical diffusion the amplitude of waves predicted by the Euler scheme is substantially damped. The second-order three-time-level scheme preserves the amplitude of waves much better, at no additional computational cost and only a moderate increase in memory requirements. In Fig. 5c the position of a partially submersed square cylinder with only a rotational degree of freedom subjected to waves is shown. Fig. 5d shows the angular position of the cylinder as a function of time.

References

[1] M. Arai and T. Miyauchi. Numerical study of the impact of water on cylindrical shells, considering fluid-structure interactions. In M.W.C. Oosterveld and S.G. Tan, editors, *Practical Design of Ships and Mobile Units*. Elsevier Science B.V., 1998.

[2] S. Muzaferija and M. Perić. Computation of free-surface flows using interface-tracking and interface-capturing method. In O. Mahrenholtz and W. J. Minkowycz, editors, *Nonlinear Water Wave Interaction*, pages 59–100. Computational Mechanics Publications, 1999. Chapter 2.

[3] S. V. Patankar and D. B. Spalding. A calculation procedure for heat, mass and momentum transfer in three-dimensional parabolic flows. *Int. J. Heat and Mass Transfer*, 15:1787–1806, 1972.

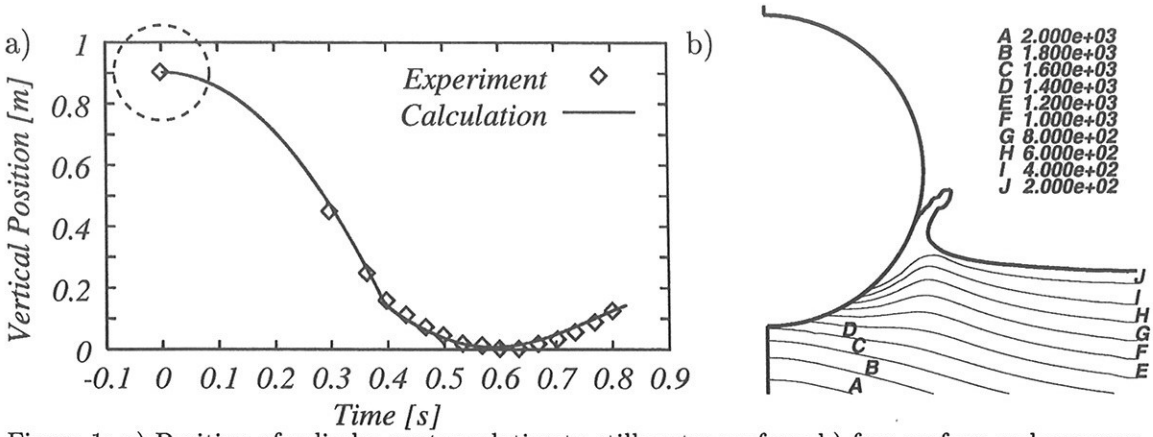

Figure 1: a) Position of cylinder center relative to still water surface; b) free surface and pressure contures at time $t = 0.4871$ s.

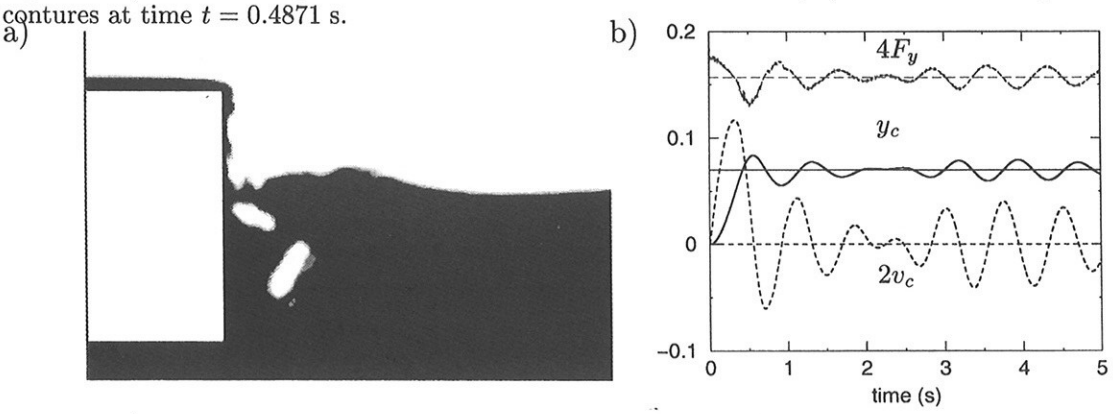

Figure 2: a) Free-surface and body position at time $t = 0.6$ s; b) Integral vertical force F_y, velocity v_c and position y_c of body center in time.

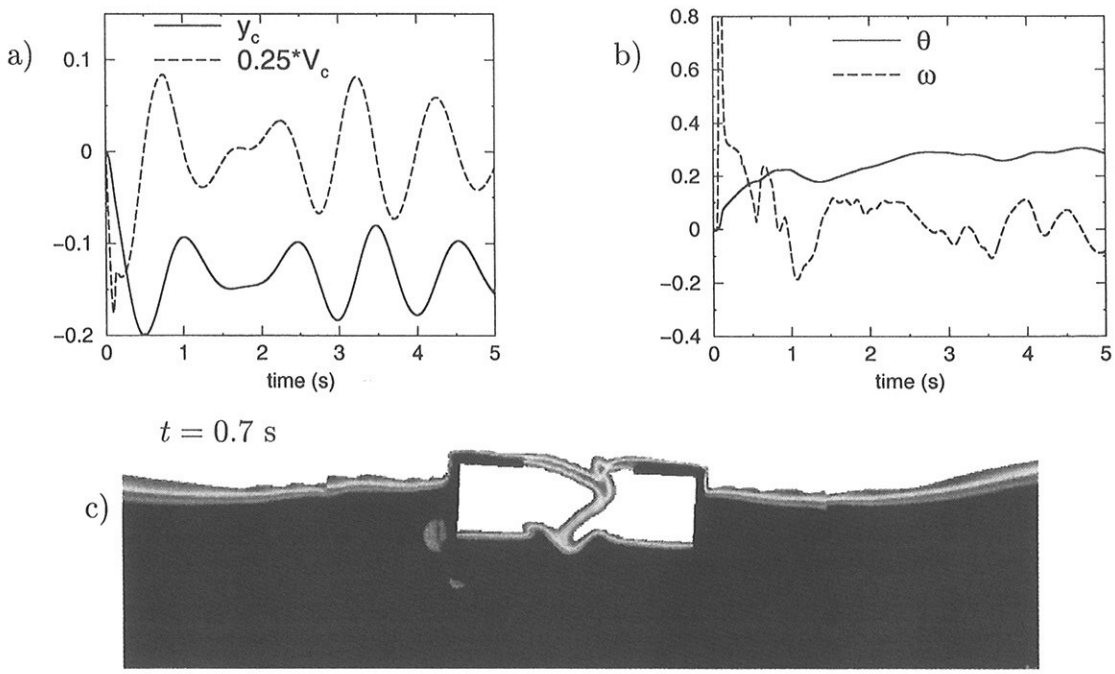

Figure 3: a) Position and velocity of body center; b) angle and the angular velocity of the body; c) Free-surface and body position at time $t = 0.7$ s.

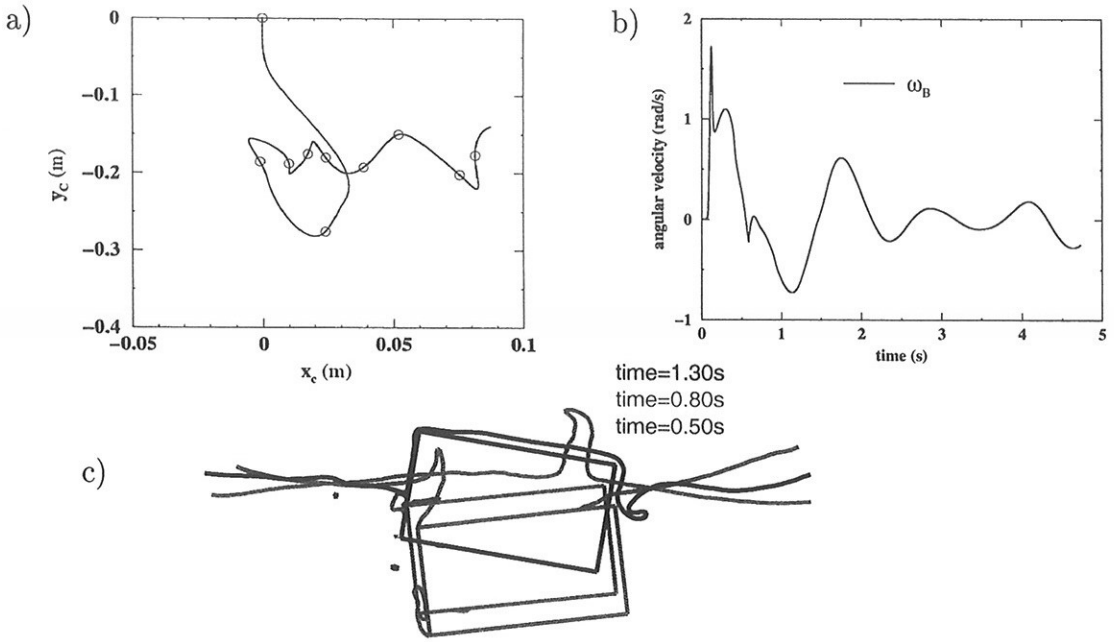

Figure 4: a) Trajectory and b) angular velocity for a falling rectangular cylinder; c) Free-surface and body position at times $t = 0.5$, 0.8 and 1.3 s. Points in a) indicate locations 0.5 s apart.

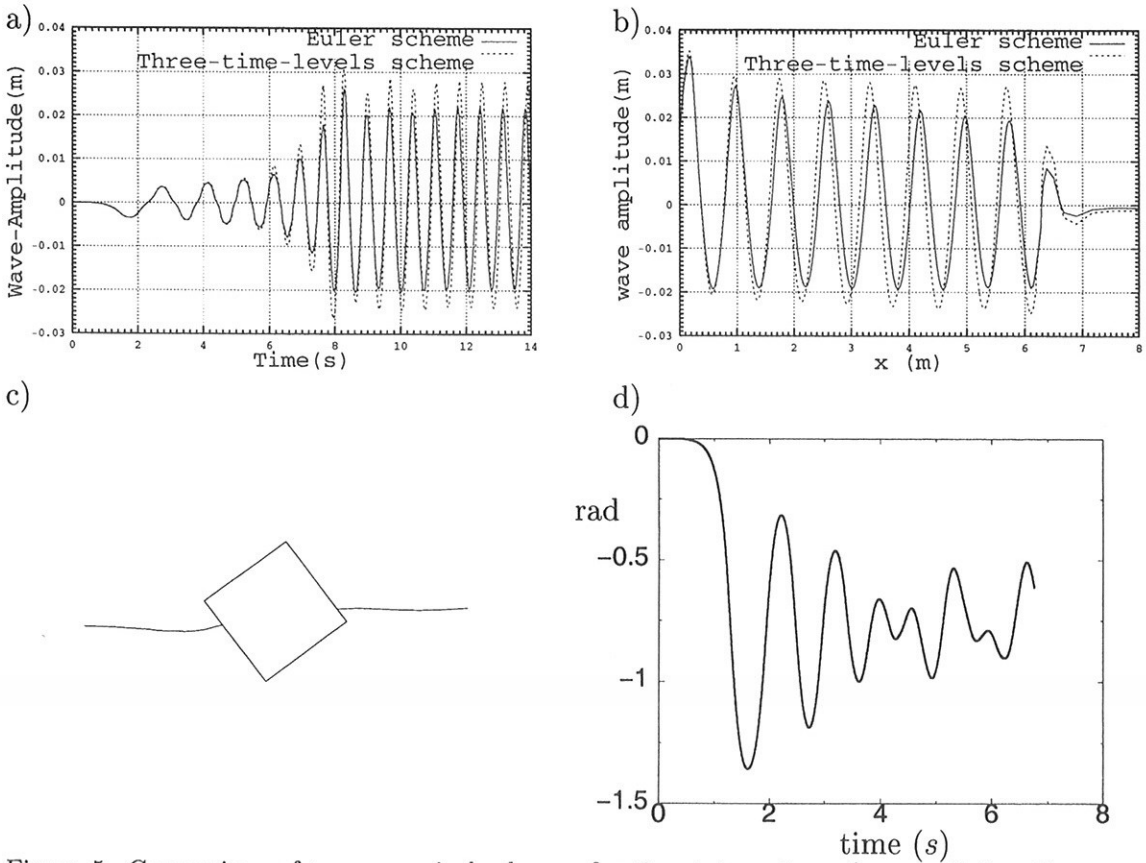

Figure 5: Comparison of two numerical schemes for time integration when predicting the wave generation: a) free-surface elevation at $x = 4$ m; b) free-surface shape at an instant of time c) Free-surface and body position at time $t = 5s$. d) Angular position of the body in time.

Free-Surface RANSE Computations Employing Parallel Computing Techniques

Dieke Hafermann, Jochen Laudan, Volker Bertram, HSVA, Hamburg, bertram@hsva.de
Samir Muzaferija, ICCM, Hamburg, samir@iccm.de

Full details on the finite-volume discretization method behind the commercial code COMET used here are given in Demirdzic and Muzaferija (1995), Muzaferija and Peric (1998). We will therefore be very brief in outlining the fundamentals of the approach.

We solve the RANSE with a k-ε RNG turbulence model. The conservation equa-tions of mass, volume concentrations and momentum are solved in time for free-surface flows. In order to solve the governing equations, the solution domain is first subdivided into an arbitrary number of control volumes (CVs) or cells. Control volumes can be of an arbitrary polyhedral shape allowing for local grid refinement, sliding grids, and blocks of grid with non-matching block interfaces. In principle, this simplifies grid generation and enables a more effective distribution of grid points by clustering them in the regions of strong variation of variables. The values of all dependent variables are stored in the center of each CV.

The governing equations are integrated over each CV. The volume and surface integrals are calculated using second-order approximations (linear interpolation, central differences, and midpoint rule integration). The method is fully implicit, i.e. the spatial integrals are evaluated at the new time level while the old values appear only in the approximations of the time derivative. The pressure-correction equation derived from the discretized continuity and momentum equations is used to determine the pressure. The resulting system of nonlinear and coupled algebraic equations is solved iteratively in a sequential manner. The linearized equations are solved using solvers from the family of conjugate-gradient methods. Iterations are repeated within each time step until the nonlinear equations are satisfied within acceptable tolerances. The momentum and continuity equations were approximated by a central differencing scheme, the turbulence equations by a upwind differencing scheme.

The discretization of the convective part of the volume fraction conservation equation needs special attention. Ideally, its discretization should neither produce numerical diffusion nor unbounded values of the volume fraction, i.e. the value of the volume fraction in each cell should lie between the minimum and maximum value of the neighbor cells. The demand for a scheme to be bounded implies that the computed fluxes of volume fraction do not underflow or overflow the cells. The HRIC scheme employed here satisfies these conditions, Muzaferija and Peric (1998).

Starting from an IGES description of the KRISO container ship (KCS), www.iihr.uiowa.edu/gothenburg2000/KCS/container.html, a computational grid was generated with the standard grid generation software ICEM-CFD. The grid consisted of several blocks. Initial grids with non-matching grid boundaries did not yield plausible results and the reasons for this behavior are not yet understood as other test cases with non-matching boundaries did not exhibit similar problems. A block-structured grid with matching boundaries performed much better and the results for this grid are shown here. The grid had 446613 cells. The cylindrical grid had a radius of 1.5 L_{pp} and extended 1 L_{pp} ahead of FP and 2 L_{pp} behind AP. The region above the calm waterline was discretized up to 0.065 L_{pp}. The innermost cells were such that $20 < y^+ < 170$. The grid was split into 3 blocks, Fig.1. One block covered the forward part of the domain, one block the aft part below the free surface, and the last block the aft part with fine resolution of the free surface. The grid on the hull was designed to resolve areas with high gradients in flow quantities finer, Fig.2.

The computations were performed for model Reynolds number $R_n=1.59\cdot10^7$ and Froude number $F_n = 0.26$ only for the condition without operating propeller. Note that the experiments were performed at $R_n=1.4\cdot10^7$, i.e. the viscosity in the computations was higher.

At the upstream inlet, we set uniform velocity of model speed both above and below the calm waterline. The turbulence intensity of the water was set at 3% at the inlet. The characteristic length was set at 0.4 m. The upper boundary and the center-plane were defined as planes of symmetry. On the ship hull, we enforced the no-slip condition. The k-ε RNG turbulence model employed a wall function. The time step interval was set at 0.01s. Within each time step, 10 iterations to reduce the residuals were performed.

The convergence criterion was based on pressure and frictional resistance. Fig.3 shows the convergence history for the finest grid. The average of the oscillatory forces was taken. While the

The total resistance ($C_T = 3.89\ 10^{-3}$) was 9% higher than measured ($C_T = 3.56\ 10^{-3}$). The frictional resistance is 12% lower than the C_{F0} according to ITTC. As C_{F0} contains already some form factor, the frictional resistance is plausible and the error is due the pressure resistance. We suspect that skewed cells in the aftbody are responsible to high numerical diffusion which must have affected the pressures in this region. To some extent the higher viscosity will increase this tendency, but the main source of error should be the grid.

The wetted surface was computed by summing the area of the cell faces on the hull multiplied with the fraction of water in the cells. This wetted surface was S/L^2=0.185, 4% larger than the wetted surface measured in the experiments. The wave profile over a major part of the hull agrees rather well with experiments, Fig.4. The kink in the profile behind the transom stern is due to matching the wave on the center line to the one on the hull from two different curves. The bow wave is not captured completely and this error propagates further out becoming even more apparent at the wave cut y/L = 0.1509, Fig.5. The stern wave is even more underpredicted and this explains largely the error of 9% in resistance prediction.

Further away from the hull, at the wave cut y/L = 0.1509, the problems with numerical dissipation become apparent. The computed waves follow reasonably well the main minima and maxima, but underpredict the wave amplitudes especially downstream behind the stern, Fig.5. The waves created at the ship hull are quickly dissipated further away from the ship. This prevents the optical impression of a typical Kelvin wave pattern observed in inviscid panel codes or experiments. The pressure distribution in the aftbody is largely plausible, but shows kinks in the part where the large flare in the stern appears, Fig.6. These are attributed to the grid which shows skews and jumps in size at this part of the hull.

The computations were performed on a PC cluster under Linux. We used a new parallel computer architecture at HSVA, namely 8 Pentium III processors and one master PC to coordinate the cluster. The cluster configuration follows the principle of the "Beowulf clusters" (www.beowulf.org). The cluster nodes communicate via the parallel communication system MPI. For each time step, the computations required approximately 40s giving total computational times of approximately 60 CPU hours. Looking at the convergence history, a shorter time of 40 CPU hours would probably have sufficed for practical purposes.

We intend to repeat computations with less time pressure to investigate how grid smoothing and various blending schemes in the finite difference operators will affect the results. We believe that a significant part in the errors was due to our handling of the code and thus not inherent in the approach.

Laudan, J.; Gatchell, S.; Bertram, V.; Muzaferija, S.; Peric, M. (2000), *Free-surface computations for the KCS containership*,Gothenburg'2000 Workshop

Demirdzic, I.; Muzaferija, S. (1995), *Numerical method for coupled fluid flow, heat transfer and stress analysis using unstructured moving meshes with cells of arbitrary topology*, Comput. Methods Appl. Mech. Engrg. 125, pp.235-255

Muzaferija, S.; Peric, M. (1998), *Computation of free surface flows using interface-tracking and interface-capturing methods*, Nonlinear Water Wave Interaction, Computational Mechanics Publications, Southampton, pp.59-100

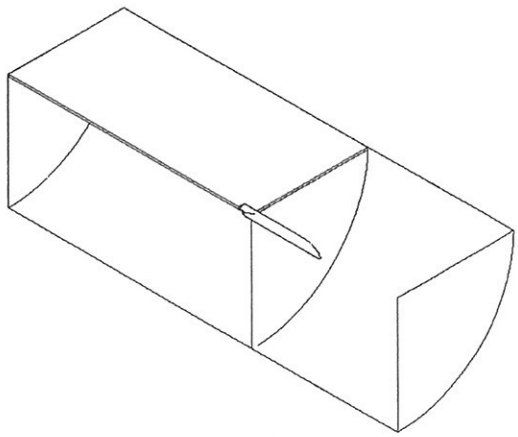

Fig.1: Grid structured into 3 blocks

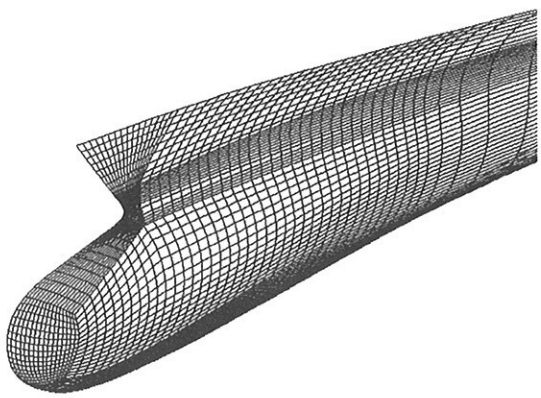

Fig.2: Detail of grid at bow

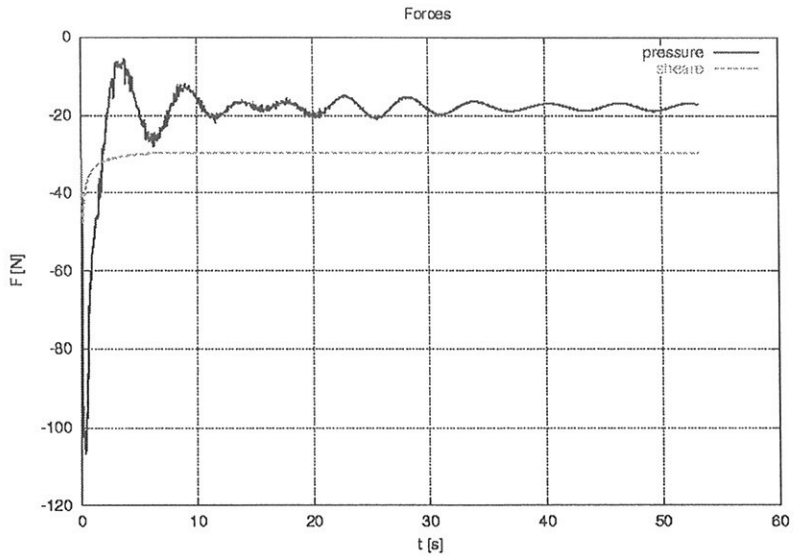

Fig.3: Convergence of resistance; resistance values averaged over oscillations

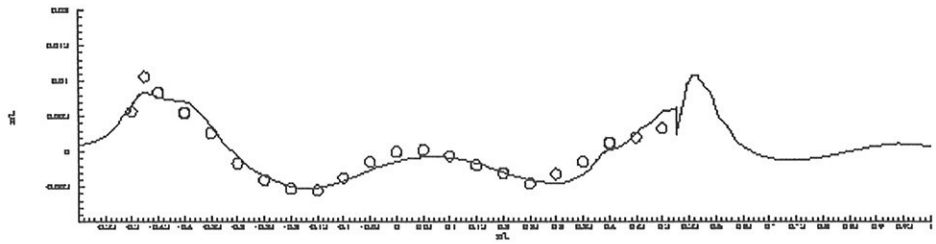

Fig.4: Wave profile on hull, ahead and behind transom

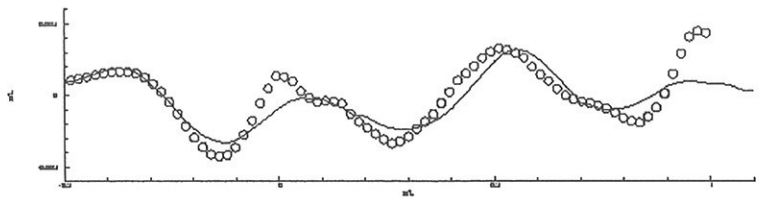

Fig.5: Wave cut a y/L = 0.1509

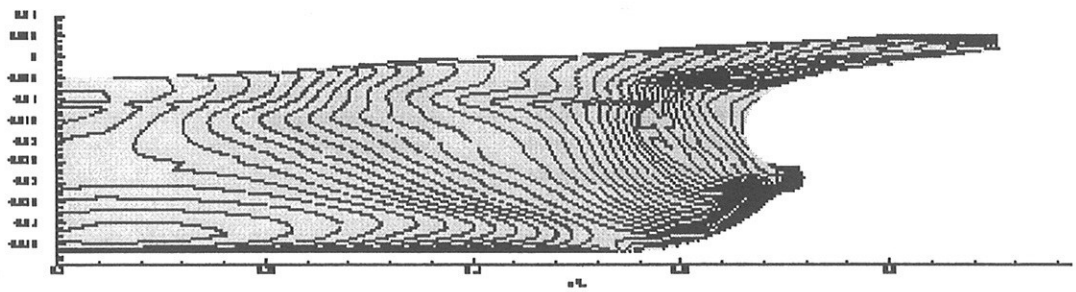

Fig.6: Hull pressure contour lines, $\Delta C_P = 0.01$

Application of Wave Pattern Analysis in a CFD Based Hull Design Process

Justus Heimann, TU Berlin, *heimann@ism.tu-berlin.de*

Wave pattern analysis in the sense of system identification can be a powerful tool in CFD based minimization of calm water wave resistance and wave-wash of ship hulls. An indication will be given here. Currently the implementation of an optimization scheme utilizing wave pattern analysis is in progress. Details of the scheme will be presented on some other occasion. The present results and conclusions are in consonance with the closely related investigations carried out within the scope of the European project CALYPSO at the Berlin model basin VWS, Nowacki et al. (1999).

In addition to the usual integral wave or residuary resistance values, e.g. from hull pressure integration or the k-factor method, wave pattern analysis yields distinct information of the ship wave system in terms of wave spectra. These can be utilized in ship hull form optimization allowing a minimization of transverse and diverging waves separately and a correlation between cause and effect of local hull variations and wave pattern changes. As an additional benefit, computed wave patterns and hence wave pattern analysis prove to be less sensitive to flow field discretization than pressure integration. This is a tentative result of detailed studies concerning that topic, e.g. by Raven and Prins (1998) or Janson (1997).

To illustrate the potentials of the method, wave pattern analysis has been applied to experimental and numerical wave cuts of two variations of a ferry hull [1] (indicated by Hull A and B). Both hull variants are of twin screw type and fitted with a skeg. They mainly differ in the forebody and afterbody. Hull B is elongated compared to Hull A. Hull A is designed with a wedge shaped transom, whereas Hull B is fitted with a wide and flat transom (see Fig. 1).

Numerical wave patterns (Fig. 2) have been computed at TU Berlin with the aid of the nonlinear free surface Rankine panel code SHIPFLOW (Vers. 2.6, customized by C.-E. Janson, FLOWTECH Int. AB, Göteborg). During all calculations the free surface panelization extended $0.5\,L_{PP}$ upstream, $4.0\,L_{PP}$ downstream of the fore perpendicular and $1.6\,L_{PP}$ to the side, considering the Kelvin angle. Laterally from the hull a minimum of $30\,panels/wavelength$ were placed in the longitudinal direction. In total, close to 10 000 panels were employed with 80% covering the free surface. All computations were performed with the same free surface panelization, but slightly different hull panelizations for Hull A and B.

Wave Pattern Analysis

Wave pattern analysis methods yield the wave pattern resistance based on conservation of momentum in a control volume around the hull. Essential assumptions are an unbounded ideal fluid and the existence of "free waves" with increasing distance from the disturbance. Though the calculation of the ship wave system by SHIPFLOW is fully nonlinear, the wave pattern analysis itself is based upon linear theory assuming only a weak effect of nonlinear contributions in the spectral analysis.

Here the longitudinal wave cut method following Sharma (1966) has been implemented. In case of a symmetrical ship wave system, a single infinitely long wave cut parallel to the ship's advance direction is ideally required. However, because of limited computer resources (CFD) and restrictions due to tank wall reflections (EFD) the wave cut has to be truncated at some distance aft. In order to retain the signal of the transverse waves downstream of the truncation point, a truncation correction based on an analytical asymptotic extension of the cut, as suggested by Sharma, is applied here.

A right-handed system is considered. The origin is fixed at the fore perpendicular in the undisturbed free surface, x pointing downstream and z pointing up. Note: During the analysis all vectors and wavenumbers are nondimensonalized by the basic wavenumber $k_0 = g/V^2$. Thus: $\hat{x} = x\,k_0$ *etc.*, $s = \sec(\theta) = w/k_0$ $(s \in [1, \infty))$ for the longitudinal and $u = s\sqrt{s^2 - 1}$ $(u \in [0, \infty))$ for the transverse wavenumber. A stationary ship wave system is assumed, composed by a superposition of planar linear waves of different component wave directions θ $(\theta \in [0, \pi/2))$, complying with the steadiness condition for the phase velocity $c_W(\theta) = V\cos(\theta)$. From conservation of momentum the wave pattern resistance, in a notation following Havelock, is given by

$$R_{WP} = \frac{\rho V^2}{{k_0}^2}\,\pi \int_0^{\pi/2} \left[A_S(\theta)^2 + A_C(\theta)^2\right] \cos^3(\theta)\, d\theta \qquad (1)$$

[1] The hull shapes and experimental data were kindly made available by Meyer Werft internally within the scope of the CALYPSO project. (The Meyer Werft ship results include model test data obtained in the MARIN model basin).

and the wave pattern resistance coefficient is defined as (S_{Ref}: wetted hull surface area at rest)

$$C_{WP} = \frac{R_{WP}}{0.5\,\rho\,S_{Ref}\,V^2} \quad \text{or} \quad C_{WP}(\theta) = \frac{\pi}{0.5\,S_{Ref}\,{k_0}^2}\,\left[A_S(\theta)^2 + A_C(\theta)^2\right]\cos^3(\theta)\,. \tag{2}$$

A_S and A_C in (1) and (2) are called the free wave spectra

$$A_S(\theta) = \frac{s}{\pi}\,\left[S^*(s,\hat{y})\cos(u\hat{y}) + C^*(s,\hat{y})\sin(u\hat{y})\right], \quad A_C(\theta) = \frac{s}{\pi}\,\left[S^*(s,\hat{y})\sin(u\hat{y}) - C^*(s,\hat{y})\cos(u\hat{y})\right] \tag{3}$$

and S^* and C^* denote weighted Fourier transforms

$$S^*(s,\hat{y}) = \int_{-\infty}^{\infty} \sqrt{s^2-1}\;\hat{\eta}(\hat{x},\hat{y})\;\sin(s\hat{x})\,d\hat{x}, \quad C^*(s,\hat{y}) = \int_{-\infty}^{\infty} \sqrt{s^2-1}\;\hat{\eta}(\hat{x},\hat{y})\;\cos(s\hat{x})\,d\hat{x}\,, \tag{4}$$

with $\sqrt{s^2-1}$ being the "weight" and $\hat{\eta}(\hat{x},\hat{y})$ the wave signal at ($\hat{y}=const.$). Special assumptions are needed in order to account for the signal of the transverse waves beyond the truncation point $\hat{x}_e$. Sharma suggests the following approach to analytically extending the wave cut infinitely downstream

$$\hat{\eta}(\hat{x},\hat{y})|_{\hat{x}_{e+}} \simeq \frac{c_1\cos(\hat{x}) - c_2\sin(\hat{x})}{\sqrt{c_3+\hat{x}}} \quad \text{for } \hat{x}\to\infty\,, \tag{5}$$

where the coefficients $c_{1,2,3}$ are determined by fitting (5) to the tail end of the wave cut signal up to $\hat{x}_e$. The contribution of the integration $\hat{x}_e \le \hat{x} < \infty$ then can be derived by evaluation of (4) with the wave signal replaced by (5) and the integration bounds adapted accordingly. Because of the strong asymptotic decay of the wave elevation for $\hat{x}\to-\infty$, according to Sharma, practically no correction is needed to account for the truncation of the wave cut upstream.

The application of longitudinal wave cut analysis mainly depends 1. on the lateral distance of the cut, 2. on the utilizable length of the signal until truncation and 3. on the speed of the ship or wavenumber. The first two influences are in opposite direction. In order to fulfill the requirement of a free wave system, the cut has to be far enough aside of the ship to be virtually free of local wave effects. On the other hand, the greater the lateral distance, the shorter is the utilizable signal before truncation due to the effects of tank wall reflections. From a practical point of view, the lateral distance of the cut should be as small as possible in order to retain as much information as possible of the wave signal. But, still a minimum lateral distance of the wave cut has to be maintained. Tests indicate that stable analysis results are to be expected already at a minimum distance of $y/L_{PP}\approx 0.2$, provided that the cut extends far enough downstream (several times the basic wavelength). This is in agreement with similar investigations, e.g. Lalli et al. (1998).

Results

In Fig. 4 measured (MARIN) and computed (SHIPFLOW) longitudinal wave cuts at $y/L_{PP} = 0.1814$ are compared for both hull variants and different Froude numbers. A close correlation between measured and computed wave cuts beside the hulls ($0 \le x/L_{PP} \le 1.5$) can be noted. In the downstream region ($x/L_{PP} > 1.5$), the computed wave amplitudes are too large when compared to the measurements. Because of the absence of viscous damping the stern waves are overestimated here within the computations, which is typical for Rankine panel methods. This effect is amplified with increasing F_n. In addition a phase shift of the calculated waves towards increasing wavelengths can be noticed. This defect appears to be more present with decreasing F_n and in case of Hull B. The latter might be explained by a deviation of trim and sinkage between experiments and computations, which was present only in the case of Hull B. That again might be caused by the large transom of Hull B compared to A or perhaps by a different realization of the trials in the experiments and computations.

The wave cuts presented in Fig. 4 have been analyzed by means of wave pattern analysis. A proper analysis requires a "clean" wave cut free of reflections as they originate from tank walls in experiments. Such undesired interactions are present in the measured wave cuts at $x/L_{PP} > 3.0$ and for lower F_n. For that reason, wave signals have been considered consistently in the analysis only up to an estimated truncation point of x/L_{PP}: ≤ 3.9 ($F_n = 0.36$), ≤ 3.5 ($F_n = 0.331$) and ≤ 2.9 ($F_n = 0.303$).

In Fig. 5 the spectral results of the wave pattern analysis are presented in terms of wave pattern resistance coefficients $C_{WP}(\theta)$. The trends (humps and hollows) of $C_{WP}(\theta)$ reveal a good overall correlation between experiments and computations, especially at higher F_n and for Hull A. The amplitudes of $C_{WP}(\theta)$ appear to be greater in case of the computations than for the experiments, particularly in the range of the transverse

waves ($\theta < 35°16'$). Notably, there is a phase shift in the computational results for Hull B towards smaller wave angles θ. That again corresponds to greater wavelengths of the transverse waves. Obviously, the trends, already seen in the wave cuts for the experiments and the computations, as mentioned above, are reconfirmed here within the analysis results. And, it should be noted that more or less the whole wave pattern range is characteristically affected by the differences in the hull shapes at the forebody and afterbody, both in the computations and in the experiments.

Furthermore, the comparison of integral resistance coefficients in Fig. 3 indicates, that wave pattern analysis applied to numerical wave pattern (SHIPFLOW) is an appropriate tool on practical grounds because its results correlate well enough with both experiments and CFD pressure integration when comparing different major hull form variants. The wave spectral information may be more indicative of cause and effect in hull form changes than are pressure integrals. The results of CFD wave spectra analysis may not be so precise physically as measurements or certain local calculations, but are still a valid guidance in design comparisons in the spirit of system identification of characteristic traits of a hull form and F_n effects. This seems to be true especially for $F_n \geq 0.3$. However, it is a well known, but still remarkable fact that the wave pattern resistance always is less than the residuary and wave resistance.

References

JANSON, C.-E.: *Potential Flow Panel Methods for the Calculation of Free-surface Flows with Lift*, Ph.D. Thesis, School of Mechanical and Vehicular Engineering, Chalmers University of Technology, Göteborg, 1997.

LALLI, F.; FELICE, F.Di.; ESPOSITO, P.; MORICONI, A.: *Some Remarks on the Accuracy of Wave Resistance Determination from Wave Measurements Along a Parallel Cut*, 22^{nd} Symp. on Naval Hydrodynamics, ONR, Washington D.C., 1998.

NOWACKI, H.; HARRIES, S.; SCHULZE, D.; STINZING, H.-D.: *Verification of Wave Cut Design Methodology*, Brite EuRam III Project CALYPSO, "Computational Fluid Dynamics in the Ship Design Process", Deliverable 1.8, TU Berlin, 1999.

RAVEN, H.C.; PRINS, H.J.: *Wave Pattern Analysis Applied to Nonlinear Ship Wave Calculations*, 13^{th} Workshop on Water Waves and Floating Bodies, Alphen a/d Rijn, 1998.

SHARMA, S.D.: *An Attempted Application of Wave Analysis Techniques to Achieve Bow-Wave Reduction*, 6^{th} Symp. on Naval Hydrodynamics, ONR/ACR-136, Washington D.C., 1966.

Hull:	A	B
λ	19.5	
L_{PP}	130 m	
T_F, T_A	5.9 m	
L_{OS}	139.5 m	144.5 m

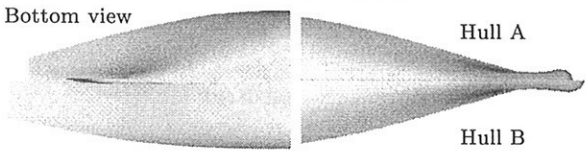

Fig. 1: Hull parameters and hull renderings.

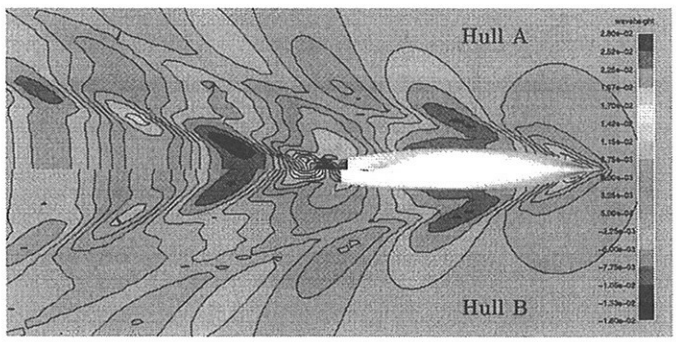

Fig. 2: Nonlinear wave pattern by SHIPFLOW, $F_n = 0.36$.

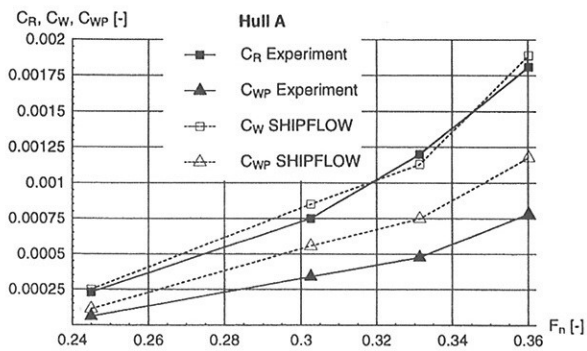

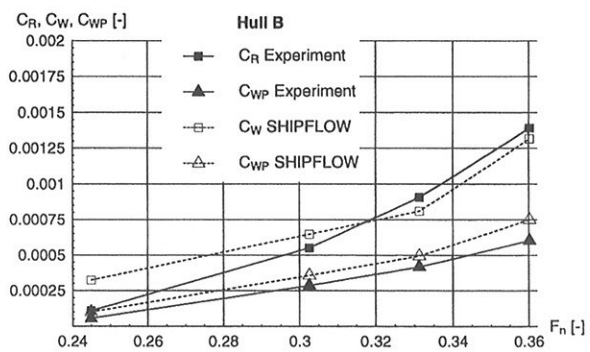

Fig. 3: Resistance coefficients against F_n (Hull A left). The residuary resistance (C_R) is calculated by the k-factor method with the following k-factors given by MARIN: $k = 0.244$ (Hull A) and $k = 0.215$ (Hull B).

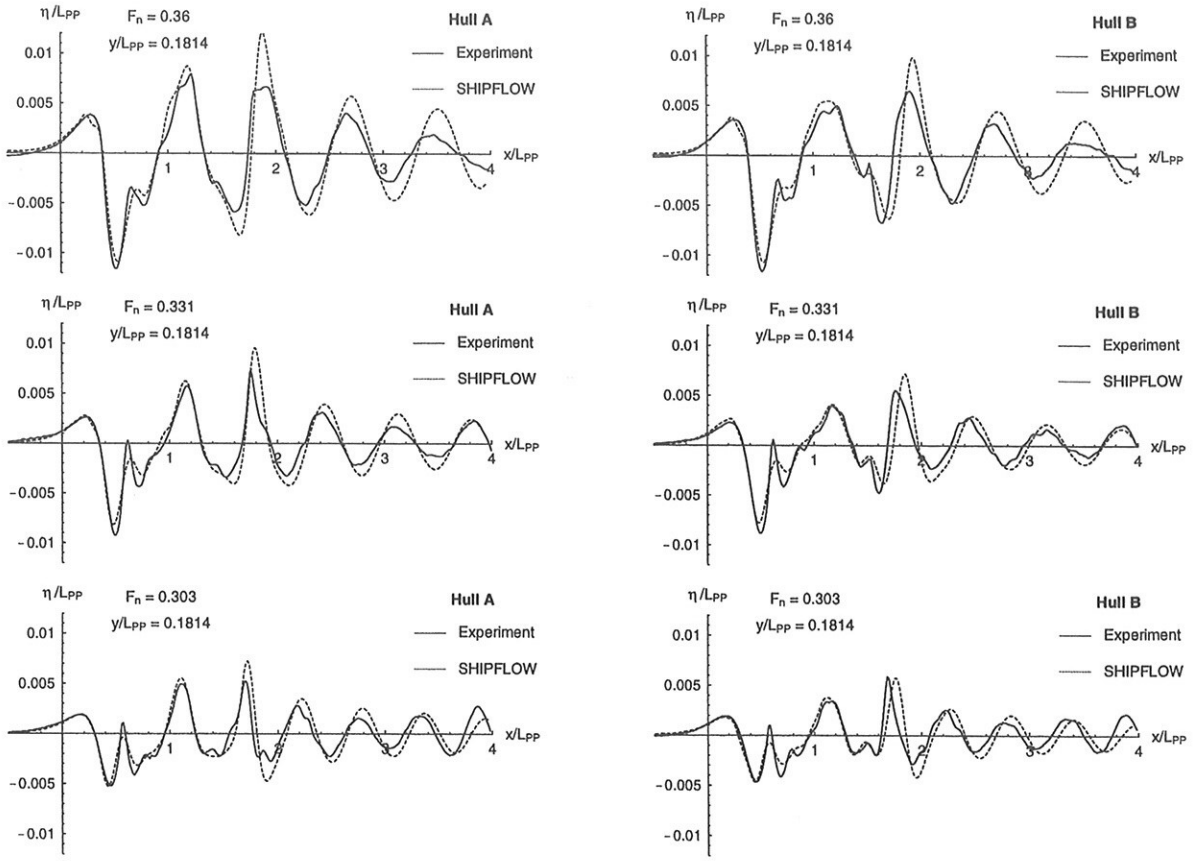

Fig. 4: Longitudinal wave cuts at $y/L_{PP}=0.1814$, fore perpendicular at $x/L_{PP}=0$. (Hull A left).

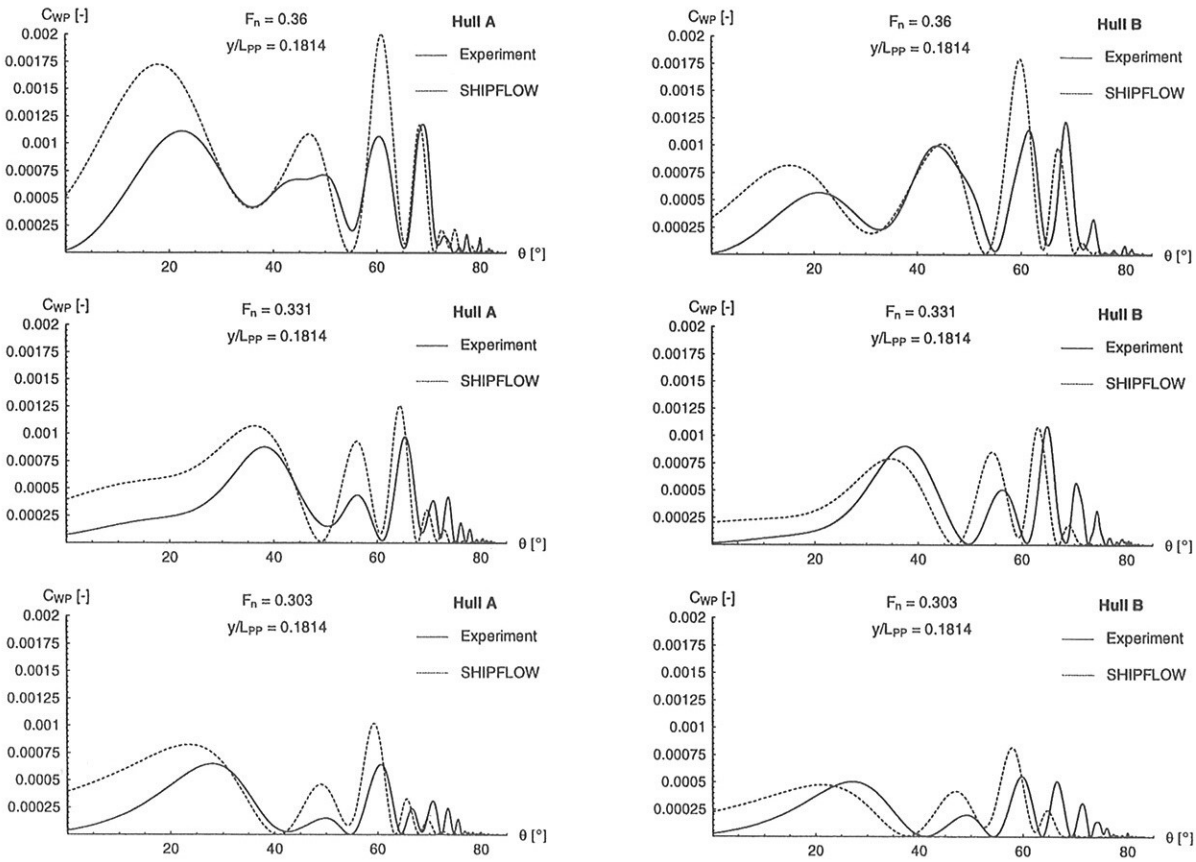

Fig. 5: Wave pattern resistance coefficients $C_{WP}(\theta)$ against component wave direction θ (Hull A left).

Flow around a ship section, heave and sway motion. Numerical and experimental results.

Håvard Holm[*] Aslaug Stakkestad[†] and Bjørnar Pettersen[‡]
Department of Marine Hydrodynamics
Norwegian University of Science and Technology (NTNU), N-7491 Trondheim, Norway

Abstract

Flow around a rectangular section moving in heave and sway is calculated by a Navier-Stokes code and compared to experimental results. Governing equations describing viscous flows are discretised by a finite volume method and the method of artificial compressibility is used to step time. The resulting equations are solved using an approximate Newton relaxation approach and development of the free surface is ensured by a moving grid technique. In the experiments, a particle Image Velocimetry (PIV) technique is used to capture details in the flowfield close to the corners of the section and close to the free surface.

Introduction

In recent years, CFD has become a useful design tool in several marine application areas. The increase in computer capacity has made it possible to model more complex physical problems, i.e. nonlinear free surface elevation and viscous flow around a moving ship. Calculation of viscous flow is interesting because it may give insight in the physics of flow problems. This insight is valuable in a design process since the shape of the body will affect the flowfield and the forces acting on the body.

Detailed measurements of the flow field is important when evaluating results from numerical simulation programs. Especially for complex flow situations, experiments and numerical simulations go hand in hand in verifying and validating results and methods. Recording the flow field by using a camera results in a large amount of data at every time instant. Several methods exist for analyzing images to extract velocity fields from the recorded pictures. Common to them all is that tracer particles are introduced to follow the flow and by that giving enough information.

The goal of this work is to study how viscous flow effects interact with the free surface when a 2D section is given heave and sway motion.

Navier-Stokes solver

Governing equations

The governing equations are the two-dimensional time dependent incompressible Navier-Stokes equations. Laminar flow and constant viscosity are assumed. p, u and v denotes the pressure and Cartesian velocity components respectively and $\dot{r}$ represents the velocity of the boundary.

In integral form the Navier-Stokes equations can be expressed as :

$$\frac{d}{dt}\int_{\Omega} U' dV + \int_{\partial\Omega} (F - U'\dot{r})\,\vec{n} ds = 0 \qquad (1)$$

where F is the flux vector, and we define

$$U = \begin{bmatrix} p \\ u \\ v \end{bmatrix}, U' = \begin{bmatrix} 1 \\ u \\ v \end{bmatrix} \qquad (2)$$

p is the modified pressure, defined by

$$p = p^* + \frac{y}{F_r^2} \qquad (3)$$

where p^* is the original pressure and F_r is the Froude number $\frac{\bar{U}}{\sqrt{g\bar{L}}}$. $\bar{U}$ and $\bar{L}$ is characteristic velocity and length respectively.

Boundary conditions

Boundary condition on the ship section is imposed as no slip condition. In the far field the flow is supposed to be calm, therefore the velocities and the pressure are set to be zero. At the free surface we have two boundary conditions: the kinematic and the dynamic condition. The kinematic condition states that a particle on the free surface will remain on the free surface.

[*]haavard.holm@marin.ntnu.no
[†]aslsta@marin.ntnu.no
[‡]bjornar@marin.ntnu.no

The dynamic boundary condition states that the stress tensor should be continuous over the free surface. Surface tension and viscous effects at the free surface are neglected, which results in zero stress tensor. Due to the zero tangential stress condition, the velocity boundary condition is zero gradient extrapolation. The zero normal stress condition lead to the Dirichlet condition for pressure on the free surface : $p = p_a + h/F_r^2$, where p_a is the atmospheric pressure and h is the wave height.

Spatial discretisation and time integration

A finite volume method is used to discretize the domain. The spatial discretization is divided into a viscous part and an inviscous part. F_{vis} is calculated using a central differencing scheme and F_{inv} is calculated using Roe's upwind scheme with second-order differencing. A fully implicit time integrating scheme is used. The scheme can be rewied in Holm and Pettersen [1].

Evolution of the free surface

To step the free surface in time, the kinematic boundary condition is used. Traditionally the boundary condition is rewritten to $\frac{\partial h}{\partial t} = v - u\frac{\partial h}{\partial x}$. For a cell centered discretisation v and u are usually taken as the average of the cells on the left and right hand side closest to the free surface. $\frac{\partial h}{\partial x}$ is usually calculated using a higher order upwind scheme.

The method has been used with success for a wide range of applications.

Experimental measurements with Particle Image Velocimetry (PIV)

When using PIV to study the two-dimensional flow, small seeding glass particles (nearly neutral buoyant), with average particle diameter of $d_{pi} = 41.6\mu m$, are added to the fluid. The fluid is illuminated by a thin, pulsating laser sheet. The puls separation is δt_p. Every fluid particle will move a certain distance, Δs_i, during a given time interval, Δt. See figure 1. The principle of PIV is to measure this distance, Δs_i. The local fluid velocity vector, U_i, is then calculated from $U_i = \Delta s_i / \Delta t$.

Δt is equal to the time between each laser light pulse, δt_p. It is assumed that the particles follow the flow, and that the velocity of the particles is equal to the velocity of the fluid.

A camera is used to capture images of the flow with the illuminated particles. The camera records the position of each particle at each light pulse. At least two pulses (or particle positions) must be recorded on each image. In the present experiments the time between each light puls was set to 12ms and the camera shutter speed was set to 1/15s (66ms). This means that every

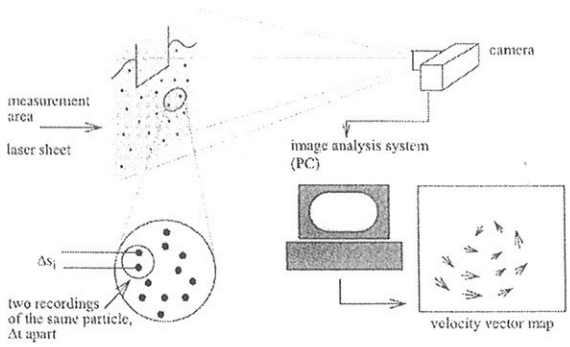

Figure 1: Schematic description of the PIV system.

particle will be given at least 5 light pulses and will be recorded at least 5 times in one image. This mode of recording images is called autocorrelation mode.

A computer program is used to analyze the images and give as a result the velocity vectors [2].

Experimental setup

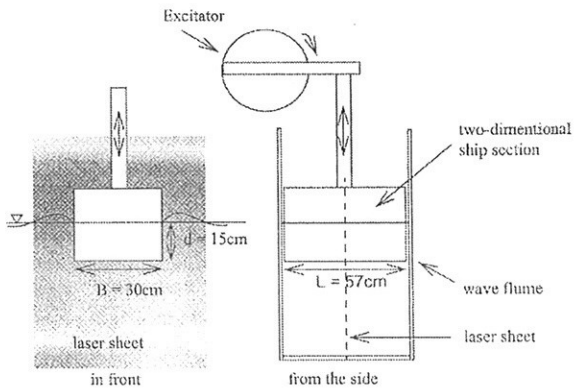

Figure 2: Heave excitation of ship section

Figure 2 shows the model of the rectangular ship cross section and how it is forced into heave motion [3]. The dimensions of the section are shown in the figure. The experiments were conducted in a research wave flume special built for visualization and detailed measurements. The bottom and side walls are all of glass.
For sway motion, the same setup was used, turned 90° with small modifications.

Computer analysis of images

Figure 3(a) shows an image where every particle is recorded 5-6 times with 12ms interval. To find the fluid velocities, U(x,z), from this image, the particle displacement, $\Delta s(x, z)$, has to be found first. The image is divided into small parts called interrogation areas (IA), see figure 3(b). It is assumed that the velocity is constant within each IA. Δs is then found by computing the statistical most probable Δs in each IA, using

the autocorrelation function principles.

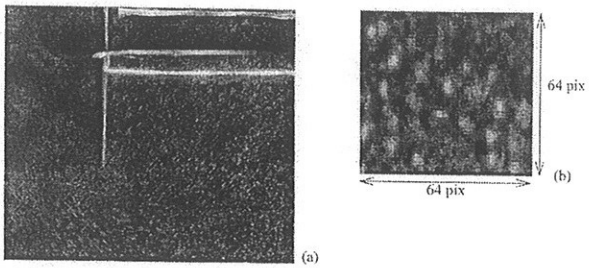

Figure 3: (a): Image recorded with autocorrelation mode. The shutter speed is 1/15s (66ms) and the laser scan period is 12ms, allowing 5-6 positions of each particle to be recorded on the image. (b): Example of interrogation area (IA).

Errors in PIV

The errors involved in these PIV measurements can be divided into three main parts. First, errors due to the physics of the measurement principle. We assume that the particles follow the flow and that the velocity within each IA is constant. This is not true if the velocity gradient is high within an IA. We have to consider this when choosing size of the IA. Second, recording errors. The results from the image analyzing process is highly dependent on the quality of the image. These errors are due to the laser light system, camera and lense. Third, analysis errors. These errors include: digitalization/calibration errors, errors related to the autocorrelation and to the autocorrelation peak finding process.

Ship section in heave

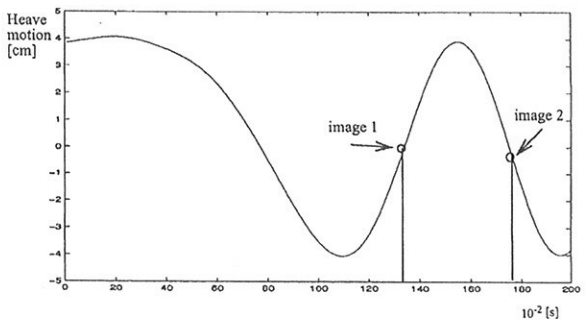

Figure 4: Numbering of nodes and cells

Figure 4 shows the measured heave motion for the section. The figure also show at which points in the oscillation the images presented here are taken. The oscillation amplitude is set to 4cm. The oscillation period is 0.8 sec. An upstart period of 2 sec, is also numerically simulated. (Startup is a separate issue).

Several images were recorded at the same time instant in the oscillation period (see figure 4) in separate runs to assure that the repeatability was good.

Figure 5 and 6 shows two images recorded with autocorrelation mode. Figure 7 and 8 shows the computer analysis of the two images respectively, and figure 9 and 10 show the numerical calculations. In image 1 (figure 5,7 and 9) the section is on its way up. The velocities in the measurement area are relatively high. The fluid is sucked under the bottom of the section, and a strong vortex is generated. This is clearly shown in the numerical calculations. In image 2 (figure 6, 8 and 10) the section is on its way down, and a relatively large vortex has been formed at the side of the section.

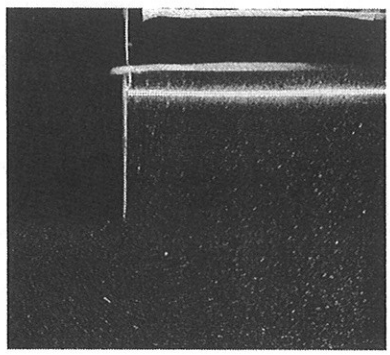

Figure 5: Picture 1

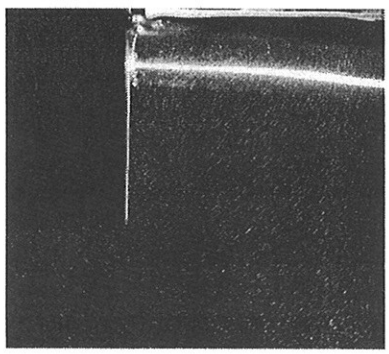

Figure 6: Picture 2

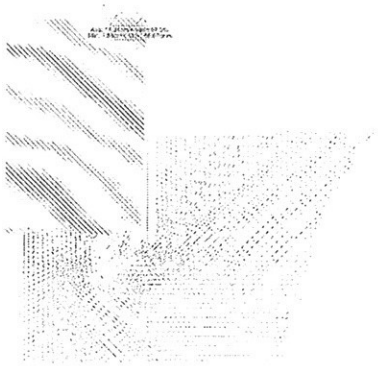

Figure 7: Analyzed picture 1

Figure 8: Analyzed picture 2

The outcome of the computer analysis of the images depends, among other things, on the velocities in the fluid. The minimum velocity possible to measure by PIV-technique is given by the particle image diameter, d_{pi}, and the laser puls separation, δt_p. It is important that it is possible to distinguish between two (or multiple) exposures of the same particle. If this is not the case, it is impossible to find Δs. The size of IA puts limitation on the maximum velocity possible to detect. If Δs is to be found there has to be a sufficient number of image pairs of particles (or image groups, if the particles are exposed several times) within the IA.

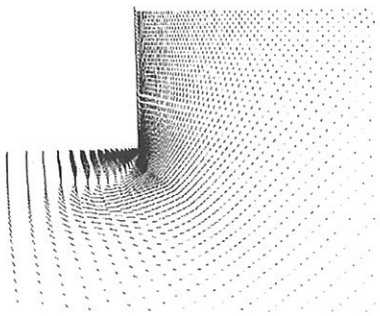

Figure 9: Calculation 1

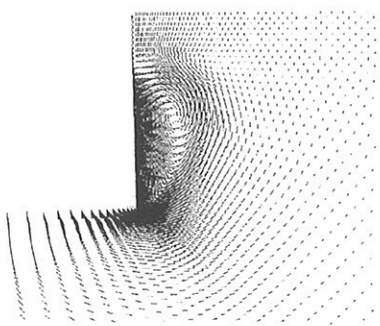

Figure 10: Calculation 2

Ship section in sway

The experiments for sway-motion are still not finished, but will be presented at the conference.

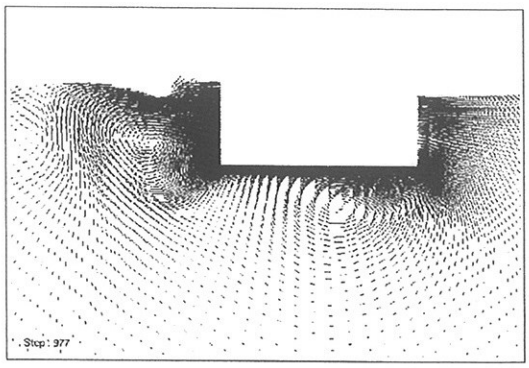

Figure 11: Calculated flow in sway motion

References

[1] Holm, Håvard and Pettersen, Bjørnar, *Free surface flows*, NUTTS 1999.

[2] Lader, Pål, *Geometry and kinematics of breaking waves*, PhD thesis, Department of Marine Hydrodynamics, Norwegian University of Science and Technology. (2000)

[3] Stakkestad, Aslaug, *Viscous flow around two-dimensional ship sections. Numerical calculations and experimental results*, Master's degree, Department of Marine Hydrodynamics, Norwegian University of Science and Technology. (2000)

ASSESSMENT OF TURBULENCE MODELS FOR STERN AND WAKE FLOW PAST A MODERN VLCC HULL FORM

Sung-Eun Kim (sek@fluent.com)
Fluent Inc.
10 Cavendish Court, Centerra Resource Park
Lebanon, NH 03766-1442, U.S.A.

Robert Nyiredy (rpn@fluent.se)
Fluent Sweden
Vestagatan 2A,
416 64 Gothenburg, Sweden

INTRODUCTION

Accuracy of computational fluid dynamics (CFD) predictions for turbulent flows around ship hulls is largely determined by turbulence modeling. One of the most frequently asked questions is: what turbulence model is most appropriate or best for modeling turbulent flows around ship hulls? This arguably ill-posed, yet legitimate question remains largely unanswered or has been "partially" answered, at best, by the earlier numerical studies. Different mesh resolutions and discretization schemes adopted in the individual studies make it difficult to offer an answer.

This article attempts to address that lingering question by employing eight turbulence models, in combination with a wall function approach for the flow past a modern tanker hull form. The hull considered here is a 1:58 scale model (Re_L = 4.6 x 10^6) of the 300K VLCC tested at the Korean Institute of Ship and Ocean Engineering (KRISO) in Korea (Van *et al.*, 1998) and selected as one of the benchmark cases at the Gothenburg 2000 CFD Workshop in ship hydrodynamics. The flow in question belongs to the category of "complex" turbulent shear flow by all measures, being featured by turbulent boundary layer with significant crossflow and ensuing streamwise vortices under the influence of pressure gradient and streamline curvature.

All the computations were carried out using FLUENT V5.3, a general-purpose CFD code. The computations were made using high-order numerics on a sufficiently fine mesh for which mesh-independence of the numerical solutions is ensured. The predictions are evaluated by comparing the numerical results with the experimental data in terms of axial velocity distribution in the propeller plane, resistance (drag), and nominal wake-fraction. The use of a single code enables us to isolate the effects of turbulence modeling and make fair assessments of the various turbulence models in popular use today for the flow around full ship hulls.

NUMERICAL METHOD AND TURBULENCE MODELS

FLUENT employs a cell-centered finite-volume method along with a linear reconstruction scheme that allows use of computational elements (cells) with arbitrary polyhedral topology, including quadrilateral, hexahedral, triangular, tetrahedral, pyramidal, prismatic, and hybrid meshes. The velocity-pressure coupling and overall solution procedure are based on SIMPLE algorithm (Patankar, 1972) adapted to unstructured mesh. The discretized algebraic equations are solved using a pointwise Gauss-Seidel iterative algorithm. An algebraic multigrid method is employed to accelerate solution convergence. The details of the numerical method are described by Mathur and Murthy (1997) and Kim *et al.* (1998).

Eight popular turbulence models were chosen for this study, ranging from one-equation model to Reynolds-stress transport models based on second-moment closure. They are:

1) Eddy viscosity transport model of Spalart and Allmaras (1992) (S-A)
2) k-ε (SKE) model of Jones and Launder and Spalding (1974)
3) Renormalization-Group based (RNG) k-ε model of Yakhot and Orszag (1986)
4) Realizable k-ε (RKE) model (Shih *et. al*, 1995)
5) k-ω model of Menter (1994)
6) k-ω model of Wilcox with corrections for free flows (1998)
7) Reynolds stress transport model of Gibson and Launder (1979) (RSM-GL)
8) Reynolds stress transport model of Speziale *et al.* (1991) – RSM-SSG

For the near-wall treatment, we chose to employ a wall function approach based on Launder and Spalding's (1974) wall functions and related hypotheses in favor of its practicality for high-Reynolds number flows. Employing the wall function approach significantly reduces the number

of cells and the computational effort, inasmuch as the viscosity-affected near-wall region does not need to be resolved and instead can be bridged by the wall functions.

Block-structured hexahedral meshes were employed. Grid-convergence of numerical solutions was ensured with three different sizes of meshes. The results presented in this article were obtained using a 200,000-cell mesh, for which y^+ at the wall adjacent cells is in the range of 30 – 80 over most of the hull surface.

RESULTS

Stern and wake flow structure

One of the most outstanding features of the flow around the subject hull form is the streamwise vortices emanating from the stern boundary layer, which are a consequence of the crossflow in the boundary layer driven by transverse pressure gradient. The surface boundary layer carrying crossflow leaves (separates from) the hull surface in the form of a free vortex-sheet, being rolled up as it is convected downstream. The fidelity with which the location and strength of the streamwise vortices are predicted is of great interest to CFD practitioners in ship hydrodynamics, since the vortices have significant impacts on the resistance and propulsion characteristics of ships.

The streamwise vortices can be visualized most conveniently via axial velocity contours and crossflow velocity vectors on transverse planes. The contours of the measured axial velocity in the propeller plane are shown in Figure 1. The contours feature a very unique shape that resembles rabbit's ears.

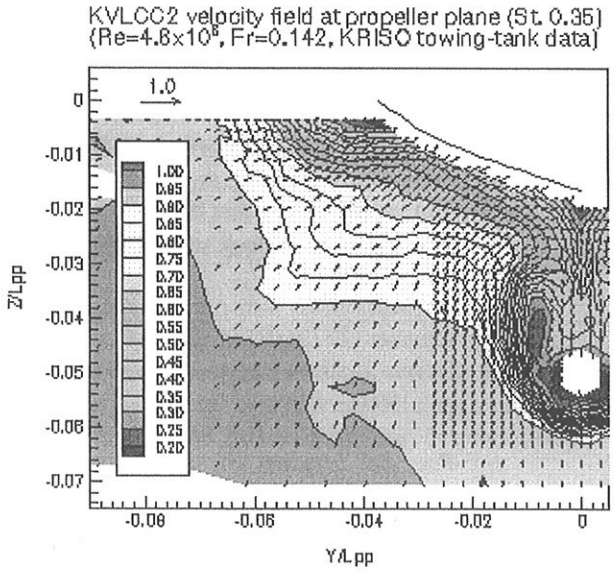

Figure 1. Measured axial velocity contours at propeller plane

Figure 2 shows the contours of the axial velocity and the crossflow velocity vectors in the propeller plane predicted by the eight turbulence models. The degree to which the predictions capture the unique shape (rabbit's ears) varies widely among the turbulence models employed. Among others, the S-A model and the SKE model fail to capture the characteristic shape. The crossflow and subsequent roll-up of the vortex sheet is significantly underpredicted by these models. More recently proposed two-equation model such as RKE, RNG, and k-ω models perform appreciably better than the first two models in that they yield stronger crossflow and more pronounced roll-up. Yet there are still a substantial gap between the predictions and the measurement. The result of the k-ω model by Wilcox stands out among the group of the isotropic eddy-viscosity based models, quite closely reproducing the rabbit's ears. The best result, however, is obtained by the Reynolds stress transport models. The two RSM models are seen to faithfully reproduce the rabbit's ears in the contours. This is quite remarkable and encouraging, considering that wall functions are employed in the calculations.

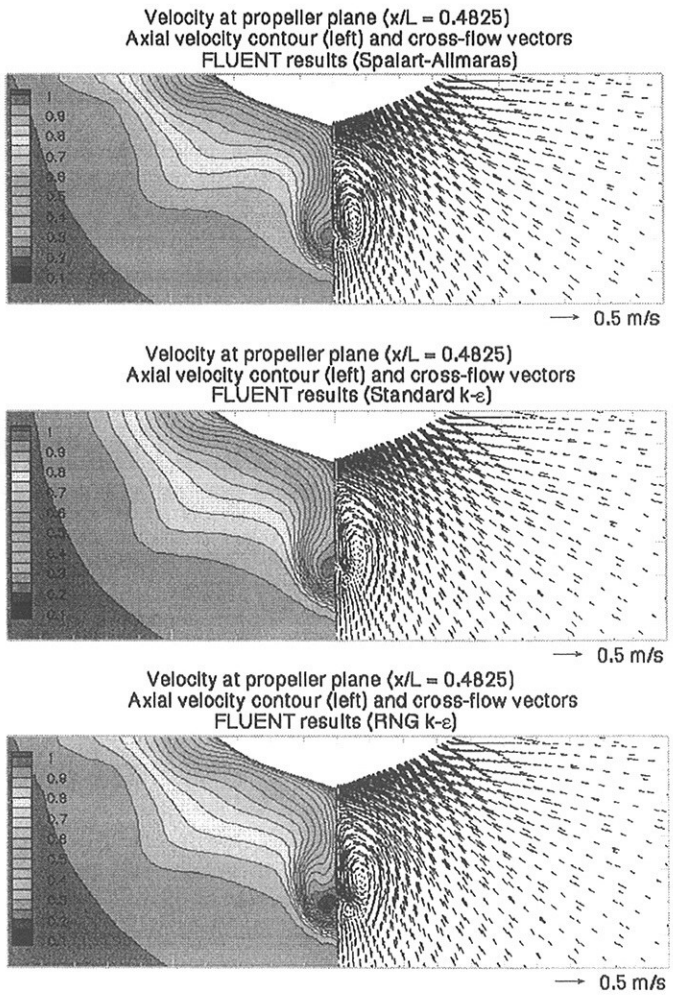

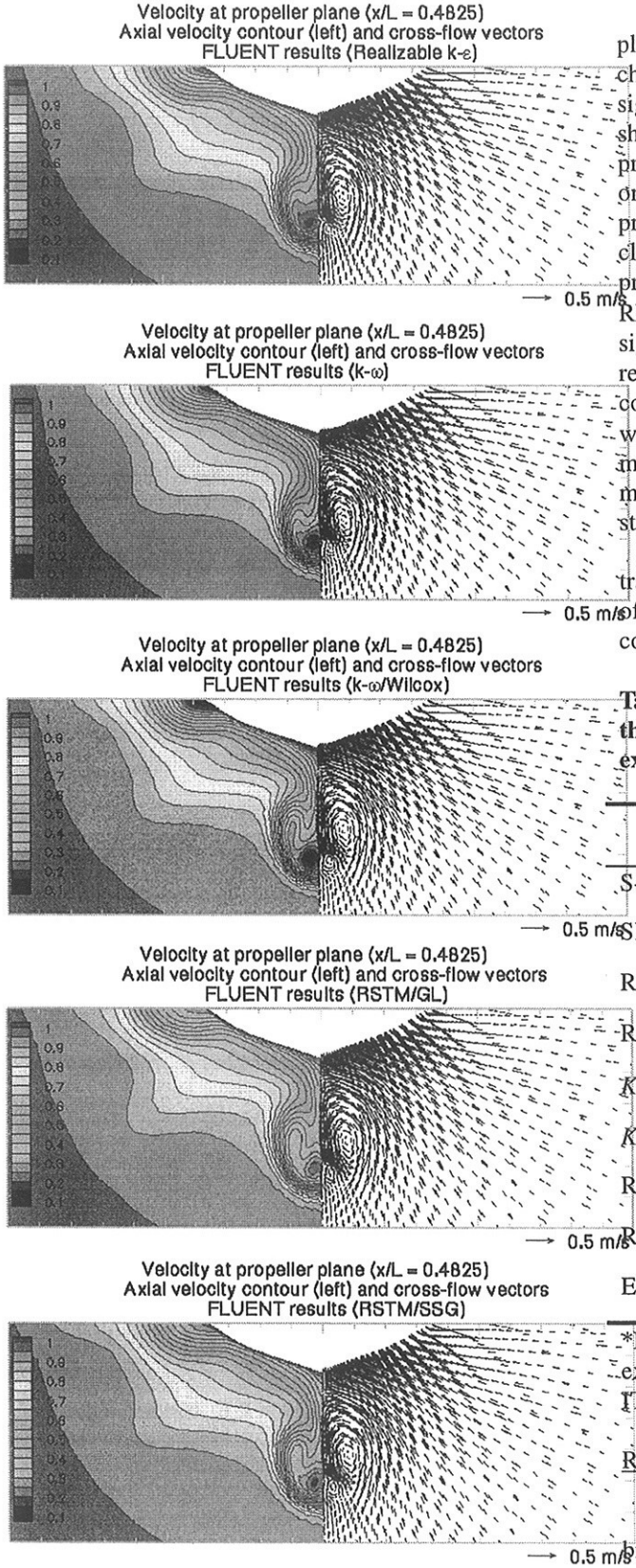

Figure 2. Contours of axial velocity at the propeller plane predicted by eight turbulence models

Nominal wake fraction

The nominal wake-fraction at the propeller plane is an important quantity, inasmuch as it characterizes the inflow to propellers and significantly impacts propulsive performance of ships. Table 1, in the left-most column, shows the predicted nominal wake fractions and the measured one. Quite obvious among others are the poor predictions by S-A and SKE models, which is closely related with the failure of these models to predict the formation of the streamwise vortices. RNG, RKE, and k-ω models, which performed significantly better than the S-A and SKE models in reproducing the unique shape of the velocity contours, again better predict the wake-fraction as well. Worthy of mentioning is the Wilcox' k-ω model which overpredicts the wake fraction. The most accurate predictions come from the Reynolds stress transport models.

These results show that the Reynolds stress transport models adopted in this study are capable of predicting, with remarkable accuracy and consistency, the stern and wake flow characteristics.

Table 1. Resistance coefficients computed from the numerical solutions and measured from the experiment

	Nominal Wake	1000 C_{VT}	1000 C_F	1000 C_{VP}	(1+k)
S-A	0.486	4.051	3.360	0.691	1.206
SKE	0.482	4.216	3.503	0.713	1.204
RNG	0.537	4.145	3.416	0.728	1.213
RKE	0.539	4.149	3.402	0.746	1.219
K-ω SST	0.538	4.200	3.387	0.814	1.240
K-ω Wilcox	0.583	4.258	3.427	0.831	1.242
RSM-GL	0.561	4.048	3.293	0.756	1.229
RSM-SSG	0.560	4.060	3.357	0.702	1.209
Exp.	0.557	4.056	3.396	0.660	1.194

*Note) The resistance coefficients from the experiment were computed based following the ITTC 1978 recommendation.

Resistance Predictions

It is long tradition that the total resistance is broken down into viscous and wave-making resistance, with the former being further broken down into frictional resistance and viscous pressure (form) drag. CFD enables one to readily evaluate the resultant forces on ship hulls and its components. Table 1 shows the resistance components (C_{VT}, C_F, C_{VP}: total, frictional, and

form drag, respectively) predicted by the 8 turbulence models along with the measured ones. It should be mentioned that the measured total resistance was analysed following the 1978 ITTC's recommendation to "derive" the frictional and the viscous pressure resistance coefficients.

As shown in the table, all the two-equation turbulence models tend to overpredict the total resistance. Particularly noteworthy is the prediction by the Wilcox' k-ω model which deviates most from the experimental data. The major discrepancy comes from its form drag prediction, which is much larger than the experimental value and those predicted by other models. The predictions by the RST models are in best agreements with the experimental data. It is also noted that RSM-GL model gives slightly larger form drag than the RSM-SST model.

The fidelity of the resistance predictions, as demonstrated by the present results, demonstrates the efficacy of the wall function approach adopted in the present calculations.

CONCLUSIONS

- The performance of the isotropic eddy-viscosity based turbulence models varies in a wide range. The Spalart-Allmaras model and the standard k-ε model fall short of predicting the major characteristics of the flows around full hull forms. Some of the more recent two-equation turbulence models including RNG k-ε, realizable k-ε, and k-ω models tend to improve the predictions. However, their performance is mixed.
- The Reynolds stress transport models give the best predictions from the all aspects considered here. They not only capture the characteristic shape of the axial velocity contours successfully but also predict the resistance and the wake-fraction with remarkable accuracy and consistency.
- The wall function approach adopted in this study, when combined with accurate numerics and reliable turbulence models, is capable of predicting the salient features of the turbulent shear flows around full ships. The results clearly demonstrate that the wall function approach is a viable choice in the near-wall modeling of high-Reynolds number flows such as ship flows.

ACKNOWLEDGEMENTS

The authors gratefully acknowledges that the mesh used in the present calculations is originally provided by the CFD group at the Marine Transportation Systems Research Center of the KRISO.

REFERENCES

Van, S.H. et al., Experimental Study on the flow characteristics around VLCC with different stern shapes, Proc. 3rd International Conference on Hydrodynamics (ICHD), Seoul Korea, 1998.

FLUENT 5 User's Guide, FLUENT Inc., 1998.

Mathur, S.R. and Murthy, J.Y., A Pressure-Based Method for Unstructured Meshes, *Numerical Heat Transfer*, Vol.31, pp. 195-215, 1997.

Kim, S.-E., Mathur, S.R., Murthy, J.Y., and Choudhury, D., A Reynolds-Averaged Navier-Stokes Solver Using Unstructured Mesh-Based Finite-Volume Scheme, AIAA-Paper 98-0231, 1998.

Kim, S.-E., Unstructured Mesh Based Reynolds Stress Transport Modeling of Complex Flows, To be presented at 39th Aerospace Science Meeting and Exhibit, Reno, Nevada, 2001.

Spalart, P. and Allmaras, S., A One-Equation Turbulence Model for Aerodynamic Flows, AIAA Paper 92-0439, 1992.

Launder, B.E. and Spalding, D.B., The Numerical Computation of Turbulent Flows, *Comp. Meth. Appl. Mech. Eng.*, Vol. 3, pp. 269-289, 1974.

Yakhot, V. and Orszag, S. A., Renormalization Group Analysis of Turbulence I. Basic Theory, *J. Scientific Computing*, Vol. 1, No. 1, pp. 1-51, 1986

Shih, T.-H., Liou, W.W., Shabbir, A., and Zhu, J., A New k-ε Eddy-Viscosity Model for High Reynolds Number Turbulent Flows - Model Development and Validation, *Computers & Fluids*, Vol. 24, No. 3, pp. 227-238, 1995.

Menter, F.R., Two-Equation Eddy-Viscosity Turbulence Models for Engineering Applications, *AIAA J.*, Vol. 32, No. 8, August 1994.

Wilcox, D.C., Turbulence Modeling for CFD, 2nd Edition, DCW Industries, Inc., 1998.

Gibson, M.M. and Launder, B.E., Ground Effects on Pressure Fluctuations in the Atmospheric Boundary layer, *J. Fluid Mech.*, Vol. 86, pp. 491--511, 1978.

Speziale, C.G., Sarkar, S. and Gatski, T.B., Modeling the Pressure-Strain Correlation of Turbulence, *J. Fluid Mech.*, Vol. 227, pp. 245-272, 1991.

FURTHER DEVELOPMENTS IN THE NUMERICAL SIMULATION OF SEAKEEPING

Claudio Lugni, Maurizio Landrini, Andrea Colagrossi

INSEAN, *The Italian Ship Model Basin*

We summarize here our more recent experience in the numerical computations of the flow field around ships advancing through waves. The problem is attacked by a potential flow model and is solved numerically by a Rankine panel method in time domain. The resulting code has been applied to a large variety of ships, from mathematical geometries to practical hull forms, either mono- of multi-hulls. For some of these hulls an experimental activity has been developed.

Mathematical and numerical modeling The unsteady motion of a ship in a seaway is studied by an inviscid model. We consider the case of small oscillations $\boldsymbol{\alpha}$ around the mean trim and sinkage attained by the ship advancing in calm sea, with constant forward velocity U in the x–direction. In the following, $\boldsymbol{W}$ denotes the basis–flow. The perturbation velocity potential φ satisfies the Laplace equation $\nabla^2\varphi = 0$, the standard no–penetration boundary condition on the mean wetted hull $\mathcal{B}$:

$$\varphi_n = (\boldsymbol{\alpha}_t + \nabla \times (\boldsymbol{\alpha} \times \boldsymbol{W})) \cdot \boldsymbol{n} - \varphi_{0,n} \qquad (1)$$

and the linearized kinematic and dynamic free surface conditions on the mean free surface level $\mathcal{F}$:

$$\begin{aligned} \eta_t &= \varphi_z - \nabla\eta \cdot \boldsymbol{W} + \eta \boldsymbol{W}_z \cdot \boldsymbol{k} + \tfrac{\nabla W^2}{2g} \cdot \nabla\varphi \\ \varphi_t &= -g\eta - \boldsymbol{W} \cdot \nabla\varphi \end{aligned} \qquad (2)$$

g is the gravity acceleration, ρ is the fluid density, η is the wave height and t the time. Lower suffices stand for partial derivatives. The potential vanishes at large distances, leaving unaffected the potential of the incoming waves φ_0. The above fluid dynamic problem is coupled with the body motion through the hydrodynamic loads, evaluated by direct pressure integration in the numerical procedure. In turn, the body motions affect the flow field via the body boundary condition (1).

The problem is solved in two steps. At a given instant of time, the potential $\varphi|_{\mathcal{F}}$ on the free surface and the normal gradient $\varphi_n|_{\mathcal{B}}$ on the body boundary are known and the resulting mixed Neumann–Dirichlet boundary value problem for the Laplace equation is solved by a standard panel method. Once the velocity potential is computed on the boundary domain, the free surface equations, as well as the equations of the body motion, are stepped forward by a fourth-order Runge–Kutta scheme.

The fluid pressure $p = -(\varphi_t + \boldsymbol{W} \cdot \nabla\varphi)/\rho$ on the hull is needed to compute the hydrodynamic loads. To the purpose, the time derivative of the potential, φ_t, is computed by solving the auxiliary problem

$$\begin{aligned} \nabla^2\varphi_t &= 0 \\ \varphi_{nt} &= (\boldsymbol{\alpha}_{tt} + \Omega_t \times \boldsymbol{W}) \cdot \boldsymbol{n} \quad \text{on } \mathcal{B} \\ \varphi_t &= -g\eta - \boldsymbol{W} \cdot \nabla\varphi \quad \text{on } \mathcal{F} \end{aligned} \qquad (3)$$

Because of the similarity of the problem (3) with the problem for φ, the same (already discretized) boundary integral equations can be used to determine φ_t with a negligible effort.

In the present version of the code, the tangential derivative $\nabla\eta$ (see the first eq. (2)) is converted into $\nabla\eta = -[\nabla\varphi_t + \nabla(\boldsymbol{W} \cdot \nabla\varphi)]/g$. This term requires the already computed $\nabla\nabla\varphi$, while the term $\nabla\varphi_t$ is obtained by a small extra–effort after the computation of φ_t. This allows to better deal with unstructured free surface meshes.

Outgoing waves are damped out by dissipative terms $-2\nu\eta + \nu^2/g\,\varphi$ inserted in the kinematic free surface boundary condition. The coefficient, ν, is nonzero only in a damping frame surrounding the inner physical free

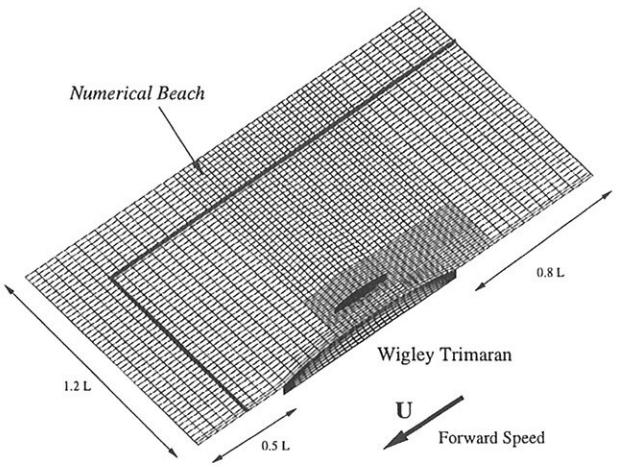

Figure 1: Example of discretized boundary domain for a Wigley trimaran. Typical dimensions are normalized by the ship length L. The damping frame is bounded by the thick line.

surface. A smooth increase from zero up to an empirically determined maximum value is used.

Figure 1 show a typical computational domain around a tri-hull made by Wigley forms. An apparent feature of the adopted discretization is the use of a non structured grid for the free surface. This is a key point to easily deal with multi-hulls and transom stern and also to allow an easy local mesh refinement.

DDG 51 The combatant DDG 51 is an example of a standard frigate. It is characterized by transom stern and sonar dome at the bow. In fig. 2, we show the typical arrangement of the free surface panels. We use an unstructured grid in the downstream region, where it is more difficult to follow the ship profile. The transom stern is handled by using a fictitious body to smoothly reconcile the hull with the surface level.

In the developed algorithm, we take advantage from the possibility of deducing the (linear) response operator over a wide range of wavelengths by analyzing the ship response to a given compact (in time) wave induced excitation (transient test technique). If a large number of frequencies has to be considered, this procedure results in a shorter simulation time with respect to fully 3D frequency domain codes and significantly reduces the gap with respect to strip-theory codes.

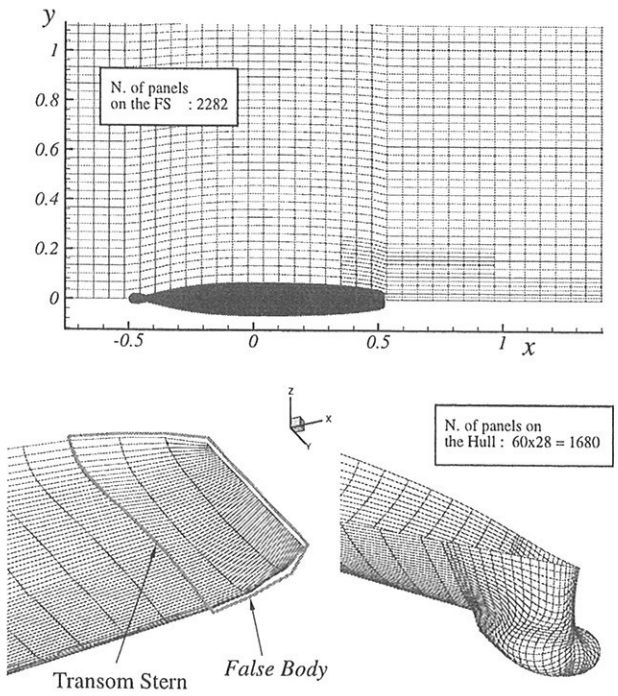

Figure 2: Simulation of DDG 51 seakeeping. Top: typical discretization of the free surface. Bottom: details the discretization of transom and bow regions.

A similar procedure has been employed in the physical towing tank of INSEAN. Results from this and more traditional tests are summarized in plots 3-4 together with the numerical simulation (solid lines). In the whole, a satisfactory agreement is obtained. We

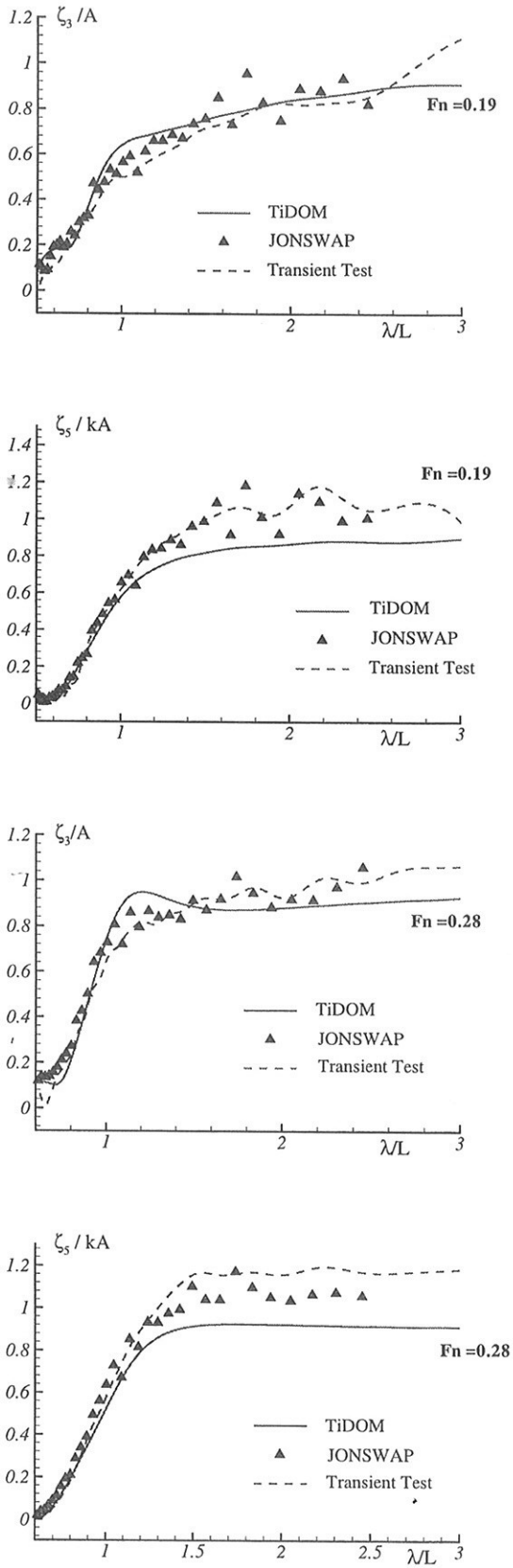

Figure 3: Numerical and experimental DDG 51 seakeeping: heave ζ_3 and pitch ζ_5 response amplitude operators for $Fn = 0{\cdot}19$ and $0{\cdot}28$.

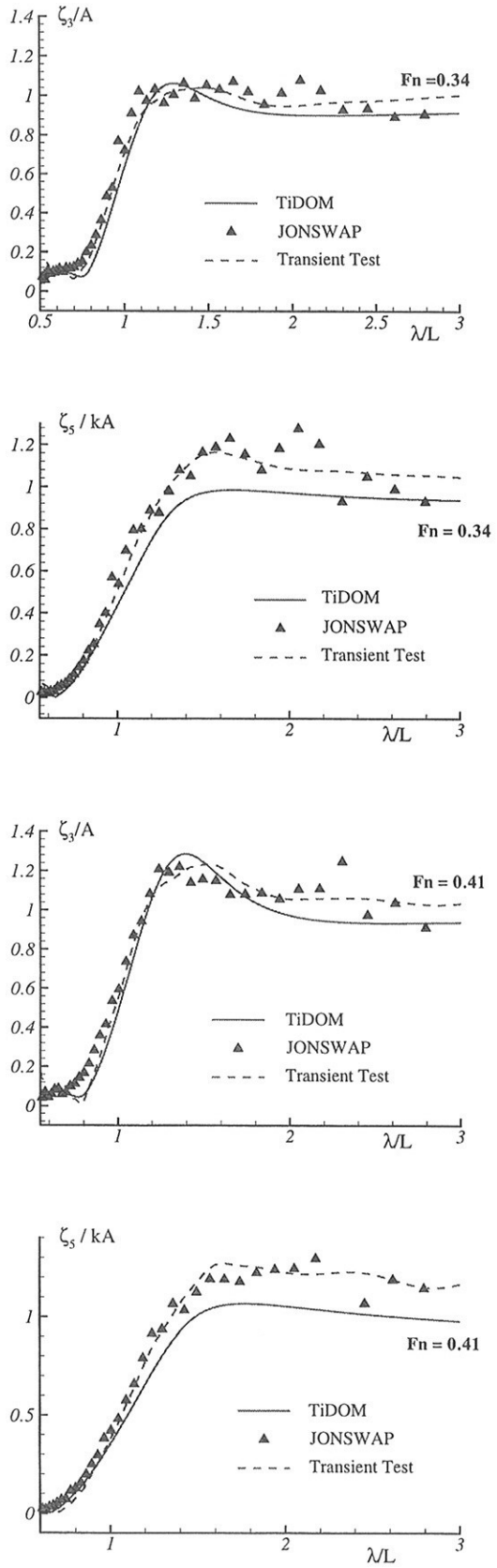

Figure 4: Numerical and experimental DDG 51 seakeeping: heave ζ_3 and pitch ζ_5 response amplitude operators for $Fn = 0{\cdot}34$ and $0{\cdot}41$.

have to observe, though, a trend to under-estimate the pitch response at the peak as Fn increases.

Wigley Trimaran We consider a prototype of multi-hull vehicle made by assembling three parabolic (Wigley) hulls. In fig. 5, we report a subset of the computations and of the experiments performed for this hull. We also show the comparison with strip-theory computations. We recall that, usually, standard strip-theory codes neglect the interaction between hulls. This is suitable for catamarans at high speed but is progressively wrong when decreasing Fn and hull spacings. Therefore, we decided to compare our computations with an improved strip-theory where hull interference is taken into account (Söding, private communication).

The speed of advance is increasing from top down, and plays a relevant role in determining shape and amplitude of the response operator. For $Fn = 0{\cdot}2$, our fully three-dimensional model nicely agrees with the measured data over the entire range of wavelengths λ. The strip theory recovers the correct location of the two peaks ($\lambda/L \simeq 0{\cdot}85$ and $1{\cdot}2$) featured by the response amplitude operator. The corresponding amplitudes are over-predicted and (largely) under-predicted, respectively.

As the velocity increases, experiments show an increase of the first peak and a decrease of the second one (center plot). Our model clearly over-predicts the second peak, which now is halfway between strip-theory and three-dimensional results.

At the highest velocity, bottom plot, we recover a good agreement in the high-λ range, but the peak for smaller wavelengths is largely over-predicted. In the strip-theory computations, the second peak almost disappears and the response is globally over-predicted.

Series 60, $C_b = 0.8$ We conclude by showing some results concerning a blunter hull: a Series 60 model with block coefficient $C_b = 0.8$. In this case, we enjoyed the availability of a careful set of experiments performed by H. Iwashita at Hiroshima University. An extended discussion concerning this cooperative effort will be given at the workshop. In figure 6, we compare numerical and experimental transverse cuts of radiated wave field during forced heave motion (top plot) and the corresponding heave added mass and damping coefficients. A good agreement is generally obtained.

Discussion Some results by a seakeeping code under continuous improvement have been presented and compared with experimental data.

So far, the numerical method appears as robust and accurate as other three-dimensional seakeeping codes in frequency domain. With respect to those, a significant speed-up has been achieved by exploiting the idea

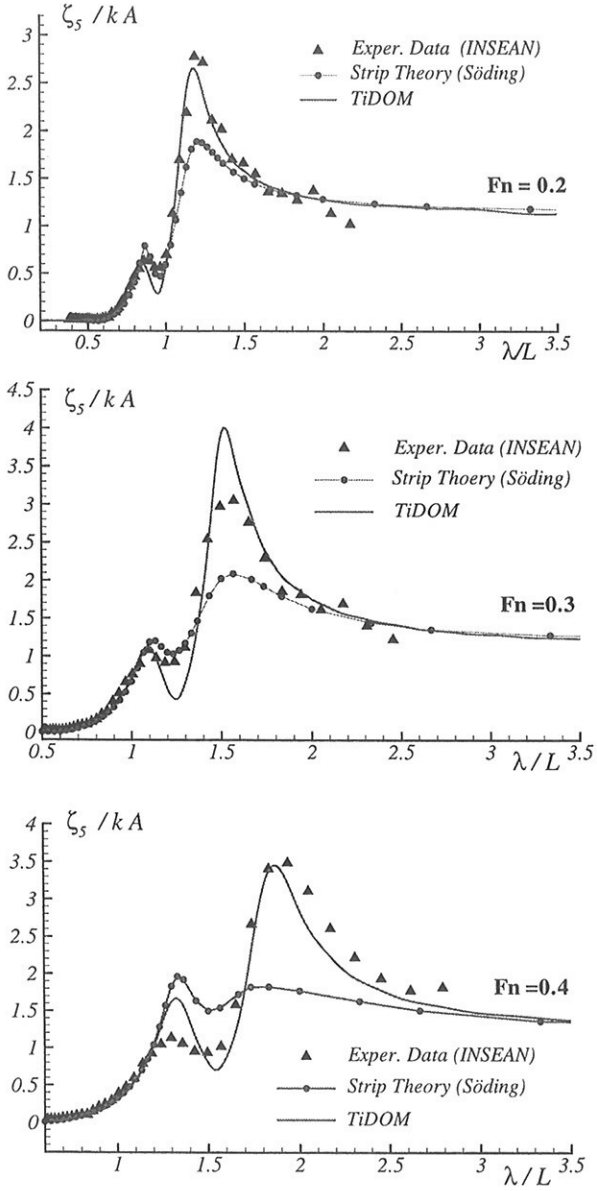

Figure 5: Wigley Trimaran: numerical prediction of pitch response amplitude operator for $F = 0{\cdot}2$ and $0{\cdot}4$.

of transient tests.

Computations and experiments for a mathematical tri-hull provide an example where the (still faster) strip-theory experiences difficulties, probably related to the neglected three-dimensional effects.

A carefull comparison with and extensive set of measurements provided by H. Iwashita for a blunt Series 60, $C_b = 0.8$, is under development and will be discussed at the workshop.

The research activity of the first three authors is supported by the Italian *Ministero dei Trasporti e della Navigazione* through INSEAN Research Program 2000–2002.

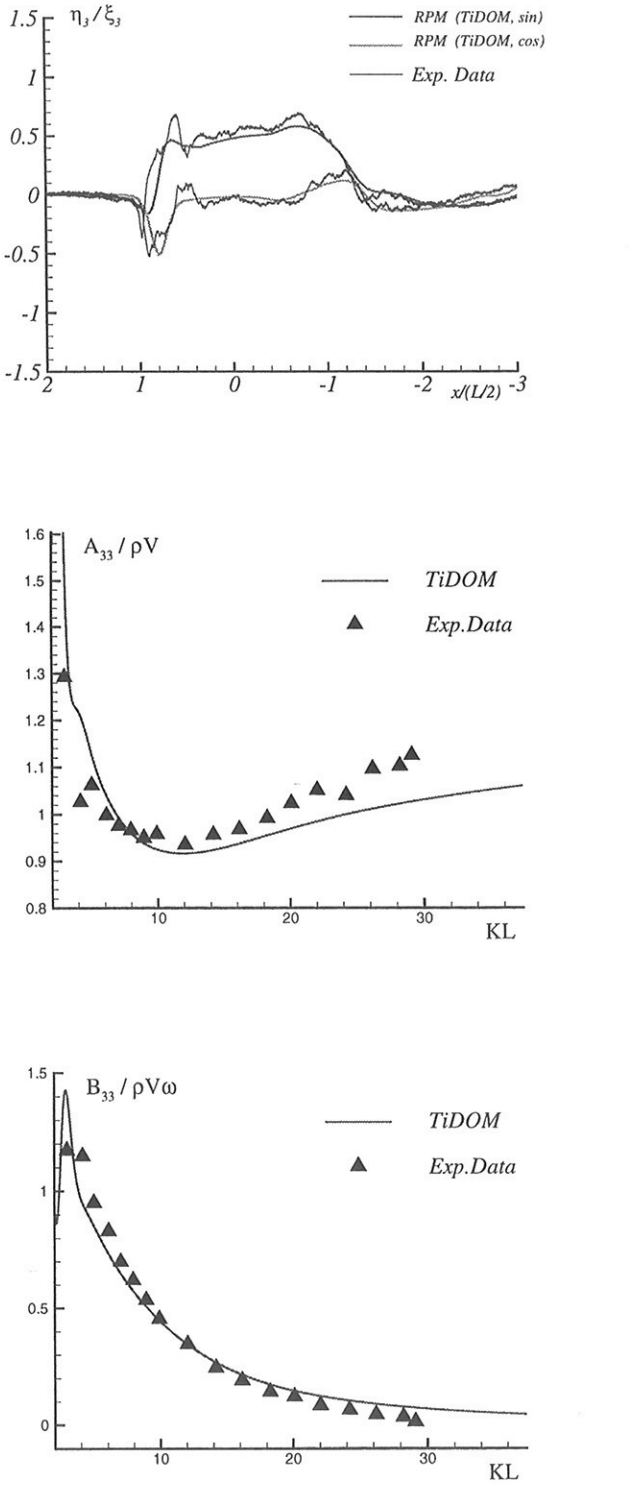

Figure 6: Series 60 $C_b = 0.8$. Top plot: longitudinal cut of the radiated wave pattern during forced heave motion ($\omega^2 L/g = 7$). Center and bottom plts: added mass and dampiing coefficients for heave. Experiments have been performed by H. Iwashita at the Hiroshima University.

Application of a Body Force Method to the Study of the Wake past a Ship Hull

R. Muscari, A. Di Mascio, R. Broglia

INSEAN – Via di Vallerano, 139 – 00128 Roma – Italy

In naval hydrodynamics it is often required the study of ship hulls with complex geometries. Besides the hull, rudders, propeller shafts, stabilizers, etc. must be taken into account.
As a consequence, the construction of a body-fitted numerical mesh becomes one of the main items in the whole process of flow simulation. In this work, the authors will study the possibility to represent the bare hull alone with a fitted mesh, adopting a body-force approach for all the appendages. It is the authors' opinion that the presence of the appendages influences the global characteristics of the ship, for example the resistance coefficient, only in that they modify the flow around the hull and not for the resistance they offer by themselves. If this is the case, the detailed features of the flow around the appendages is not relevant and the body-force approach could be positively exploited to reduce the difficulties bound to the construction of a fully fitted mesh, while retaining an accurate prediction of global characteristics.
The body-force approach has already been used in a number of different problems typically involving moving ([1]) as well as complex ([2], [3]) geometries. For the study of non-steady problems some kind of feed-back has to be considered, which adapt the body forces to the instantaneous flow conditions ([2]). For steady flows, such those we are going to study in the present paper, the feed-back is not necessary and an easier approach can be used. In particular, we will employ the one described in [4].
As a preliminary problem, we studied the laminar flow around a cylinder with both an O-grid fitted on the cylinder and a cartesian grid plus external forces. In both cases the number of cells is 64×64. The Reynolds number based on the undisturbed streamwise velocity and the cylinder diameter is $\mathrm{Re} = 25$.
As can be seen in fig. 1 the isolines patches for the streamwise velocity are almost identical in the two cases. In fig. 2 are shown the u vs. y graphs at two downstream locations, i.e. for $x = 6$ and $x = 8$. Even in this case, the results are in very good agreement. These results, and others not shown here, seem to confirm that apart from the detailed flow near the body, that necessarily suffers from the lack of a solid wall, the macroscopic features of the downstream flow are not modified if we substitute the physical body with suited volume forces that mimic its presence.
In the full paper a more interesting case will be considered, i.e. a three–dimensional ship hull with appendages such as rudder, propeller shaft, stabilizer (fig. 3). All these appendages will be simulated by body-forces and the results compared with those obtained with a fully fitted mesh.

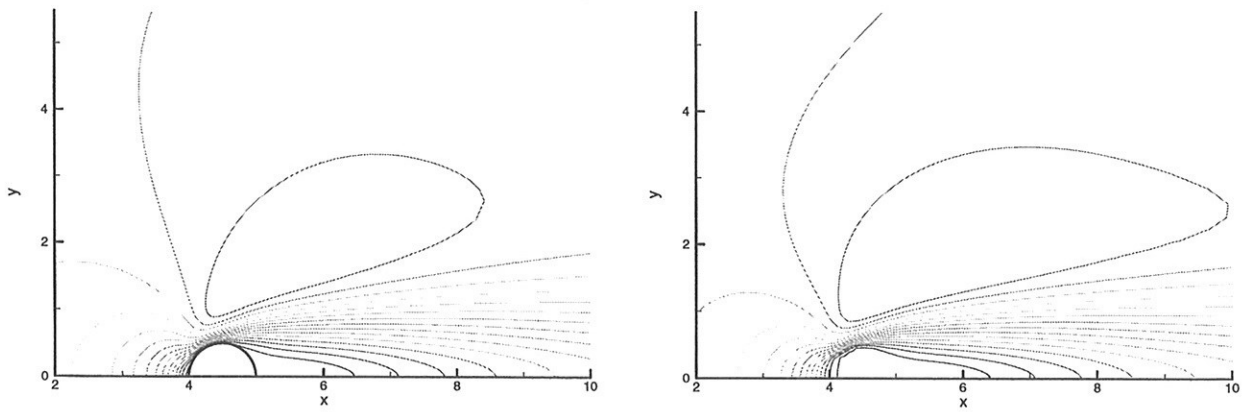

Figure 1: Streamwise velocity isolines. Body-fitted (left) and body-forces (right).

References

[1] C. S. Peskin, *Flow patterns around heart valves: a numerical method*, J. Comput. Phys., vol. 10, pag. 252, 1972.

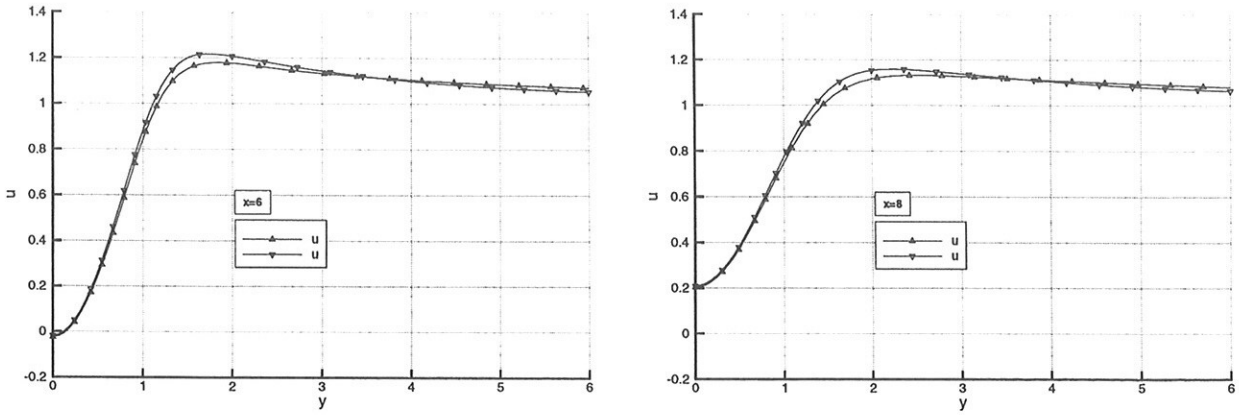

Figure 2: Streamwise velocity vs. y. $x = 6$ (left) and $x = 8$ (right).

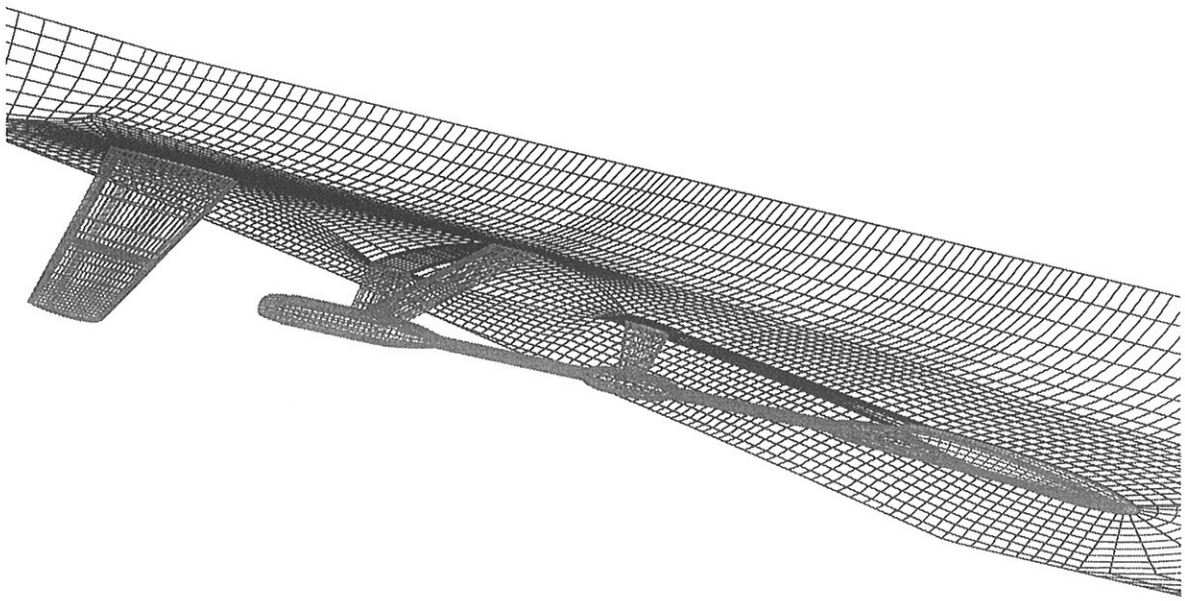

Figure 3: Hull to be studied

[2] D. Goldstein, R. Handler, L. Sirovich, *Modeling a no–slip flow boundary with an external force field*, J. Comput. Phys., vol. 105, pag. 354, 1993.

[3] R. Verzicco *et al.*, *LES in complex geometries using boundary body forces*, Center for Turbulence Research, Proceedings of the Summer Program, 1998.

[4] D. Dommermuth *et al.*, *Numerical simulation of bow waves*, 22nd Symposium on Naval Hydrodynamics, Preprints, 1998.

Numerical simulation of a simplified water entry problem

Kristian Bendix Nielsen *
Department of Naval Architecture and Offshore Engineering
Technical University of Denmark

Stefan Mayer †
Department of Mathematical Modelling
Technical University of Denmark

1 Introduction

In ship and offshore design, the prediction of water impact loads are of great importance. In offshore design it is used to calculate loads on horizontal members of offshore structures, in prediction of green water loads on FPSO's, and in ship design for accurate prediction of slamming loads.

To simplify the impact problem this paper will analyze the water impact of cylindrical structures into water at rest. This problem has been studied experimentally by Faltinsen et al [2], analytically by Faltinsen et al [2], Garrison [3] and Greenhow [4]. Similar problems have also been modeled numerically by Aray et al [1].

This paper presents an attempt of numerically simulating the problem, using well know Computational Fluid Dynamics (CFD) methods. The problem is simplified to two-dimensions, and uses the Reynolds Averaged Navier-Stokes Equations (RANSE) solver NS3 developed at the former International Research Center for Computational Hydrodynamics (ICCH) [6]. The results in this paper are intended to form a benchmark for validation of the CFD code, in order to make it applicable to more complicated 2D/3D water entry problems.

*kbn@ish.dtu.dk
†stm@imm.dtu.dk

2 Test case

The experimental data for comparison which is used as the benchmark test,has been obtained by Faltinsen et al [2]. The test setup is shown schematically in Fig 1, and the tests were carried out in the Ship Model Basin in Trondheim. The cylinder model was made from an aluminum tube, with a diameter of 0.35 m, and a length of 0.40 m. The model was then forced vertically through water at rest with a constant speed (V), using a hydraulic ram. The tests were carried out for two velocities: V = 0.9 m/s and V = 1.35 m/s. The resulting vertical force on the cylinder is obtained as a function of submergence rate H/R (=V· t/R , t = time). The uncertainty for the measures vertical force was reported to be at least +/- 10 %.

3 Numerical methods

The basic spatial and temporal discretization implemented in the incompressible Navier-Stokes solver, NS3, follows Mayer *et al* [6]. It uses a projec-

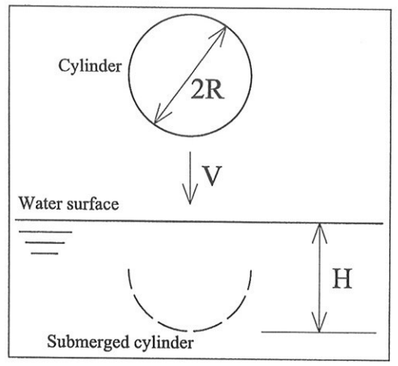

Figure 1: *Water impact problem*

tion method, which is second order accurate in time, and employs a finite volume method with cell-centered variable layout on general multi block grids.

To model the free surface a volume fraction method, the Compressive Interface Capturing Scheme for Arbitrary Mesh (CICSAM) [7] is applied. CICSAM is based on Normalized Variable Diagrams [5], and switches between upwind and downwind differencing depending on the orientation of the volume fraction field gradient. The k-ω model of Wilcox [8] is applied to model turbulence.

The numerical grid used in the calculations consist of $n_r \times n_\theta$ cells, where n_r is the number of cells in the radial direction, and n_θ is the number of cells in the circumferential direction. The grid is stretched in the radial direction of the cylinder, and the stretch factor defines the fraction between the radial height of the cells at the cylinder wall to the radial height of the cells at the computational boundary, i.e. a high stretch factor indicates small cells at the near cylinder domain, and vise versa. The code uses a variable timestep, which depends on the convective Courant-Friedrichs-Lewy (CFL) number, defined as:

$$CFL = \frac{\Delta t \, F_{cell}}{V_{cell}} \qquad (1)$$

where Δt equals timestep, F_{cell} is the cell flux and V_{cell} is the cell volume. The CFL criterium requires that the (constant) CFL number is not exceeded, in all cells, throughout the computation.

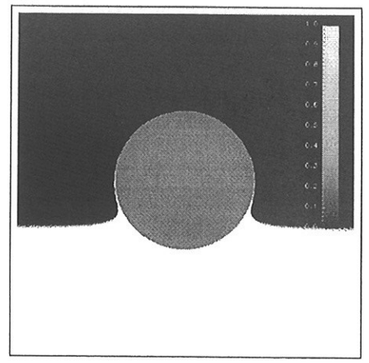

Figure 2: *Volume fraction, $V = 0.9$ m/s, $H/R = 0.3$*

In the numerical simulation the cylinder is steady, contrary to the experiments, and fluid is moving upwards with a constant vertical inflow velocity.

4 Results

The vertical force on the cylinder is obtained as a function of the cylinder submergence rate (H/R). In the initial stage of the impact (H/R $<$ 0.05) numerical noise appear in the calculated impact force, which is studied in the following section.

4.1 Initial impact

In Fig 3 the calculated vertical impact force is shown as a function of submergence rate in the early stage of the impact, and compared to the experimental result. The calculations are carried out for five meshes in order to investigate the effect of mesh size and mesh stretching on impact force. The experimental data show no fluctuations, but

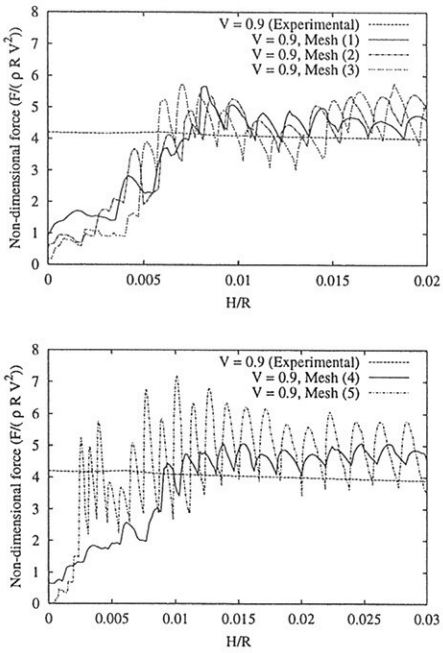

Figure 3: *Vertical force at initial impact*

Mesh	$n_r \times n_\theta$	Stretch factor
(1)	64×512	100
(2)	96×512	100
(3)	128×512	100
(4)	128×512	40
(5)	128×512	400

Fig 3 show that the results obtained in the numerical simulation is grid dependent. In the top graph of Fig 3, identical mesh stretching is used in all three grids, and only the number of cells in the radial direction vary. The results are ambigous, but one tendency is noticed: the impact force oscillates for all meshes, and an increase in number of cells gives higher amplitude of the impact force oscillations. Also, the variation in amplitude seems to be of the same order as the grid refinement. The bottom graph in Fig 3 show a similiar tendency, but in this case the number of cells is constant and only grid stretching differs. The period of the oscillations equals the time required to fill one cell at the cylinder boundary. The results indicate, that the code has problems dealing with sharp pressure gradients, but further investigations are required, in order to locate these problems.

4.2 Total submergence

The comparison between the experiments and the numerical simulation (Fig 4) shows in general good agreement for the vertical force during the whole submergence. The calculations with the remaining grids gives identical results, when submergence rate (H/R) exceed 0.15.

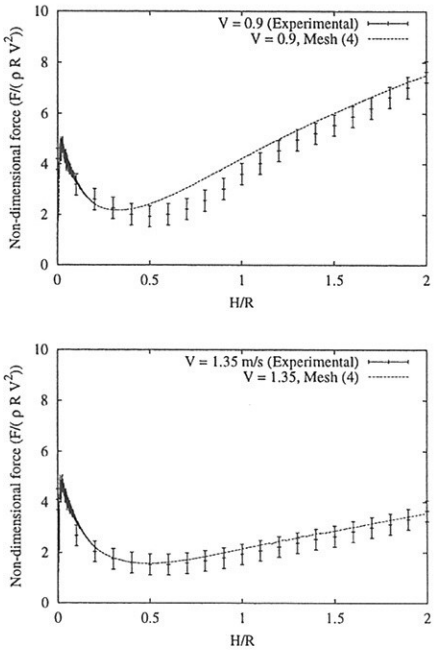

Figure 4: *Vertical force, $V = 0.9$ m/s (top), $V = 1.35$ m/s (bot)*

Although the code gives reasonable prediction of the force, visually the computed flow field is somewhat different from what the experiments show. In the experiments separation of fluid from the cylinder surface occurs at the submergence level H/R $\simeq$ 0.5. In the simulation separation does not occur at the innermost layers of the cylinder wall, and instead the fluid follows the cylinder boundary at high velocity, see (Fig 2). In the layers above flow separation occur, but not to the extent seen in the experiments. If additional viscosity is added, or the grid resolution is lowered, flow separation from the cylinder wall is increased, but the agreement with the experiments is lowered.

5 Conclusion

This paper shows, that modeling submergence problems with the applied CFD methods is not sufficient to describe the full problem, but that forces on immersing structures can be calculated with engineering accuracy. In the initial impact phase, the calculated vertical force oscillates, and the oscillation amplitude is a function of grid resolution in the near cylinder domain. The oscillation increases when the grid resolution is increased. The numerical model have problems in dealing with fluid separation from the cylinder wall which was seen in the experiments.

References

[1] Arai, M., Cheng, L.Y. and Inoue, Y. Hydrodynamic impact loads on horizontal members of offshore structures. In *Offshore Mechanics and Arctic Engineering*, pages 199–206 (1995). Volume 1-A, Offshore Technology.

[2] Faltinsen, O., Kjærland, O., Nøttveit, A. and Vinje, T. Water impact loads and dynamic response of horizontal circular cylinders in offshore structures. In *Offshore Technology Conference*, pages 119–126 (May 2-5 1977).

[3] Garrison, C.J. Water impact loads on circular structural members. *Applied Ocean Research*, **18** (1996): pages 45–54.

[4] Greenhow, M. Water-entry and -exit of a horizontal circular cylinder. *Applied Ocean Research*, **10** (1988) (4): pages 191–198.

[5] Leonard, B.P. The ULTIMATE conservative difference scheme applied to unsteady one-dimentional advection. *Computational Methods in Applied Mechanics and Enginering*, **88** (1991): pages 17–74.

[6] Mayer, S., Garapon, A. and Sørensen, L.S. A fractional step method for unsteady free-surface flow with applications to non-linear wave dynamics. *International Journal for Numerical Methods in Fluids*, **28** (1988): pages 293–315.

[7] Ubbink, O. *Numerical prediction of two fluid systems with sharp interfaces*. Ph.D. thesis, University of London (1997).

[8] Wilcox, D.C. *Turbulence Modeling for CFD*. Griffin Printing, Glendale, California (1994).

FLOW INDUCED BY THE FORCED ROLL MOTION OF A HULL SECTION

S. Parisi[‡] *M. Landrini*[‡] *G. Graziani*[†]

INSEAN–Italian Ship Model Basin[‡] – Via di Vallerano, 139 – Rome – Italy

University of Rome *La Sapienza* (Mech. Aer. Dept.)[†] – Via Eudossiana, 18 – Rome – Italy

INTRODUCTION

The analysis of the roll motion of a ship is interesting as well as complicate due to the variety of involved effects. A generic incident cross wave system gives rise to forces and moments on the ship that induce the roll motion. For obvious reasons of crew comfort, safety and ship manoeuvering, damped oscillations and limited amplitudes are required. Such effects depend on the hull shape and on the mass distribution through the vorticity generation and shedding from the ship. The study of the vortical systems arising along the hull helps explaining the time behavior of the roll motion as well as of the evolution of the involved forces and moments.

The development of a numerical solution procedure can integrate the experimental data which are, however, not easily available. To reduce the huge computational and programming effort due to the study of a three dimensional flow, we can approach a simplified analysis through the solution of a sequence of two-dimensional flows for different hull sections. Furtherly, in order to obtain a first evaluation of the effect of roll induced vortex shedding, we don't consider in this paper the presence of the free surface. Hence, a completely submerged rolling body is assumed with a prescribed motion. Different hull sections are studied through their double-model in order to investigate the induced flow field.

The numerical solution of the governing equations will emphasize a strong vorticity generation in some particular regions of the body. This generation is sometimes concentrated in two zones while, for different hull shapes, four regions with strong vorticity appear. The datailed information which are provided by the numerical results allow to separate the contribution to the damping moment due to pressure and to viscous stress.

MATHEMATICAL MODEL

We presently study the motion of a viscous incompressible fluid generated by the forced roll motion of a two dimensional rigid body in an unbounded domain Ω, in the absence of an ambient cross-flow. This flow can be described through the Navier–Stokes equations written in terms of vorticity transport

$$\frac{D\,\zeta}{D\,t} = \nu\nabla^2\zeta \qquad \forall t,\ \forall \boldsymbol{x} \in \Omega \tag{1}$$

where $\boldsymbol{\zeta} = \nabla \times \boldsymbol{u} = \zeta \boldsymbol{k}$, ($\boldsymbol{k}$ is the unity vector of z-axis) and $\frac{D}{D\,t}$ is the material derivative.

We consider an initial value problem by assuming an unperturbed flow at the initial instant $t{=}0^-$. The known angular velocity $\omega(t)$ of the body varies sinusoidally in time as is prescribed by the angular position time law: $\phi = \Phi\cos(\omega_0\,t) + \phi_0$

Hence, the total velocity of a generic point of the field contour $\partial\Omega$, must be equal to that of the corresponding point on the body surface in order to satisfy the no–slip and no–flow boundary conditions.

An Operator-Splitting scheme

Two different time scales, due to advection and diffusion, affect the dynamics of the vorticity field for large Reynolds number flows. Hence, the problem can be split in two simplified subsequent flows: the first one is purely convective, and the vorticity is transported by an ideal fluid. The second one is totally diffusive, and the vorticity is rearranged within the field by viscous effects. Among the variety of numerical approaches which can be used to solve these equations, we adopt a *Viscous Vortex Method* which can be easily coupled with a boundary integral formulation for the velocity field (see below) and shares the appealing features of the grid free methods. Hence the vorticity field is approximated by a distribution of point vortices of circulation Γ_j as:

$$\zeta(\boldsymbol{x},t) = \sum_{j=1}^{N_{vor}} \Gamma_j \delta(\boldsymbol{x}-\boldsymbol{x}_j) \tag{2}$$

During the advection step the vorticity is transported in a material way, i.e. it remains constant along the motion of each particle:

$$\frac{\partial \zeta}{\partial t} + (\boldsymbol{u}\cdot\nabla)\zeta = 0 \tag{3}$$

Consequently, the evolution of the vorticity field is obtained by solving the equations of motion. In this way the vortices are advected with the field velocity while retaining their strength. Now the velocity field $\boldsymbol{u}(\boldsymbol{x},t)$ is evaluated through the Biot–Savart formula that is written, for a single point vortex, as:

$$\boldsymbol{u}(\boldsymbol{x}_i) = \frac{\boldsymbol{\Gamma}(\boldsymbol{x}_j,t)\times \boldsymbol{r}_{ij}}{2\pi|\boldsymbol{r}_{ij}|^2} \tag{4}$$

where $\boldsymbol{x}_i$ is the position where the velocity is calculated, $\boldsymbol{x}_j$ is that of the vortex with circulation $\Gamma(\boldsymbol{x}_j,t)$ and $r_{ij}=|\boldsymbol{x}_i-\boldsymbol{x}_j|$. In the presence of many vortical particles, the sum of each individual contribution appears on the RHS of eq. (4).

Eq. (4) yields the velocity field in an infinite domain. In order to account for the presence of the body, and in case also of the free surface, a distribution of sources σ and of a concentrated vortex sheet with a constant circulation density γ can be adopted [1],[2]. In this way we can express the velocity at each internal point $\boldsymbol{x}^\star$ in an integral form according to:

$$\boldsymbol{u}(\boldsymbol{x}^\star) = -\nabla^\star \int_{\partial\Omega} \sigma G\, d\ell + \nabla^\star \times \int_{\partial\Omega} \gamma G\, d\ell + \boldsymbol{u}_\zeta(\boldsymbol{x}^\star)\,, \tag{5}$$

where the last term on the RHS accounts for the contribution of the field vortices (see eq. 4). Now the intensity of the vortex sheet γ is a new unknown which is evaluated through the Kelvin's theorem by enforcing the conservation of the total circulation. In order to calculate the strength of the sources distribution an integral equation obtained from eq. (5) when the point $\boldsymbol{x}^\star$ is on the domain boundary has been solved through a standard technique.

At the end of the inviscid step, after the solution of the integral equation for the velocity field, the no-slip condition on the body surface is no more satisfied. In order to enforce the correct boundary condition, a vortex distribution which induces an equal but opposite slip velocity is generated along $\partial\Omega$. These contour vortices are furtherly diffused together with the other field vortices according to

$$\frac{\partial \zeta}{\partial t} = \nu\nabla^2\zeta \tag{6}$$

Due to the linearity of eq. (6), the vorticity field after a time interval Δt_d can be obtained as the sum of the contribution of each individual vortex.

$$\zeta(\boldsymbol{x},t+\Delta t_d) = \sum_{j=1}^{N_{vor}} \frac{\Gamma_j}{4\pi\nu\Delta t_d} e^{-\frac{|\boldsymbol{x}-\boldsymbol{x}_j|^2}{4\nu\Delta t_d}} \tag{7}$$

The evaluation of the velocity of each one of the N_{vor} vortical particles is a cumbersome operation which implies a corresponding computational cost of the order of N_{vor}^2. In order to obtain a more efficent computational procedure, the multipoles decomposition of the vorticity field has been performed [3]. In this case the computational effort is of the order of $N_{vor} log(N_{vor})$, which is comparable with that of other efficent numerical solution techniques.

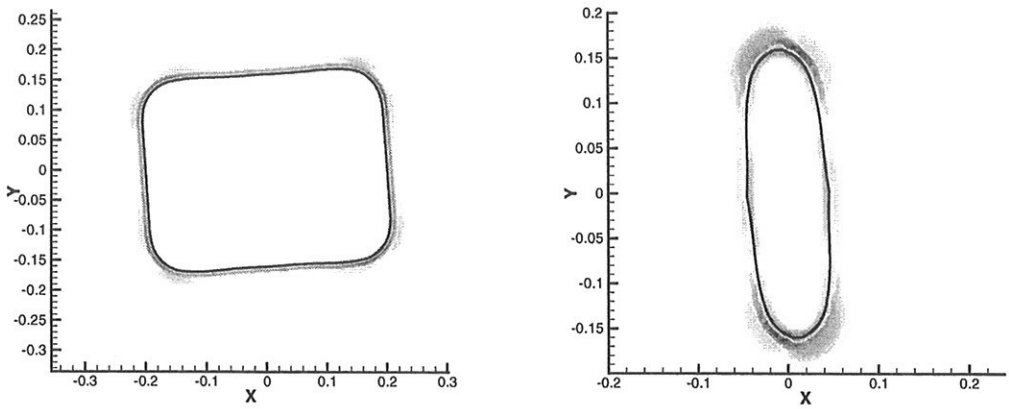

Figure 1: Vorticity field past sections A (left) and B (right).

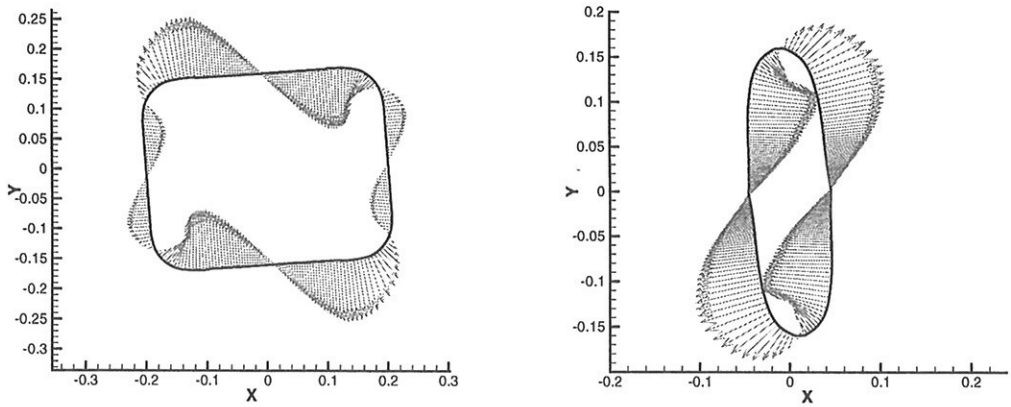

Figure 2: Wall pressure for sections A (left) and B (right).

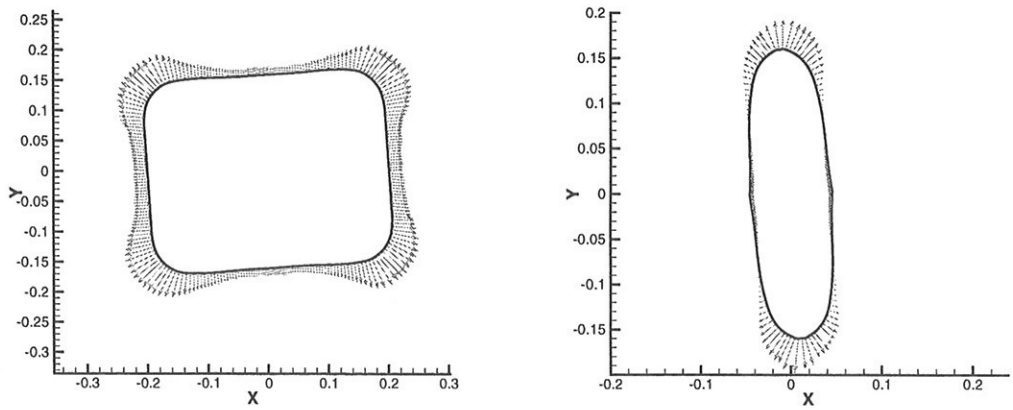

Figure 3: Wall vorticity for sections A (left) and B (right).

Roll Motion of a hull section

The harmonic forced roll oscillation of a two dimensional body is analyzed in this section by means of the just described computational procedure. The relevant non dimensional parameters for this flow are the Keulegan–Carpenter and the Reynolds numbers. If we refer to U_R, L, T, and ν as the reference velocity, length oscillation period and kinematic viscosity, respectively, the governing parameters are: $Re = \frac{U_r L}{\nu}$ and $K_c = \frac{U_r T}{L}$. If Φ is the maximum oscillation amplitude, the maximum angular velocity is $\Omega = \frac{2\pi\Phi}{T}$ and the reference velocity can be defined as $U_r = \Omega L$.

Due to the body motion, vorticity is generated along the whole contour with a dominant sign that is opposite to the body angular velocity. The flow separation points need not to be predefined, as it usually occurs with potential solutions, due to the presence of the viscous effects. The generation process is strongly intensified near the bilges and the further vortex shedding is largely responsible of the roll damping moment.

Two different hull sections are here considered for a Series 60 ($C_B = 0.8$) tanker: section A corresponds to $x/L = 0.5$ while section B is for $X/L = 1/6$ (where $x = 0$ corresponds to the bow). In both cases, the shed vorticity always remains close to the body due to the absence af an ambient flow and to the small value of K_C: the body undergoes reduced displacement within each period and the vortex particles are mostly moving due to the mutual induction. In this case the flow field around each bilge is noticeably independent from the other parts of the fluid domain and a periodic solution is quickly displayed.

Fig. (1) shows the vorticity fields past section A and B, on the left and right respectively, for $\Phi = 4$ and $T = 2$. It can be noted that a vortex couple is generated around each keel bilge: four in the first section but only two in the other. However stronger vorticity generation occurs in the bow section due to the small value of the curvature.

The roll damping moment is due both to the pressure on the body and to the shear stress. This latter quantity can be further express as the product of the wall vorticity times the viscosity. These quantities can be separately analyzed for a closer investigation of the involved effects. The distribution of the pressure along the two hull sections is shown in Fig. (2) and it is mostly due to the motion of the body: infact an opposite sign can be detected on the upwind and on the downwind side of the body. On the other hand, the contribution of the wall vorticity retains the same sign along the whole contour: Fig. (3) displays this quantity for both sections and it must be stressed that a much larger scale factor was used with respect to the pressure contribution. As it was already stated, the time history of the roll damping moment soon becomes periodic, and the contributions due to pressure and shear stress can be separate. This latter remains always much smaller than the former and displays a little phase shift. This plot is not shown here due to lack of space but will be presented in the oral discussion.

References

[1] G. Graziani, M. Ranucci, R. Piva. *From a Boundary Integral Formulation to a Vortex Method for Viscous Flows.* Comput. Mech., **15**, 4, 301–314. 1995

[2] M. Landrini. *Fenomeni non lineari nella propagazione di onde di superficie libera.* Tesi di Dottorato di ricerca in Meccanica Applicata e Teorica. Università La Sapienza, Roma. 1993

[3] L. Van Dommelen, E.A. Rundensteiner. *Fast adaptive summation of point forces in two-dimensional Poisson equation.* J. Comput. Phys., **83**, 126–147. 1989

A RANS-based Technique and its Application to Free Surface Flow Phenomena of Relevance in Marine Technology

Tanmay Sarkar, K.B. Salui & Dracos Vassalos
Ship Stability Research Centre University of Strathclyde Glasgow , UK
e.mail:tanmay.sarkar@strath.ac.uk

In marine technology almost all the important flow phenomena are dominated by the presence of free surface. Hence, ability to track free surface is an important aspect for success of any numerical technique used for predictions of these flow phenomena. So far most of the methods used for this purpose are based on potential flow assumptions. Methods based on potential flow invariably fail to produce accurate results when viscous effects play an important role e.g. separation, vortex generation, interaction of free surface and viscous separating flow. With the development of computing power over the last decade attention has now shifted to explore the possibility of application of the RANS (Reynolds Averaged Navier Stokes) techniques for simulation of the free surface flows. Normally two types of approaches are prevalent. These refer to free surface tracking and free surface capture techniques. In free surface tracking grid is adjusted every time instant to comply with the movement of the free surface and conservation equations are solved in the new position of the grid. In free surface capture, the technique solution domain is extended above the free surface to include part of the air. An additional transport equation for a scalar called void fraction (VOF) is solved. Computational cells full of water are initialised with a value 1 for VOF and those with air is given a value of zero or vice versa. Cells filled partly with air or water are given a fractional value of VOF and located at the free surface. At the end of each time step new positions of the free surface are determined from the new positions of the cells with fractional values of VOF. Methods based on free surface capturing technique can capture extreme phenomena such as wave breaking. In this paper a newly developed free surface capturing technique by Muzaferija et al known as High Resolution Interface Capturing (HRIC) scheme is used for simulating a number of important flow phenomena such as sloshing, slumping of a water column, moving body near the free surface and flow past a heaving and rolling body at the free surface. This method is available in the proprietary software ICCM-Comet used in the simulations presented here.

The solver Comet is based on an unstructured collocated grid technique and uses a variation of the SIMPLE scheme for pressure correction. The scheme HRIC used for free surface capturing helps in reducing numerical diffusion and in enhancing accurate definition of free surface. The following paragraphs present sample results from applications of this technique to different test cases.

Sloshing:

In this test case non-linear liquid sloshing in a rectangular tank is simulated. The tank is subjected to a sinusoidal horizontal acceleration A(t) with amplitude A_0 and frequency • . Simulation results are compared with results obtained for the same test case by Yamada & Takikawa and with analytical solutions. Comparisons are very good and serve to substantiate the efficiency of the present method.

Slumping of a Water Column

As a second test case for the free surface modelling ability of the adopted method, the problem of a slumping water column on a horizontal floor is considered. At the beginning of the process the right wall is suddenly removed, and hence the water column starts to collapse under the influence of gravity and to form an advancing water wave. Experimental results for this problem are reported in Martin and Moyce for the position of the leading edge of the water versus time as water flows to the right. Numerical analysis of the same test case are also carried out by Hirt and Nicholas and Jun and Spalding.

Comparisons of the results for this case with available experimental and numerical results clearly show the ability of the present method to tackle problems with free surface.

Flow Past a Body Near the Free Surface

In this example simulation of flow past a rectangular body near the free surface is considered. This is an interesting flow phenomenon, which has a number of practical applications in ship and offshore hydrodynamics, for example the motion of AUV (Autonomous Under Water Vehicle) or submarine near the free surface. This example tests the present technique in its ability to simulate flow in the presence of a moving or floating body near the free surface. Results show that the elevated/depressed free surface in front/behind the body could successfully predicted. Three separated recirculating regions are observed, namely, the largest recirculating region behind the body, the small region just below the body and the third near the free surface viscous region due to free surface viscous flow and wave breaking. The velocities are increased at the top and bottom of the body. Similar flow characteristics are also observed by Wan, Miao & Dai. The ability of the present technique to capture the viscous phenomena like wave breaking associated with flow past a body near the free surface demonstrates the future potential of application of a RANS based technique to seakeeping problems. These methods are better suited than potential flow based techniques to resolving complex flow phenomena like wave breaking which are dominated by viscous effects and are frequent in nature and seakeeping applications.

Heaving

Flow is simulated past a heaving cylinder of dimension 2*2m. The draught of the cylinder is taken as 1m. The cylinder is subjected to forced heaving by moving the grid with time. Amplitudes of forced heaving are varied from 0.2 to 0.6m. The solution is considered assuming the flow as two-dimensional. A large solution domain is considered to avoid reflections of the radiated wave from the boundaries of the solution domain during the simulation. The solution domain is divided vertically into three parts. The middle part is allowed to move with the body. The other two parts alternately expand and contract depending on the direction of heaving motion.

Figure 1 presents velocity vectors and the free surface at four different time instants for large amplitude heaving oscillation of the cylinder. These are 0.999T, 1.247T, 1.499T and 1.814T respectively. T is the time period of the oscillation. The figures show intricate details of the vortex/vorticity generation around the heaving body. A similar nature of flow variables is also observed by Yeung & Ananthkrishnan.

Figure 2 shows the heave force time history for a typical case (amplitude=0.3B, B is the beam of the body), where it can be seen that the viscous component of the force is very small and almost negligible compared to the dynamic component. Similar results were obtained by Yeung & Anantakrishnan and Gentaz et al. Comparison of the heaving force (pressure and viscous) from the present simulation with that obtained by Gentaz et al. is very good with the exception of a small difference in phase. Large negative values of the force are found at the starting point. This results from singularity in stress found in impulsively started motion of bodies. Similar types of force histories are also found for other amplitudes of motion considered in the present simulation. From these typical results it is obvious that the present method could successfully simulate the main features of the flow past a heaving cylinder.

Rolling

The dimensions of the cylinder are 0.4*0.4. A solution domain extending from –4.0m to 4.0m in x direction is taken. In y direction the solution domain extends from –1.4m to 1.4m. The cylinder is placed at the origin. Initial draught of the cylinder is taken as 0.2m. It is assumed that the cylinder is rolling at an undisturbed free surface. The cylinder is forced to roll by means of an external harmonic forcing function. The grid consists of two parts. One part is allowed to move with the cylinder and the other part is fixed. The moving part of the grid slides with respect to the fixed part with the same velocity as the roll velocity of the cylinder. Figure 3 presents the velocity vectors around the cylinder at different stages of roll motion. The cyclic nature of the flow around the cylinder is evident from these figures. The results are shown for a roll amplitude equal to 11.5• . Similar results are also obtained for other amplitudes. Figure 4 presents a typical plot of added moment of inertia (a_{44}) and damping coefficients (b_{44}) obtained by the present method compared with a number of other numerical techniques and experimental results for a typical amplitude of roll equal to 2.87• . It can be seen from the comparisons of the results that the present method could successfully predict added moment of inertia and damping coefficient in roll. Similar results are also obtained for rolling of a triangular and a U-shaped body near the free surface.

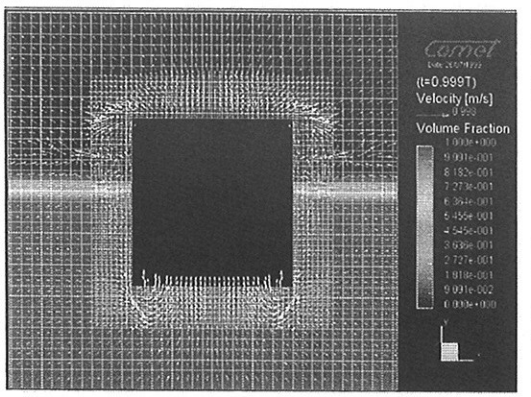

(a) t = 0.999T

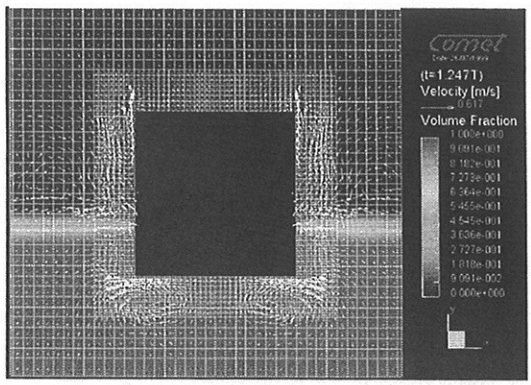

(b) t = 1.499T

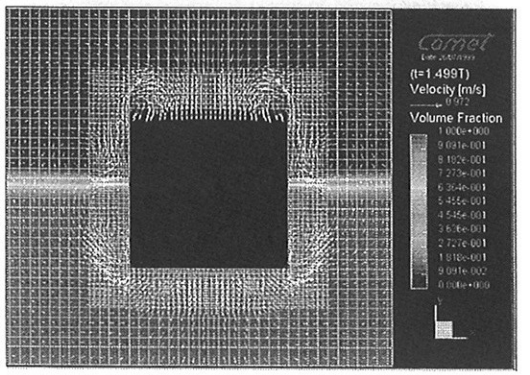

© t = 1.247T

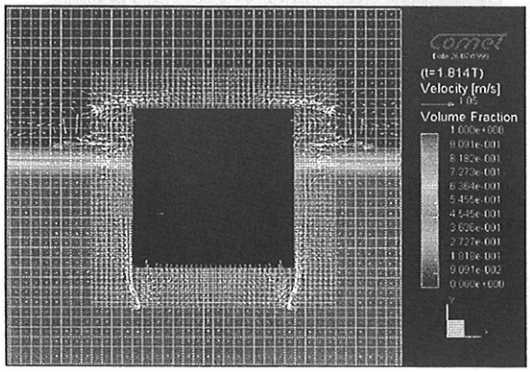

(d) t = 1.814T

Fig. 1. Velocity Vectors & Free Surface (VOF=0.5) Plots for Heaving Cylinder

Conclusion

In this paper, results of application of a RANS-based technique in simulating a number of important flow phenomena are presented. The results show that the present technique could successfully simulate the key characteristics of the physical flow. In viscous flows, results produced are better than those obtained from inviscid techniques. This is particularly true for the roll added moment of inertia and damping coefficients. However, extensive validation tests including extension to practical 3-D hull forms are required before contemplating the application of the technique to real life problems.

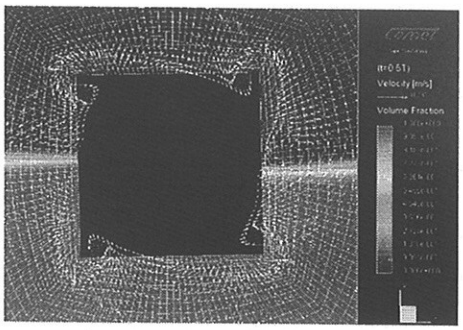

(a) t/T = 0.5

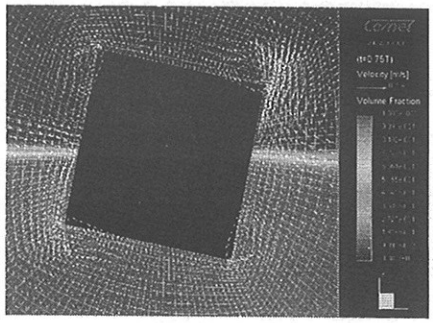

(b) t/T = 0.75

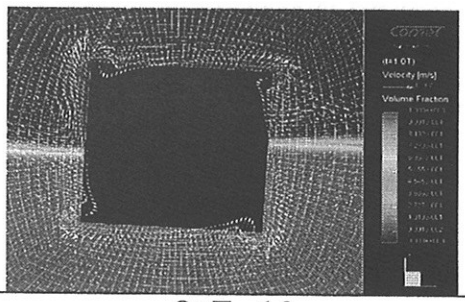

© t/T = 1.0

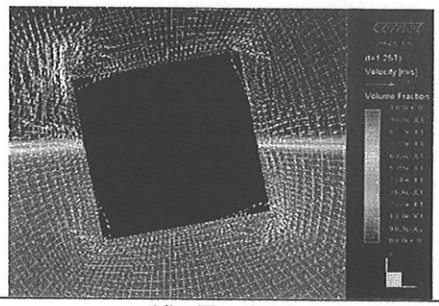

(d) t/T = 1.25

Fig. 3. Velocity Vectors in Roll Motion

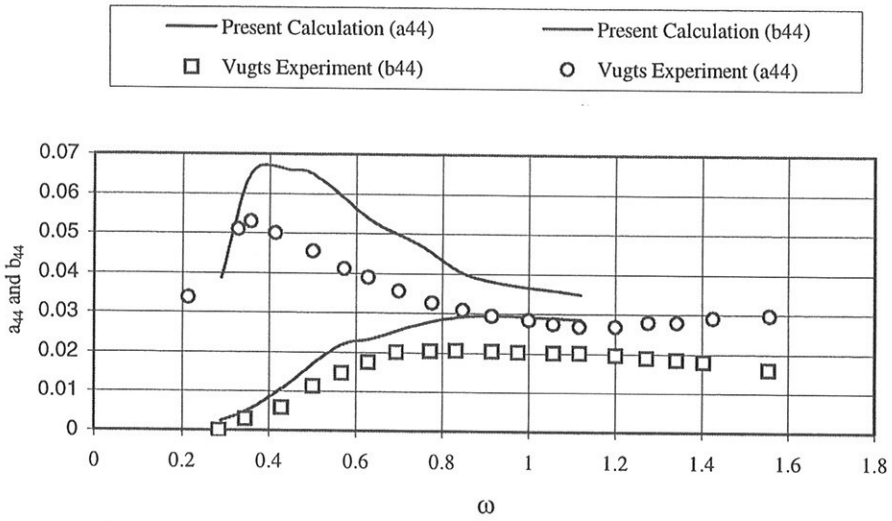

Fig.4 Added Moment of Inertia and Damping Moment Coefficient (2.87 degree)

Two Eulerian Approaches for Free-Surface Problems

Vladimir SHIGUNOV, *Lars* MUCK
AB 3-13, Technical University Hamburg-Harburg, Hamburg, Germany

The paper presents two Eulerian methods for solving problems with moving contact boundaries of fluids. The first method uses direct density advection to follow different fluids. It is based on a Godunov-type approximation for flow variables and a preconditioned dual-time stepping scheme for pressure-velocity coupling. The second method represents a level set approach with a segregated solution scheme and a SIMPLE-type scheme for pressure-velocity connection. Both methods were tested on the example of a broken dam problem in a closed container.

1 Mathematical Model and Discretization Method

The problem concerned is about two contacting viscous incompressible fluids with different physical properties. Variable density of the two-fluid system is used as a marker function for different materials. Thus, the conservation of mass must be used:

$$\frac{\partial \rho}{\partial t} + \nabla \cdot (\rho \mathbf{v}) = 0 \tag{1}$$

together with conservation of momentum

$$\frac{\partial}{\partial t}(\rho \mathbf{v}) + \nabla \cdot (\rho \mathbf{v} \otimes \mathbf{v} - \mathcal{P}) = \rho \mathbf{b} \tag{2}$$

and incompressibility constraint

$$\nabla \cdot \mathbf{v} = 0. \tag{3}$$

Hier, ρ is the mass density, $\mathbf{v}$ is the velocity vector, $\mathbf{b}$ is the external body force acceleration, and $\mathcal{P}$ is the stress tensor, that reads

$$\mathcal{P} = \mu \left[\nabla \mathbf{v} + (\nabla \mathbf{v})^T \right] - \mathcal{I} p, \tag{4}$$

where μ is the variable dynamic viscosity, p is the pressure, and $\mathcal{I}$ denotes the unit martix.

The above formulation does not account for any interfacial effects, such as surface tension. It can be taken into account by an appropriate treatment of the body-force term in (2). Formulation (1)–(3) allows a single-domain description of the two-fluid system and does not require any boundary conditions at the interface due to the full conservative formulation and discretization.

The numerical approach for discretization of the governing equations is based on the conservative finite difference (finite volume) method in space and the second-order implicit trapezoidal scheme in time. For storage of different flow variables, collocated grids are used in both methods.

2 Direct Density Advection Scheme

The system of flow equations (1)–(3) was preconditioned by adding pseudo-time derivatives either to all equations or only to the continuity equation. This approach alters the type of the inviscid part of the incompressible Navier-Stokes equations from parabolic to totally hyperbolic and thus allows to apply established time-marshing methods from gas dynamics to incompressible problems. With this formulation, time-accurate solution is approached asymptotically at a given physical time level as a steady state solution in pseudo-time, which is called dual time-stepping procedure.

With the dual time-stepping formulation, the left sides of all the equations (1) to (3) have the same hyperbolic structure and can be solved in a fully coupled manner, which seems to be the greatest advantage of the artificial compressibility-based formulations.

To advect a large density jump across the contact boundary, a discontinuous, Godunov-type approximation[1] was used to represent flow variables. To reconstruct numerical inviscid flux across cell interfaces, approximate Riemann solver of Roe was used. To obtain cell face states for Riemann solver, high order upwind biased reconstruction schema of TVD (total variation diminishing) type was applied.

Viscous fluxes were approximated with central differences in both methods.

Physical time-stepping and dual time-stepping schemes are implicit. To solve resulting algebraic system, noniterative one-parametric implicit lower-upper approximate factorization scheme was developed. To accelerate convergence of dual time subiterations, local adaptive pseudo-time step was used. CFL-number of pseudo-time iterations as well as the parameter of factorization scheme and pseudo-compressibility parameter were adjasted in test calculations to obtain the best convergence rate.

3 Level Set Scheme

Instead of using the mass conservation equation (1) direct, the level set approach represents the density as an one-argument function of the level-set function $\phi(\mathbf{r}, t)$, then Eq. (1) leads to the transport equation for the level set function ϕ:

$$\frac{\partial \phi}{\partial t} + \nabla \cdot (\phi \mathbf{v}) = 0, \tag{5}$$

Since the level set function has no strictly physical sence of a conserved variable, Eq. (5) was solved in the non-conservative advection form:

$$\frac{\partial \phi}{\partial t} + (\mathbf{v} \nabla) \phi = 0. \tag{6}$$

To make possible the use of usual smooth reconstruction schemes, the exact density field in this solver was artificially smoothed in a transition zone of finite thickness near the contact boundary. To keep the thickness of this transition zone constant, PDF-based reinitialization procedure was used.

Solution of the system (2), (3), and (6) at each physical time step was obtained in a segregated manner, so that one equation is solved in step. To eliminate decoupling and linearization errors, some number of outer iterations was carried out at every time step. Each equation was solved by usual SIP oder CG-type iterative solvers.

Pressure-velocity coupling follows the idea of SIMPLE-type pressure-iteration procedures. To exclude pressure-velocity decoupling probleme connected with collocated grid arrangement, some additional correction terms were included in the pressure equation.

Since the density field is obtained with this solver indirect, through the level set function, we must expect both local and global mass conservation errors. Because of full conservative treatment used for the momentum equation, the local mass conservation error leads to local inconsistency of momentum transport and then may deteriorate the solution process.

Instead of using non-conservative treatment of density in the momentum equations to solve this problem, a simple correction of the present conservative scheme was developed by explicit inclusion of the mass conservation into discretized momentum equation. Resulting algorithm does not show any disturbances even for the overturning stage of motion.

[1] Godunov-type approximation implies evaluation of solution that is discontinuous across cell interfaces. This is achieved by solution of Riemann problem for each cell interface with the following reconstruction of cell-averaged states at the next time level. Godunov-type approximations were successfully applied in shock-capturing solvers in gas dynamics and recently also for contact boundary problems.

4 Numerical Example

Both the above methods were applied to simulation of a broken dam problem in a closed container.

Comparison of calculation time characteristics for both methods is shown in Fig. 1. Note preferable performance of the continuum density advection method for finer grid due to the coupled character of solution in the dual time-stepping method.

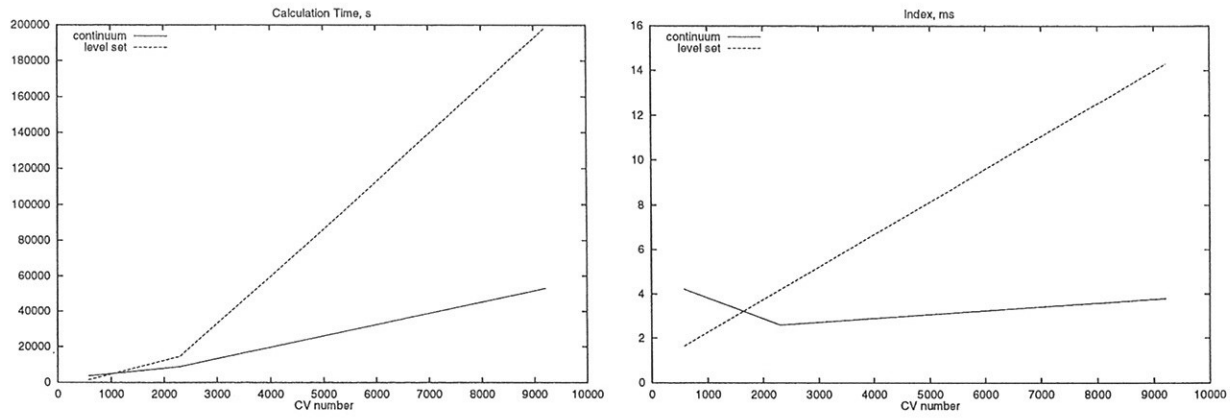

Figure 1: Calculation time for 1500 physical time steps (left frame) and the index $\frac{\text{CPU time}}{\text{number of time steps} \times \text{number of cells}}$ (right frame) for the continuum density advection method (solid line) and the level set based method (dotted line)

Front position and the height of water volume depending on time are shown in Fig. 2 compared with the experimental results of *Martin & Moyce* [2], while some instants of the evolution of the fluid volume from the left to the right side of the container with following overturning are shown in Fig. 3 (free surface position, velocity vector plots and pressure fields).

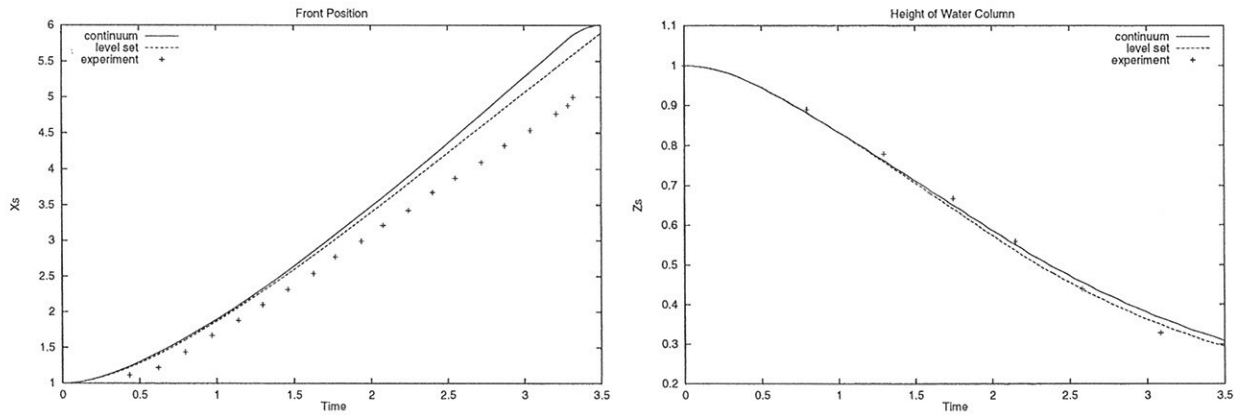

Figure 2: Front position (left frame) and height of water volume (right frame) depending on time compared with the experimental results of *Martin & Moyce* [2]

References

[1] V. Shigunov, *Development of Eulerian Approaches for free-surface problems*, Shipbuilding Dept. of Technical University Hamburg-Harburg Report Nr. 606, ISBN 3-89220-606-6 (2000)

[2] J. C. Martin, and W. J. Moyce, An experimental study of the collapse of liquid columns on a rigid horizontal plane, *Phil. Trans. Royal Soc. London A* **244,** 312 (1952).

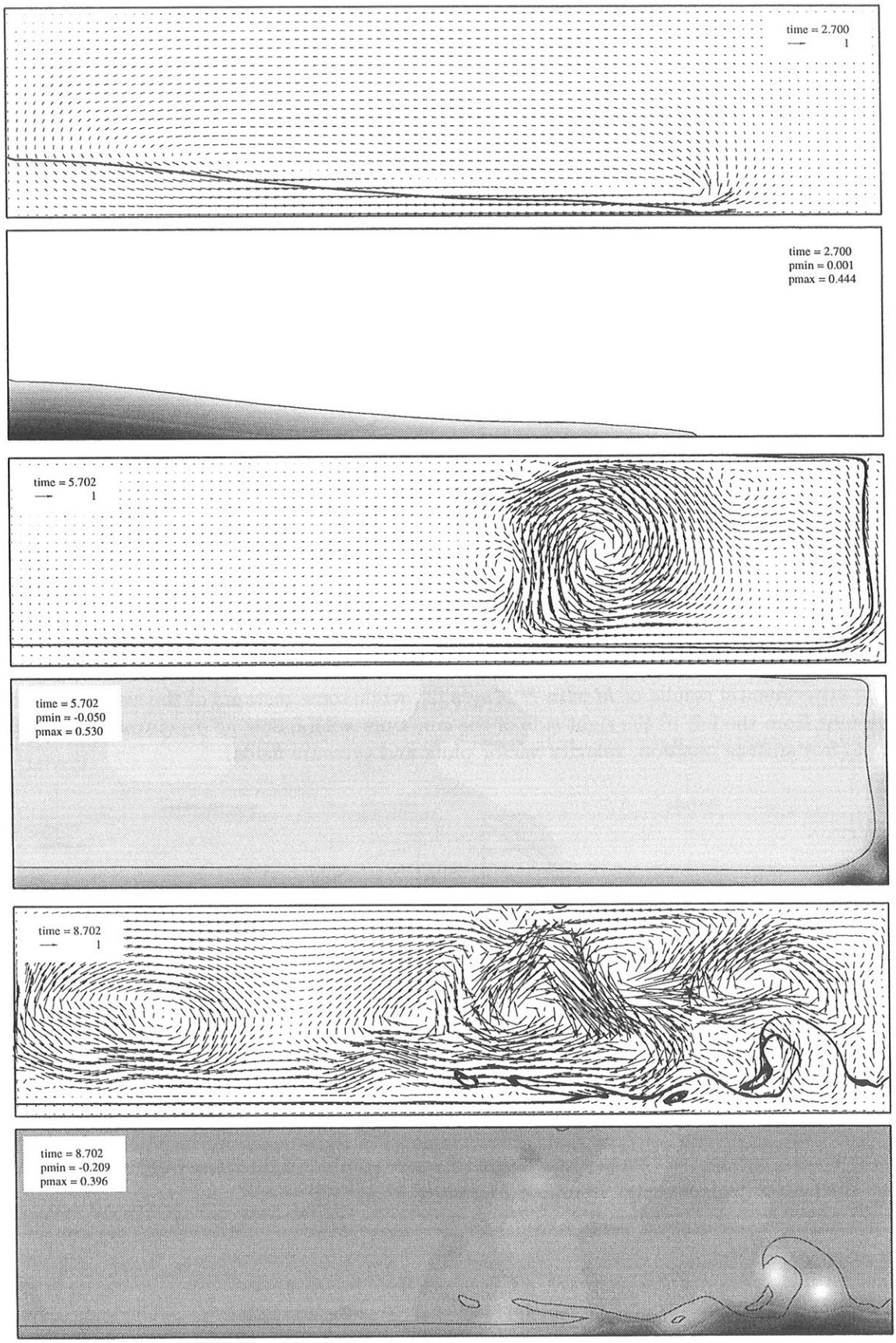

Figure 3: Velocity vector fields and density contour plots with corresponding pressure distributions obtained with the first method

A Test of Turbulence Models for Steady Flows Around Ships

S. U. Svennberg

Naval Architecture and Ocean Engineering, Chalmers University of Technology, 412 96 Göteborg, Sweden

Abstract. The steady flow field around the KRISO 300K VLCC (KVLCC2) without free surface has been simulated with eight turbulence models. These are ranging from k-ε and k-ω models to a Reynolds-stress model (RSM). The RSM model gave the best results, but it was not in perfect agreement with the experimental results. Both Menter's shear stress transport model (SST) and the Craft et al's nonlinear k-ε (CLS) model gave results in close agreement to the RSM model.

Introduction. The flow around the stern of a ship hull is very complex: high Reynolds-number, three-dimensionally curved surfaces and often a pair of strong longitudinal vortices. These are created where the flow passes over the region of high curvature between the bottom and the side of the hull (the bilge). The bilge vortices hit the propeller disk and cause a distortion of the flow into the propeller. Such distortions affect the efficiency of the propeller and can cause vibration, noise and cavitation. Lifting surfaces such as propeller blades have strong tip vortices that can also induce cavitation and thereby noise. For the design of the propeller and hull it is therefore important to be able to predict these vortices.

Over the years there have been a number of international workshops on ship flow calculations: SSPA-ITTC Workshop on Ship Boundary Layers 1980[1]; SSPA-CTH-IIHR Workshop 1990[2]; CFD workshop in Tokyo 1994[3]. A major problem pointed out by these workshops is the prediction of the bilge vortices. The most important reason for the difficulties is one of the following reasons or a combination of them: the turbulence modelling; the grid resolution; the accuracy of the discretisation. A review of CFD in Ship Design covering not only turbulence modelling can be found in Larsson[9].

In the present paper some results of an ongoing project for testing turbulence models for vortices in naval applications are presented. The test is carried out for four different cases: A vortex in a free-flow with three different axial velocities in the vortex core[14], a vortex pair embedded in a turbulent boundary layer[13], the flow around a ship[19] and the tip vortex from a wing[7]. This paper is focused on the third case, the flow field around a ship.

Turbulence modelling. Eight turbulence models ranging from k-ε and k-ω models to a Reynolds-stress model have been tested. These are: Standard k-ε[4] (KE), k-ε modified due to renormalization group theory[12] (RNG), standard k-ω[21] (KO), two combined k-ω/k-ε models[11] (BSL, SST) two algebraic stress-models, one with a second-order[8] (GS) and one with a third-order[5] (CLS) constitutive relation, and a standard Reynolds-stress-model[10] (RSM).

Solver. The turbulence models presented above have been used in the commercial program FLUENT 5.2[22]. Three of the models, KE, RNG and the RSM, are available in FLUENT 5.2. The other five models have been implemented into the FLUENT 5.2 code by the author using user defined functions and user defined scalars. The FLUENT 5.2 code is a finite volume code with collocated storage of the variables in the cell centre. A second order upwind scheme has been used for the momentum and turbulence quantities and second order interpolation has been used for the pressure where values of the different quantities were needed on the cell surfaces. The SIMPLE algoritm has been used for the coupling between the pressure and momentum equations.

Grid. The computational grid consisted of 15 structured and 4 unstructured blocks. The total number of cells was 662100. The grid used the symmetry in the double model and coverd therefore just one quarter of it.

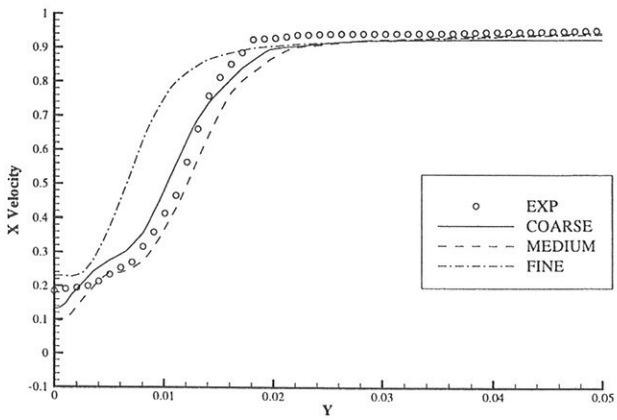

FIGURE 1. Axial velocity, Z=-0.05

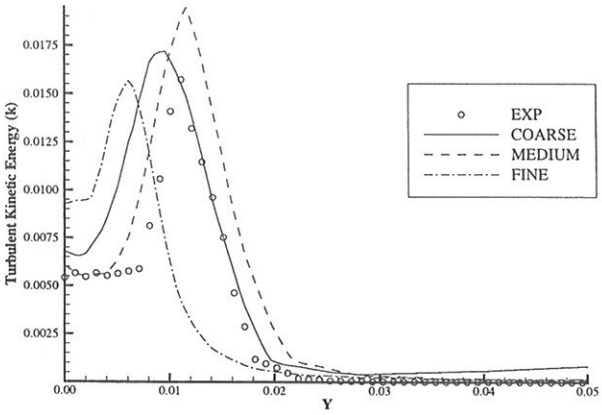

FIGURE 2. turbulent kinetic energy, Z=-0.05

The form of the grid was a quarter of a cylinder with half spheres at the ends. It had a length of two and a width of half a ship length. A grid refinement test including two coarser grids has been done. The flow structure in the propeller plane changes considerably between the different grids. There is no monotonic convergence. This can be seen in Figure 1 and Figure 2 where the axial velocity and turbulent kinetic energy are plotted along the Z=-0.05 line for the three different grids. The verification methodology suggested by Stern et al[15] needs monotonic convergence for a verification using only three grids. The coarsest grid is too coarse so its no idea to make a coarser grid, so a finer grid will be created.

Results and discussion. Calculated resistance coefficients are presented in Table 1 below. The experimental data (EXP) comes from the towing-tank test[20] while all the flowdata in the present paper come from wind-tunnel test[19]. The viscous drag coefficient C_F (C_{F0}) for the EXP data is calculated using the ITTC-57 line and the pressure coefficient C_P is the residuary resistance from the towing tank experiment, i.e. both the wave and pressure drag is included in this figure. The form factor k is calculated using $k = C_T/C_{F0} - 1$. The total resistance is overpredicted by all the tested models. The SST model that predicts the lowest drag has a limit on the turbulent viscosity close to the wall. Low viscosity close to the wall gives lover viscous drag and the SST model underpredicts the viscous drag.

The flow field in the propeller plane computed with some of the models can be found in Figure 4 - Figure 8 and the experimental data from the wind-tunnel test[19] are plotted in Figure 3. Contours of the axial velocity are plotted in the left part of the figures and vectors of the secondary velocity components are plotted in the right part of the figures, only every third vector is plotted to make the figures readable. The velocities are normalised by the undisturbed free stream velocity and the reference vector equals a velocity of magnitude one.

From the figures its obvious that no one of the models manages to predict the flow field in the propeller plane perfectly, but all models show that there are bilge vortices present. The RSM model predicts the flow field in closest agreement with the experiments, but both the SST model with its limit on the turbulent viscosity and the CLS model with its nonlinear constitutive relation give results close to the RSM model.

Table 1: Resistance coefficients

Model	C_P*10^3	C_F*10^3	C_T*10^3	k
EXP	0.680	3.450	4.130	
KE	0.855	3.764	4.619	0.3390
RNG	0.873	3.679	4.552	0.3195
KO	0.915	3.681	4.596	0.3324
BSL	0.925	3.555	4.480	0.2989
SST	0.951	3.441	4.392	0.2732
GS	1.413	5.382	6.794	0.9696
CLS	1.158	4.427	5.586	0.6192
RSM	1.035	4.383	5.418	0.5707

Deng and Visonneau[6] have showed that the wall reflection term in the present RSM model reduces the secondary velocities close to the wall. This reduction affects the strength of the bilge vortices and might explain the overprediction of the resistance.

Deng and Visonneau[6] also shoved that the assumption of local equilibrium between production and dissipation of turbulence is not valid at the propeller plane of a similar flow. Nonlinear algebraic RSM models such as the GS and the CLS models are based on an asumption of local equilibrium. These models should therefore not be expected to give accurate results since this condition is not fullfilled at the propeller plane.

The GS model gave more pronounced hook shape in the iso contours of the axial velocity than the KE model that it is based on, but less than the CLS model. In fact it is quite close to the hook shape predicted with the KO model, and it is therefore not plotted in this short paper.

The CLS model is also based on the KE model in this test. Comparing the results of the KE model with the results of the CSL model it can be seen that the anisotropic terms in the constitutive relation are of great importance even though the equilibrium condition is not satisfied in this flow. The nonlinear terms reduce the production of turbulent energy in the vortex.

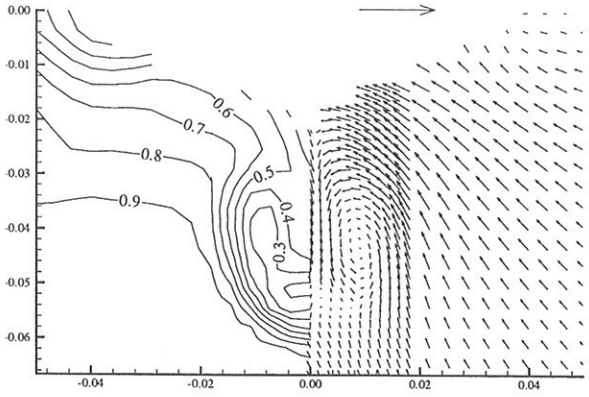

FIGURE 3. Experimental data

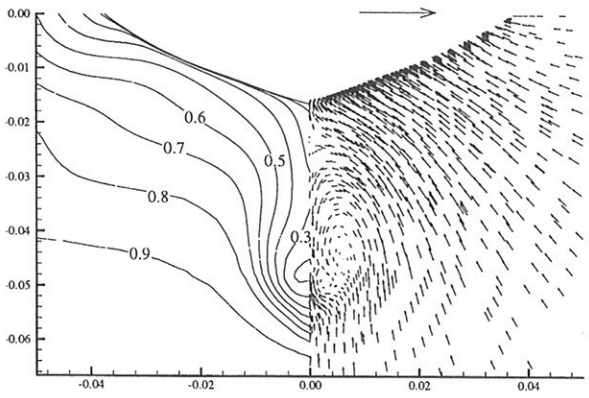

FIGURE 4. KE model.

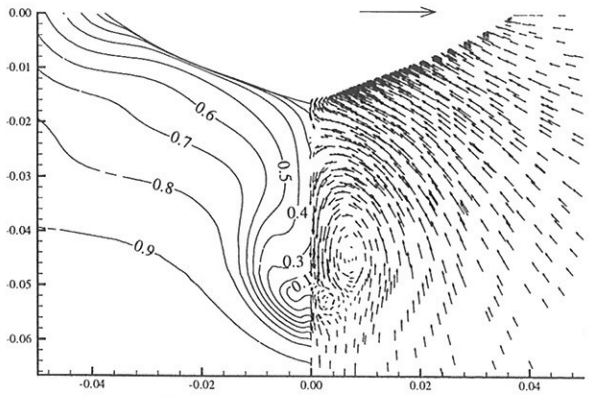

FIGURE 5. KO model.

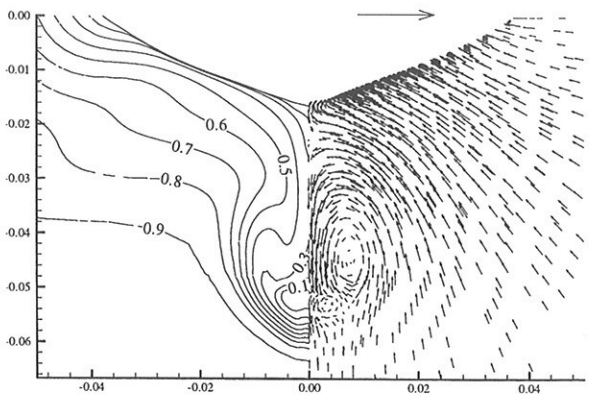

FIGURE 6. SST model

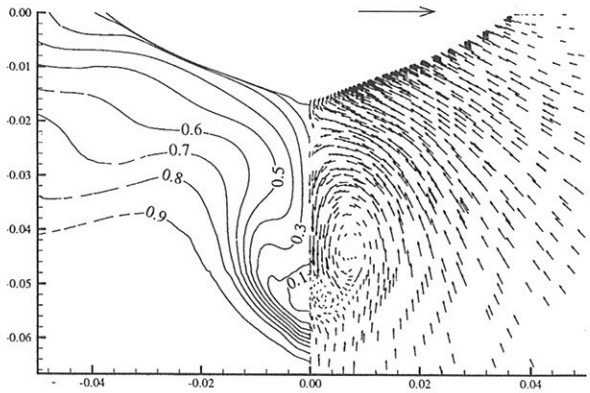

FIGURE 7. CLS model

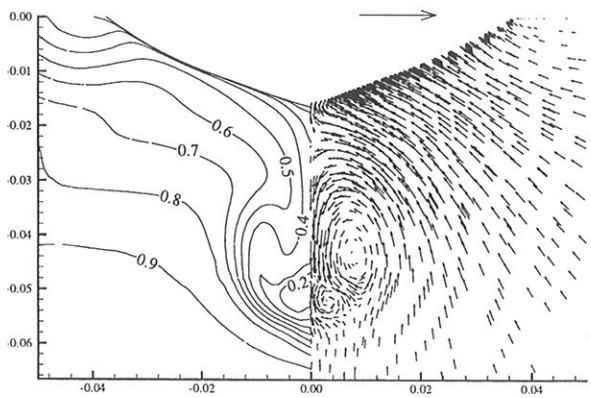

FIGURE 8. RSM model

The KO model gave results that are slightly better than the result from the KE model. The KO model is less sensitive to adverse pressure gradients than the KE model. The BSL model gave almost exactly the same results as the KO model, so it is not plotted here. This shows that the limitation on the turbulent viscosity is responsible for the improvement of the SST results because the only difference between the SST model and the BSL model is this limit. It is also known from the workshops mentioned above that limiting the turbulent viscosity can improve the prediction of the bilge vortices.

In the first parts of this test of turbulence models[16,17] it can be seen that an axial velocity difference between the vortex centre and the surrounding flow is reduced too fast with all models no matter if there is a wall present or

not. This can explain why the hook shape in the axial velocity contours is less pronounced in the computations than in the experiment while the vortex strength and position seems to be of the right size, as can be seen in Figure 9 below.

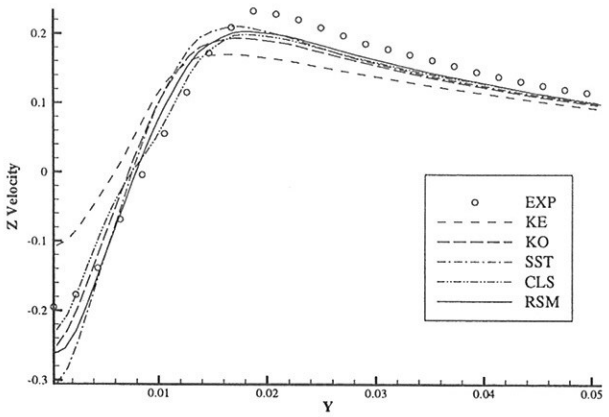

FIGURE 9. Vertical velocity along a horizontal line trough the vortex centre

All the different models predict not just the bilge vortex they also predict a second smaller vortex. The KE, RNG, GS and CLS models predict a weaker secondary vortex than the other models. In the experimental data this vortex is just seen as a small disturbance in Figure 3 but the experimental data is not completely symmetric and this vortex is more pronounced on the other side of the centerline. The data on the other side of the centerline are not plotted in the figure to make the iso-contours more visible. The propeller hub is cut off straight in the experiments while it is rounded in the calculations. This rounding comes from the surface mesh provided by the organisers of the Gothenburg 2000 workshop. This mesh is used as surface description in the computations. The round tip can strengthen such vortices.

A more complete presentation and discussion of the results in this test will soon be published[18].

Conclusions. Eight turbulence models have been tested on the steady flow around the KRISO 300K VLCC (KVLCC2) without free water surface. It is a challenging task to predict the complex flow field at the stern of a ship. No one of the tested turbulence models manages to reproduce the flow field completely. Simple modifications such as the limitation of the turbulent viscosity in the SST model can give considerable improvements of the results. Even thoug the RSM model gives results in closest agreement with the experimental data and with a pronounced hook shape in the iso-contours of the axial velocity, there is considerably more to be done to reach a perfect simulation result.

References

[1] Proceedings, "SSPA-ITTC Workshop on Ship Boundary Layers" (1980), Ed. L. Larsson, SSPA Report No. 90, 1980, Göteborg, Sweden.

[2] Proceedings, "1990 SSPA-CTH-IIHR Workshop on Ship Viscous Flow" (1990), Eds. L. Larsson, V. C. Patel and G. Dyne, Research Report No. 2. Flowtech International AB, 1991 Göteborg, Sweden.

[3] Proceedings, "CFD Workshop Tokyo 1994", (1994) Ed. Y. Kodama, Ship Research Institute, Tokyo, Japan

[4] Chen H. C. and Patel V. C., AIAA Journal, June 1988, vol. 26, No. 6, pp. 641-648

[5] Craft T. J., Launder B. E. and Suga K., Int. J. Heat and Fluid Flow, vol. 17, no. 2, April 1996

[6] Deng G. B. and Visonneau M., Seventh International Conference on Numerical Ship Hydrodynamics, July 1999, Nantes, France

[7] Fruman D., Dugue C., Pauchet A., Cerruti P., Briancon-Marjolet L., Nineteenth Symposium on Naval Hydrodynamics, 1992, Seoul, Korea

[8] Gatski T. B. and Speziale C. G., Journal of Fluid Mechanics, vol. 254, 1993, pp. 59-78

[9] Larsson L., Ship Technology Research, July 1997, vol. 44, no. 3, pp. 135-154.

[10] Launder B. E. and Shima N., AIAA Journal, 1989, vol. 27, No. 10, pp. 1319-1325

[11] Menter F. R, AIAA Journal, August 1994, vol. 32, No. 8, pp. 1598-1605

[12] Orzag S. A., Yakhot V., Flannery W. S., Boysan F., Choudhury D., Maruzevsky J. and Patel B., Near wall Turbulent Flows, page 1031. Elsevier Science Publishers B. V., 1993

[13] Pauley W. R. and Eaton J. K., AIAA Journal, 1988 vol. 26, No. 7, pp. 816-823

[14] Phillips W. R. C. and Graham J.A.H., Journal of Fluid Mechanics, 1984, vol. 147, pp. 353-371

[15] Stern F., Wilson R. V., Coleman H. W., Paterson E., G., Iowa Institute of Hydraulic Research, IIHR Report No. 407, September 1999

[16] Svennberg S. U., "A Test of Turbulence Models for a Vortex in a Free-Stream", Licentiate Thesis, Department of Naval Architecture and Ocean Engineering, Chalmers University of Technology, Göteborg Sweden, CHA/NAV/R-96/0047

[17] Svennberg S. U., "A Test of Turbulence Models for a Vortex Pair Embedded in a Turbulent Boundary Layer", Department of Naval Architecture and Ocean Engineering, Chalmers University of Technology, Göteborg Sweden, CHA/NAV/R-98/0055

[18] Svennberg S. U."A Test of Turbulence Models for Bilge Vortices", Dapartment of Naval Architecture and Ocean Engineering, Chalmers University of Technology, Göteborg Sweden, CHA/NAV/R-98/0056

[19] Van S.H., Kim W.J., Kim H. R., and Lee S.J. "Wind Tunel Test on Flow Characteristics of KRISO 300K VLCC double model", Proceedings of Japan-Korea Joint Workshop on Marine Hydrodynamics (JAKOM99), Fukuoka, Japan.

[20] Van, S.H., Kim, W.J., Yim, G.T., Kim, D.H., and Lee, C.J., 1998, Proceedings 3rd Osaka Colloquium on Advanced CFD Applications to Ship Flow and Hull Form Design, Osaka, Japan

[21] Wilcox D.C., "Turbulence Modelling for CFD" DCW Industries, 1993, ISBN 0-9636051-0-0

[22] www.fluent.com

Simulation of Viscous Flow about "ESSO OSAKA" in Maneuvering Motion

Noritaka Takada, R&D Center Nagasaki, Mitsubishi Heavy Industries, Ltd.
Ould M. El Moctar, Hamburg Ship Model Basin, elmoctar@hsva.de

Introduction

Recently, CFD has turned to prediction methods to simulate the viscous flow about ship in maneuvering motion. We apply here two RANSE solvers to the simulation of viscous flow about the VLCC "ESSO OSAKA", Table 1, in various maneuvering motions. Simulation results are validated against experiments.

Table 1 Principal particulars of "ESSO OSAKA"

	Model	Ship
Length	4.600 m	325.00 m
Breadth	750.92 mm	53.000 m
Draft	307.95 mm	21.73 m
Displacement	882.57 kg	319040 t
Speed	0.611 m/s	9.99 kn
Froude No.	0.091	
Reynolds No.	2.5×10^6	1.5×10^9

Model tests

Maneuvering captive model tests were performed for the "ESSO OSAKA" in trial condition at the Nagasaki R&D Center. The model was towed with propeller revolution and zero rudder angle δ. The hydrodynamic forces acting on the model (total), rudder and propeller were measured by load cells. The forces acting on the bare hull are obtained by:

$$Y_H = Y_{HPR} - Y_P - (1+a_Y)\hat{Y}_R$$
$$N_H = N_{HPR} - N_P - (1+a_N)(\hat{Y}_R(x_R - x_G) + Q_R)$$
$$\hat{Y}_R = -F_N \cos\delta + F_T \sin\delta \qquad (1)$$

Y is the sway force, N the yaw moment. The suffixes denote hull (H), propeller (P) and rudder (R). x_R is the x position of the rudder axis, x_G the center of gravity. x points forward, y to starboard and z downward. F_N, F_T and Q_R are the normal and the tangential forces and the torque acting on the rudder, respectively. a_Y, a_N are the interference coefficient between hull and rudder obtained by rudder angle tests.

Numerical methods

"NICE"

An unsteady flow simulation method was developed on basis of the "NICE" code developed by Kodama (1992). The Navier-Stokes equations in the conservative form for an incompressible fluid in the artificial compressibility method are formulated as follows:

$$\frac{\partial q}{\partial \tau} = -\frac{\partial}{\partial x}(F+F_v) - \frac{\partial}{\partial y}(G+G_v) - \frac{\partial}{\partial z}(H+H_v) + K = -R = 0 \qquad (2)$$

$$q = \begin{pmatrix} u \\ v \\ w \\ p \end{pmatrix}, F = \begin{pmatrix} u^2+p \\ uv \\ uw \\ \beta_p u \end{pmatrix}, G = \begin{pmatrix} vu \\ v^2+p \\ vw \\ \beta_p v \end{pmatrix}, H = \begin{pmatrix} wu \\ wv \\ w^2+p \\ \beta_p w \end{pmatrix}$$

$$F_v = -\nu \begin{pmatrix} \tau'_{xx} \\ \tau'_{xy} \\ \tau'_{xz} \\ 0 \end{pmatrix}, G_v = -\nu \begin{pmatrix} \tau'_{xy} \\ \tau'_{yy} \\ \tau'_{yz} \\ 0 \end{pmatrix}, H_v = -\nu \begin{pmatrix} \tau'_{xz} \\ \tau'_{xyz} \\ \tau'_{zz} \\ 0 \end{pmatrix}$$

(u,v,w) are the fluid velocity components in the body-fixed coordinate system and p the pressure. τ is the pseudo-time and β_p the artificial compressibility parameter. ν is the coefficient of effective viscosity. τ_{xx} etc. are the Cartesian components of the Stokes tensor. K denotes the components of the body forces.

To solve unsteady flows, a time-accurate formulation is formulated as:

$$\frac{\partial q}{\partial \tau} + \frac{\partial \hat{u}}{\partial t} = -R, \quad \hat{u} = (u,v,w,0)^T \qquad (3)$$

The artificial compressibility relation is introduced in a fashion very similar to the steady-state case. When this equation is iterated in pseudo-time until $\partial q/\partial\tau = 0$, the divergence of velocity is 0 at each physical time, step Δt. Applying an implicit Euler finite difference formula to the pseudo-time derivative and a second-order backward-difference formula to the physical time derivative gives:

$$I_{t\tau}(q^{n+1,m+1}-q^{n+1,m}) = -R^{n+1,m+1} - \frac{I_m}{\Delta t}(1.5q^{n+1,m} - 2q^n + 0.5q^{n-1})$$
$$I_{tt} = diag\left[\frac{1}{\Delta\tau}+\frac{1.5}{\Delta t},\frac{1}{\Delta\tau}+\frac{1.5}{\Delta t},\frac{1}{\Delta\tau}+\frac{1.5}{\Delta t},\frac{1}{\Delta\tau}\right], \quad I_m = diag[1,1,1,0] \tag{4}$$

n,m are the physical time and the pseudo-time levels, respectively. The body force term consists of the inertia force caused by the transformation of coordinate and is given by

$$\hat{f} = -2\hat{\omega}\times\hat{u} - \hat{\omega}\times(\hat{\omega}\times\hat{r}) - \dot{\hat{\omega}}\times\hat{r} - (\dot{\hat{V}} + \omega\times\hat{V}) \tag{5}$$

$\hat{\omega}$ is the angular velocity vector $(0,0,r')$ and $\hat{r}$ the position vector (x,y,z) of the point defining the fluid velocity and $\hat{V}$ the translational velocity vector $(u',v',0)$. Four terms in the RHS of Eq. (5) indicate the Coriolis force, the centrifugal force and the unsteady forces due to angular and translational accelerations, respectively.

The numerical scheme to solve Eqs. (4) uses the approximate factorization approach. The inviscid fluxes are obtained using a third-order MUSCL-type flux and the viscous fluxes using a second-order central differencing. The modified Baldwin-Lomax model improved for simulating the boundary layer in the vicinity of the stern is adopted.

"COMET"

The RANS solver Comet is based on the finite-volume method. The conservation equations for mass and momentum in their integral form are numerically approximated using the midpoint rule approximation. The discretized continuity equation is transformed in to a pressure-correction equation following the SIMPLE algorithm, adapted to colocated grids. The momentum component equations are linearized using the Picard Iteration scheme. The RNG-k-ε Model with wall functions is used. The solution method is designed to use unstructured grids with cell-wise refinement. For more details see Demirdzic and Muzaferija (1995).

Results

Both codes used the same grid to eliminate the influence of grid errors in the comparison of the two approaches. The innermost layer of cells was chosen such that an average y^+=80 was obtained. The structured grid consisted of 160,000 cells for both ship sides together. The flow was assumed to be fully turbulent. Due to the low Froude number, free surface effects on side forces and moments can be assumed to be negligible. Thus the computations modelled the free surface as plane of symmetry. The propeller was modelled treated by the body force method with the infinite wing theory approach. This approach is justified as the time-scale of the ship motion is much larger than that of the propeller rpm. The rudder was not modelled. Hull forces are made nondimensional with density ρ, speed U, ship length L and draft d:

$$X' = \frac{X_H}{0.5\rho LdU^2}, \qquad Y' = \frac{Y_H}{0.5\rho LdU^2};$$
$$N' = \frac{N_H}{0.5\rho dL^2U^2}$$

The PhD thesis of El Moctar (to appear in late 2000) will give a detailed investigation of the effect of rudder and propeller on the hull forces and moments using finer grids.

Oblique tow motion

The turbulent flow around "ESSO OSAKA" Tanker were computed for a nondimensional sway velocity between –0.2 und 0.2, corresponding to drift angles $-11.54° \le \beta \le 11.54°$. The computed longitudinal forces and yaw moments differ little between the two methods, Fig.1. Side forces differ by 5%, yaw moments less. Computed and measured results agree well considering the coarse mesh, Fig.2. The longitudinal force was not measured.

Circular motion

The flow for the tanker model was computed for steady turning with speed U=0.611m/s and non-dimensional turning rates -0.4<r'=rL/U<0.4. r is the turning rate. The computation used a rotating coordinate system in which the flow appears to be steady. Computed forces agree well with each other, Figs.3 and 4. Computed side forces agree well with experiments except for r'=-0.2, Fig.5. Yaw moments agree also well with experiments, Fig.5.

Pure sway and yaw motions

Pure swaying motion is given by:

$$u' = \sqrt{1 - v'^2}, \; v' = \overline{v'} \sin\left(\frac{\sqrt{gL}}{U} \omega'' t' \right), \quad r' = 0 \quad (*)$$

$\overline{v'}$ is the non-dimensional sway velocity amplitude, g=9.81 m/s^2, $t'(= tU / L)$ the non-dimensional time, $\omega''(= \omega / \sqrt{g/L})$ the non-dimensional angular frequency. Pure yaw motion is given by the non-dimensional yaw rate r' function in a corresponding manner. Computations were performed in conditions that $\overline{v'} = 0.3$, $\omega'' = 0.15$ in pure sway and $\overline{r'} = 0.3$, $\omega'' = 0.15$ in pure yaw. Experimental results show results using Fourier analysis. Both computations estimate frequency and phase of forces and moments well. However, the computed amplitudes of forces and moments are smaller than measured, Figs.6 and 7.

References

Kodama, Y. (1992), "*Computation of Ship's Resistance Using an NS Solver with Global Conservation*", J. Soc. Naval Arch. Japan 172

Demirdzic, I.; Muzaferija, S. (1995), "*Numerical method for coupled fluid flow, heat transfer and stress analysis using unstructured moving meshes with cells of arbitrary topology*", Comput. Methods Appl. Mech. Engrg. 125, pp.235-255

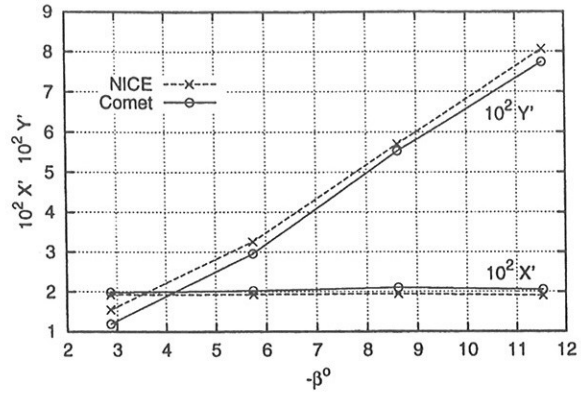

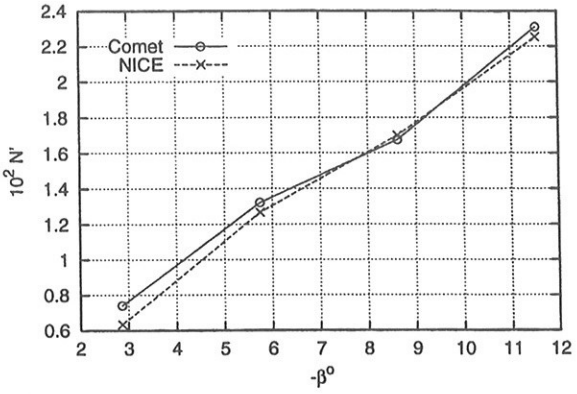

Fig. 1: Computed forces and moments, ship in oblique flow without Propeller

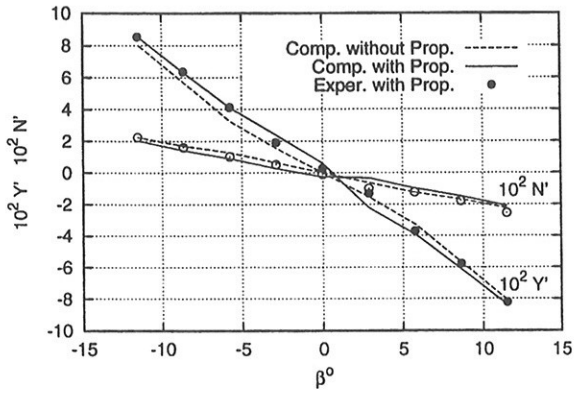

Fig. 2: Measured and NICE-computed forces and moments (oblique flow)

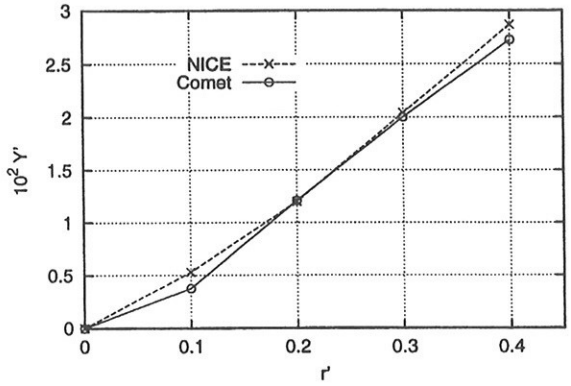

Fig. 3: Computed side force, ship in circular motion without Propeller

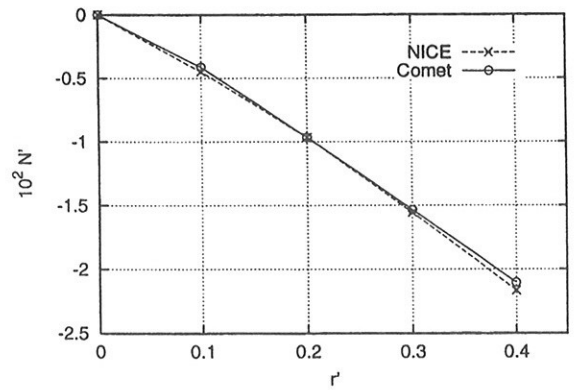

Fig. 4: Computed yaw moment, ship in circular motion without Propeller

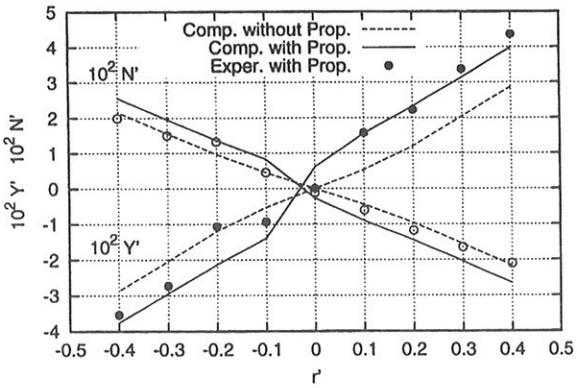

Fig. 5: Measured and NICE-computed forces and moments (circular motion)

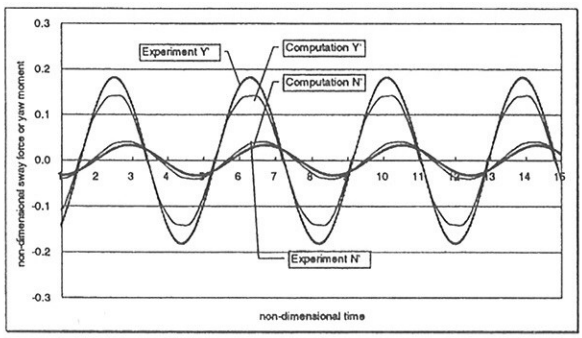

Fig. 6: The time history of the sway force and yaw moment in pure swaying motion

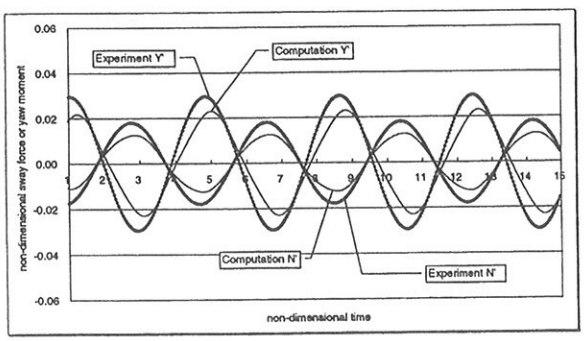

Fig. 7: The time history of the sway force and yaw momen in pure yawing motion

Adaptive grid flow solutions around a Mariner hull at drift

Turnock, S.R., Wright A.M., Pattenden, R., Pemberton R.
School of Engineering Sciences, Ship Science, University of Southampton, Southampton. U.K.
Tel No: 44 (0)23 80592488 Fax No: 44 (0)23 80593299 Email: steve@ship.soton.ac.uk

Introduction

Flow solutions around realistic ship hull forms require a high quality mesh, which has adequate resolution in areas of interest and yet minimises the total computational effort. In the case of a ship at an effective angle of drift, for example during a low speed manoeuvre, the hull behaves like an extremely low-aspect ratio wing and the magnitude of the side force is controlled by the rotational flow generated over the keel. In this case it is not possible *a priori* to identify where the vortical flow exists and hence where high grid resolution is required. This work examines for the Mariner hull[1] at drift how the flow code ERIC[2], currently under development at Southampton, is used to capture correctly the flow and hence calculate the side force.

A conventional multi-block structured mesh is still the most common approach for sub-dividing the fluid domain into discrete finite volumes. A hyper-cube approach allows the addition of smaller blocks at suitable locations away from the hull surface[3]. However, this may require a progressive level of solutions at each stage - solving a coarse mesh, generating a new finer block structure and then resolving. The approach taken in this work is to operate on individual finite volume cells through a process of sub-division during solution convergence. The control of this sub-division process is determined by the local pressure gradient, as well as a quantified measure of geometrical grid quality.

Flow Solver

ERIC (EuleR Incompressible Code) uses artifical compressibility [4] within a flux vector splitting framework upon a node centred Euler solver. Unstructured data allows the use of arbitrary polyhedrals and hence no restrictions are placed on mesh adaption. An explicit Runge-Kutta method is used to march the solution to steady state.

The basic format of artificial compressibility replaces the density term in the mass conservation equation with a pressure term which allows evolution through time. During time marching this set of equations will have no physical meaning but in steady state the time derivatives tend to zero and satisfy the standard Euler equations. The format of the governing equations, adapted for artificial compressiblity, are -

$$\frac{\partial \mathbf{U}}{\partial t} + \theta \left(\frac{\partial \mathbf{F}}{\partial x} + \frac{\partial \mathbf{G}}{\partial y} + \frac{\partial \mathbf{H}}{\partial z} \right) = 0 \tag{1}$$

$$\mathbf{U} = \begin{bmatrix} p \\ u \\ v \\ w \end{bmatrix} \quad \theta = \begin{bmatrix} \mathbf{c^2} & 0 & 0 & 0 \\ 0 & 1 & 0 & 0 \\ 0 & 0 & 1 & 0 \\ 0 & 0 & 0 & 1 \end{bmatrix} \quad \mathbf{F} = \begin{bmatrix} u \\ u^2 + p \\ uv \\ uw \end{bmatrix} \quad \mathbf{G} = \begin{bmatrix} v \\ uv \\ v^2 + p \\ vw \end{bmatrix} \quad \mathbf{H} = \begin{bmatrix} w \\ uw \\ vw \\ w^2 + p \end{bmatrix}$$

θ can be viewed as a preconditioning matrix, with $\mathbf{c}$ being the *artificial* speed of sound. From this an analogy with the equation of state for compressible flow can be drawn -

$$p = \mathbf{c}\rho_a \tag{2}$$

Thus ρ_a is an artificial density, hence the term artificial compressibility.

The initial selection of a value for the artificial speed of sound, $\mathbf{c}$, is that derived by Farmer et al (1994) -

$$\mathbf{c^2} = \mathbf{MAX}\left(\mathcal{K}(u^2 + v^2 + w^2), \mathbf{c^2_{MIN}}\right) \tag{3}$$

where $\mathcal{K}$ is a constant.

The flux terms of the conservative form of the Euler equations (1) can be split according to the direction of the characteristics via the directionalised Jacobian. Taking the one dimensional problem as a case study, if $\mathbf{F}^+$ is discretised with a backward difference scheme and $\mathbf{F}^-$ discretised with a forward difference then the concept of the upwind scheme

will be realised. The subscript i defines the discrete spatial position while the superscript n defines the timestep. This formulation results in

$$\begin{aligned} \mathbf{U}_i^n &= -\frac{\partial t}{\partial x}(\mathbf{F}^*_{i+\frac{1}{2}} - \mathbf{F}^*_{i-\frac{1}{2}}) \\ where\ \mathbf{F}^*_{i+\frac{1}{2}} &= \frac{\mathbf{F}_{i+1} + \mathbf{F}_i}{2} - |\mathbf{A}|\frac{\mathbf{U}_{i+1} - \mathbf{U}_i}{2} \end{aligned} \tag{4}$$

This scheme is 1^{st} order accurate in both time and space. A higher order scheme (e.g. MUSCL) has not been implemented so far due to the unstructured nature of the spatial grid and the resultant unstable nature of higher order schemes.

The calculation of the individual split eigenvalues is accomplished in the same manner as that by [5]. -

$$\lambda^{\pm} = \frac{\lambda \pm \sqrt{\lambda^2 + \varepsilon^2}}{2} \tag{5}$$

The ε is added because of the lack of continual differentiablity at zeros of the eigenvalue (i.e. sonic and stagnation points). It should be noted that for the case of artificial compressibility only stagnation points are of interest due to the flow being sub-*pseudo*sonic at all times.

Thus we have a first order scheme where the conservative vector and flux vector states at each of the nodes surrounding a face are combined to produce the flux through the face. This is purely one dimensional, but can be expanded into three dimensions by the adoption of the generalised Jacobian matrix $\mathbf{K}$ and the summation of the flux through all surrounding faces, such that the flux integral, $\mathbf{C}$, is defined as

$$\mathbf{C}(U) = -\frac{\Delta t}{\Delta V} \sum_{\alpha=1}^{no.faces} \mathbf{F}^*_\alpha Area_\alpha \tag{6}$$

This generalised nature of the flux and conservative variables vectors allows the use of arbitrary polyhedral control volumes. The explicit time marching scheme is a four stage Runge-Kutta Method.

Adaption Control

A statistical analysis of all the cells is conducted based on pressure gradient and those outwith set limits (typically two standard deviations from the mean) are either split or fused. Once an individual cell is designated to be split the process is carried out by first defining the direction of maximum pressure gradient. A cutting plane can then be defined through the volumetric centre of the cell. All the cell faces which are cut by this plane are split along the dividing line and two new cells are formed either side of the cutting plane. The cell inter-connections of the parent are kept through the use of a tree structure. Fusion of cells can then be carried out simply on all but the initial coarse mesh.

It is possible to measure the geometric properties of a finite volume cell and determine how they relate to the local solution quality. The results of such an analysis show that of the primitive variables, solution accuracy is most sensitive to pressure gradients. However, geometrical properties have a marked effect upon solution accuracy and convergence, with skew being of greatest importance [6]. Figure 1 shows the results of such studies. Mesh quality is maintained through the solution cycle by periodic readjustment of the position the control nodes defining the position of faces between control volumes. A least squares process is used to adjust the control nodes to minimise facial skew, deviation from planarity, and control aspect ratio.

An initial coarse mesh is generated using a block structured mesh generator, *Fleximesh*[7]. For maximum effectiveness the number of blocks should be kept to a minimum. On commencement of the iterative solution process a periodic mesh refinement process is carried out. This is controlled by a given drop in the level of average residuals. Progressive refinement is carried out until a fixed number of finite volume of cells are in existence. Once this level has been achieved coarser elements are fused if further refinement is required.

Mariner Hull Test Case

The geometric shape of the hull previously used for surface panel calculations [8] of sideforce was used as an input into the block structured mesh generation program *Fleximesh*. An initial structure of 16 blocks was used. Figure 2 shows the double hull surface representation of the Mariner form.

Results will be presented for an angle of drift of 7.5°, with particular emphasis upon the increased resolution of the vortical flow for a constant number of control volumes. In addition, experimental results from the truncated hull based on the Mariner tested in the 3.5m x 2.5m wind tunnel [9] will be used for comparative purposes.

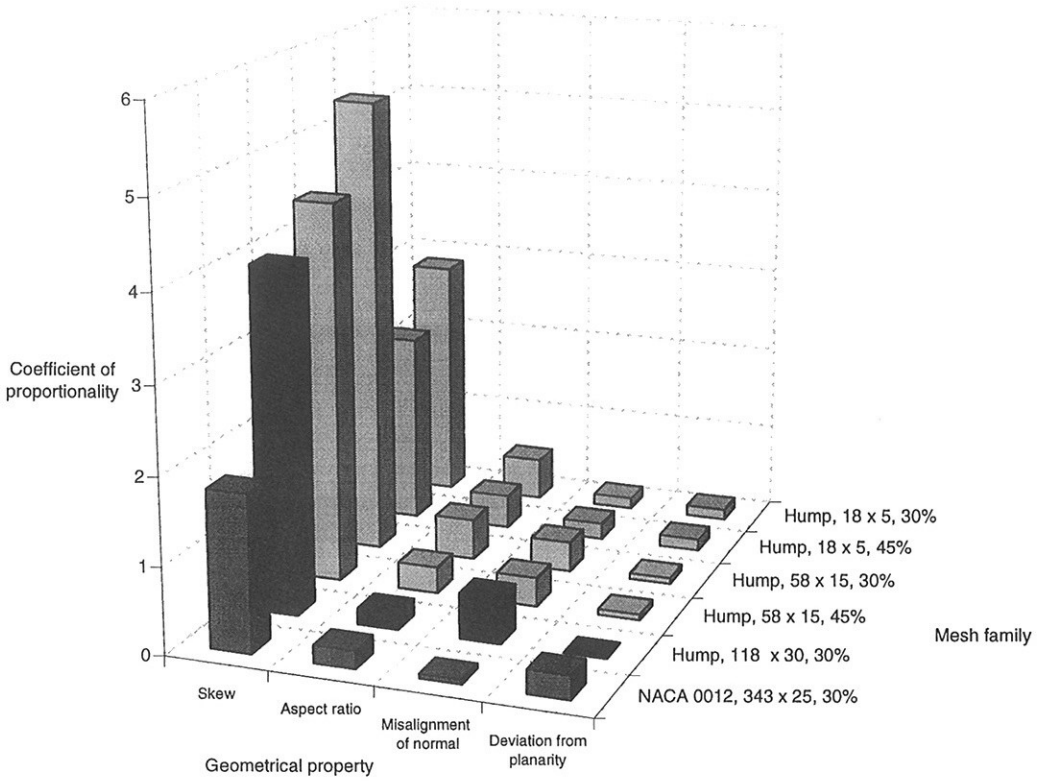

Figure 1: Relative importance of geometrical properties for mesh distortions

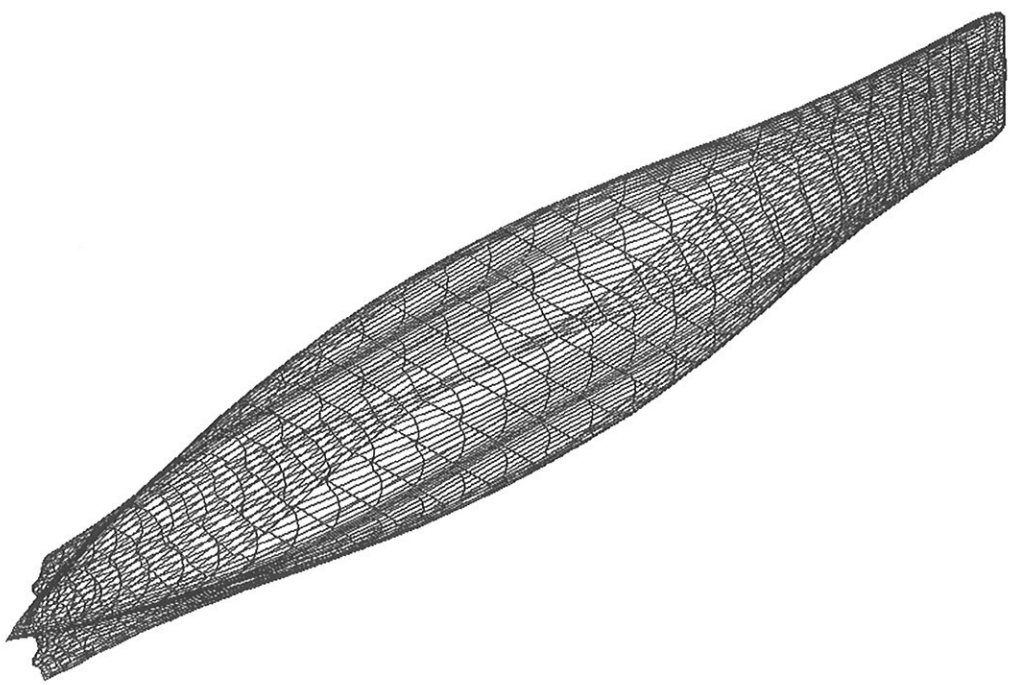

Figure 2: Mariner Double hull

References

[1] V.L. Russo and E.K. Sullivan. Design of the mariner-type ship. *Transactions of SNAME*, 61, 1953.

[2] A. M. Wright. *"Automated adaptation of spatial grids for flow solutions around marine bodies of complex geometry"*. PhD thesis, to be submitted University of Southampton, 2000.

[3] J. F. Thompson, B. K. Soni, and N. P. Weatherill, editors. *"Handbook of Grid Generation"*. CRC Press, 1999. ISBN 0-8493-2687-7.

[4] A. J. Chorin. "A numerical method for solving incompressible viscous flow problems". *Journal of Computational Physics*, 2:12–26, 1967.

[5] J. L. Steger and R. F. Warming. "Flux vector splitting of the inviscid Gasdynamic equations with applications to finite difference methods". *Journal of Computational Physics*, 40(2):263–293, April 1981.

[6] A. M. Wright and S. R. Turnock. "Efficient multi-level adaptation methods for unstructured polyhedral computational meshes". Ship Science Report 109, Department of Ship Science, University of Southampton, 1999.

[7] N. C. Rycroft and S. R. Turnock. "3-D Multiblock Grid Generator; FLEXIMESH". Ship Science Report 101, Department of Ship Science, University of Southampton, 1997.

[8] S.R. Turnock, Molland, A.F. The effects of shallow water and channel walls on the low-speed manoeuvring performance of a mariner hull with rudder. In *Proc. of International symposium and workshop on forces acting on a manoeuvring vessel, MAN'98*, Val de Reuil, France, 1998.

[9] A.F. Molland and S.R. Turnock. Wind tunnel tests on the effect of a ship hull on rudder-propeller interaction at different angles of drift. Ship Science Report 76, University of Southampton, 1995.

SELF – PROPULSION CALCULATIONS PAST A FAST FERRY

G.Tzabiras , V.Papakonstantinou, T.Loukakis

Department of Naval Architecture and Marine Engineering, National Technical University of Athens,

Heroon Polytechniou 9, Zografos 157 73, Athens, Greece (Tel. +30 1 7721038 , Fax. +30 1 7721032)

(e-mail : tzab@fluid.mech.ntua.gr , vkpapnav@central.ntua.gr)

1. Abstract

Prediction of the flow around a fast ferry has been made using a double body N-S solver. The Reynolds equations are solved in the physical space using orthogonal curvilinear staggered grids, generated with conformal transformation. The k-• turbulence model is with wall functions has been employed to calculate the full-scale case. The self-propulsion problem is studied under the actuator disk approximation.

2. Introduction

Advanced CFD methods can be used today with success in various stages of ship design. Although an accurate calculation of a ship's horsepower may have not yet been succeeded, there may provide an extremely valuable assistant to extrapolate towing tank results as well as to study local phenomena. In this respect, the aim of the present work is to show how a numerical method may help for investigating the trends of crucial parameters, for designing local devices or improving lines whenever unfavorable situations occur. The original goal of the present research has been the hydrodynamic design of the struts, which support the propeller axis of a twin–screw fast ferry. All computations were carried out using the software, which has been developed, at the Laboratory for Ship and Marine Hydrodynamics of the National Technical University of Athens during the last fifteen years.

3. Description of the adopted method

A multi block numerical procedure [1], [2] is followed to discretize the computational domain around the hull. Three overlapping blocks are introduced, i.e. the first one covers the bulbous bow region the second covers the parallel middle body and the third one both the stern and the near wake. The numerical solution is performed successively and independently in each sub-domain by calculating the input boundary conditions at the second and third blocks from the previous solutions. This procedure is allowed by the dominance of the longitudinal velocity component that, at the high Reynolds numbers that are examined, produces strong convective terms over the major part of the hull. The grids, which cover the corresponding sub-domains, are generated by conformal mapping technique [1], [3]. The conformal transformation of transverse sections or waterlines on the unit circle leads to a rapid generation of successive plane orthogonal grids, which are linked to cover a particular sub-domain.

The Reynolds, continuity and turbulence model equations, which govern the turbulent flow field, are first transformed to the local orthogonal curvilinear co-ordinate systems and then they are integrated in staggered control volumes according to the finite volume approach [1], [4], [5]. The standard k-• turbulence model with the wall function boundary conditions has been adopted to carry out computations at the full scale Reynolds number. The external flow velocity and pressure boundary condition are approximated by the potential flow solution around the actual body while a marching solution with successive grid refinement is followed to solve the equations within each sub-domain [1].

In order to compute the self-propultion parameters the propeller effect has been modeled through body forces according to the actuator disk approximation. [2]. The self-propulsion point is defined following an iterative procedure [2], where the body forces are updated by equating successively the propeller thrust to the body resistance, until convergence of the two values is obtained.

3. The test case

The present calculations refer to the project "optimum design of a fast ferry" which is underway in the Department of naval Architecture and Marine Engineering of the National Technical University of Athens. The principal characteristics of the full-scale ship are depicted in Table 1. As already mentioned, the main purpose of the particular study has been the calculation of the stern flow field at the region of the V-brackets in order to explore their proper orientation. A 1:50 model has also been tested in the Towing Tank of the Laboratory for Ship and Marine Hydrodynamics of the National Technical University of Athens.

Table 1 : Characteristics of the Fast Ferry "ALKYON 2000"

L_{pp} =172 m	C_b = 0.577
L_{bulb} = 7.50 m	Vs = 27 kn
B = 25 m	Tunnel stern with skeg
T = 6.5 m	Transom stern exceeding 6.89 m after A.P.

Since the double body approximation is used in the prescribed approach, the wave resistance component cannot be calculated. In order to obtain a realistic estimation of self-propulsion parameters, the total ship resistance coefficient is approximated as

$$C_{Ts} = C_{Wm} + C_{Ds} \quad (1)$$

Where C_{Ts} represents the total resistance coefficient, C_{Wm} the wave resistance coefficient and C_{Ds} the value of the local resistance of the ship considered as double body. Evidently the last one is derived by integrating the pressure and ship friction values on the hull. The value of C_{Wm} is computed empirically as:

$$C_{Ws} = C_{Tm} - C_{Dm} \quad (2)$$

Where C_{Tm} is the measured total resistance coefficient of the model in the towing tank at the same Froude number, and C_{Dm} the calculated total resistance coefficient of the double model.

Calculations at full scale were performed at Re = 2.067 x 10^9. The "C" grid around the bow had 71 x 81 x 46 nodes, where the first number denotes nodes along the hull, the second in the circumferential direction and the third normal to the body surface. The corresponding grid sizes in the second and the third blocks had, 121 x 45 x 60 and 196 x 45 x 60 nodes, respectively. Twenty external iterations were needed to achieve balance between the total resistance and the propeller thrust. The calculated trust deduction factor (1-t) was found equal to 1.02. Apart from the numerical errors, which may be responsible for this unexpected result, a careful examination of the calculated flow-field shows that there is a realistic explanation, which is related to the actuator disk, model that is adopted. Since the propellers are located far from the hull surface, the suction area does not influence practically the hull pressure field in front of them. On the contrary, the rapid increase of the pressure after the propeller disk affects more drastically the whole stern field and when integrated on the inclined hull surface, results in a reduction of the viscous pressure component.

Owing to the position on the propeller, the calculated effective wake fraction (1-w) exhibits also a high value of 0.958, which is close to the nominal 0.962. In order to obtain this result, a numerical open water test associated with the Wagenigen–B series has been performed, as described in [6].

In Figs. 1 and 2 numerical results concerning the local behavior of the stern flow field are presented. The surface flow lines in Fig.1 show a trend for separation due to the inflected stern at the aftermost part of the hull. Since the adopted turbulence model tents to overestimate velocities, there is a strong possibility that this result represents reality. Therefore a change of the stern frame geometry may be necessary. In Fig.2 the cross-flow velocity components show clearly the vorticity imposed by the propeller torque. The later is computed under the assumption of the open water test [6] and it is distributed as circumferential body forces on the control volumes, which intersect the propeller disk. However this cross-flow formulation did not change the formation of streamlines at the V bracket region located in front of the propeller.

References

1) G.D. Tzabiras, "Numerical evaluation of Reynolds scale effects on the resistance and propulsion characteristics of ships", Advances in Fluid Mech. series, Special volume: Flows at large Reynolds numbers, ed. H. Schmitt, CMEM pub., 1997, pp. 251-290

2) G.D. Tzabiras, "A numerical study of additive bulb effects on the resistance and self-propulsion characteristics of a full ship form", Ship Technology Research, 44, May1997, pp. 98-108

3) G.D.Tzabiras " Numerical study of the viscous flow past a ship's model with asymmetric stern" MARIND-96 Conf., 1996, Varna, pp. III.41-III.57

4) G. D. Tzabiras, "Resistance and self propulsion numerical experiments on two tankers at model and full scale", Ship Technology Research, 40, February 1993, pp. 20-38

5) G.D. Tzabiras "Numerical prediction of self-propulsion characteristics of full ship forms" STG-Yearbook, vol. 89, 1995, pp. 322-326

6) G.D. Tzabiras, " A numerical study of actuator disk parameters affecting the self-propulsion of a tanker", International Shipbuilding Progress, April 1996, pp. 5-47

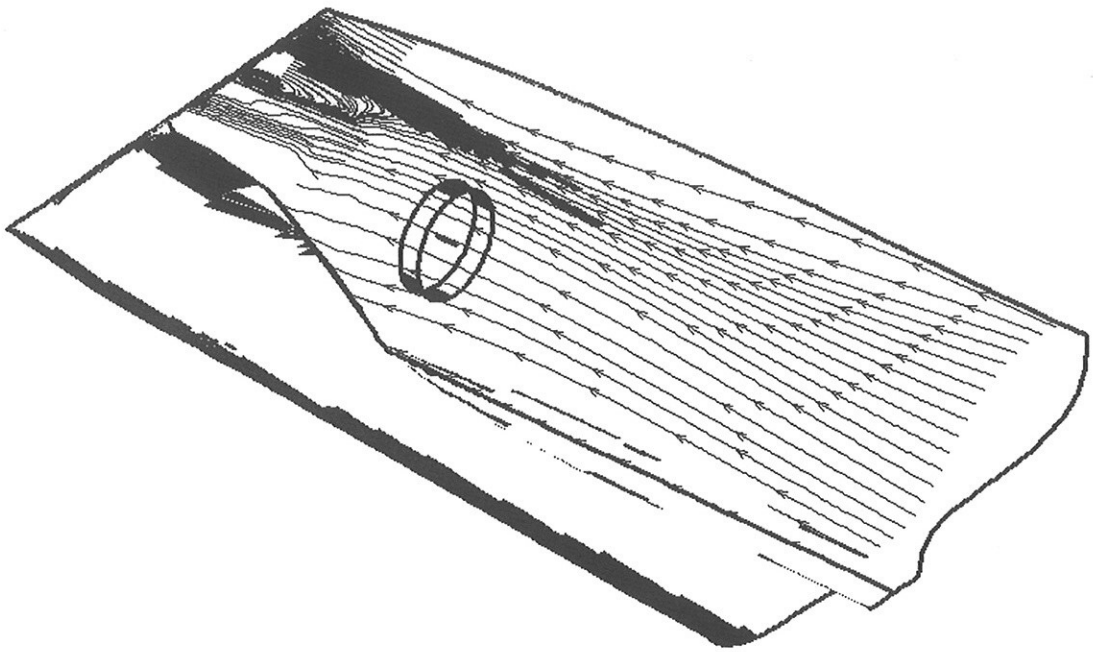

Fig. 1 The stern surface flow lines

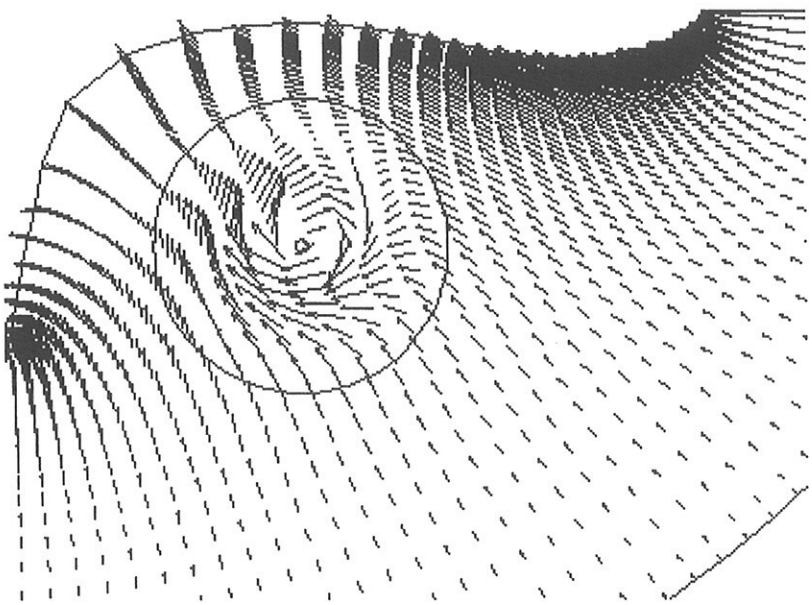

Fig. 2 The cross flow velocity components at x = 168 m from F.P.

OBLIQUE VISCOUS FLOW AROUND A TWIN SKEG TANKER MODEL

Mathias Vogt, Hamburg Ship Model Basin, email: vogt@hsva.de

INTRODUCTION

A twin-skeg ice-breaking tanker is to be dynamically positioned i.e. to be held in a fixed position under the influence of forces from the fluid flow, for instance current, wind and waves, acting on the hull. To stay in a fixed position the ship has to generate corresponding forces with its own propulsion systems.

With an inlet velocity U=0.253 m/s, the flow around the tanker is computed for different drift angles, β, between 0 and 50° with an in-house RANSE solver Neptun. Neither the free surface nor the propeller were taken into account in the computations. Due to the very low inlet velocity, the wave induced drag was considered negligible and the propellers were omitted to avoid even more difficulties by the grid generation. The ships main dimensions are: length L=228 m, draft D=13 m and breadth B=32 m. Computations were made for the draft D=0.3714 m of the model corresponding to D=13 m at full scale and for the deep water case. In the model tests it was shown that there were no tank floor influences for a water depth of 25 m (0.714 m at model scale). The Reynolds number was Rn=1.65 10^6.

METHOD

The viscous oblique flow is computed solving the Raynolds averaged Navier-Stokes equations and the continuity equation. Reynolds stresses are modelled with a k-ω turbulence model and here wall functions were used.

The conservation equations are discretised on a body fitted non-matching block structured grid using a finite volume method. All unknowns are defined at the cell centres. The diffusion terms are approximated with central differences and the convected velocities in the momentum fluxes with the linear upwind differencing scheme. Mass fluxes are interpolated according to Rhie and Chow and the SIMPLE algorithm is used to solve the resulting system of non-linear equations. For a more detailed description of the method see [3].

On the hull the no slip condition is enforced. Slip condition was used on the outer horizontal boundary, the symmetry plane and for β=0° on the outer lateral boundaries. At the inlet planes, undisturbed flow was assumed i.e. velocity is prescribed and the turbulent kinetic energy, k=10^{-5} and its specific dissipation rate, ω=10. At the outlet planes, the homogeneous Neumann condition was used for the velocities and the turbulent parameters while the Dirichlet condition was used for the pressure.

GRID

Different from a symmetrical computation, a grid on both sides of the ship is needed in the non-symmetrical case, which implies larger computational domain and more grid nodes. Since the free surface and effects thereof e.g. sinkage and trim (Froude number based on the depth Fn<<0.5) play a minor role here, the double body case is considered. The inlet was placed at one ship length in front of the FP, the outlet at one ship length behind the AP and the side boundaries as well as the bottom boundary were placed one ship length away from the symmetry planes. With 34 patches on one side of the hull, of which most of them in the stern region, half of the grid was build with about 80 blocks. Many of these were matching and could have been merged giving a grid with fewer blocks. The grid consisted of a total of 350 000 cells. Figure 1 shows a part of the hull surface grid at the stem and at the stern including a grid surface in a block outside the hull. It can be seen how the fore body, rudders, stern tunnel and the stern tubes are discretised to avoid grid singularities.

COMENTS ON THE COMPUTATIONS

To numerically solve these kinds of problems is difficult and it becomes more and more difficult to achieve convergent solutions with higher drift angles since the flow is fully non-symmetrical and partly highly turbulent. Another reason is that the strong main stream becomes less significant with higher drift angles. Further, the fluid flow is more complex than for the case of a symmetrical flow, with vortex generation, separation and reattachment at the stern but also at the stem. So, it is usually not possible to reach a satisfactory convergence for larger drift angles (>20°). In figure 7 the fully unsymmetrical pressure distribution for β=50° is shown. Lately, more papers have addressed related topics. In [1,2,4,5] the well known Series 60 ship was chosen as a test case. Measurements are available for $\beta \leq 20°$ and results for larger angles might therefore not have been reported.

In the computed case an additional difficulty was the very weak flow around the tanker, which yields a very low model Reynolds number. Consequently, laminar effects that could be strongly different from side to side at non-symmetrical flows could appear. The commonly used turbulence models cannot or can only very roughly predict transition from a laminar flow to a turbulent flow. For instance, the k-ω model predicts it too early. Therefore, it

is often assumed that the flow is fully turbulent from the FP. Alternatively, the turbulence model could be 'turned on' where the turbulence generating sand paper stripes on the model are applied. But for the case of oblique flows at low Reynolds numbers with unknown, differently long parts with laminar flow on the two ship sides, none of the alternatives are attractive.

In spite of the mentioned difficulties, computations were successfully carried out for drift angles up to 50° with satisfactory convergences. A laminar solution was then used as a start field for the following turbulent computation and the under relaxation parameters had to be set lower than usual.

RESULTS

Computations were carried out for drift angles β=0, 5 ,10, 15, 20, 25, 30, 40 and 50° (from starboard) and with an inlet velocity U=0.253 m/s. Below, a selection of the results is shown. In the figures showing velocity contours, they are the axial velocity normalised with the velocity at the inlet. The ship length is L.

Figure 2 shows the computed axial velocity contours and the corresponding vector field at *0.2L* for β=10°. Two vortices have arisen in the lower part on the leeward side of the fore body. These vortices develop downstream and are at *0.3L* more pronounced, figure 3. For β=30° both vortices are clearly visible, figure 4. Independent of drift angle, the 'keel' vortex stays attached while the second vortex separates and changes its position even more with higher drift angles.

Figures 5 and 6 show the velocity contours and vectors fields of cross sections at *0.95L* and at the AP. Contrary to the stem, the stern figures are shown from a view from behind. The starboard rudder is excluded in the figure 5. For β=0° there is a secondary flow in the tunnel. For larger values of β there are vortices arising at the leeward side of both skegs and the one in the tunnel is stronger than the one on the port side. Both vortices separate downstream, earlier with higher drift angles. The vortex in the tunnel growes and for β=30° it fills the whole propeller tunnel.

Figure 8, 9 and 10 show the computed and measured values of the resistance X', side force Y' and the yaw moment N', respectively, referring to the mid ship section. All quantities are made non-dimensional with the density of the water ρ, the inlet velocity U and the ship length L:

$$X' = \frac{X}{\frac{\rho}{2} L^2 U^2} \qquad Y' = \frac{Y}{\frac{\rho}{2} L^2 U^2} \qquad N' = \frac{N}{\frac{\rho}{2} L^2 U^2}$$

While the agreement between the computed and measured side forces, figure 9, are satisfactory, larger differences are observed for the resistance and the yaw moment, figures 8 and 10. It should be noticed that very small forces were measured at the model tests. Such measurements are more susceptible to large errors than measurements at larger velocities.

The computed resistance, figure 8, decreases with higher drift angle and even becomes negative for $\beta \geq 35°$. This is an effect due to the forward pointing component of the generated lift force. The computed resistance for β=0° differs about 30% compared to the empirical value of the friction resistance according to the ITTC-line 1957. However, there only a small form factor is used. The measured values are very different from the computed ones. It is not made clear whether the mentioned inaccuracy is alone responsible for those or not.

The computed curve of yaw moments is, for lower drift angles, linear and smooth. At about 30° the curvature changes, which seems to be reasonable because, sooner or later, the yaw moment has to decrease. The measured values oscillate strongly but the magnitude is similar to the computed ones.

REFERENSES

[1] Alessandrini, B. and Delhommeau, G., *Viscous free surface low past a ship in drift and in rotating motion,* 22th Symposium on Naval Hydrodynamics, Washington, D.C.,USA, Vol. 1, 1998

[2] Campana, E.F., Esposito, P.G. and Penna, R., *Numerical simulation of the drift motion of a ship,* 20th Symposium on Naval Hydrodynamics, Santa Barbera, California, USA, Vol. 1, 1994

[3] Cura Hochbaum, A., *A Finite-Volume Method for Turbulent Ship Flows,* Ship Technology Research 41/3 1994

[4] Cura Hochbaum, A., *Computation of the turbulent flow around a ship model in steady oblique motion,* 22th Symposium on Naval Hydrodynamics, Washington, D.C. USA, Vol. 1, 1998

[5] Tahara, Y., Longo, J., Stern, F. and Himeno, Y., *Comparison of cfd and efd for the series 60 cb=0.6 in steady yaw motion,* 22th Symposium on Naval Hydrodynamics, Washington, D.C.,USA Vol. 1, 1998

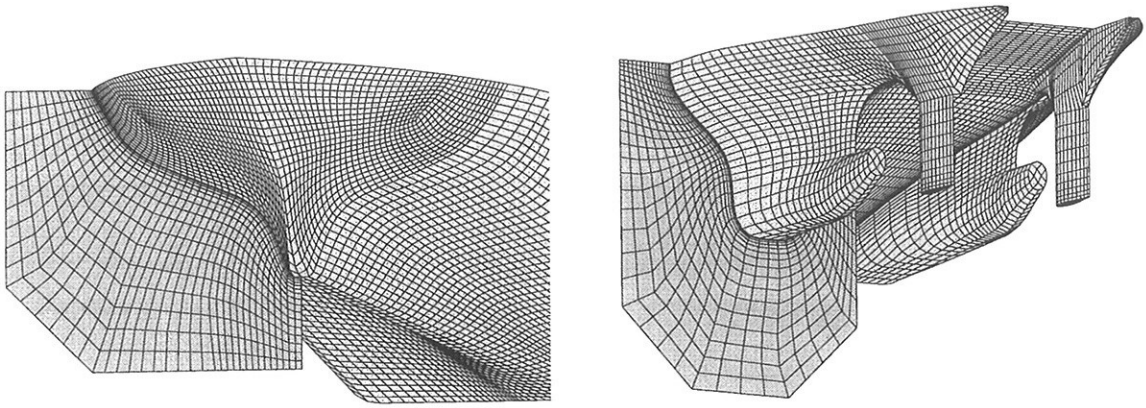

Fig.1 Views of the numerical grid.

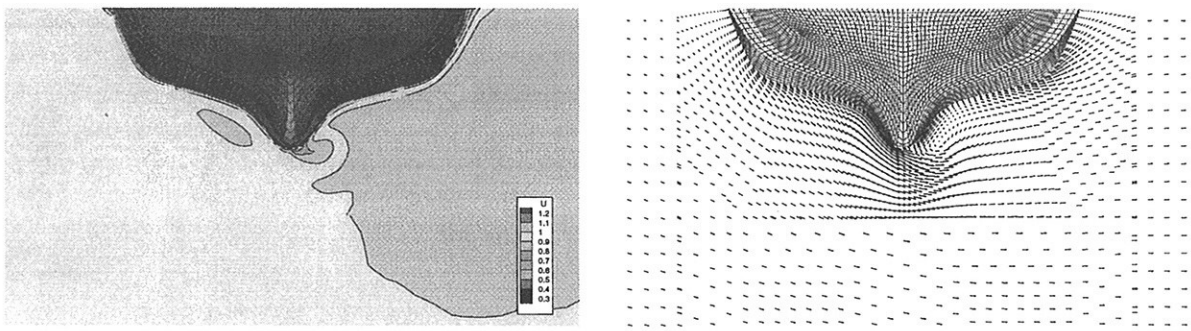

Fig.2 Computed velocity field for $\beta = 10^o$ at 0.2L.

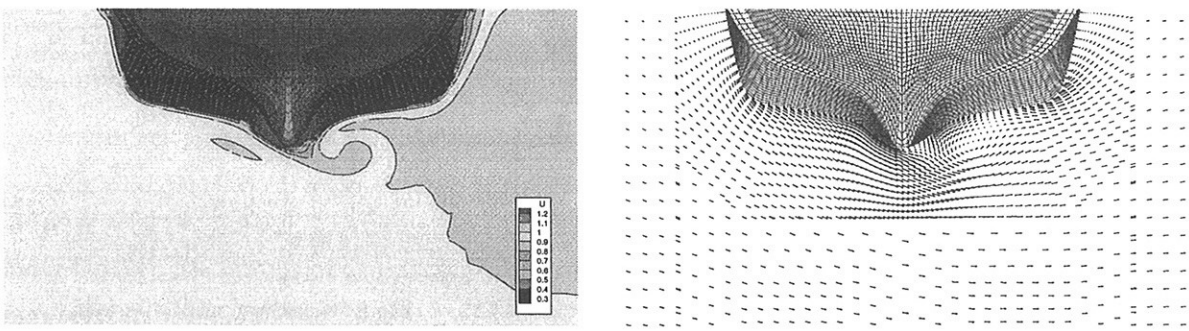

Fig.3 Computed velocity field for $\beta = 10^o$ at 0.3L.

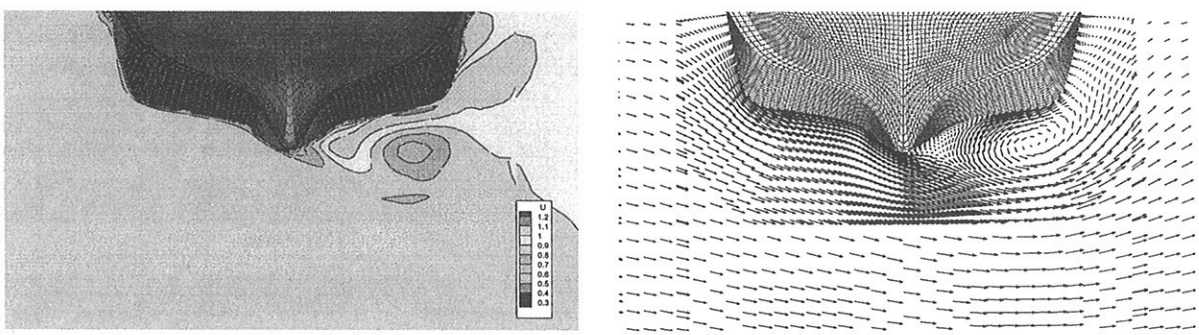

Fig.4 Computed velocity field for $\beta = 30^o$ at 0.3L.

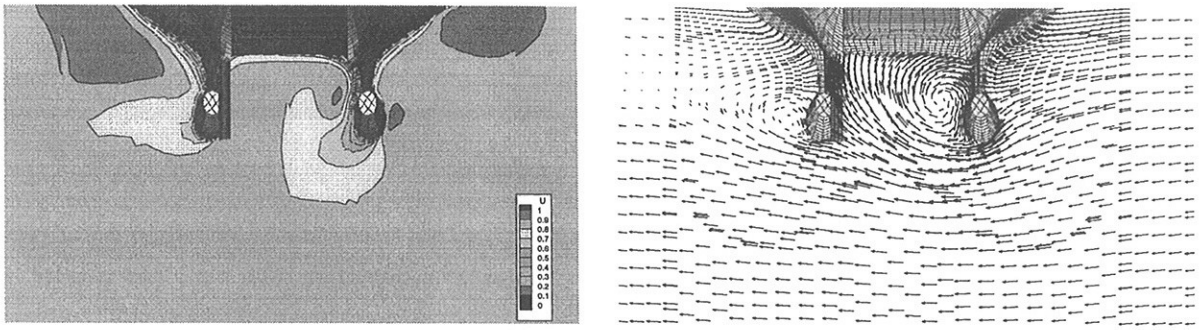

Fig.5 Computed velocity field for $\beta = 30^o$ at 0.95L.

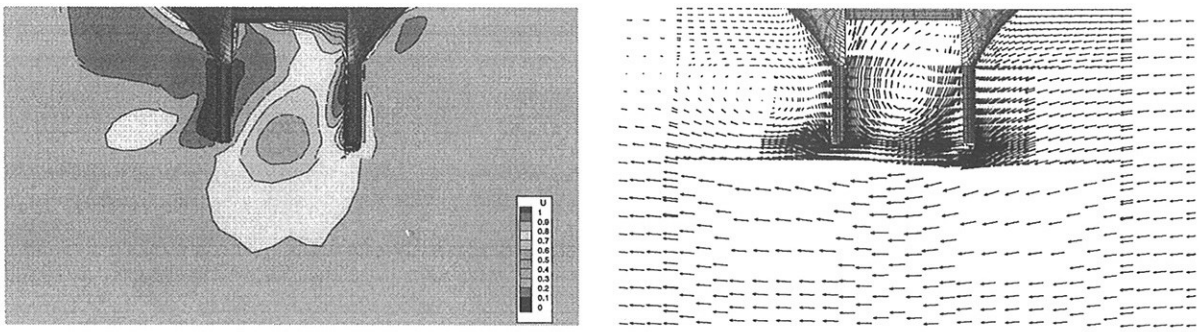

Fig.6 Computed velocity field for $\beta = 30^o$ at the AP.

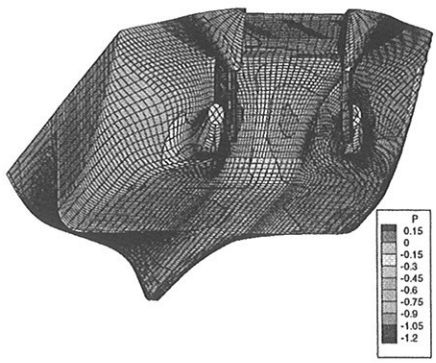

Fig.7 Computed pressure distribution for $\beta = 50^o$.

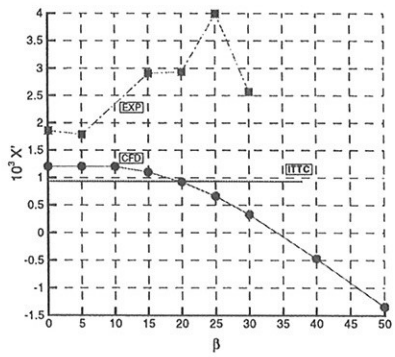

Fig.8 Measured and computed resistance vs. β

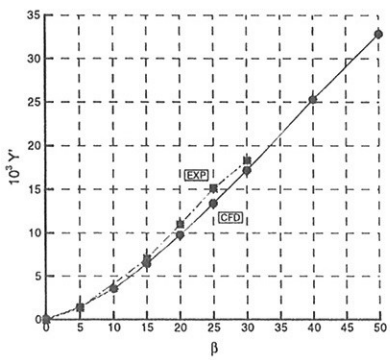

Fig.9 Measured and computed side force vs. β.

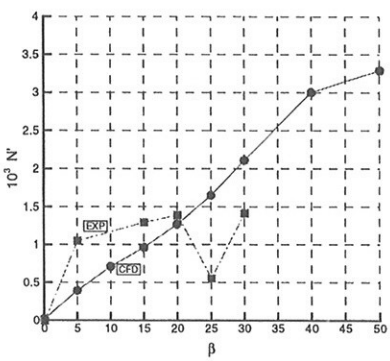

Fig.10 Measured and computed yaw moment vs. β.

Viscous Flow Prediction around a VLCC using Adaptive Grid Techniques

Peter Bull, Stephen Watson, Defence Research and Evaluation Agency, Haslar

This work is part of an ongoing programme to predict the full scale flow around a fully appended, powered ship. The primary objective of the work is to realise the potential of Reynolds Stress Models (RSM) in conjunction with solution adaptive grid techniques for a ship hull. The nominal wake as typified by a VLCC is a stage on this route. Flow predictions are made using both fixed and adaptive grids to the VLCC and several simpler geometries. The second aspect of the work addresses the consequences of the particular form of the dissipation rate equation. The object of this analysis is to form a basis to separate local effects from history effects. Observations are made on the basis of consistency when one turbulence model is allowed to develop on fixed velocity fields, which have been predicted by other turbulence models. Where possible, analytic estimates of source differences are developed.

Introduction

The quality of predictions of viscous flows around marine structures has always been dependent on both turbulence model and grid. With decreasing computing cost, very large grids of high quality can be built, on which predictions exhibit grid independence under widening range of conditions. In consequence, the differences due to choice of turbulence model are becoming clear to see. For ship hydrodynamics, the questions are what order of modelling is appropriate, when and why.

Second moment Reynolds stress closures are recognised as a general and powerful class of turbulence models, but not as the most efficient. RSM is becoming common place because the requisite technical knowledge is widespread, on average they are better than other models, and their computing costs are reducing. However, a hallmark of the last thirty years is that increased generality has produced better predictions only on average, rather than consistently. There is a danger that this will only be compounded when grid adaptation is added to the solution process.

To provide a validation path, several geometries were chosen to prototype the viscous flow and grid adaptation on the basis that structured grids of high quality could be generated:

1. boundary layer with an adverse pressure gradient / a finite flat plate
2. flow through an axi-symmetric diffuser
3. thick axi-symmetric boundary layer on a cylinder
4. axi-symmetric flow past a body of revolution (supported by by struts)
5. flow past a modified Wigley hull

The boundary layer was chosen the weight of analysis that can be brought to bear on it. The axi-symmetric flows were chosen because they exhibit the loss of the logarithmic overlap within the hull shear layer. The flow through the diffuser while simple geometrically presents significant difficulties for most of the current generation of turbulence models. Finally, the modification of the Wigley hull introduces weak secondary flows over an intermediate ship-like geometry, and was suggested by model tests reported by IHI at the first Osaka colloquium in 1987. Potentially, these secondary flows can be introduced in a gradual manner through varying the parameter controlling the fullness of the form.

Predictions are to be made on fine block-structured grids in order to base-line the adaptive predictions. The flow adaptation is initially being made of the basis of geometric curvature of boundaries and flow gradients. The unstructured grid approach is hybrid with prisms, possibly degenerate, being grown from viscous boundaries and above which, the interior is filled with tetrahedra (see Figure 1).

Flow Predictions around VLCC

Work to date has centred on the VLCC geometry itself to scope the potential effects of geometric quality on the adaptive process and to identify associated problems not inherent in the simpler geometries within the program.

The RSM chosen for the predictions the VLCC is the Launder Reece Rodi model. Given the problems associated with constructing wall reflection, the model for the pressure-strain correlation due to Speziale, Sarkar & Gatski has been used. The RSM predictions are initialised by RNG k-ε predictions on the coarsest grid. The initial

Reynolds stresses are estimated from the standard isotropic k-ε model of the stresses, but clipped so that they satisfy the Schwarz inequality. Standard wall functions have beenused; it is intended vary details of their formulations in future calculations.

Grid adaptation has been limited to three grid refinements. No adaptation is performed normal to the hull in the prism layers. Grid coarsening is limited to the coarsest grid level. Although moderately well-converged predictions have made (see Figure 2), problems arising from geometry are posing problems to further adaptation of the solution. This primarily because the underlying geometric surfaces are used within the adaptation process.

The definition of the geometry was the IGES file posted on the Gothenburg 2000 web site. The geometry defined within this file was somewhat imperfect, particularly near the keel at the junction of the bow and the main hull. A certain amount of redefinition of geometry was undertaken via bi-cubic patches. The modified definition has not yet been checked against the original file and point definitions (also posted). However, we believe our re-defined geometry is close to original over the majority of the hull. Even so, the curvature of the hull on the modified region is still a matter for concern as there is excessive adaptation to this region, not warranted by the flow itself (see Figure 3).

Analysis of turbulent dissipation rate

For RSM to produce significant benefits consistently, the key controlling performance need to be clearly highlighted. For example, the treatment of wall reflection terms is important for wall bounded flows. Yet Wilcox[1] has suggested that the major benefit of wall reflection treatments makes good the deficiencies of the dissipation rate equation, rather than as a fundamental aspect of the RSM model.

The weakness for turbulence models based on single-point closures of whatever order is the equation for the dissipation terms in the Reynolds stress equations which is complex and subject to many assumptions and approximations. Nevertheless, the Reynolds stresses are dependent on both velocity and length scales. For RSM, this dependence is implicit as it is for one-equation models such as Baldwin-Barth and Spalart-Allmaras; for two equation models, the relationship is explicit.

For certain cases such as the development of a boundary layer on a flat surface, the implications of the form of the dissipation equation can be assessed. For example, on the basis of perturbation analysis, Takemitsu[2] suggests that the k-ε model requires modification to exhibit a wall function solution, while Wilcox,[3] suggests that his k-ω model can be integrated through the laminar sub-layer and that the ω equation does exhibit a wall function solution for channel flow. A similar type of analysis by Wilcox and Henkes[3] indicates that for boundary layers with adverse pressure gradients, SMCs, k-ω and at least one algebraic model outperform k-ε model in accuracy of predictions. While Wilcox's ω equation appears better behaved than an ε equation, the ω equation is an approximation and by no means certain that it will perform well in all cases and that the ω equation an optimum prescription. This suggests the question – what form would a differential length scale equation have to take to reproduce, or even to outperform an algebraic model consistently? Regarded only as systems of model equations, such modifications to differential turbulence models are easy to contemplate. For example, although homogeneous turbulence decays in the absence of velocity gradients, the asymptotic behaviour of higher order models can easily be altered to reproduce the constant levels predicted by simpler models via sources for prescribed values of k, τ_{ij}, ε and ω.

The starting points for most turbulence models are averaged moments of the Navier-Stokes equations. The standard k equation is derived from the equation for the trace of the Reynolds stresses and by approximating the two remaining unclosed correlations. The original equation and the derived k equations are relatively uncontroversial, and therefore are used as a basis for comparison, together with a set of algebraic stress models. Using these equations, differential length scale equations are developed for the Baldwin-Barth, Spalart-Allmaras and Baldwin-Lomax models via MAPLE 6. In the first instance, the distance to the nearest wall is left as an unclosed function. The differences in source terms between the derived equations and the ε equation are derived and evaluated for the simple geometric cases and numerically for the VLCC.

1. Wilcox. 1998. *Turbulence Modelling for CFD*. DCW Industries.
2. Takemitsu. 1990. *An Analytic Study of the Standard k-ε Model*. J. Fluids Eng. 112. pp 192-198.
3. Henkes. 1998. *Scaling of Equilibrium Boundary Layers Under Adverse Pressure Gradients Using Turbulence Models*. AIAA 36.3. pp.320-326.

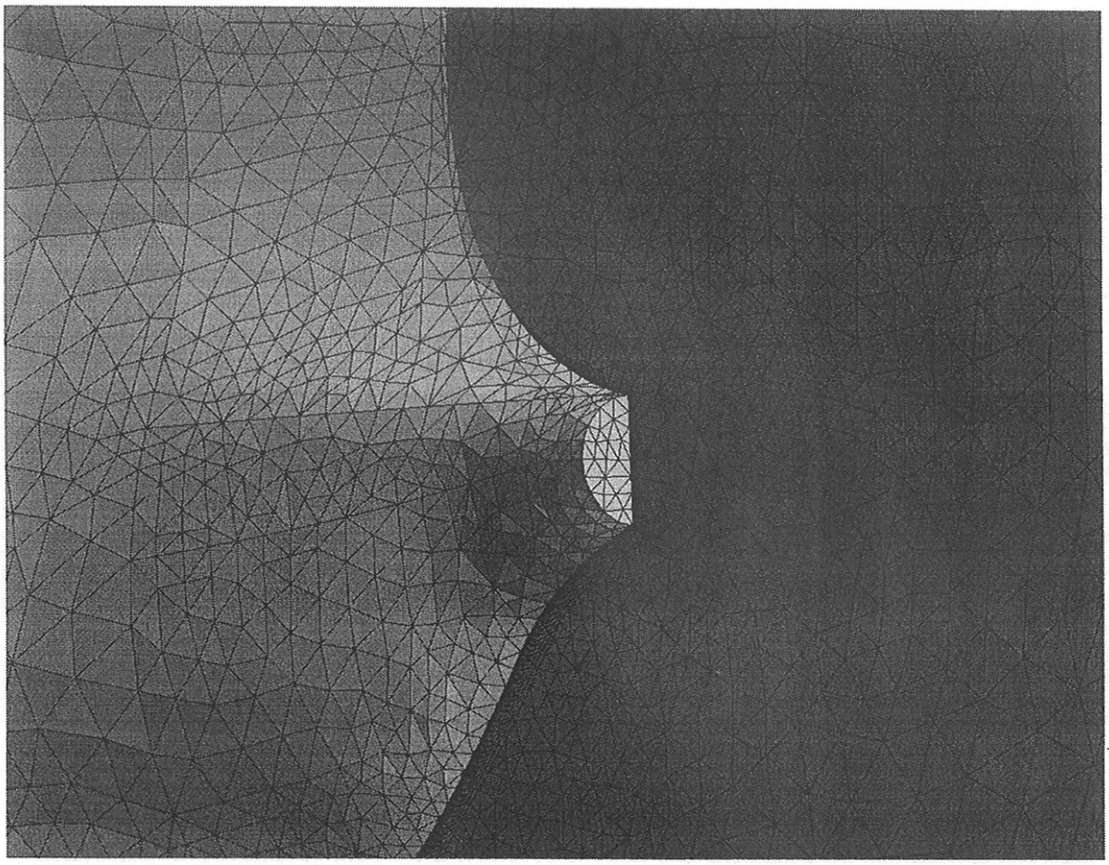

Fig.1: Detail of grid at stern of VLCC

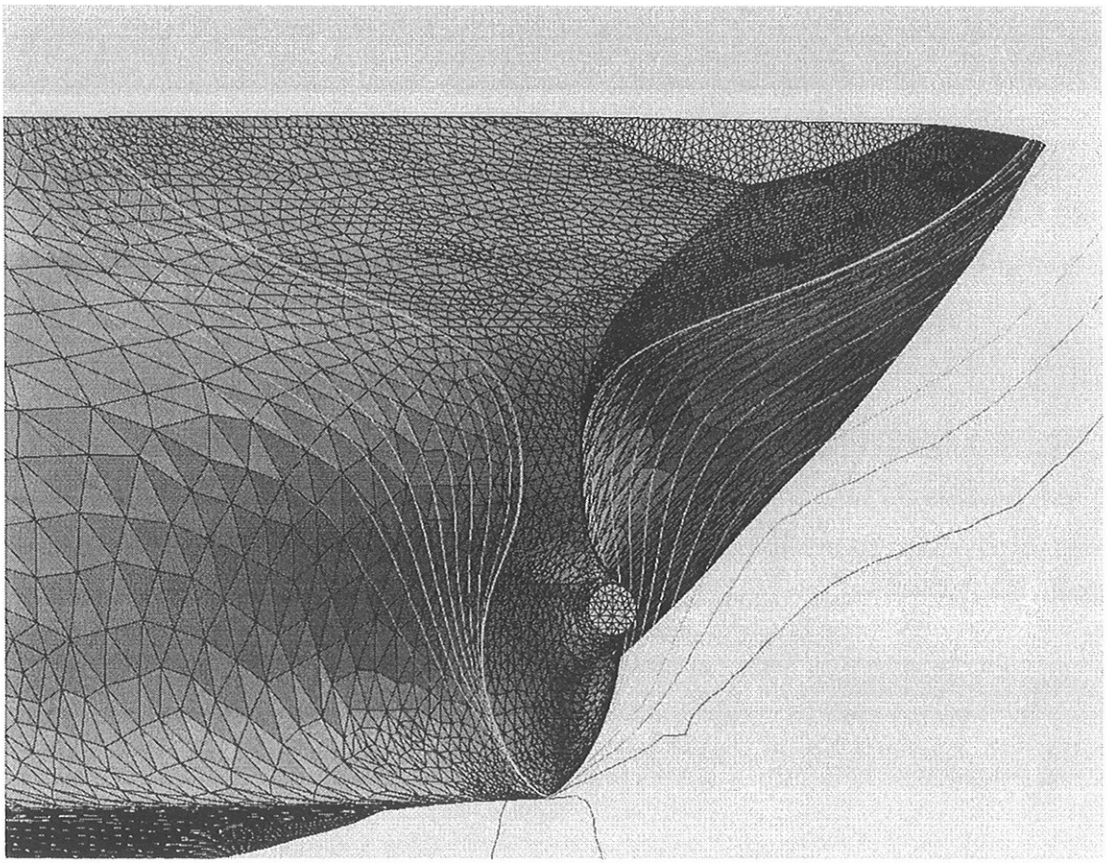

Fig.2: Contours of Axial velocity at the Stern of VLCC

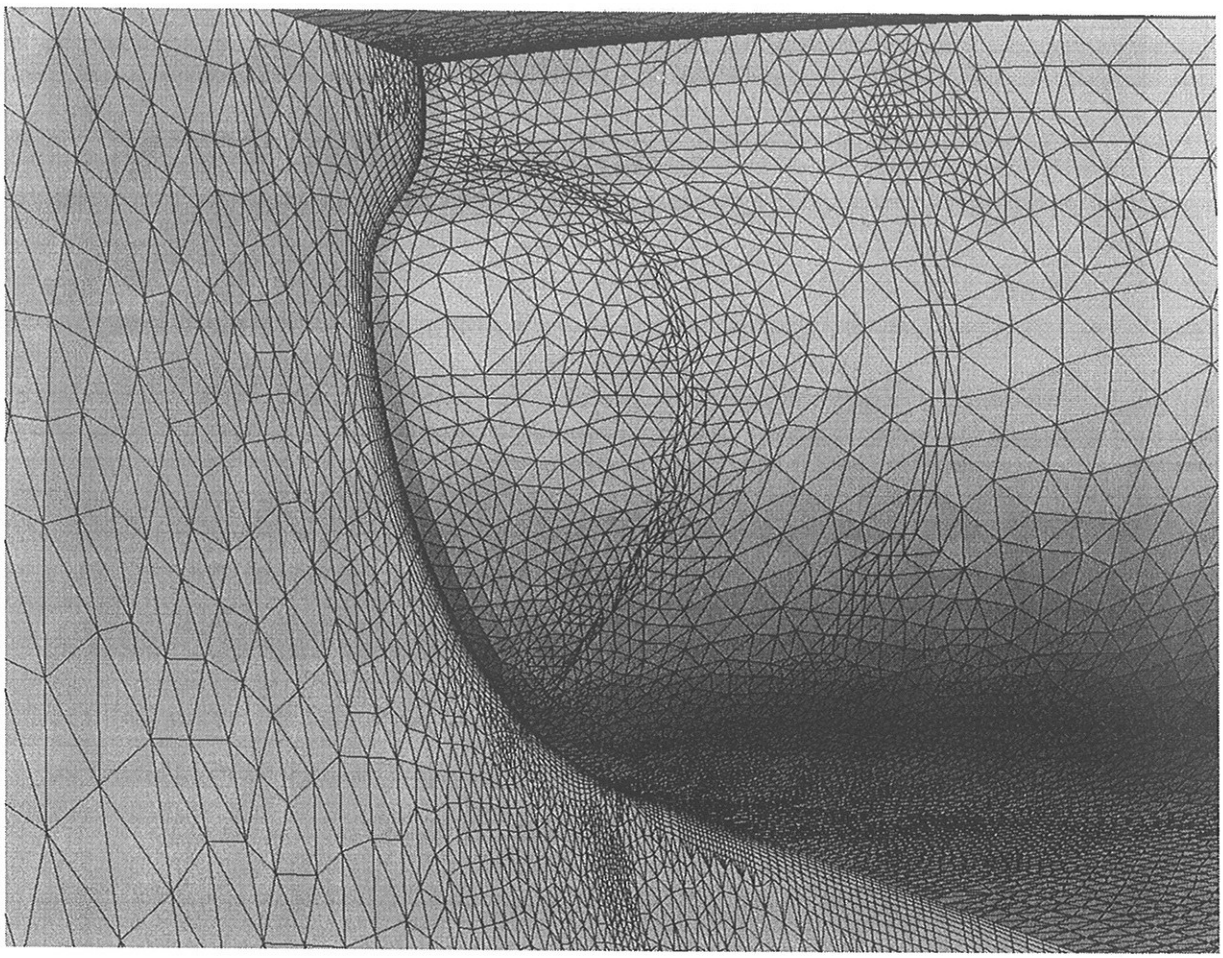

Fig.3: Detail of Grid near bow of VLCC

A composite procedure for ship viscous flow with free surface

JAAP WINDT, HOYTE C. RAVEN
Maritime Research Institute Netherlands (MARIN), P.O. Box 28, 6700 AA Wageningen, Netherlands

1 Introduction

One of the most active fields of ship hydrodynamics research today is the development of methods for computing the steady viscous flow with free surface around a ship hull. Compared to the classical separate consideration of wave making and viscous flow, such methods aim at making a step forward by incorporating free-surface effects on the viscous flow, and viscous effects on the wave pattern. Methods proposed generally solve the RANS equations subject to dynamic and kinematic free-surface boundary conditions (FSBC's).

While appreciable progress has been made in recent years, the problem is not really solved yet. Mostly a good prediction of the wave profile along the hull is obtained, but the wave pattern away from the hull usually is rather poor due to substantial numerical damping, unless dense grids with several millions of cells are used. Moreover, virtually all methods consider a time-dependent problem and integrate in time until a steady result is obtained; but the approach to steady state may be quite slow due to transient waves, reflections at open boundaries, and small permissible time steps. The resulting large calculation times and reduced robustness complicate the effective use in practice and make it hard to achieve grid-independent solutions, in particular for lower Froude numbers. Consequently, these methods are only rarely used routinely in ship design.

Most RANS computations in practical ship design therefore still use a double-body approximation. However, a step forward is possible without any significant computation time penalty. As many validations have demonstrated, *inviscid* methods can predict most of the wave pattern very efficiently and accurately. An obvious procedure therefore is to first run a panel code to determine the wave pattern, and next to compute the viscous flow, imposing free-slip boundary conditions at the wave surface. In this non-interactive formulation, most free-surface effects on the viscous flow are taken into account, but not the viscous effects on the wave pattern, which are known to be localised near the stern.

Surprisingly, this possibility seems to have been largely disregarded so far, except for the similar work at NTUA [6] in which viscous flow was computed under a *measured* wave surface.

2 The composite procedure

Wave pattern calculation The first step is the calculation of the wave pattern, using a nonlinear free-surface potential flow method. We use the code RAPID[1], an iterative 'raised-panel' method using a source distribution on the hull surface and on a surface at a specified distance above the wave surface. On the hull, zero normal velocity is imposed; in collocation points on the wave surface, the kinematic condition (flow tangential to the wave surface) and the dynamic condition (pressure atmospheric at the wave surface) are imposed. Iteration continues until both conditions are satisfied, and until there is no further change of the wave elevation and the trim and sinkage of the ship. The method is known to predict the wave pattern accurately, with as principal exception the overestimation of the stern wave system due to the neglect of viscous effects.

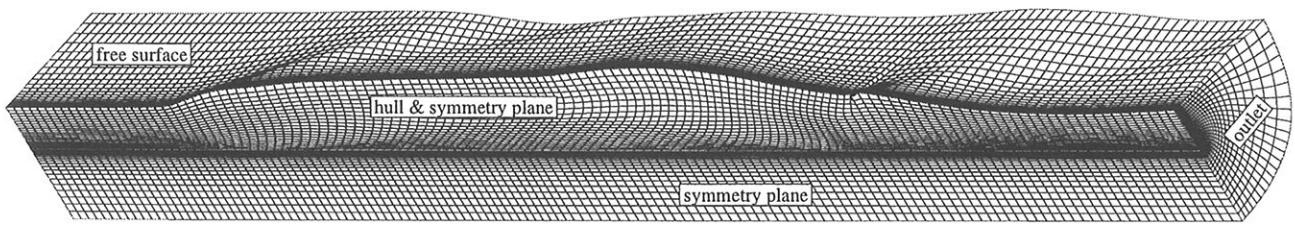

Figure 1: Grid used in viscous flow calculation under precomputed wave surface. Only every second line in each direction shown.

Grid generation The next step is the generation of a grid for the viscous flow calculation (Fig. 1). The domain is basically cylindrical, and the grid has an H-O topology. Cross sections are bounded by the ship centreplane, the hull surface, the wave surface, and an outer boundary at some distance away from the hull. The wavy surface is given as a B-spline surface fitted through the free-surface collocation points found in the wave pattern calculation. A nearly orthogonal grid on the wavy surface is generated by Elliptic grid generation. Care is needed in particular for the intersection with the hull, since the points closest to the waterline may still be about 0.5 - 1 % L off the waterline. The actual waterline can be found either by extrapolation, or from the pressure distribution on the hull. In the immediate vicinity of the bow and stern, both ways were found to introduce some local errors.

Viscous flow calculation For computing the steady viscous flow around a ship hull we use the code PARNASSOS [2, 3]. It is based on an iterative process, primarily acting on the pressure distribution, consisting of repeated downstream sweeps through the domain. Each sweep consists of a sequence of solutions for transverse planes. An algorithm is used that avoids the uncoupling of the continuity condition that underlies pressure correction or artificial compressibility methods. This gives the method a large robustness and efficiency. While originally 'Reduced' RANS equations were solved, the same method is now applied to the full RANS equations.

The wave surface being given, we have one degree of freedom less than in the original free-surface problem. Consequently, we can impose 3 boundary conditions and need to sacrifice one. The set of boundary conditions imposed models a free-slip surface: we retain the kinematic FSBC and the tangential components of the dynamic condition,

$$\vec{v}.\vec{n} = 0\,, \qquad \vec{t}_\alpha.\tau(\vec{v}).\vec{n} = 0 \quad \text{for} \quad \vec{x} \in \mathscr{S}\,.$$

Here, $\vec{n}(\vec{x})$ is the unit normal vector to the wave surface $\mathscr{S}$, $\vec{t}_\alpha(\vec{x})$ are orthogonal unit vectors tangential to $\mathscr{S}$ and τ denotes the viscous stress tensor. We thus ignore the normal component of the dynamic condition (which, however, was already imposed in the *inviscid* calculation). The error in this condition, i.e. the deviation from atmospheric pressure at the wave surface, indicates the validity of the given wave surface for *viscous* flow.

3 Application

As an illustration we here take the Series 60 $C_B = 0.60$ model at $Fn = 0.316$, $Rn = 3.4 \times 10^6$, as tested at IIHR [5]. The wave pattern calculation was made using 2197 hull panels and 32×196 free-surface panels per symmetric half, and took 5 to 10 minutes CPU time on a CRAY C90 machine. Fig. 2 compares the computed and experimental wave pattern and illustrates that the agreement is good except for the familiar overestimation of the stern wave system.

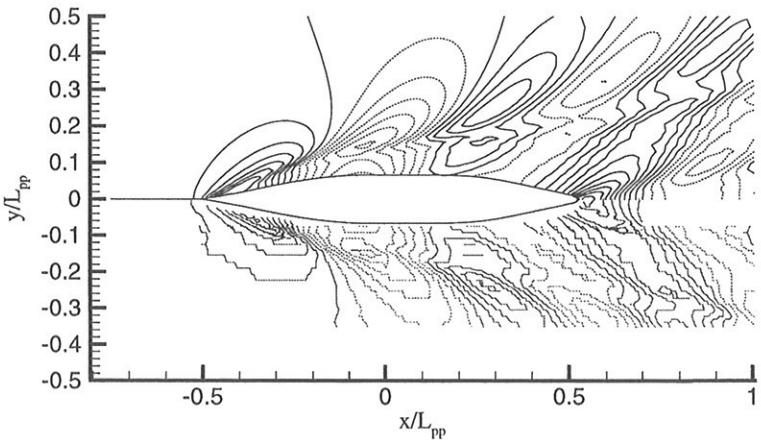

Figure 2: Wave elevation contours ($z/L = -0.02, -0.018, \ldots, 0.02$). Upper part: potential flow method; lower part: measurements.

The viscous flow calculation under the wave surface was made using two geometrically similar grids of $273 \times 101 \times 45$ and $137 \times 51 \times 23$ nodes in streamwise, normal and girthwise direction respectively. Convergence behaviour and computation time are comparable with a double body calculation, i.e. approximately 40 to 60 minutes on a CRAY C90 for the fine grid.

Fig. 3 shows the deviation from atmospheric pressure at the wave surface, represented as a wave elevation difference according to $\Delta z/L = \frac{1}{2} Fn^2 (Cp_{atm} - Cp_{FS})$. Note that the increment between isolines is 4 times smaller than that in Fig. 2. On the finest grid, the error is significant only locally along the bow wave and in the

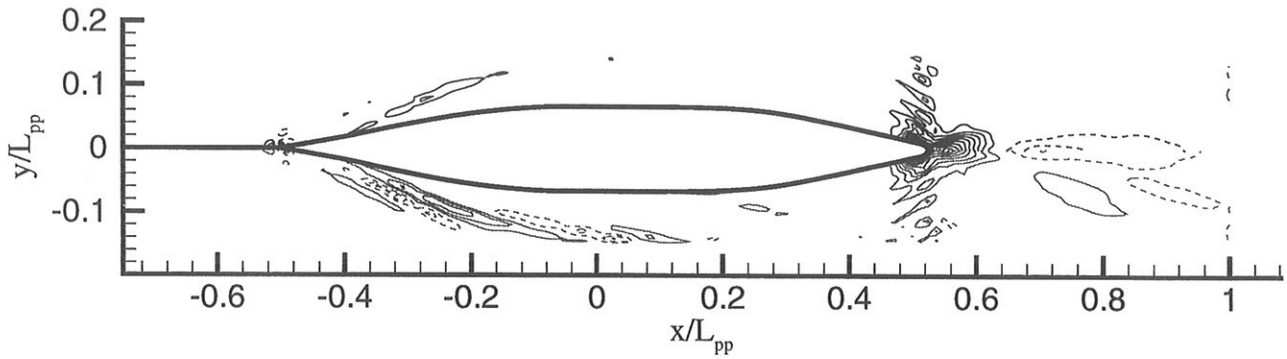

Figure 3: Pressure deviation at wave surface, related to wave elevation.($\Delta z/L = -0.02, -0.0195, \ldots, 0.02 \setminus \{0.0\}$). Upper part: fine grid; lower part: coarse grid.

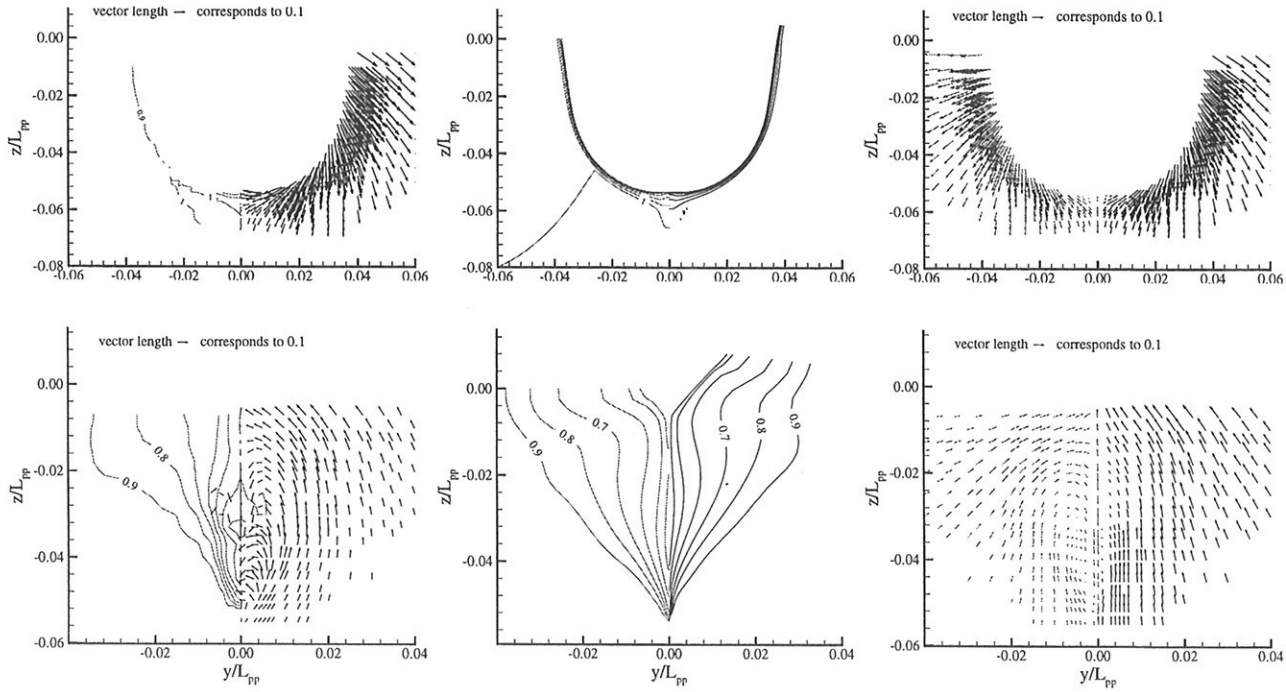

Figure 4: Axial and transverse velocity field at $x/L = 0.2$ (upper part) and $x/L = 1.0$ (lower part). The figures to the left show the measurements[5], the figures at the middle and at the right show the predicted wake field using the double body approach (left) and (one step) composite procedure (right).

stern area, and is negligible everywhere else (less than 0.0005 L, or 2.7 % of the maximum wave elevation). Comparison of the coarse and fine grid solutions, and of intermediate solutions obtained by the successive grid refinement stages of the solution procedure[1], shows excellent convergence of the pressure distribution on the wave surface by grid refinement. At most places it converges to almost zero, indicating that the pressure deviations are only due to discretisation errors in the finite-difference solution. Some disturbances do not disappear upon grid refinement, and these are caused by viscous effects on the wave pattern, or to discretisation errors in the inviscid solution.

If the calculated pressure differences would be simply used to correct the wave elevation, they would indeed reduce the stern wave height; but iteration is then needed to account for the wave pattern changes downstream. But such changes have no significant effect upstream, so it may well be concluded that a valid RANS/FS solution has been obtained everywhere except the stern wave system itself and in the wake.

Fig. 4 shows the computed axial and transverse velocities for two $x =$ constant planes using the double-body approach and the (one step) composite procedure. As expected, the quality of the predicted axial and transverse velocities close to the waterplane improves definitely by the composite approach. However the

1. using 35×51 and 69×51 nodes (coarse grid) and 69×101 and 137×101 nodes (fine grid) on the wave surface.

longitudinal vortex in the wake seems to be overshadowed by the vertical velocity. The latter is most likely somewhat too large due to the overestimation of the stern wave system, but further investigation is essential. First of all, for accurate wake field prediction we need to (and intend to) apply a more appropriate turbulence model like the Menter model or $k-\omega$ model. Secondly, the stepsize in streamwise direction is too large to obtain a grid independent solution (we used an equidistant node distribution, focusing on the pressure on the water surface). Both changes usually improve the prediction of longitudinal vortices.

4 Discussion and conclusions

In the calculations made so far, the major free-surface effect on the viscous flow was found to be non-interactive, and can be captured in a single step of the composite approach. The pressure difference across the wave surface partly results from the different numerical methods used in the inviscid and viscous calculations, and then was found to vanish upon grid refinement; partly it indicates where viscous effects on the wave pattern are present. The latter indication is very well correlated with the location of observed differences of the wave elevation with experimental data, and is a very limited area aft of the stern.

The method proposed disregards this viscous effect on the wave pattern, and the additional 'displacement effect' of the boundary layer and wake. In a recent study also the latter has been found to be only significant for the stern and near wake area. A full, interactive RANS/FS solution would be needed there (but only there) to include these effects.

The application considered is a slender hull form, and for fuller hull forms a stronger (and sometimes qualitative) change of the wave elevation due to viscous effects takes place. However, even in those cases those changes are confined to the stern area. On the other hand, the case studied here exaggerates the wave/viscous interaction, due to the unusually low Reynolds number and the rather high Froude number, and the presence of a cusped stern.

Therefore, the composite procedure proposed here for most of the domain can provide a solution equivalent to a full RANS/FS solution on a dense grid, with an effort just marginally larger than that for a double-body RANS solution. This easy and most efficient procedure will soon replace the double-body approach for most of our practical computations. The task of RANS/FS can then be limited to the stern area where it is really needed. Work on a new RANS/FS method, solving the steady problem by iteration, is underway [4], and will hopefully supplement the composite procedure.

References

[1] Raven, H.C., *"Inviscid calculations of ship wave making — capabilities, limitations and prospects"*, 22nd Symp. Naval Hydrodynamics, Washington DC, 1998.

[2] Hoekstra, M., *"Numerical simulation of ship stern flows with a space-marching Navier Stokes method"*, Thesis, Technical University of Delft, October, 1999.

[3] Van der Ploeg, A., Hoekstra, M., and Eca, L., *"Combining accuracy and efficiency with robustness in ship stern flow computation"*, 23rd Symp. Naval Hydrodyn., Val de Rueil, France, 2000.

[4] Raven, H.C., and Van Brummelen, H., *"A new approach to computing steady free-surface viscous flow problems"*, 1st MARNET-CFD workshop, Barcelona. To be downloaded from `http://www.marin.nl/publications/pg_resistance.html`

[5] Toda, Y., Stern, F., and Longo, J., *"Mean-flow measurements in the boundary layer and wake field of a Series 60 $C_b = .6$ ship model for Froude numbers .16 and .316* IIHR Report No. 352, Iowa Institute of Hydraulic Research, August, 1991.

[6] Garofallidis, D.A., *"Experimental and numerical investigation of the flow around a ship model at various Froude numbers,"* Doctor's Thesis, National Techn. Univ. Athens, 1996.

Nonlinear Time Domain Analysis of Ship Motions in Regular Head Waves

Hironori YASUKAWA, *Nagasaki Experimental Tank, Mitsubishi Heavy Industries**

Introduction

In this paper, we propose a nonlinear time domain analysis method of ship motions in waves. This method can be regarded as an extension of the method for free-surface flow of a high speed vessel proposed in NuTTS'99[1]. In the previous paper, no ship's attitude change was assumed. We put a scheme of ship motion computation to the original method for the free-surface flows by a panel method. As a result, it becomes possible to compute wave-making resistance including effect of attitude change, and ship motions in waves including nonlinearity of free-surface and hull boundary conditions. We present the computed results of ship motions and wave deformations in regular head waves for a modified Wigley hull.

Basic Equations

Let us consider a ship advancing in a towing tank. It is assumed that a ship moves with speed $U(t)$ which varies as the function of time t. The coordinate system fixed in the space is employed. The x-axis is defined as direction from ship stern to the bow, y-axis to port and z-axis vertically upward. The $x-y$ plane is the still water surface. Deep water is assumed.

3 ship's motion displacements with respect to surge, sway and heave in the fixed coordinate system are defined as ξ_1, ξ_2, ξ_3 respectively, and the vector $\boldsymbol{\xi}$. Euler angles with respect to roll, pitch and yaw are represented as φ, θ, ψ respectively, and the vector $\boldsymbol{\Omega}$. Incident waves are generated by the flap-typed wave maker attached tank wall.

The perturbation velocity potential due to ship moving in the tank is defined as $\phi(x, y, z, t)$. Then, ϕ has to fulfill the following boundary conditions:

$$\frac{\partial \phi}{\partial t} = -g\zeta - \frac{\partial^2 \phi}{\partial t \partial z}\zeta - \frac{1}{2}(\nabla\phi)^2 \quad \text{on } z = 0 \tag{1}$$

$$\frac{\partial \zeta}{\partial t} = \frac{\partial \phi}{\partial z} + \frac{\partial^2 \phi}{\partial z^2}\zeta - \frac{\partial \phi}{\partial x}\frac{\partial \zeta}{\partial x} - \frac{\partial \phi}{\partial y}\frac{\partial \zeta}{\partial y} \quad \text{on } z = 0 \tag{2}$$

$$\frac{\partial \phi}{\partial n} = (\boldsymbol{v} + \boldsymbol{\omega} \times \boldsymbol{r}) \cdot \boldsymbol{n} \quad \text{on } S_H \tag{3}$$

$$\frac{\partial \phi}{\partial n} = v_0 \quad \text{on } S_W \tag{4}$$

where $\nabla = (\frac{\partial}{\partial x}, \frac{\partial}{\partial y}, \frac{\partial}{\partial z})$. ζ denotes wave height, g the gravity acceleration. S_H and S_W mean hull and tank wall surfaces respectively.

Eqs.(1) and (2) are free-surface conditions employed in this paper. For simplicity, we employ the 2nd order conditions with respect to ϕ and ζ obtained by Taylor expansion at $z = 0$. Eq.(3) is hull surface condition, and has to be satisfied on actual wetted surface S_H. Here $\boldsymbol{v}$ denotes ship velocity vector defined in the coordinate system fixed to ship, and $\boldsymbol{\omega}$ the angular velocity vector. $\boldsymbol{v}$ includes the component of ship speed $U(t)$. Relations between $\boldsymbol{v}$ and $\boldsymbol{\xi}$, and between $\boldsymbol{\omega}$ and $\boldsymbol{\Omega}$ are as follows:

$$\boldsymbol{v} = [E(\boldsymbol{\Omega})]\dot{\boldsymbol{\xi}}, \quad \boldsymbol{\omega} = [H(\boldsymbol{\Omega})]\dot{\boldsymbol{\Omega}} \tag{5}$$

where

*3-48 Bunkyo-Machi, Nagasaki 852-8131, JAPAN, email: yasukawa@ngsrdc.mhi.co.jp

$E(\varphi, \theta, \psi) =$

$$\begin{bmatrix} \cos\theta\cos\psi & \cos\theta\sin\psi & -\sin\theta \\ \sin\varphi\sin\theta\cos\psi - \cos\varphi\sin\psi & \sin\varphi\sin\theta\sin\psi + \cos\varphi\cos\psi & \sin\varphi\cos\theta \\ \cos\varphi\sin\theta\cos\psi + \sin\varphi\sin\psi & \cos\varphi\sin\theta\sin\psi - \sin\varphi\cos\psi & \cos\varphi\cos\theta \end{bmatrix} \tag{6}$$

$$H(\varphi, \theta, \psi) = \begin{bmatrix} 1 & 0 & -\sin\theta \\ 0 & \cos\varphi & \cos\theta\sin\varphi \\ 0 & -\sin\varphi & \cos\theta\cos\varphi \end{bmatrix} \tag{7}$$

In eq.(3), $\boldsymbol{r}$ denotes the coordinate of hull surface position, and $\boldsymbol{n}$ the outward normal vector of the hull surface.

Eq.(4) is boundary condition of tank wall surface, and v_0 means normal velocity on S_W. When generating waves in the tank, we have to give a proper value to v_0 on the tank wall with wave maker. On tank wall without wave maker, we set $v_0 = 0$.

Velocity potential ϕ is represented using source strength σ as follows:

$$\phi(P) = \iint_{S_H+S_F+S_W} \sigma(Q) G(P;Q) dS \tag{8}$$

where

$$G(P;Q) = \frac{1}{\sqrt{(x-x_1)^2 + (y-y_1)^2 + (z-z_1)^2}} \tag{9}$$

$P = (x, y, z)$ is filed point, and $Q = (x_1, y_1, z_1)$ the singular point. S_F denotes the free-surface position ($z = 0$). Substituting eq.(8) to eqs.(3) and (4), the following equations are obtained:

$$\iint_{S_H+S_F+S_W} \sigma(Q) \frac{\partial G(P;Q)}{\partial n} dS = f_H(P) \tag{10}$$

where

$$f_H(P) = \begin{cases} (\boldsymbol{v} + \boldsymbol{\omega} \times \boldsymbol{r}) \cdot \boldsymbol{n} & \text{for } P \text{ on } S_H \\ v_0 & \text{for } P \text{ on } S_W \end{cases} \tag{11}$$

The eq.(10) which represents boundary conditions on the hull and tank wall surfaces is basic equation to be solved.

Numerical Scheme

1. Accelerations of ship motions ($\ddot{\boldsymbol{\xi}}^{k+1}, \ddot{\boldsymbol{\Omega}}^{k+1}$), and time derivatives of wave height and velocity potential on free-surface (ζ_t^{k+1}, ϕ_t^{k+1}) respectively at $k+1$-th time step are assumed using values at k-th step. Here suffix t represents time derivation.

2. According to Newmark's β method, ship motion velocities and displacements at $k+1$-th step are estimated as: (Herein, only $\dot{\boldsymbol{\xi}}^{k+1}$ and $\boldsymbol{\xi}^{k+1}$ are written.)

$$\dot{\boldsymbol{\xi}}^{k+1} = \dot{\boldsymbol{\xi}}^{k} + \Delta t \left(\ddot{\boldsymbol{\xi}}^{k} + \ddot{\boldsymbol{\xi}}^{k+1} \right) / 2 \tag{12}$$

$$\boldsymbol{\xi}^{k+1} = \boldsymbol{\xi}^{k} + \Delta t\, \dot{\boldsymbol{\xi}}^{k} + \frac{(\Delta t)^2}{2} \ddot{\boldsymbol{\xi}}^{k} + \beta (\Delta t)^2 (\ddot{\boldsymbol{\xi}}^{k+1} - \ddot{\boldsymbol{\xi}}^{k}) \tag{13}$$

   where Δt is time increment, and β the acceleration factor.

3. Using eq.(5), $\dot{\boldsymbol{\xi}}^{k+1}$ and $\dot{\boldsymbol{\Omega}}^{k+1}$ are transformed to $\boldsymbol{v}$ and $\boldsymbol{\omega}$.

4. Ship hull and free-surface panels are arranged using given ship speed and motions.

5. According to Newmark's β method, wave height and velocity potential on free-surface at $k+1$-th step are estimated as:

$$\zeta^{k+1} = \zeta^k + \Delta t \left(\zeta_t^k + \zeta_t^{k+1}\right)/2, \quad \phi^{k+1} = \phi^k + \Delta t \left(\phi_t^k + \phi_t^{k+1}\right)/2 \tag{14}$$

6. Influence functions are calculated for free-surface, ship hull and tank wall surfaces to make a matrix for determining source strength. Basic equations are discretized using constant panels.

7. Solving eqs.(8) and (10), source strengths on free-surface, hull and tank wall surfaces are obtained.

8. Using eqs.(1) and (2), ϕ_t^{k+1} and ζ_t^{k+1} are calculated. Then, velocity components on free-surface are calculated analytically using the source strengths. The derivatives of ζ with respect to x and y are obtained numerically using finite differential technique.

9. Hydrodynamic forces acting on hull are calculated by Bernoulli's equation. Obtaining the hydrodynamic forces, $\dot{v}$ and $\dot{\omega}$ are calculated from the motion equations of the ship.

10. Using eq.(5), $\dot{v}$ and $\dot{\omega}$ are transformed to $\ddot{\xi}$ and $\ddot{\Omega}$.

11. $\ddot{\xi}, \ddot{\Omega}$, ζ_t and ϕ_t obtained in step 8 and 10 are compared with those assumed in step 1. When the difference between both is sufficiently small, $\ddot{\xi}, \ddot{\Omega}$, ζ_t and ϕ_t are regarded as reaching to the convergence. Otherwise, return to step 2 and calculations are continued using $\ddot{\xi}, \ddot{\Omega}$, ζ_t and ϕ_t obtained in step 8 and 10 until obtaining converged solution through this iteration.

12. One time step is increased and return to step 1.

Computed Results

Analysis of ship motions in regular head waves for a modified Wigley Hull is carried out. The hull is a mathematical form expressed as follows:

$$y' = (1-x'^2)(1-z'^2)(1+0.2x'^2) + z'^2(1-z'^8)(1-x'^2)^4 \tag{15}$$
$$\text{where} \quad x' = x/(L/2),\ y' = y/(B/2),\ z' = z/d$$

with $L/B = 10.0$ and $B/d = 1.6$. The calculated results are compared with experimental data conducted in Delft University. To obtain the experimental data, we read the data from figures in the paper presented by Sclavounos et al.[2] who used the data for comparison with their calculated results.

In the present computations, a numerical absorbing beach is put to only face-side wall against wave maker. As the absorbing technique, we apply the method proposed by Cointe et al.[3] where proper damping is added to free-surface conditions. On side walls, we don't impose any numerical beach technique and allow of wave reflections similar to actual towing tank.

Fig.1 shows comparison of heave and pitch. Froude number based on ship length F_n is 0.3. 4000 panels for free-surface, 2400 panels for tank wall, and 800 panels for ship hull are used. Computed wave amplitude of incident wave is about $0.0025L$. The calculated amplitude and phase angle for heave and pitch are agreed well with experiments.

Fig.2 shows 2 snap shots of the computed wave patterns generated by a modified Wigley hull advancing in regular head waves with λ/L=1.0. In the figure, wave contours are shown of 0 and 90deg for phase angle against incident wave from the top. The steady Kelvin waves, incident waves, scattering waves and reflected waves at tank side walls are realistically demonstrated.

References

[1] Yasukawa, H.: *Unsteady Wash Computation for a High Speed Vessel*, NuTTS'99 (1999).

[2] Sclavounos, P.D. and Nakos, D.E.: *Ship Motions by a Three-Dimensional Rankine Panel Method*, 18th Symp. on Naval Hydrodynamics (1990), Ann Arbor.

[3] Cointe, R., Geyer, P., King, B., Molin, B. and Tramoni, M.: *Nonlinear and Linear Motions of a Rectangular Barge in Perfect Fluid*, 18th Symp. on Naval Hydrodynamics (1990), Ann Arbor.

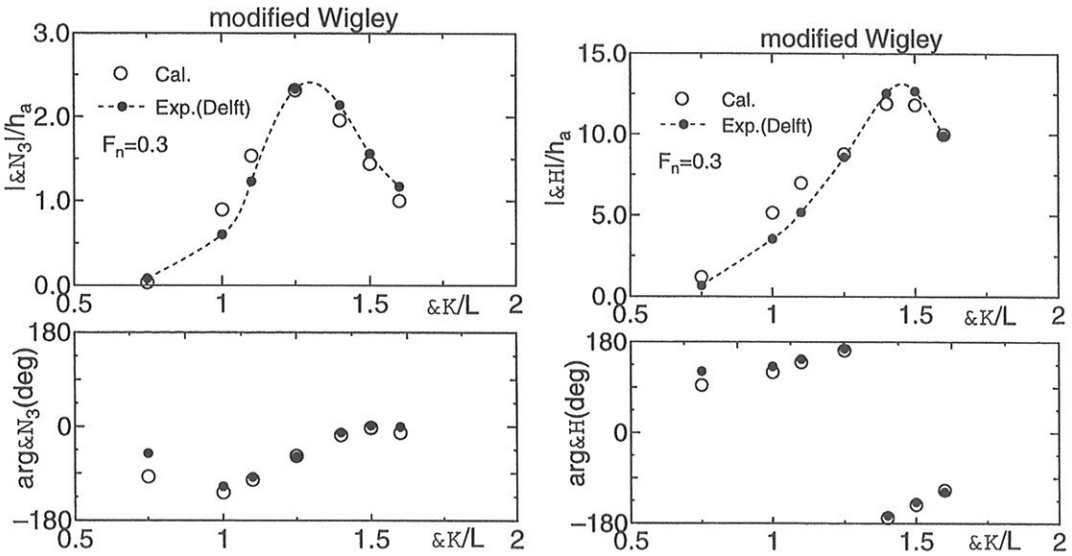

Fig.1: Comparison of heave and pitch in regular head waves

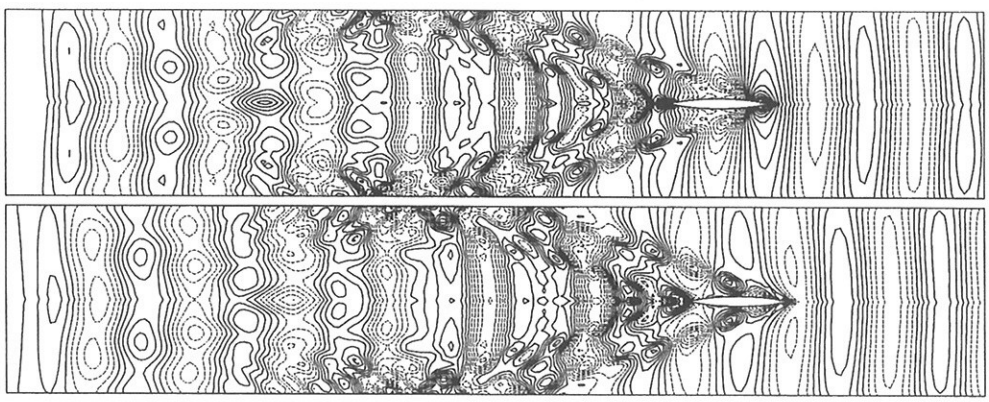

Fig.2: Computed wave patterns around a modified Wigley hull advancing in head waves (F_n=0.3, λ/L=1.0). The phase angles against incident wave are 0 and 90deg from the top.

4th Numerical Towing Tank Symposium (NuTTS'01)

Hamburg, Germany, 23-25 September 2001

Topics:

- Nonlinear flows around marine structures (LES, RANSE, Euler with or w/o free surface)
- Free-surface flows around marine structures (3-d ship seakeeping, free-surface viscous flows)
- Related topics (validation experiments, numerical techniques, grid generation, etc)

Deadlines:	Early feedback:	30 June 2001
	Abstracts received:	**30 July 2001**
	Notification of acceptance:	7 August 2001
	Last possible update:	7 September 2001

Sponsor: AEA Technology GmbH

NuTTS has steadily grown since ist start in 1998. The positive response has motivated me to take the burden once more and organise the event in 2001 in Hamburg. This time, the event is dedicated to Professor Heinrich Söding on occasion of his retirement.

You are invited to participate in the above event. The objective of the event is to provide a forum for informal discussions among experts in the field and to disseminate latest results. Younger workers and Ph.D. students are especially encouraged to participate. The event will be held at Haus Rissen in Rissen/Blankenese. All participants stay and have meals together to maximize interaction and discussion.

The abstracts of the proposed talk will be directly reproduced in the proceedings. There will be no final full papers. Rather, the symposium is intended to give 'sneak previews' to full papers. Work in progress, encountered problems, etc. should be discussed in an open, informal atmosphere among colleagues. The first page of the extended abstract should be headed with the title and authors' names and address in a compact form to economise on space. Extended abstracts should be limited to 4 pages in a field 17cm by 25cm per page. Copies of the extended abstract should be sent in good quality to the host.

An early reply will help us in organising the event better. For the early feedback, a tentative title or topic will suffice.

Following the tradition of previous NuTTS events, the fees will be kept low to allow a maximum number of scientists to attend.

Volker Bertram, Osterstr 95, D-20259 Hamburg, Germany
bertram@hsva.de